Experimental Studies of the Mechanism of Photon Absorption on Light Nuclei

Steven A. Morrow, B.Sc.

A thesis submitted to the University of Edinburgh for the degree of

Doctor of Philosophy

in the Department of Physics & Astronomy

September 13, 2000

Abstract

A measurement of the reaction ^{12}C(γ,pγ') has been made with tagged photons in the range $49.47 < E_\gamma < 70.24$ MeV. The relative population of a triplet of states, ($7/2^-$,$1/2^+$,$5/2^+$) at $E_{ex} \simeq 7$ MeV in the residual nucleus ^{11}B, following the reaction ^{12}C(γ,p), has been made by directly resolving their de–excitation γ-ray decay to the ground state of ^{11}B. This measurement constitutes the highest resolution ever achieved in determining the excitation function of the residual nucleus after a (γ,p) reaction ($\sim$48 keV FWHM at $E_{ex} \simeq 7$ MeV). Comparison has been made with the data of Kuzin *et al.*, who also measured the relative populations, with a resolution of $\sim$270 keV at $E_{ex} \simeq 7$ MeV. The $7/2^-$ state at 6.74 MeV has been observed to be the most strongly excited state of the triplet in agreement with Kuzin *et al.* Disagreement has been found for the relative strengths of the $1/2^+$ and $5/2^+$ states in the triplet. An estimation of the maximum effect of angular correlations, between the ejected proton and de–excitation γ-ray, has been included in the analysis. This effect increases the disagreement between the 2 measurements.

A study of the reaction ^{12}C(e,e$'$p) has been made in the missing momentum region $260 < \mathbf{p}_m < 320$ MeV/c. A Rosenbluth separation of the reaction cross section has been carried out in parallel kinematics to measure the structure functions W_L and W_T. The experimental data have been compared with Complete Distorted Wave Impulse Approximation calculations and Random Phase Approximation calculations. The latter, when including virtual photon absorption on 2–body currents (Meson Exchange Currents + Isobar Currents) are seen to describe the reduced cross sections better than 1–body current or Complete Distorted Wave Impulse Approximation calculations.

For the 1st time a comparison between the ^{12}C(γ,p) reaction and the transverse part of ^{12}C(e,e$'$p) reaction cross section has been made. This comparison suggests that the mechanism of the 2 reactions converge when both are studied in equivalent kinematics, resolving the long standing issue of anomalous excitation of the $\sim$7 MeV triplet in ^{11}B, following ^{12}C(γ,p), not seen in the ^{12}C(e,e$'$p) case.

In a further use of the (γ,pγ') reaction, the relative population of the 4.44 MeV (T=0) & 15.1 MeV (T=1) states in ^{12}C, following ^{14}N(γ,pn), have been measured, with tagged photons in the range $50.20 < E_\gamma < 71.40$ MeV. A strong suppression for population of the T=1 state in the residual nucleus, as compared to the T=0 state was observed. This is consistent with the picture of photon absorption on T=0 ($^3S_1$) p–n pairs in nuclei. A measurement of the ^{14}N(γ,d) reaction has also been made, in which the converse population of states in ^{12}C was observed.

Declaration

The data presented in this thesis were obtained in experiments carried out by the Edinburgh University Nuclear Physics group, in collaboration with the Nuclear Physics groups at the Universities of Lund and Glasgow and the EMIN group at the National Instuut voor Kernfysica en Hoge–Energiefysica (NIKHEF), Amsterdam. I have played a major role in the experiments performed at MAX–LAB, Lund. The data analysis and interpretation are my own work. This thesis has been written by myself.

Steven A. Morrow

Acknowledgements

I would like to thank my supervisor, Prof. Derek Branford, for his help during this project. I would also like to thank my second supervisor, Prof. Alan Shotter. My thanks go to the other students who have been in the Edinburgh Nuclear Physics group during my time (esp. Alison, Will, Darren, Jason and Feraidoun) and also Alessia for creating an enjoyable atmosphere in which to work. More recently Frédéric Sarazin has been a great help in keeping me sane during the last hectic months of my PhD. An especially big thanks goes to Tom Davinson, without whom most of the experiments with which I was involved could not have happened and whose help with analysis was invaluable. Also thanks go to Gordon Turnbull for his technical help during experiments.

A very big thank you must go to my family (Mum, Dad and Jane) for their unwavering support, both moral and financial. I am sure it seemed to them that I would never finish! Also the Porters, from Dunfermline; the frequent Sunday dinners reminded me of living at home.

To the people in Lund, I would like to thank Bent Schröder for his hospitality, and the many times he arranged accommodation for me. I would especially like to thank Jan-Olof Adler for his kindness as well as the opportunity to analyse the ^{14}N data presented in this thesis. And to Jan-Olof an extra thank you is required for paying for my last trip to Lund in February '00 to discuss the analysis. Thanks to Magnus Lundin for the many conversations which helped pass the long night shifts. Thanks also to all the other students and staff at MAX–LAB who helped on the experimental shifts and of course the Melbourne people, who kept us all in craic.

I would like to thank Cameron M^{c}George for being present to offer his help during my experiments and also to Klaus Föhl, both of whom helped on many long hours of shifts when only 3 people were available to give 24 hour attention to the experiments. I'd also like to thank John Annand from Glasgow for his technical help.

The people I met at NIKHEF were all very helpful, mostly for having put up with my many stupid questions. Thank you to Louk Lápikus and Gerard van der Steenhoven, who have both been very helpful. Louk Lápikus especially for undertaking to teach me, in 3 weeks, everything I needed to know to analyse (e,e$'$p) data and for arranging my accommodation during my visits. I'd also like to thank Marcel van Batenburg, without whose tireless assistance, patience and willingness to help, I would not have managed.

Jan Ryckebusch was kind enough to provide calculations to compare with the data presented here. Also calculations were provided by Dimitri Van Neck,

but were finally not used.

A big thank you goes to my friend Glenn Cunningham for dutifully proof reading this thesis. This is despite the fact that he never saw fit to return his corrections to me; Cheers Glenn!

Finally I wish to acknowledge the financial support of the Engineering and Physical Sciences Research Council (EPSRC) throughout the 1st three years of this project.

Contents

Abstract iii

Declaration v

Acknowledgements vii

List of Figures xiii

List of Tables xvii

List of Abbreviations xix

1 Introduction 1

2 Motivation 5

2.1 Proton Knockout with Electromagnetic Probes 5

2.2 Motivation for the study of (γ,p) on ^{12}C 11

2.2.1 Discrepancy between (e,e′p) and (γ,p) 11

2.2.2 A review of recent ^{12}C(γ,p) data 16

2.3 Using ^{12}C(γ,pγ') as a means of measuring high resolution ^{12}C(γ,p) 23

2.3.1 The Measurement of Kuzin *et al.* 24

2.3.2 The Present Measurement 26

2.4 ^{12}C(e,e′p) for Comparison to ^{12}C(γ,p) 28

2.5 Isospin Selection Rules in ^{14}N(γ,d) and ^{14}N(γ,pn) 29

2.6 Overview of the Remainder 33

3 Real Photon Experiments at MAX–LAB **35**
3.1 Electron Beam 36
3.2 Photon Tagging 38
3.3 Targets 42
3.4 Detecting Reaction Products 42
3.4.1 Charged Particles 44
3.4.2 De–excitation γ-rays 47
3.5 Detector Configuration 50
3.5.1 Run #1 (^{12}C(γ,pγ')) 50
3.5.2 Run #2 (^{14}N(γ,Xγ')) 52
3.6 Electronics 53
3.7 Count Rates 53
3.8 Summary Table 58

4 Real Photon Induced Proton Knockout from ^{12}C **59**
4.1 Analysis of Charged Particle Telescope Information 60
4.1.1 Particle Identification 60
4.1.2 Tagger Calibration 61
4.1.3 Calibration of Proton Telescope 61
4.1.4 Identification of Tagged Photons 68
4.1.5 Reconstruction of E_{ex} 69
4.2 Analysis of De–excitation γ-rays 73
4.2.1 Derivation of the γ' Spectra 73
4.2.2 Calibration of HPGe 70 % Detector 74
4.2.3 Doppler Correction 75
4.2.4 Efficiency of HPGe 70 % 79
4.2.5 Response Function of HPGe 70 % 81
4.2.6 'Untagged' γ' Spectrum 84
4.2.7 Fitting Detector Response Functions to the De–excitation γ' Spectra 86
4.3 Results 90
4.3.1 Population of levels in ^{11}B 90

4.3.2 Angular Correlations 97

5 Electron Induced Proton Knockout from ^{12}C 103

5.1 Formalism of an (e,e′p) Reaction 103

5.2 Electron Scattering at NIKHEF 106

5.2.1 The MEA Accelerator and AmPS 106

5.2.2 Product Detectors and Target 107

5.2.3 Kinematical Conditions 108

5.3 Analysis 111

5.3.1 GLANCE Analysis of (e,e′p) Experiments 111

5.3.2 Finite Acceptance Effects 116

5.3.3 Error Propagation 118

5.4 The L–T Separation 120

5.5 Results 122

5.5.1 CDWIA Calculations 122

5.5.2 MEC and Δ–Isobar Calculations 130

5.5.3 Comparison to ^{12}C(γ,p) Data 131

6 Analysis and Results of the ^{14}N(γ,Xγ') Experiment 135

6.1 Charged Particle Analysis 135

6.2 E_m & ^{12}C Background Subtraction 136

6.3 Derivation of De–excitation γ' Spectra 141

6.4 Selection of the (γ,pn) Channel from the (γ,pγ') Data 143

6.5 Results 147

7 Discussion & Summary 151

Appendices 157

A Numerical Results from the ^{12}C(e,e′p) Experiment 157

B Optical Model Parameters for CDWIA Calculations 163

Bibliography 164

List of Figures

2.1 Schematic of the (e,e′p) and (γ,p) processes. 6
2.2 Momentum vectors for the (e,e′p) and (γ,p) processes. 7
2.3 **q** v's ω phase space covered in the (e,e′p) and (γ,p) reactions. 10
2.4 ^{12}C(γ,p) excitation spectrum of Shotter *et al.* 11
2.5 ^{12}C(e,e′p) excitation spectrum of van der Steenhoven *et al.* . 12
2.6 Momentum distribution for the 6.8 MeV doublet of ^{11}B. . . 13
2.7 Energy level diagram of ^{11}B, with spins and parities, [Ajz90]. 16
2.8 Springham *et al.* ^{12}C(γ,p) excitation spectrum, [Spr90]. . . . 18
2.9 Van Hoorebeke *et al.* ^{12}C(γ,p) excitation spectrum, [Hoo90]. 18
2.10 Ireland *et al.* ^{12}C(γ,p) excitation spectrum, [Ire93]. 19
2.11 Bobeldijk ^{12}C(γ,p) excitation spectrum, [Bob95]. 20
2.12 Rauf ^{12}C(γ,p) excitation spectrum, [Rau96]. 21
2.13 ^{12}C(γ,p) excitation spectrum, [Rui96]. 21
2.14 Aschenauer *et al.* ^{12}C(γ,p) excitation spectrum, [Asc97]. . . 22
2.15 ^{12}C(γ,p) E_m spectrum of Kuzin *et al.*, [Kuz98]. 26
2.16 ^{12}C(γ,pγ') spectrum of [Kuz98]. 27
2.17 ^{11}B triplet cross sections from [Kuz98]. 27
2.18 Isospin selection rule (ΔT=1) for ^{14}N(γ,d). 31
2.19 ^{14}N(γ,d) excitation spectrum, [Ire91] 32

3.1 Schematic of the MAX–LAB microtron 36
3.2 The MAX–LAB microtron and stretcher ring. 37
3.3 Idealised beam profile extracted from the stretcher ring. . . . 38
3.4 A schematic of the process of photon tagging. 39

3.5 Example bremsstrahlung spectrum. 40
3.6 Tagging efficiency ADC spectrum. 41
3.7 The tagging efficiency for run #1. 43
3.8 The tagging efficiency for run #2. 43
3.9 Schematic of a charged particle telescope. 44
3.10 Photograph of a telescope in an experimental setup. 45
3.11 HPGe #1 detector. 46
3.12 HPGe #2 detector. 47
3.13 HPGe 70 % detector. 48
3.14 Resolution of the HPGe 70 % detector v's shaping time. . . 49
3.15 Resolution of the HPGe 70 % detector v's $E_{\gamma'}$. 50
3.16 The detector setup of run #1, the ^{12}C(γ,pγ') experiment. . . 51
3.17 The detector setup of run #2, the ^{14}N(γ,Xγ') experiment. . 52
3.18 Signal processing electronics for run #1. 54
3.19 Signal processing electronics for run #2. 55

4.1 2–D particle identification plot. 61
4.2 Photon energy calibration. 62
4.3 E_{ex} spectra from thin target runs. 63
4.4 Proton energy spectra. 65
4.5 Calibration plot for HPGe proton detector. 66
4.6 Definition of angles θ_p and ϕ_p. 66
4.7 Focal plane TDC spectrum. 69
4.8 Flowchart of the analysis steps for ^{12}C(γ,pγ'). 70
4.9 E_{ex} spectrum from the 2.5 mm ^{12}C target. 72
4.10 TDC spectrum of the HPGe 70 % detector. 74
4.11 Calibration spectrum taken with HPGe 70 % detector. . . . 75
4.12 HPGe 70 % detector calibration. 76
4.13 Vector reconstruction used for Doppler correction of the γ' energy. 77
4.14 Reconstruction of beam spot on target. 78

4.15 Distribution of the angle ($\theta_{\gamma'}$) between the vectors $\mathbf{v}_r$ and $\mathbf{r}_{\gamma'}$ of fig. 4.13. 79
4.16 Effect of the Doppler correction. 80
4.17 Absolute efficiency of HPGe 70 % detector 81
4.18 Example of the γ-ray line shape function. 82
4.19 Fit to the Am–Be source spectrum at 4.439 MeV. 83
4.20 Untagged de–excitation γ' spectrum. 85
4.21 Electromagnetic transitions in ^{11}B. 86
4.22 De–excitation γ' spectrum. 87
4.23 Fits to the untagged γ' spectrum at $E_{\gamma'}\sim$5 MeV. 89
4.24 Fits to the untagged γ' spectrum at $E_{\gamma'}\sim$7 MeV. 89
4.25 Fits to the $\mathcal{P}^{\gamma'}$ spectrum at $E_{\gamma'}\sim$5 MeV. 91
4.26 Fits to the $\mathcal{P}^{\gamma'}$ spectrum at $E_{\gamma'}\sim$7 MeV. 91
4.27 E_{ex} $\mathcal{S}$ spectrum for 60.71<E_γ<70.24 MeV. 96
4.28 $\mathcal{P}^{\gamma'}$ spectrum for 60.71<E_γ<70.24 MeV and 3.3<E_{ex}<10.6 MeV. 96
4.29 Angular distribution for the 6.74 MeV γ-ray from ^{11}B. . . . 99
4.30 Normalised cross sections for the triplet in ^{11}B following ^{12}C(γ,p), without inclusion of the factor R_γ. 101
4.31 Normalised cross sections for the triplet in ^{11}B following ^{12}C(γ,p), after inclusion of the factor R_γ. 101

5.1 Scattering and Reaction planes of an (e,e′p) reaction. 104
5.2 Parallel and perpendicular kinematics in an (e,e′p) reaction. 105
5.3 QDD and QDQ magnetic spectrometers. 107
5.4 Particle vectors for each (e,e′p) measurement. 109
5.5 Phase space, (E_m,$\mathbf{p}_m$), covered in ^{12}C(e,e′p). 110
5.6 Flowchart of the ^{12}C(e,e′p) analysis. 112
5.7 Spectrum of corrected time between spectrometers. 113
5.8 An E_{ex} spectrum derived from GLANCE. 113
5.9 ^{12}C(e,e′p) excitation spectra. 115
5.10 Kinematical domains in $\mathbf{q}$ and ω. 117
5.11 Rosenbluth plots for the gs transition. 121

5.12 Momentum distributions corresponding to 1p knockout. . . . 124
5.13 Momentum distributions for the 7 MeV triplet. 125
5.14 Momentum distributions for the 1p transitions. 126
5.15 Momentum distributions for the 7 MeV triplet. 127
5.16 Structure Functions for the 1p transitions. 128
5.17 Structure Functions for the 7 MeV triplet. 129
5.18 Comparison of (γ,p) and (e,e′p) data. 132
5.19 Comparison of (γ,p) and (e,e′p) data as a function of $\mathbf{p}_m^{eff}$. . 133

6.1 Particle ID for the ^{14}N(γ,Xγ') measurement. 136
6.2 Focal plane TDC Spectrum for the ^{14}N(γ,Xγ') experiment. . 137
6.3 E_{ex} spectrum for ^{14}N(γ,p), showing ^{12}C background. 139
6.4 E_{ex} spectrum for ^{14}N(γ,p), ^{12}C background subtracted. . . . 139
6.5 E_{ex} spectrum for ^{14}N(γ,d), ^{12}C background subtracted. . . . 140
6.6 Detector threshold in ^{14}N(γ,d). 141
6.7 NaI γ-ray detector calibrations. 142
6.8 NaI #1 resolution. 142
6.9 NaI p–γ' TDC spectrum. 144
6.10 $E_{\gamma'}$ vs. p–γ' TDC for NaI detectors. 144
6.11 Energy spectrum of neutrons in NaI detectors. 145
6.12 Level scheme of ^{13}C showing the relative position of ^{12}C + n system. 145
6.13 De–excitation γ-ray spectrum from ^{14}N(γ,pγ'), E_{ex}<4.95 MeV. 146
6.14 De–excitation γ-ray spectrum from ^{14}N(γ,pnγ'). 146

List of Tables

2.1 A review of recent ^{12}C(γ,p) measurements made using tagged photons. 16

3.1 Table of parameters for experimental runs #1 and #2. . . . 58

4.1 Electromagnetic transitions in ^{11}B. 93
4.2 The population of levels in ^{11}B. 94
4.3 Estimated effect of angular correlations. 100
4.4 The population of levels in the $\sim$7 MeV ^{11}B triplet including the angular correlation effect. 102
4.5 Normalised cross sections at θ_p=70° for the levels in ^{11}B. . . 102

5.1 Central kinematics for the (e,e′p) measurements. 110
5.2 Systematic errors on the (e,e′p) cross sections. 118
5.3 CDWIA parameters. 130

6.1 The relative population of levels in ^{12}C following ^{14}N(γ,pn). 148

A.1 Reduced cross sections for the 5 resolved transitions. 158
A.2 Kinematics for the 1p transitions. 159
A.3 Kinematics for the triplet states. 160
A.4 Structure functions for the 5 resolved transitions. 161

B.1 Optical potential parameters used in CDWIA calculations. . 163

List of Abbreviations

ADC	**A**nalogue–to–**D**igital–**C**onverter
AMP	**AMP**lifier
AmPS	**Am**sterdam **P**ulsed **S**tretcher
CDWIA	**C**omplete **D**istorted **W**ave **I**mpulse **A**pproximation
DE	**D**ouble **E**scape peak
CFD	**C**onstant–**F**raction–**D**iscriminator
DKO	**D**irect **K**nock**O**ut
DSSSD	**D**ouble **S**ided **S**ilicon **S**trip **D**etector
DWIA	**D**istorted **W**ave **I**mpulse **A**pproximation
FSI	**F**inal **S**tate **I**nteraction
FWHM	**F**ull **W**idth at **H**alf **M**aximum
Ge	**Ge**rmanium
GLANCE	**GL**obal **A**nalysis of **C**oincidence **E**xperiments
gs	**g**round **s**tate
HPGe	**H**igh **P**urity **Ge**rmanium
IA	**I**mpulse **A**pproximation
IC	**I**sobar **C**urrent
IPSM	**I**ndependent **P**article **S**hell **M**odel
J^{π}	Spin–Parity
LEGe	**L**ow **E**nergy **Ge**rmanium
LN_2	**L**iquid **N**itrogen
L–T	**L**ongitudinal–**T**ransverse
MAXLAB	**M**icrotron **A**ccelerator for **X**–rays **LAB**oratory
MEA	**M**edium **E**nergy **A**ccelerator
MEC	**M**eson **E**xchange **C**urrents
MWDC	**M**ulti–**W**ire **D**rift **C**hamber
NIKHEF	**N**ational **I**nstuut voor **K**ernfysica en **H**oge–**E**nergie**F**ysica
PA	**P**re–**A**mplifier
Pb	Lead
PP	**P**hoto**P**eak
PWIA	**P**lane **W**ave **I**mpulse **A**pproximation
QDD	**Q**uadrupole–**D**ipole–**D**ipole
QDQ	**Q**uadrupole–**D**ipole–**Q**uadrupole
QFK	**Q**uasi **F**ree **K**nockout
RPA	**R**andom **P**hase **A**pproximation
SE	**S**ingle **E**scape peak
Si	**Si**licon
TDC	**T**ime–to–**D**igital–**C**onvertor
TFA	**T**iming–**F**ilter–**A**mplifier

Chapter 1

Introduction

The nucleus is commonly viewed in terms of strongly interacting protons and neutrons. This picture disguises the underlying structure of quarks and gluons, from which these constituents are themselves composed. However, the simpler picture of nuclei as composed of nucleons, moving in a mean field and subject to *residual strong interactions*, has been successful in describing many nuclear phenomena. The experimental study of nuclei on this level has provided much useful information. In addition, probing the nuclear interior via the electromagnetic interaction is regarded as a particularly useful way of gleaning information at this level of structure. Since photons are the force carriers of this interaction they allow us to examine the nucleus in two different ways: by the absorption of real photons, or the exchange of virtual photons with the nucleus. The exchange of virtual photons is induced by the scattering of charged leptons from the nucleus; therefore, both real photon (γ-ray) and electron beams may be used as experimental probes.

Electromagnetically induced nuclear reactions may be considered a better probe of the nucleus than reactions involving hadronic beams. In the latter case, both the entrance and exit channels involve the strong interaction which, as the subject of study, is by definition not well understood. For electromagnetic probes, since their interaction is described accurately by the theory of quantum electrodynamics (QED), only the coupling of the

photon to nuclear currents includes ambiguous mechanisms. Also, due to the relative weakness of the electromagnetic field (with respect to the strong force), the perturbation of the nucleus under investigation is weak. Therefore the system being studied is not altered greatly by the measurement and the whole nuclear volume may be explored. From a theoretical view point therefore, the electromagnetic interaction is a very useful tool for studying nuclear structure.

From an experimental standpoint, however, the study of nuclei with electromagnetic probes is challenging. For the very reason that the perturbation of the nucleus is weak, reaction cross sections are low. This gives rise to difficulties in making coincidence experiments, which are required to study exclusive reactions where the final state is completely determined. For the specific case of real photons, it is also true that the production of intense, highly energetic γ-ray beams (of known energy) is non-trivial. However the promise of good quality data on the structure of nuclei has been motivation enough for this probe to be widely used.

Information on the single particle properties of nuclei have been studied extensively with the electromagnetic interaction using nucleon knockout reactions. Single nucleons, or clusters of nucleons, are knocked out of the nucleus depending on the level of structure wished to be studied. For example, the scattering of electrons has been used to study proton knockout through the exclusive inelastic reaction (e,e$'$p). The resulting data have uncovered evidence for under–occupancy of nuclear levels below the Fermi surface, as compared to the predictions of the Independent Particle Shell Model (IPSM), and non–zero occupancy of levels above the Fermi surface. Occupancies of $\sim$40–50 % of the IPSM predictions have been measured for levels below the Fermi surface, [Wit90]. This is an indication that correlations between nucleons play an important role in nuclei. It also implies that such reactions do not simply proceed via direct knockout of the detected nucleon, with the remaining nucleus behaving as a spectator.

Therefore, although these results have proven very useful for extracting the desired information, it is necessary to separate the reaction mechanism

from the nuclear structure effects. Specifically, the mechanism of real photon absorption on nuclei, in the energy region used to study single nucleon properties, is still under debate. Understanding this mechanism is necessary in order to uncover the underlying nuclear structure information available from photonuclear reactions (i.e. those induced by *real* photons).

This thesis will concentrate on a series of experiments designed to help understand the mechanism of photonuclear reactions. To this end a set of high resolution data will be presented, on both real and virtual photon induced knockout reactions, made on two light (N=Z) nuclei, C and N. As will be described, achieving a sufficiently high energy resolution to distinguish transitions from individual nuclear states, has proven difficult in certain cases. To remedy this, the study of real photon induced reactions presented here has employed a novel technique. The de–excitation γ-ray decay of the residual nucleus to its ground state is measured in coincidence with the knocked out nucleon. This provides high resolution data on the excitation function of the residual nucleus. The next chapter will give the scientific motivation for the three experimental measurements presented in this thesis and section 2.6 will outline the contents of the remainder of this thesis.

Chapter 2

Motivation

This chapter will outline the scientific motivation for the experimental studies presented in this thesis. Section 2.1 will explain the complimentary information which can be gained from photon and electron induced proton knockout reactions. The reaction ^{12}C(γ,p) is discussed in section 2.2. This leads on to the motivation for the first two measurements in this thesis, described in sections 2.3 and 2.4, which were the study of the reactions ^{12}C(γ,pγ') and ^{12}C(e,e$'$p), respectively. Next, section 2.5 explains the motivation for a measurement made of two nucleon knockout from ^{14}N, induced by real photons. Finally, section 2.6 gives an overview of the remainder of this thesis.

2.1 Proton Knockout with Electromagnetic Probes

As stated in the introduction, electromagnetic probes consist of both real photons and electrons (which exchange virtual photons with the nucleus). This section will describe how both probes may be used to study proton momentum distributions in nuclei, through the knockout reactions (γ,p) and (e,e$'$p). The method of comparison presented here is taken from [Ire94]. In the quasi–elastic region, the (e,e$'$p) reaction involves emission of a proton

induced by the exchange of a virtual photon. The (γ,p) reaction involves the emission of a proton induced by the absorption of a real photon. Fig. 2.1 shows a schematic of each process.

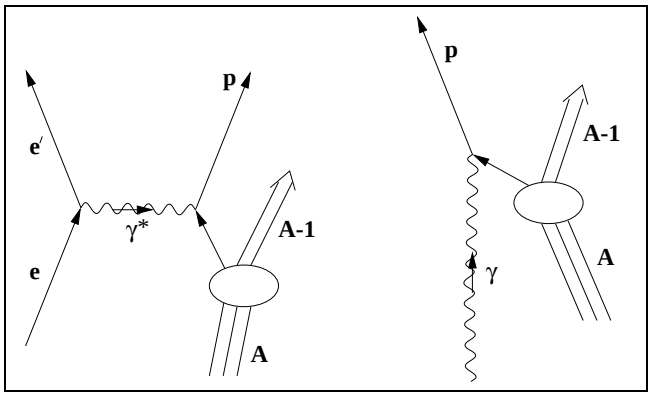

Figure 2.1: *Schematic of the (e,e′p) and (γ,p) processes.*

When presenting results from each reaction it is common practice to define the quantities missing momentum, $\mathbf{p}_m$, and missing energy, E_m, in the following manner

$$\mathbf{p}_m = \mathbf{p}' - \mathbf{q} \tag{2.1}$$

$$E_m = \omega - T_p - T_r \tag{2.2}$$

where $\mathbf{p}'$ and T_p are the momentum and kinetic energy of the outgoing proton; T_r is the kinetic energy of the residual, A-1, nucleus and $\mathbf{q}$ and ω are the momentum and energy imparted to the nucleus in the reaction, respectively. For electron scattering $\mathbf{q}$ and ω are the momentum and energy lost by the scattered electron, whereas for (γ,p) they are simply the momentum of the absorbed photon ($\mid \mathbf{q} \mid = \omega = E_\gamma$). Fig. 2.2 shows the definition of $\mathbf{p}_m$ for both (e,e′p) and (γ,p). The missing energy, E_m, is related to the excitation energy of the residual nucleus by

$$E_{ex} = E_m + Q_{gs} \tag{2.3}$$

where Q_{gs} is the Q–value for the reaction to take place to the ground state of the residual. The missing energy therefore corresponds to the energy with

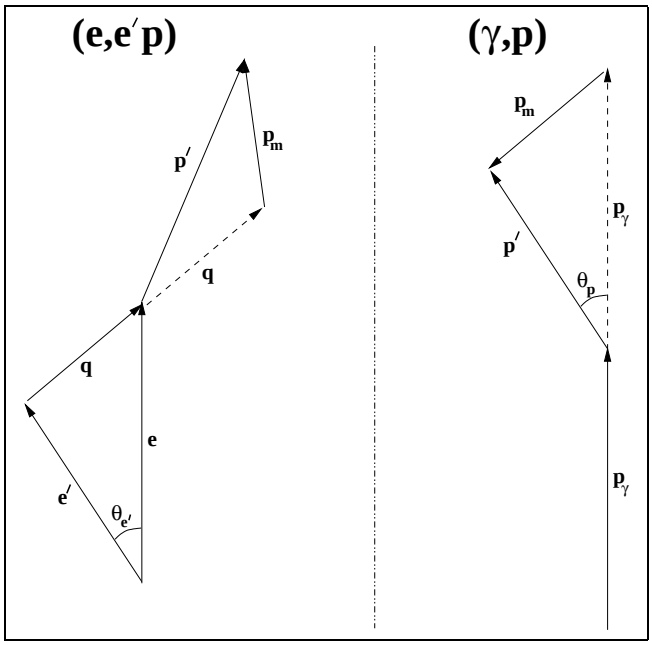

Figure 2.2: *Momentum vectors for the (e,e'p) and (γ,p) processes, showing the definition of the vector* $\mathbf{p}_m$ *in each case.*

which the knocked out proton was bound within the target nucleus.

In each case the missing momentum, $\mathbf{p}_m$, is the momentum carried away by the residual system. This momentum is typically large, and, since the target may be assumed to be at rest in the laboratory before the reaction, the missing momentum is interpreted as the initial momentum of the struck proton within the target nucleus. The quantities E_m and $\mathbf{p}_m$ therefore allow the mapping out of the excitation energy and proton momentum dependence of the knockout reactions.

So, by knocking out a nucleon (here a proton) from a nucleus and looking at the excitation spectrum of the recoiling A-1 system, it is possible to observe transitions to single particle levels. Further, the momentum dependence of these levels may be interpreted as the square of the overlap wave function between the initial and final states, $|\phi(\mathbf{p}_m)|^2$, in the momentum space of the struck proton. See for example [Wit90, Wit96] for a review of such experiments with electron scattering, and [Owe91, Fin77, Fin78] for the photonuclear case.

The momentum distribution of the proton may be derived from the measured cross sections for both reactions in the simplest theoretical framework, the plane–wave impulse–approximation (PWIA) [Fru84]. In the PWIA, where the outgoing proton is approximated by a plane wave, the (e,e′p) cross section for a transition to a specific state in the residual nucleus, when expressed as a sixfold differential, can be written in a factorised form [Bof82]

$$\sigma_{ee'p} \equiv \frac{d^6\sigma}{dE_e d\Omega_e dE_p d\Omega_p} = \mathrm{K}\sigma_{ep}|\phi_\alpha(\mathbf{p}_m)|^2 \tag{2.4}$$

where K is a kinematical factor (K=$\mathbf{p}'E_p$), E_p is the total energy of the proton, σ_{ep} is the off–shell electron–proton scattering cross section [DeF83], and $\phi_\alpha(\mathbf{p}_m)$ is the overlap wave function (between the initial and final states) in the momentum space of the proton, for a state labelled by the quantum numbers α.

It is then possible to define a *reduced* cross section

$$\rho_{ee'p}(\mathbf{p}_m) = \frac{\sigma_{ee'p}}{\mathrm{K}\sigma_{ep}} \tag{2.5}$$

where $\sigma_{ee'p}$ is the measured cross section. Division by Kσ_{ep} removes the effects due to the electron–proton coupling and the electron kinematics, leaving only a term describing the nuclear structure effects. The quantity $\rho_{ee'p}(\mathbf{p}_m)$ (which in the PWIA reduces to the squared Fourier transform of the radial overlap wave function) can then be regarded as the proton momentum distribution modified only by the proton distortions and kinematics, (also termed final state interactions, FSI).

In the case of the (γ,p) reaction, a PWIA factorised cross section may also be defined, in the Direct Knockout (DKO) model. Again selecting a specific transition this is defined by

$$\sigma_{\gamma p} \equiv \tfrac{d\sigma}{d\Omega} = \mathrm{C}(\mathbf{p}'^2_{c.m.}\sin^2\theta_p + \frac{1}{2}g_p^2\mathbf{q}^2)|\phi_\alpha(\mathbf{p}_m)|^2 \tag{2.6}$$

where θ_p is the outgoing proton angle; $\mathbf{p}'_{c.m.}$ is the center–of–mass value of

the outgoing proton momentum; g_p (=1.792 μ_N) is the anomalous part of the proton magnetic moment; $\mathbf{q}$ is the photon momentum and C is a kinematic factor, defined as

$$\mathrm{C} = 2\pi^2(\frac{e^2}{\hbar c})(\frac{\mathbf{p}' E_p}{(m_p c^2)^2})(\frac{(\hbar c)^2}{\mathbf{q}}) \tag{2.7}$$

where E_p and m_p are the total energy and mass of the proton, respectively, and all other symbols have their usual meanings.

The first term between the brackets in equation 2.6 is due to the coupling of the absorbed photon to the convection current, and the second to the magnetic moment, of the proton. Again, the cross section has been factorised into a term representing the reaction mechanism and a term representing the properties of the proton within the target nucleus. Therefore, by analogy with the (e,e′p) case, a *reduced* cross section may also be defined for the (γ,p) case

$$\rho_{\gamma p}(\mathbf{p}_m) = \frac{\sigma_{\gamma p}}{\mathrm{C}(\mathbf{p}'^2_{c.m.}\sin^2\theta_p + \frac{1}{2}g_p^2\mathbf{q}^2)} \tag{2.8}$$

It can be seen from equations 2.4 and 2.6 that in PWIA the reduced cross sections should be identical, as both depend only on the properties of the proton within the target nucleus. Therefore, as stated in [Ire94]

$$\rho_{ee'p} = \rho_{\gamma p} = |\phi_\alpha(\mathbf{p}_m)|^2 \tag{2.9}$$

i.e., both represent the square of the overlap wave function between the initial and final state in the momentum space of the struck proton.

In the case of the (e,e′p) reaction, $\mathbf{q}$ and ω are the momentum and energy transferred to the target nucleus via the virtual photon, and may be varied independently. The shaded region of fig. 2.3 shows the phase space available in each reaction. In the (γ,p) case, where we have $|\mathbf{q}| = \omega = E_\gamma$ (= the incident photon energy), there is less kinematic freedom. This has resulted in different regions of the momentum wave function being probed for the two reactions. For the most part, recent high resolution (e,e′p) data

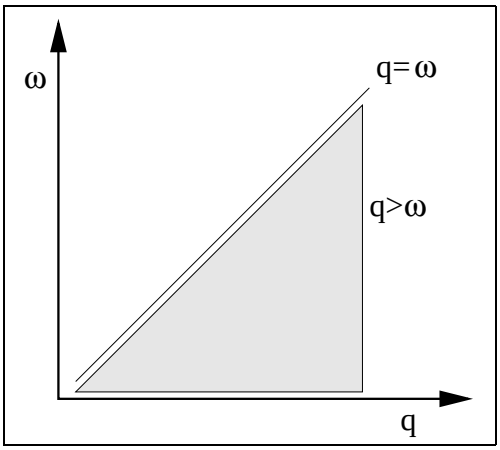

Figure 2.3: **q** *v's* ω *phase space covered in the (e,e′p) and* (γ,p) *reactions.*

have sampled low $\mathbf{p}_m$, while (γ,p) data have sampled higher values, i.e.

- $\mathbf{p}_m^{\gamma p}$ >250 MeV/c (for $|\mathbf{q}^{\gamma p}|$ ∼60 MeV/c),

- $\mathbf{p}_m^{ee'p}$ <250 MeV/c (for $|\mathbf{q}^{ee'p}|$ ∼250 − 450 MeV/c).

It may be argued then that, in the DKO framework, the two reactions are complementary in the sense that they measure the same momentum distribution, but at different $\mathbf{p}_m$. Therefore, both (e,e′p) and (γ,p) reduced cross sections would be expected to scale as a function of $\mathbf{p}_m$ if DKO is a good description of the (γ,p) mechanism.

A lack of scaling in some specific cases [Ire94] has resulted in other reaction mechanisms being put forward for (γ,p). Some have claimed that mechanisms involving two nucleons (as opposed to only one in DKO) are dominant [Gar81, Ryc88, Cav84]. Such a mechanism means that the (γ,p) reaction may not simply be used as a high momentum analogy to (e,e′p), which itself is explained well in terms of DKO [Ste88a]. Therefore models of the (γ,p) reaction are needed which will describe the reaction and enable an interpretation of its results. Such models require good experimental data as constraints.

2.2 Motivation for the study of (γ,p) on ^{12}C

In most cases the (γ,p) and (e,e′p) reactions give similar results in that the relative population of states in the residual nucleus is roughly equal in both cases for studies on the same target nucleus.

A test of the comparability of these two reactions must come from cases where they have been observed to differ. In one specific case, that of ^{12}C, there is a marked difference. In this case ^{12}C(γ,p) shows an anomalous strength in the cross section at ∼7 MeV excitation in the residual nucleus ^{11}B. This strength is not seen in ^{12}C(e,e′p). This observed discrepancy between the two reactions is highlighted next.

2.2.1 Discrepancy between (e,e′p) and (γ,p)

In a measurement of the reaction ^{12}C(γ,p)^{11}B* by [Sho88] (the first measurement to resolve individual transitions in ^{11}B) at an energy of E_γ=60 MeV, a strong excitation was observed for a region of excitation energy around ∼7 MeV in ^{11}B (see fig. 2.4). This has remained an item of interest for a

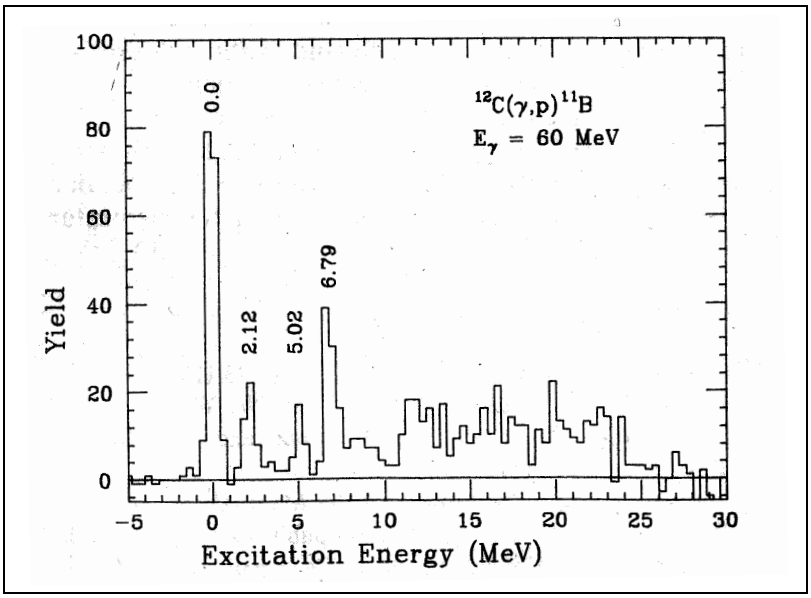

Figure 2.4: *Shotter et al. $^{12}C(\gamma,p)$ excitation spectrum, [Sho88], for 250<$\mathbf{p}_m$<320 MeV/c. The resolution is ΔE_{ex}≃500 keV FWHM.*

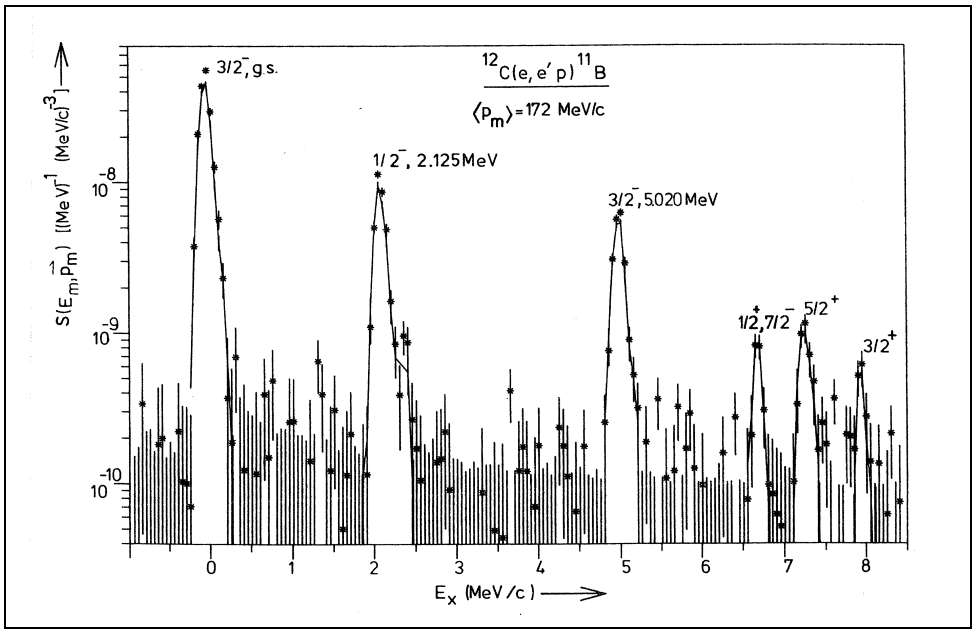

Figure 2.5: *$^{12}C(e,e'p)$ excitation spectrum, [Ste88a]. The <$\mathbf{p}_m$> (=172 MeV/c) is lower than that for the (γ,p) measurement of Shotter et al., see fig. 2.4. The resolution is $\Delta E_{ex} \simeq 150$ keV FWHM.*

number of years because this strength in the spectrum is noticeably different from that in spectra obtained in studies of the ^{12}C(e,e′p)^{11}B reaction, [Ste88a] and [Ste88b]. Compare the $E_{ex} \simeq 7$ MeV region of fig. 2.5 to that of fig. 2.4. Although the energy resolution is much better in the (e,e′p) case, both spectra show similar results for the transition to the ground state and levels at 2 and 5 MeV. The difference at ∼7 MeV may imply a different mechanism for the real photon induced reaction.

In (γ,p), transitions to the ground ($J^\pi = 3/2^-$) and first excited ($1/2^-$) states were resolved. Strength was observed at ∼5 MeV and was identified as the second $3/2^-$ state. The possible inclusion of the $5/2^-$ state at 4.45 MeV in this peak was discounted by [Sho88].

In the (e,e′p) data of [Ste88a] the momentum dependence of each resolved transition was measured out to $\mathbf{p}_m$=220 MeV/c. Fig. 2.6 shows the momentum distribution measured for the ($7/2^-$,$1/2^+$) doublet. The dotted and dashed lines show fits made using Distorted Wave Impulse Approxim-

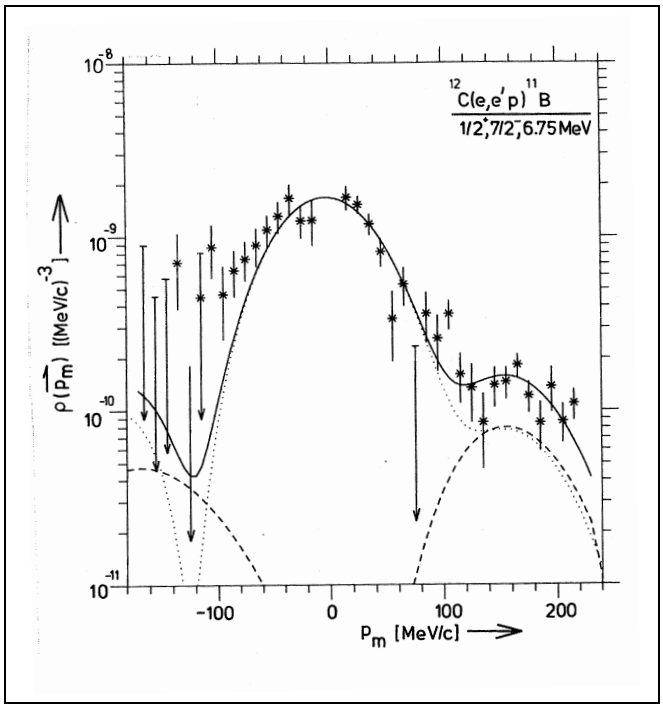

Figure 2.6: *$^{12}C(e,e'p)$ momentum distribution for the transition to the 6.8 MeV ($7/2^-$,$1/2^+$) doublet of ^{11}B, from [Ste88b]. The dotted and dashed lines are fits made with DWIA calculations for the $7/2^-$ and $1/2^+$ states, respectively. The solid line is the total.*

ation (DWIA) calculations for the $7/2^-$ and $1/2^+$ transitions, respectively. The solid line is the sum of both. The doublet is at maximum strength for $\mathbf{p}_m$=0 MeV/c, mainly due to the $7/2^-$, and falls off for $\mathbf{p}_m$>100 MeV/c. The $1/2^+$ state was not therefore regarded as a likely candidate for the (γ,p) strength by [Sho88] as the spectroscopic factor for 2s knockout was observed to be so small. The conclusion that the 4.45 MeV state ($5/2^-$) was not populated was used to state that the 7.29 MeV ($5/2^+$) was also an unlikely candidate for the strength in the triplet.

The total strength of the triplet, no matter which state is responsible, is still anomalous when compared to the ^{12}C(e,e'p) data. Numerous reaction mechanisms have since been considered for (γ,p) to explain this difference, such as:

- Photon absorption on p–n pairs, the Quasi–Deuteron Model (QDM).

  This (phenomenological) model was first suggested by Levinger [Lev51, Lev79] to describe the (γ,pn) reaction. It assumes that the γ-ray is absorbed on a correlated p–n pair, and further, that the wave function of this pair is proportional to the deuteron wave function at short inter–nucleon distances. In order to explain the (γ,p) or (γ,n) reactions the Modified Quasi–Deuteron Model (MQD) of [Sch78] is required. In it, the probability for the undetected nucleon to be reabsorbed is calculated to describe the single nucleon knockout cross section.

- Photon absorption on T=1 p–n pairs.

  This idea was put forward by Van Hoorebeke *et al.* [Hoo90, Sim92, Hoo92a]. A model was proposed in which the photon is absorbed, again on a p–n pair, as in the MQD. The population of the negative parity states was explained by the regular MQD approach. However, the strength in the unresolved triplet was explained as population of the positive parity states ($1/2^+$ and $5/2^+$) following photon absorption on T=1 p–n pairs. The p–n pairs of the original MQD are explicitly assumed to be T=0 which is the isospin of the free deuteron .

- Coupled channels (2–step) processes.

  This possible explanation, put forward by [Ste90], attempted to explain the population of the 6.74 MeV ($7/2^-$) and 4.45 MeV ($5/2^-$) levels in ^{11}B. The mechanism was one of DKO to the ground state of ^{11}B followed by inelastic excitation of the higher excited states by the exiting proton. This calculation underestimated the data by a factor of $\sim$5 and the difference was attributed to final state correlations.

  The excitation spectrum shown in fig. 2.5, showed no population of the 4.45 MeV ($5/2^-$) level following ^{12}C(e,e′p), which was later seen to be populated in ^{12}C(γ,p), [Bob95]. By measuring in non–parallel

kinematics[1] the population of this level was observed in ^{12}C(e,e′p) by [Bob92]. This was then interpreted as evidence for possible two–step processes in ^{12}C(e,e′p).

- Relativistic effects.

  Such effects in DKO and exchange current calculations were put forward by [McD88] and for DKO only by [Lot92, Joh96, Joh97]. The latter claimed that DKO was more important than Meson Exchange Currents (MEC) in the relativistic calculations, but these appeared to overestimate the data by a factor of 2, except for E_γ>120 MeV.

- Photon absorption on exchange currents.

  Calculations by [Ryc92] were made in the Random Phase Approximation (RPA) where the FSI are included as correlations between the continuum proton and individual hole states in the residual nucleus. This work suggested the importance of MEC for the population of 2–hole 1–particle (2h–1p) states in the residual, following photon absorption on 2–body currents. Initially this work proposed that the $5/2^+$ state be the likely main contributor to the ∼7 MeV strength in ^{11}B, but in the light of new data (see [Kuz98] and later) this has been changed.

All of these models have the same problem; the lack of experimental knowledge as to which members of the 7 MeV triplet of states in ^{11}B are excited and in what proportions. Therefore an experimental measurement capable of resolving the states in this triplet has been sought after for a long time. The triplet of states in question occur at excitation energies of 6.74 MeV ($7/2^-$), 6.79 MeV ($1/2^+$) and 7.29 MeV ($5/2^+$) [Ajz90]; see fig. 2.7 for a level scheme of ^{11}B. To look at how such a measurement has been attempted in the past it is necessary to review the development of experiments made on ^{12}C(γ,p).

[1] Section 5.1 will give an explanation of the term parallel kinematics.

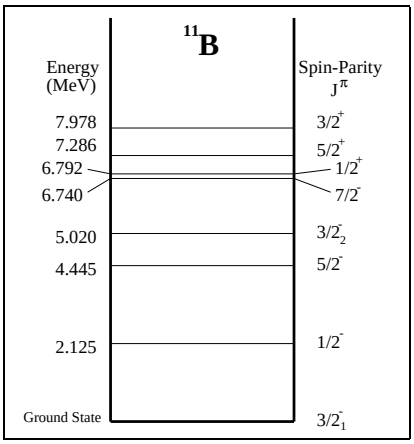

Figure 2.7: *Energy level diagram of ^{11}B, with spins and parities, [Ajz90].*

2.2.2 A review of recent ^{12}C(γ,p) data

For a more comprehensive list of (γ,p) measurements on ^{12}C, and other nuclei, see [Rau96] page 23 or [Bof96] page 261. Refer here to table 2.1 for a list of the most recent ^{12}C(γ,p) measurements, made using tagged photon beams.

Table 2.1: *A review of recent $^{12}C(\gamma,p)$ measurements made using tagged photons. (*For these experiments, absolute cross sections were made by normalising the data to those of Matthews et al. [Mat76].)*

Ref.	E_γ (MeV)	ΔE_γ (keV)	θ_p	ΔE_m (keV)	$\mathbf{p}_m$ (MeV/c)
Shotter* [Sho88]	56.5–63.5	50	65°–115°	500	250–320
Springham* [Spr90]	49–78	200	65°–115°	700	220–380
Van Hoorebeke [Hoo90]	<61> & <77.3>	330–400	<90°>	750	<280> & <320>
Ireland* [Ire93]	<60>	300	65°–120°	900	280–335
Bobeldijk [Bob95]	51–57	230	84°–130°	500	250–300
Rauf* [Rau96]	<73.5>	400	65°–120°	900	320–390
Ruijter [Rui96]	25–75	270	30°–150°	650	180–380
Aschenauer [Asc97]	41–57	230	40°–140°	570	160–280

In an early study of ^{12}C(γ,p) by Matthews *et al.* [Mat76], photons produced with a single–difference bremsstrahlung technique were used to measure absolute cross sections for ^{12}C(γ,p$_{0+1}$). Systematic uncertainties

were quoted as 22 %. The interest in experimental studies increased following the advent of tagged photon beams and high duty factor accelerators. Using a tagged photon beam, measurements of (γ,p) cross sections were extended to higher residual nucleus excitation by [McG86]. Since then many studies have been made of (γ,p) to discrete states in the residual nucleus.

A short review of some of the more recent data sets follows. This series of high resolution ($\Delta E_m \lesssim 900$ keV) measurements has been made using Si/Ge telescopes for proton detection. These experiments have all measured the cross sections for the ^{12}C(γ,p) reaction to populate the levels 0; 1; (2,3) and (4,5,6) in the final nucleus, ^{11}B, where 0=gs, 1=2.12 MeV, 2=4.45 MeV, 3=5.02 MeV, 4=6.74 MeV, 5=6.79 MeV and 6=7.29 MeV. The first of these measurements has been mentioned already.

2.2.2.1 Shotter *et al.*

This experiment, see fig. 2.4, was carried out using the 100 % duty factor microtron at the Institut für Kernphysik, Mainz University. For the first time, due to use of the tagged photon technique and a high duty factor beam, cross sections to several low lying discrete states in ^{11}B were measured, with a resolution of $\Delta E_m \simeq 500$ keV. Protons were detected with a ΔE-ΔE-E telescope comprised of Si strip detectors and a high–purity germanium (HPGe) E detector.

2.2.2.2 Springham *et al.*

This experiment [Spr90], see fig. 2.8, was again carried out at Mainz. The combination of Si strip and Ge detectors was again used to make a ΔE-ΔE-E telescope. Although an energy resolution of only $\Delta E_m \simeq 700$ keV was achieved, this measurement improved on Shotter *et al.* with better statistics.

2.2.2.3 Van Hoorebeke *et al.*

This measurement [Hoo90] was made at MAX–LAB, Lund, with an 80 % duty factor beam (see fig. 2.9). The detectors used were ΔE-E Si/Ge telescopes

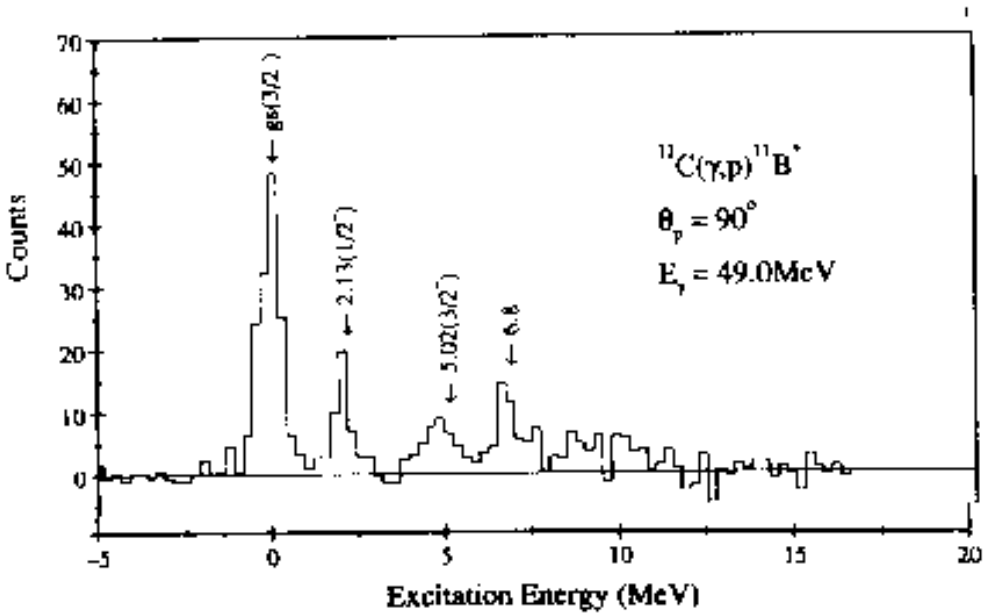

Figure 2.8: *Springham et al.* $^{12}C(\gamma,p)$ *excitation spectrum, [Spr90].*

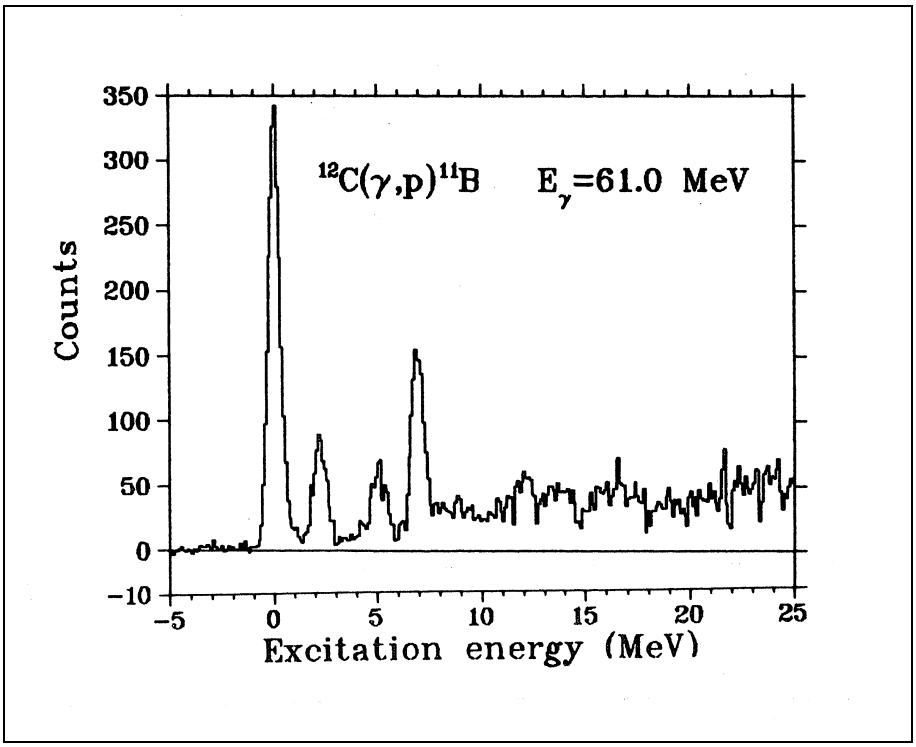

Figure 2.9: *Van Hoorebeke et al.* $^{12}C(\gamma,p)$ *excitation spectrum, [Hoo90].*

providing a resolution of $\Delta E_m \simeq 750$ keV. As well as studying ^{12}C, data were also taken on ^{16}O and ^{40}Ca.

This work, as already stated, was interpreted as providing evidence for the absorption of photons on isospin (T)=1 p–n pairs in nuclei, where, in (γ,p) the neutron is re–absorbed and the proton is excited into the continuum. In contrast to the previous measurements, the 4.45 MeV ($5/2^-$) state was considered to have been weakly populated.

2.2.2.4 Ireland *et al.*

This measurement [Ire93] was made at MAX–LAB, with a 60-80 % duty factor beam (see fig. 2.10). As in the measurements of Shotter *et al.* and Springham *et al.*, Si strip/Ge ΔE-ΔE-E telescopes were used, this time two of them. The resolution achieved was $\Delta E_m \simeq 900$ keV. Data were taken on

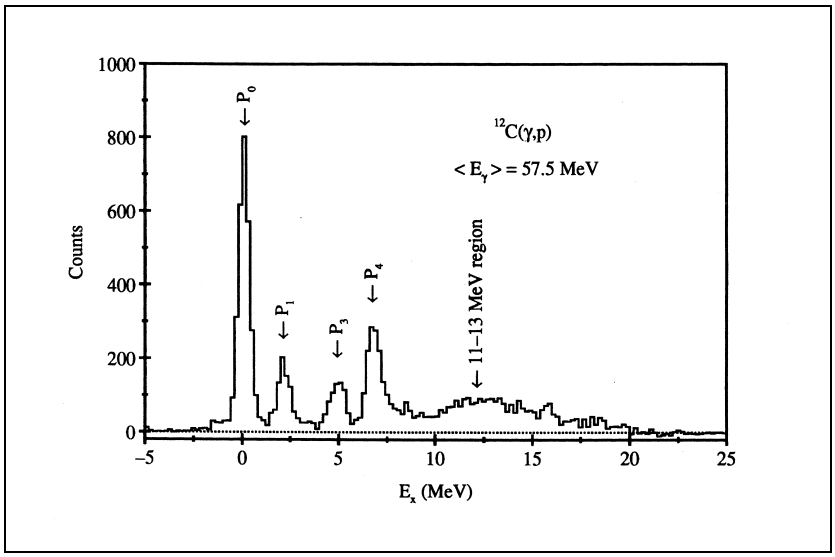

Figure 2.10: *Ireland et al. $^{12}C(\gamma,p)$ excitation spectrum, [Ire93].*

several targets, ^{14}N, ^{27}Al and ^{51}V, as well as ^{12}C. Population also of the 4.45 MeV ($5/2^-$) state was not ruled out following this measurement.

2.2.2.5 Bobeldijk

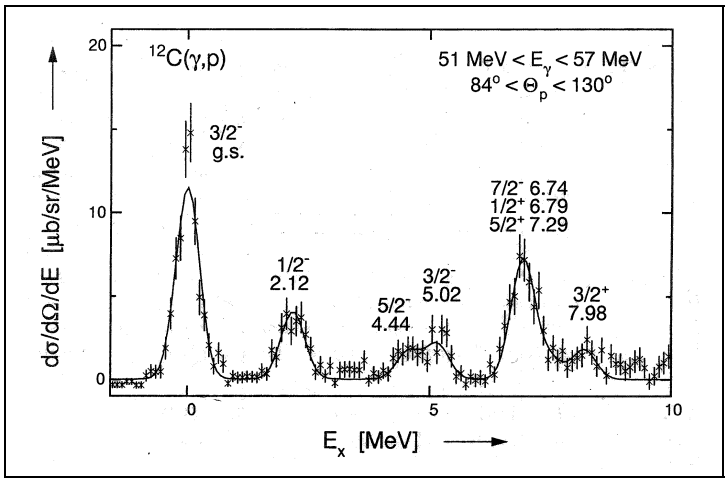

Figure 2.11: *Bobeldijk $^{12}C(\gamma,p)$ excitation spectrum, [Bob95].*

The spectrum presented in fig. 2.11 is from the thesis of Bobeldijk, [Bob95]. This measurement was taken as a calibration for an experiment studying ^{208}Pb(γ,p). It is shown here only because it shows clearly the definite population of the 4.45 MeV $(5/2^-)$ state.

2.2.2.6 Rauf

This experiment [Rau96] was also carried out at MAX–LAB with a 50 % duty factor beam (see fig. 2.12). Data were taken for three of the same targets as [Ire93] (^{12}C,^{14}N and ^{27}Al) plus ^{209}Bi, extending the kinematical regions of those measurements with higher E_γ and $\mathbf{p}_m$. There were two Si strip/Ge ΔE-ΔE-E telescopes, the same as those used in the Ireland *et al.* measurement. A resolution of $\Delta E_m \simeq 900$ keV was achieved.

2.2.2.7 Ruijter *et al.*

This measurement [Rui95a, Rui96] was made at MAX–LAB (see fig. 2.13). The data were presented as momentum distributions, covering the range $\mathbf{p}_m$=180-380 MeV/c. Si/Ge ΔE-E telescopes at 6 positions, subtending 55 msr each, were used for the measurements at high E_γ. A resolution of

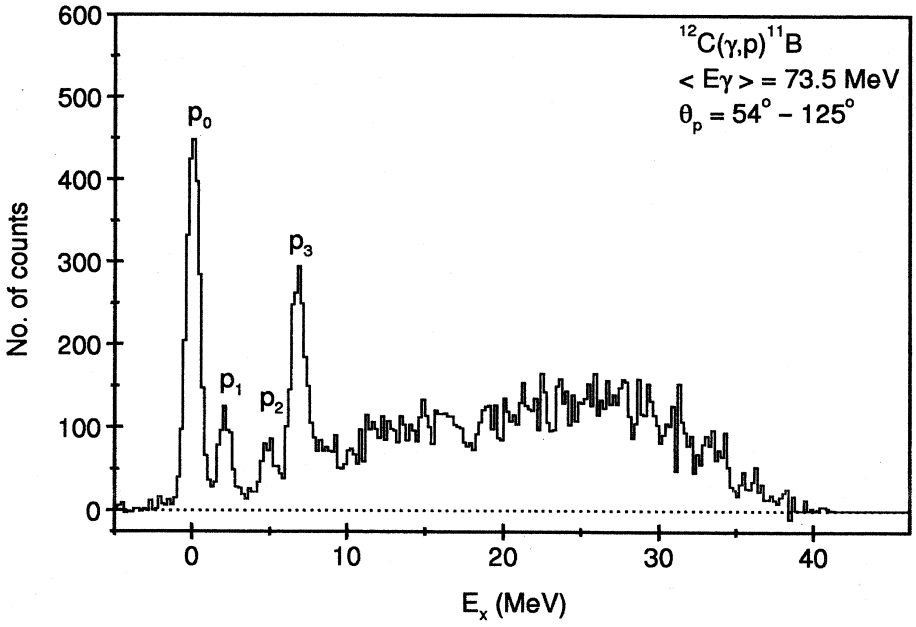

Figure 2.12: *Rauf $^{12}C(\gamma,p)$ excitation spectrum, [Rau96].*

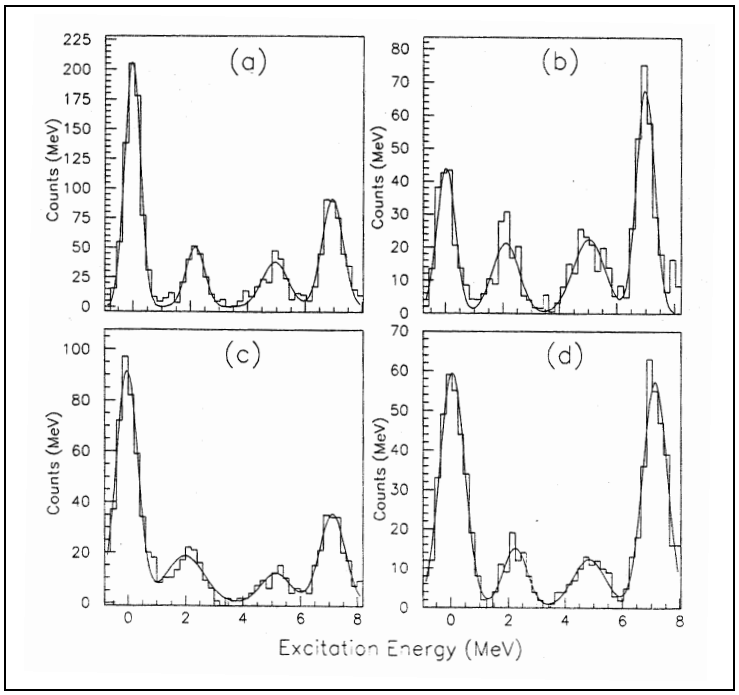

Figure 2.13: *Ruijter et al. $^{12}C(\gamma,p)$ excitation spectrum, [Rui96], for E_γ=60 MeV, θ_p=90° (a) and 120° (b); E_γ=75 MeV, θ_p=60° (c) and 90° (d).*

$\Delta E_m \simeq$650 keV was achieved. The cross sections were presented as angular distributions as well as momentum distributions and compared to (e,e′p). From the position of the triplet peak centroid it was concluded that the dominant states were in the ($7/2^-$,$1/2^+$) doublet, and not the $5/2^+$ state at 7.29 MeV.

2.2.2.8 Aschenauer *et al.*

This measurement [Asc97] was again made at MAX–LAB, Si/Ge detector telescopes were used in the measurement. The missing energy resolution quoted in this experiment was $\Delta E_m \simeq$ 570 keV, the best thus far obtained in a measurement of ^{12}C(γ,p) (see fig. 2.14). The cross sections measured were

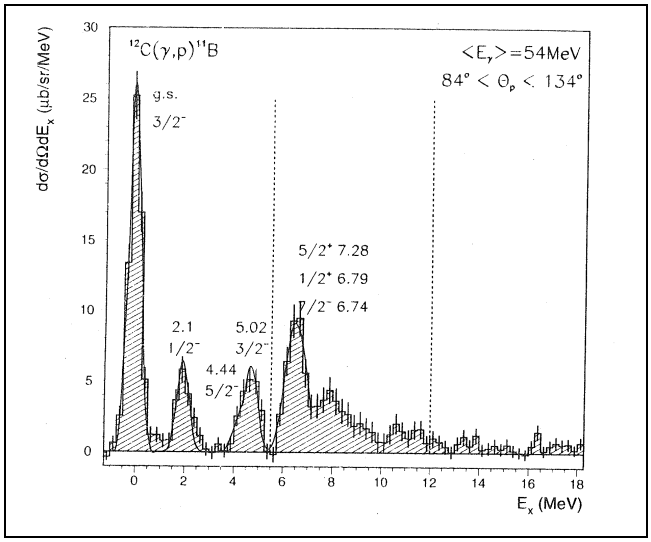

Figure 2.14: *Aschenauer et al. $^{12}C(\gamma,p)$ excitation spectrum, [Asc97].*

again presented as momentum distributions, and were compared to (e,e′p) data. The momentum distributions were measured for $\mathbf{p}_m \simeq$160-280 MeV/c, i.e. in a region were (e,e′p) data already existed.

This experiment confirmed the population of the 4.45 MeV ($5/2^-$) state in ^{11}B. The centroid of the peak at $\sim$7 MeV was measured to be at 6.77$\pm$0.05 MeV, implying the dominance of the ($7/2^-$,$1/2^+$) doublet, in agreement with the findings of Ruijter *et al.*

2.3 Using ^{12}C(γ,pγ') as a means of measuring high resolution ^{12}C(γ,p)

It is quite clear from section 2.2.2 that the experiments described do not provide sufficient energy resolution in the missing energy variable, E_m, to resolve the triplet. The best resolution reported so far in a (γ,p) experiment on ^{12}C was $\Delta E_m \simeq 570$ keV by Aschenauer *et al.* The resolution of all these experiments is dictated mainly by the resolution of the detected proton, ΔE_p, and to a smaller extent, by that of the beam photon, ΔE_γ. The proton energy resolution is degraded by the energy losses and straggling it suffers leaving the target. Reasonably thick targets (typically 0.1-30 mg/cm^2) were required in all the measurements described to obtain adequate statistics due to the low cross sections, typically of the order of μb. Therefore, it is evident that a new experimental technique is required to improve the energy resolution.

The present experiment is a study of the reaction ^{12}C(γ,pγ')^{11}B. The purpose being to measure the relative population of the three states of the triplet by *directly resolving* their de–excitation γ decays. In order to do this it was necessary to detect the γ-rays in a HPGe crystal. This is the *only* material with the required intrinsic resolution ($E_{\gamma'}<50$ keV at $E_{\gamma'}=6.8$ MeV) [Kno89]. Using the (γ,pγ') reaction the overall experimental resolution is dictated solely by the intrinsic resolution of the γ-ray detector, (except for effects of Doppler broadening which are small, $\sim$0.5 % for a suitably chosen detector geometry). Although this idea was considered before now, a high duty factor electron beam is required to make it feasible in practice, i.e. to reduce the background signals occurring from randomly tagged photons. This effect is even more important for the reaction (γ,pγ') than for (γ,p) since the total effective solid angle of the experiment is reduced by requiring a proton–γ' coincidence. (In fact, a study of the (γ,pγ') reaction when performed with tagged photons, involves a triple coincidence in order to tag the beam photon with an electron in one of the focal plane detectors, as

described in section 3.2 later.) It is necessary to detect the proton for two reasons

- The p–γ' coincidence removes signals associated with background from electrons in the γ-ray detector and also γ-rays coincident with other particles coming from (γ,X) reactions on the target, where X is neutron, deuteron, triton, etc... Therefore γ-rays from the de–excitation of ^{11}B *only* are selected.

- The excitation energy (E_{ex}) variable may be used to select specific regions of excitation in ^{11}B before looking at the coincident γ' spectra. This can be used to identify γ-ray cascade decays.

The reaction ^{12}C(γ,p) is, experimentally, a particularly good candidate for the (γ,pγ') technique as all levels below the 8.92 MeV level in ^{11}B decay by γ-ray decay only. The three states of the $\sim$7 MeV triplet γ–decay with branching ratios to the ground state of 70$\pm$2 % ($7/2^-$), 67.5$\pm$1.1 % ($1/2^+$) and 87.0$\pm$2.0 % ($5/2^+$), respectively, [Ajz90]. Therefore, resolving the γ-ray decays from these states allows their relative populations following the ^{12}C(γ,p) reaction to be measured directly[2].

It should be noted that one previous attempt at resolving these transitions with the (γ,pγ') reaction, but using a slightly different experimental approach, has already been made. It is reviewed briefly next.

2.3.1 The Measurement of Kuzin *et al.*

This was the first attempt at measuring the relative population of states in the $\sim$7 MeV triplet of ^{11}B, by using the (γ,pγ') technique [Kuz98]. The states of the triplet were, however, *not directly resolved* as the resolution for γ-ray detection was $\sim$270 keV at $E_{\gamma'}$=7 MeV. This allowed the $5/2^+$ state to be resolved from the ($7/2^-$,$1/2^+$) doublet, but the individual populations within the doublet could not be seen directly. Instead the populations of these

[2]This may not be strictly true if the effects of angular correlations in the direction of γ-ray emission are large enough, see discussion later in section 4.3.2.

levels had to be determined from the cascading γ-ray decays of ^{11}B, using the known branching ratios. After measurement of the relative populations of the three states, absolute cross sections were obtained by normalising to the data of [Spr90, Rui96].

This measurement was carried out at MAX–LAB, with tagged photons in the range 50-70 MeV and a tagging resolution of $\Delta E_\gamma \simeq 300$ keV. Protons from the reaction were detected at $\sim 70^\circ$ and $\sim 120^\circ$, with a solid angle of $\sim$840 msr. They were detected with two ΔE-ΔE-ΔE-E telescopes, comprising NE102 plastic (ΔE) and CsI (E) detectors, and a ΔE-E telescope, with a CsI (E) array (providing angular information). A missing energy resolution of $\Delta E_m \simeq 2.6$ MeV was achieved, the degradation from usual ΔE_m values mainly due to the, thicker than usual, target of $\sim$235 mg/cm^2 ($\sim$2 mm physical thickness). The de–excitation γ-rays were detected with two (25(diam)$\times$30 cm) NaI detectors, giving a resolution of $\Delta E_{\gamma'} \simeq 140$ keV at $E_{\gamma'} \simeq 2$ MeV and $\sim$270 keV at $E_{\gamma'} \simeq 6.3$ MeV. The total solid angle for detection of γ-rays was $\sim$1,125 msr.

This measurement utilised the fact the decay of the $7/2^-$ and $1/2^+$ states cascade to give γ-rays at 2.30 and 4.67 MeV, respectively. In order to resolve the 2.30 MeV cascade from the 2.12 MeV decay it was also necessary to view γ-ray spectra in coincidence with two regions of the E_{ex} spectrum (see fig. 2.15). The cuts made were $0 < E_{ex} < 3$ MeV and $5 < E_{ex} < 9$ MeV. These conditions sampled de–excitation γ-rays following either the direct population of the 2.12 MeV level in ^{11}B, or following feeding of if from higher levels. (Fig. 2.16 shows the γ' spectrum in coincidence with the $5 < E_{ex} < 9$ MeV cut.) The resulting γ' spectra were used to identify which γ-rays at 2.12 MeV were due to direct population of the state following (γ,p) and which were caused by feeding from higher energy levels. Refer to [Kuz98] for more details on their method of extracting the individual γ-ray strengths.

After a fitting procedure on the γ' spectra (see fig. 2.16) the results showed that the 6.74 MeV ($7/2^-$) state is dominant at both $\sim 70^\circ$ and $\sim 120^\circ$, as is shown in fig. 2.17. The $1/2^+$ and $5/2^+$ states were measured to be

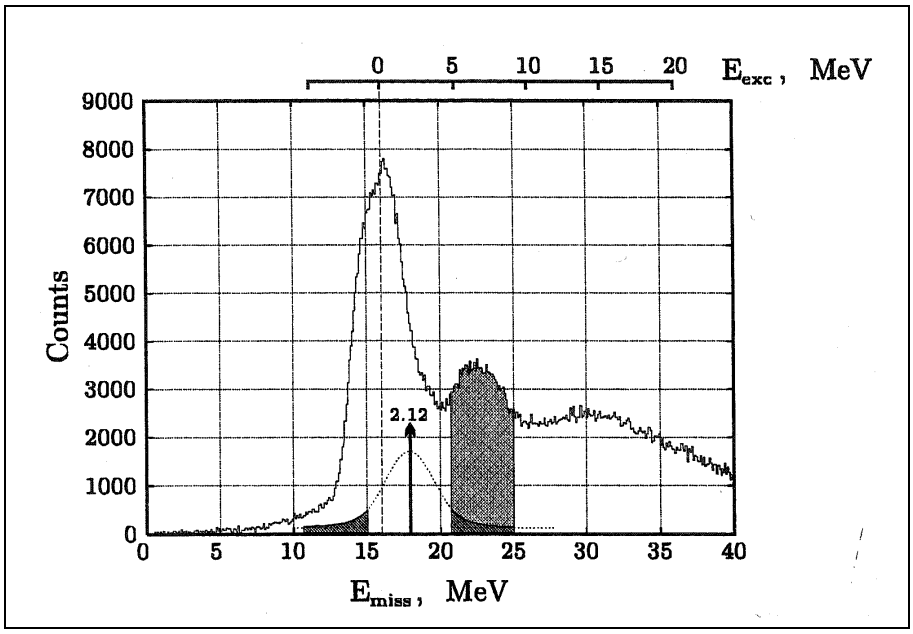

Figure 2.15: *$^{12}C(\gamma,p)$ E_m spectrum of Kuzin et al., [Kuz98].*

approximately equal in their contribution at each of these angles.

Calculations in the RPA, made by Ryckebusch [Kuz98], were compared to the data. These calculations were able to reproduce the relative contributions of each of the three states in the triplet. The conclusion was that the triplet at ~7 MeV in ^{11}B implies occupation of 2h–1p states in the target nucleus that would be empty in the Independent Particle Shell Model (IPSM) and that substantial MEC contributions are present.

2.3.2 The Present Measurement

In conclusion therefore, a ^{12}C(γ,pγ') measurement has already been made. However the experimental method was complicated by the inadequate $E_{\gamma'}$ resolution and the results were highly dependent on the procedure used to fit the γ' spectra (e.g. fig. 2.16). An independent measurement of the reaction ^{12}C(γ,pγ'), capable of directly resolving the states of interest in ^{11}B, has been performed. This measurement could only be made by using a HPGe detector for the detection of de–excitation γ-rays. The aim is to test the

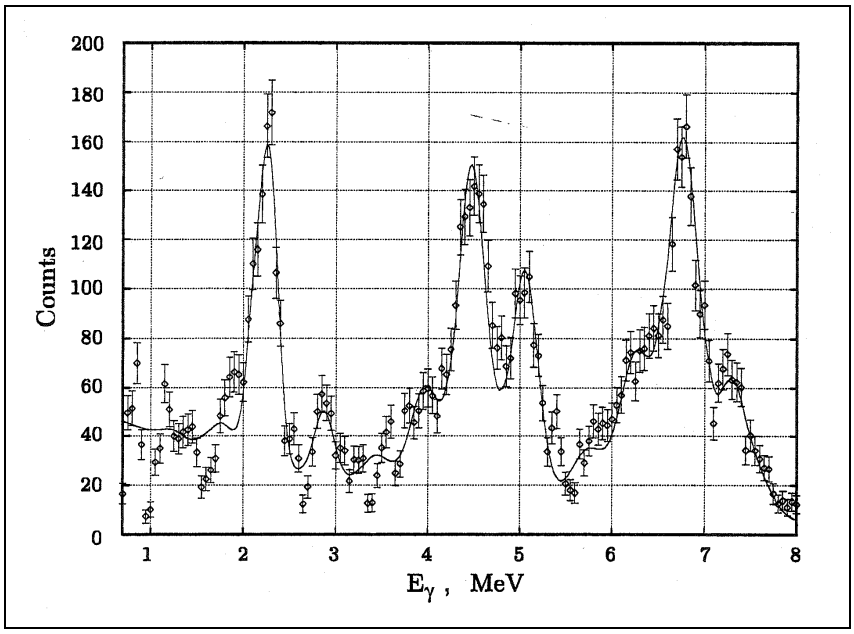

Figure 2.16: $^{12}C(\gamma,p\gamma')$ *de–excitation* γ*-ray spectrum, taken at* $\theta_p \simeq 70°$*, [Kuz98]. De–excitation* γ*-rays in coincidence with* $5 < E_{ex} < 9$ *MeV.*

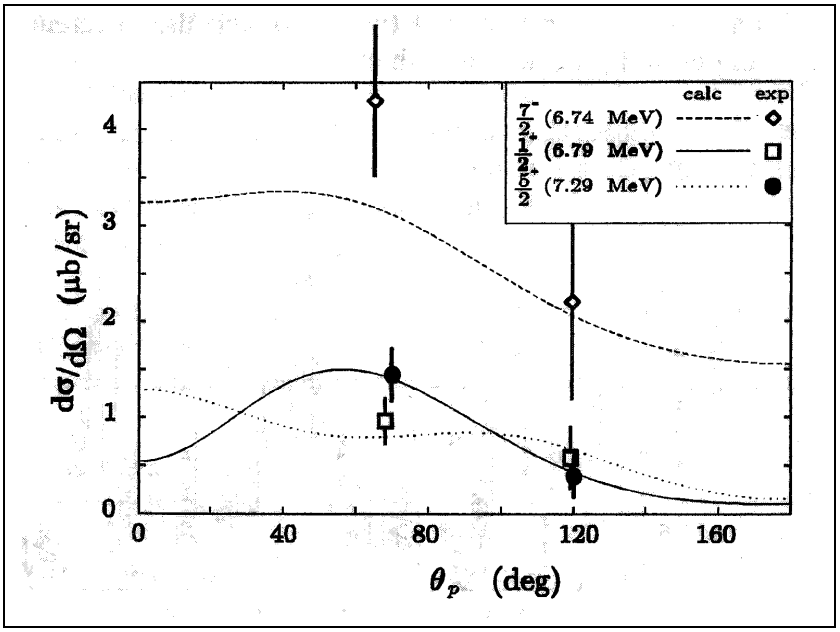

Figure 2.17: *The population of states in the* $E_{ex} \simeq 7$ *MeV* ^{11}B *triplet following the* $^{12}C(\gamma,p)$ *reaction, [Kuz98]. The relative populations have been normalised to the absolute cross section measurements of [Spr90, Rui96]. The lines represent the result of RPA calculations, which include one–body, pion–exchange and* Δ *currents.*

results of Kuzin *et al.*, by resolving each transition directly.

2.4 ^{12}C(e,e′p) for Comparison to ^{12}C(γ,p)

The motivation for studying ^{12}C(γ,pγ') described in section 2.3, is due to the anomalous strength at $E_{ex}\simeq$7 MeV in ^{12}C(γ,p). In section 2.1 it was stated that the existing data on ^{12}C(e,e′p) are predominantly at low $\mathbf{p}_m$. The (γ,p) reaction is also suspected to take place by a different reaction mechanism, making the comparison between the two reactions complicated. This is not helped by the fact that the behaviour of (e,e′p) at high $\mathbf{p}_m$ is not known. In order to help understand the reason behind the $\sim$7 MeV strength in ^{11}B for ^{12}C(γ,p) it is therefore advantageous to have data on both reactions at the same $\mathbf{p}_m$. An experiment capable of determining the one–body knockout cross section for this triplet, in the electro–induced process, at $\mathbf{p}_m$ values comparable to those of (γ,p) data is therefore required.

Data on ^{12}C(e,e′p) already exist from the NIKHEF laboratory [Ste88a, Ste88b, Kes96] covering an extensive $\mathbf{p}_m$ range. A gap in the missing momentum range covered by these data exists at the position of existing (γ,p) data. It is noted that a ^{12}C(e,e′p) measurement has been made at Mainz recently [Sau95] for $300<\mathbf{p}_m<390$ MeV/c. Momentum distributions have been measured for transitions to the $3/2^-_1$, $1/2^-$, $3/2^-_2$, $5/2^-$ and $(7/2^-,1/2^+)$ levels.

The missing momentum covered is not the only difference which may occur between the two reactions, however. For typical (e,e′p) data, the kinematics studied have been restricted predominantly to longitudinal virtual photon exchange with the nucleus. The exchanged photon polarisation may vary between purely longitudinal and purely transverse depending on the kinematics chosen. In the case of the real photons only pure transverse polarisation is possible. The two–body current effects (e.g. MEC) which are thought to dominate (γ,p) occur for absorption of a transversely polarised photon. The different photon polarisations may therefore result in a different sensitivity of each reaction to nuclear currents, such as those associated

with meson exchange. To facilitate comparison with (γ,p) it is therefore useful to study the transverse response of the (e,e′p) reaction.

In order to extract the transverse part of the (e,e′p) cross section the 'Rosenbluth separation method' [Ros50] may be used. In this method the cross section is measured at two different electron scattering angles for a constant momentum transfer, $\mathbf{q}$, to the target nucleus. Using this method, a separation of the ^{12}C(e,e′p) cross section in parallel kinematics has been performed in the $\mathbf{p}_m$ range 250–320 MeV/c, for five resolved transitions to states in ^{11}B. Using the NIKHEF experimental setup (see later), as used for the measurement of [Ste88a, Ste88b], it was possible to separate the ($7/2^-$,$1/2^+$) doublet from the $5/2^+$ state .

This measurement of ^{12}C(e,e′p) was motivated by the intention of making a comparison with the ^{12}C(γ,p) reaction more accessible. This in turn was done to help in understanding the (γ,p) reaction mechanism which leads to the strong excitation of the, so far unresolved, $\sim$7 MeV triplet in ^{11}B.

2.5 Isospin Selection Rules in ^{14}N(γ,d) and ^{14}N(γ,pn)

The third, and final, experiment included in this thesis was prompted by another anomalous result, on the reaction ^{14}N(γ,d). In studies of two nucleon knockout the electromagnetic probe may be used to study charge symmetry in the nuclear force through isospin selection rules [Eis76, Übe71, Gel53].

In a measurement made recently of the reaction ^{16}O(γ,pn) [Isa99], transitions to individual states in the residual nucleus, ^{14}N, were resolved. The quantum numbers of the ground state of ^{16}O are (J^π;T)=(0^+;0) where J^π represents the spin–parity and T the isospin. The results clearly showed population of the ground, 3.95 and 7.03 MeV states in ^{14}N (all T=0). Population of the 2.31 MeV (T=1) state was not observed. Absence of this state was interpreted as a preference for photon absorption on p–n pairs with the quantum numbers of the free deuteron, ($^3S_1$, T=0), as opposed to pairs with

the quantums numbers $^1S_0$, T=1.

This interpretation was based on the assumption of a spectator model. Following the (γ,pn) reaction, the residual nucleus is assumed to be unaffected by the process and is left in the same state as it was before the reaction [Isa96]. Considering ^{14}N as a target, the ground state of this nucleus is (1^+;0). The nucleus ^{14}N is an ideal target for the study of two nucleon knockout since it has a valence p–n pair, on top of a ^{12}C core. Assuming photon absorption on a T=0 p–n pair the ^{12}C core must also be T=0 in order that the total isospin add to T=0. The population of T=1 states in ^{12}C is therefore not expected for photon absorption on T=0 p–n pairs, provided the core remains unchanged. It should be noted that absorption of the photon on meson exchange currents implies no restriction on the isospin of the p–n pair [Isa99]. Such microscopic models may therefore predict a different population of states in the residual nucleus.

The (γ,d) reaction may also be used to provide insights into the absorption of photons on p–n pairs. Assuming the initiating photon is E1, the (γ,d) reaction requires a change in total isospin of ΔT=1 following absorption of the photon [Eis76]. Considering the reaction ^{14}N(γ,d), the ground state of ^{14}N and of the free deuteron are both T=0. By assuming a reaction mechanism involving an intermediate resonance state (see fig. 2.18) this implies that, following the selection rule for E1 photon absorption, only states of T=1 may be populated in the residual nucleus, ^{12}C. In a measurement of the reaction ^{14}N(γ,d) [Ire91], an E_{ex} spectrum (see fig. 2.19), was taken which showed some surprising results for the population of levels in ^{12}C. The lowest energy state in ^{12}C with an isospin of T=1 is at 15.11 MeV. A strong excitation of this state was expected due to the isospin considerations. This strong excitation is confirmed by the spectrum of fig. 2.19. The ground state of ^{12}C has T=0. There is no observed population of this state in the spectrum, which is also consistent with the selection rule.

However, the spectrum shows distinct structure at $\sim$4.4 MeV. This is consistent with the population of the 4.44 MeV (T=0) first excited state in ^{12}C, which would *disobey* the selection rule for E1 photon absorption on a

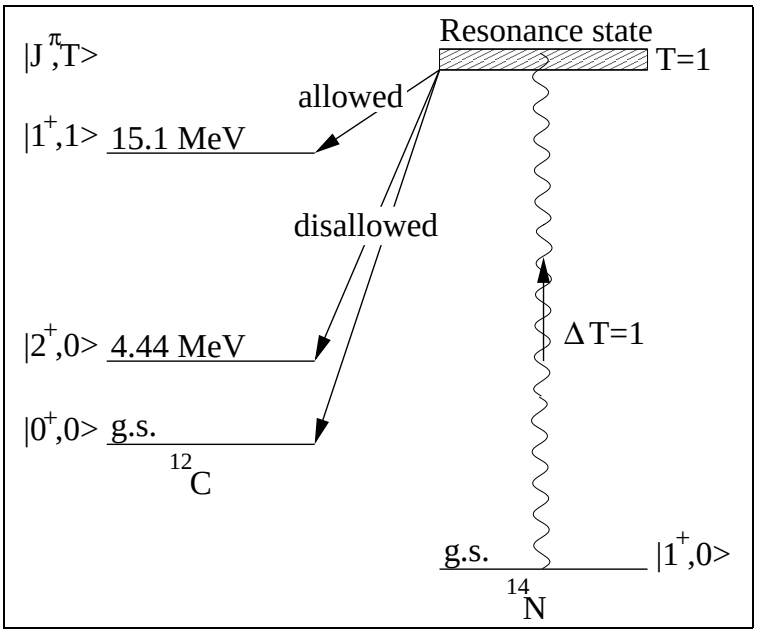

Figure 2.18: *The change in isospin induced by the reaction $^{14}N(\gamma,d)$, populating states in the residual nucleus ^{12}C. Absorption of an E1 photon populates an intermediate resonance state. By emitting a deuteron, this may only decay to a T=1 state.*

$^3S_1$ p–n pair. As stated in [Ire91] the statistics evidencing the population of this state are rather poor. There is also some structure below 4.44 MeV which cannot be real as there are *no states* below 4.44 MeV in ^{12}C, [Ajz90]. The spectrum of [Ire91] also shows a continuum from ∼5–15 MeV. This could be due to the (γ,dα) reaction channel which opens up at 7.37 MeV, and (γ,pd) which appears at 15.96 MeV in the E_{ex} spectrum of ^{12}C. The high E_{ex} cut–off is due to the threshold for deuteron detection.

After Ireland's investigation the following questions still remained

- Is the 4.44 MeV level in ^{12}C *really* populated?
- Are there any other states between 5 and 15 MeV in ^{12}C populated by this reaction?

This investigation was proposed to determine the relative population of the 4.44 and 15.11 MeV levels in ^{12}C following ^{14}N(γ,d), with better statistics than [Ire91]. This experiment also allowed the possibility to study

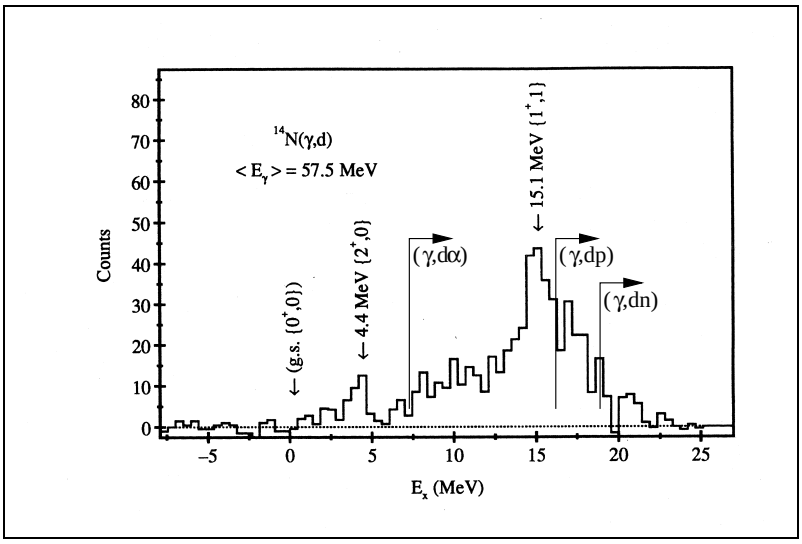

Figure 2.19: *$^{14}N(\gamma,d)$ excitation spectrum, [Ire91]*

simultaneously the (γ,pn) reaction channel, through data on ^{14}N(γ,pγ'). As in the case of the ^{12}C(γ,pγ') experiment discussed in section 2.3, detection of the de–excitation γ–decay of the residual nucleus, to its ground state, was made in coincidence with protons. Detection of the γ' allows the identification of levels in ^{12}C and therefore selects the (γ,pn) channel. This will be explained fully in chapter 6. Previous measurements of this reaction [Dog95] have not selected transitions to individual states in the residual nucleus. The present experiment is therefore a test of isospin restrictions, on the population of states in the residual nucleus, following photon absorption, leading to both the (γ,d) and (γ,pn) reactions.

Possible explanations for the population of the 4.44 MeV (T=0) state in ^{12}C, following ^{14}N(γ,d), include

- A 2–step process, such as, ^{14}N(γ,p)(p,d), allowing the T=0 state to be populated without disobeying the selection rule, ΔT=1.
- Absorption of the γ-ray on a T=1 p–n pair within the target nucleus, followed by an isospin flip to emit a deuteron (T=0).

Interpreting the absorption of the photon on a T=1 p–n pair implies the existence of 'quasi–deuterons' within the nucleus which may possess quantum

numbers other than those of the free deuteron. The existence of such quasi–deuterons has been mentioned already and was postulated by [Hoo90] (see section 2.2.1) to explain the strong population of the levels around ∼7 MeV in ^{11}B following ^{12}C(γ,p).

2.6 Overview of the Remainder

In summary, this thesis will present the results of three experiments. Two of these use the (γ,pγ') technique for determining, with high resolution, the population of states in a residual nucleus, following knockout reactions induced with real photons. The other is an electron scattering experiment prompted by a result from existing (γ,p) data which has been difficult to explain.

The remainder of this thesis will be organised as follows. Chapter 3 describes the experimental setup used at MAX–LAB to study real photon induced reactions. Chapter 4 explains the analysis and presents the results of the ^{12}C(γ,pγ') experiment, carried out at MAX–LAB and described in section 2.3. Chapter 5 briefly describes the electron scattering setup of NIKHEF, before describing in more detail the analysis and presenting results for the ^{12}C(e,e$'$p) measurement of section 2.4. Chapter 6 describes the analysis of the ^{14}N(γ,d) and ^{14}N(γ,pn) (^{14}N(γ,Xγ')) experiment of section 2.5, which was also carried out at MAX–LAB. Finally chapter 7 presents a discussion of all results.

Chapter 3

Real Photon Experiments at MAX–LAB

This chapter describes the experimental details behind the real photon induced reactions presented in this thesis. The (γ,Xγ') experiments described here were all carried out at the MAX–LAB in Lund, Sweden. More detail on the MAX–LAB acceleration system can be found in [Eri82, Lin83, Lin90, Adl90]. Note that the setup described here is now out of date since, as of the time of writing, MAX–LAB is undergoing an upgrade. The new tagging system is described in [Adl97a].

The measurements for this thesis were all made using tagged photons of energy $50 \lesssim E_\gamma \lesssim 70$ MeV incident on the target nuclei ^{12}C (described in chapter 4 and hereafter referred to as run #1) and ^{14}N (described in chapter 6 and hereafter referred to as run #2). The γ-rays were created as bremsstrahlung from a beam of electrons made to strike a radiator. Production of the initial electrons and the photon tagging are outlined in sections 3.1 and 3.2, respectively. The targets are described in section 3.3. In section 3.4 the product detectors are introduced. Section 3.5 explains the geometric setup of product detectors. Section 3.6 discusses the electronics and signal processing used in acquiring the data. In section 3.7, the estimated count rate is compared to the measured count rate. Finally, section 3.8 shows a summary table for each of the measurements made at MAX–LAB.

3.1 Electron Beam

The electron beam used to create the bremsstrahlung is first accelerated in a low duty factor racetrack microtron (MAXINE). MAXINE delivers a pulsed beam with 3 GHz time structure [Eri82] and an energy of up to 100 MeV (with an energy spread of 0.1 MeV). The microtron, as depicted in fig. 3.1, consists of one LINAC section and two end magnets, with typical field values of 1.2 T, which bend the electrons by 180°. Electrons are made to circulate

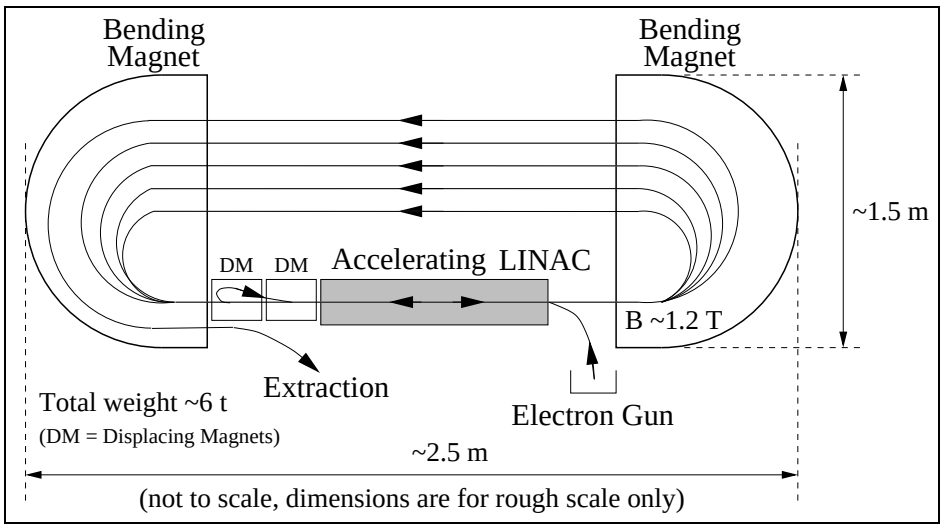

Figure 3.1: *Schematic of the* MAX–LAB *microtron (*MAXINE*) showing the path of the electrons.*

the accelerating section several times in order to gain the required energy. The electrons start off in the electron gun, where there are injected into the first LINAC section with an energy of 100 keV. After their first pass through the LINAC the electrons are turned around and make their next, and all subsequent passes, in the opposite direction, [Eri82]. With an acceleration of ∼5 MeV in each section they are required to circulate the microtron 19 times to achieve maximum energy. The beam can, however, be extracted from any orbital except the first three.

The microtron produces a pulsed beam of duration ∼0.5 μs (with a beam current of ∼10-20 nA, corresponding to ∼10^{10} electrons s^{-1}), at ∼20 ms intervals. This is injected into the beam transport and from there

taken via a 30° magnet to the stretcher ring, see fig. 3.2. A ∼0.5 μs pulse

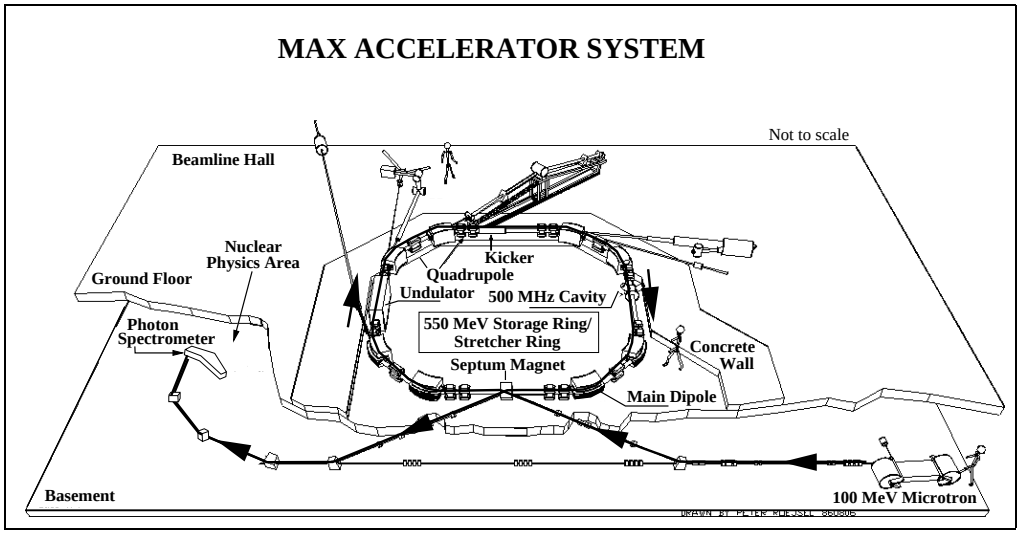

Figure 3.2: *The* MAX–LAB *microtron and stretcher ring (figure adapted from that in [Adl90]). The path of the electrons has been marked by arrows.*

corresponds to a length of ∼150 m. Therefore the leading edge of the beam pulse travels around the ring (circumference ∼32.4 m) for about 5 turns before the trailing edge enters. The effect is that the pulsed beam is stretched over the full circumference of the ring. With this procedure it is possible to obtain a duty factor of typically ∼80 %. The term duty factor (see fig. 3.3) for a uniform, well defined beam is defined as the ratio of time for which the beam is *on* to the time between pulses. A continuous, low intensity, stretched beam allows detectors to work more efficiently than with intense pulses, which lead to saturation. They also allow for a much better background subtraction when making particle coincidence measurements. The beam loses energy via synchrotron radiation as it travels around the ring. At a typical beam energy ($E_0 \simeq 95$ MeV) the energy loss due to synchrotron radiation in the ring is ∼1.12 MeV over a period of ∼20 ms. Next the beam is extracted from the ring at the septum magnet. The method of extraction is explained in [Lin83]. Since no acceleration of the beam takes place in the stretcher ring the energy, and energy spread, of the beam after extraction is equal to that of the beam injected from the microtron, except for the effects

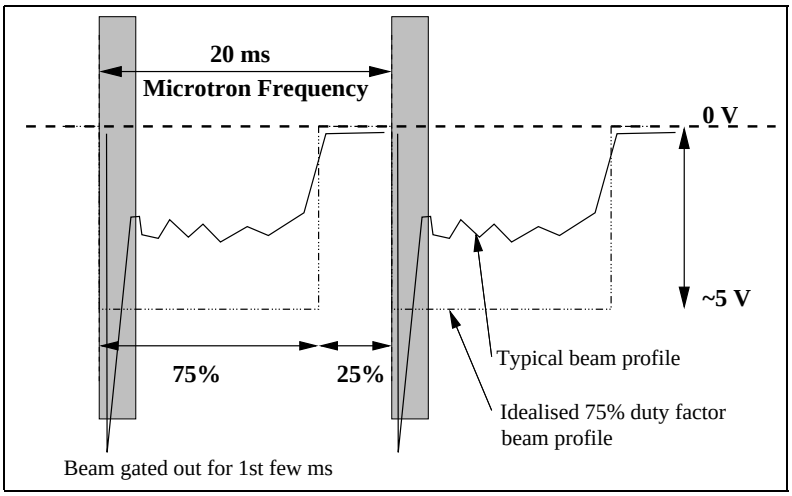

Figure 3.3: *An idealised beam profile extracted from the stretcher ring, along with a more realistic version. The duty factor illustrated is 75 %.*

of synchrotron radiation.

In principle it is possible to extract beam from the septum magnet throughout the entire 20 ms period. However, there is a large flux of beam in the ring during the period of injection from the microtron. This makes the beam unsuitable for a few ms after injection. Hence the beam is 'gated out' of the data acquisition system during this period, as shown in fig. 3.3.

Once extracted from the stretcher ring the beam is transported, via another 30° magnet, to the nuclear physics experimental area and the photon tagger (see again fig. 3.2). The next stage is the creation of the photon beam.

3.2 Photon Tagging

The electron beam is now made to strike a radiator (bremsstrahlung target), to form bremsstrahlung photons, as depicted in fig. 3.4. The radiator is an aluminium foil of thickness 50 μm, or 6×10^{-4} radiation lengths. These photons, which are radiated in a forward cone, are directed towards the reaction target (the target containing the nuclei to be studied). The spectrum of energy for these photons is of course not mono–energetic, but, is continuous from the electron beam energy, E_0, down to zero (see fig. 3.5). Since

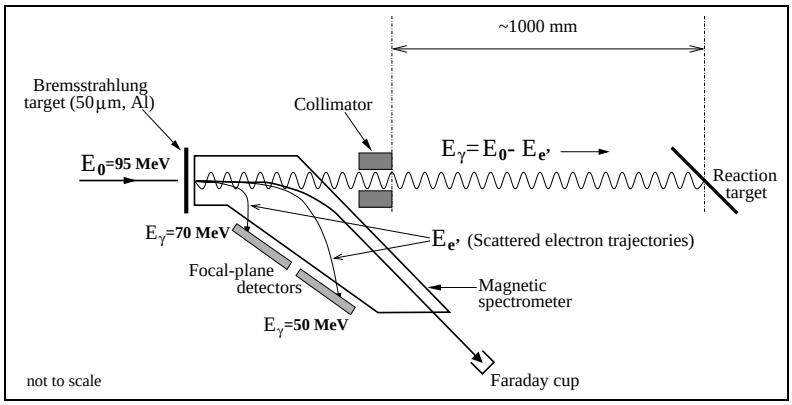

Figure 3.4: *A schematic of the process of photon tagging.*

the distribution varies mainly as e^{-E_γ}, a large number of low energy photons reach the target and contribute to background radiation.

The energy of the photon which induces a reaction must be known in order to reconstruct the kinematics. The method of measuring the beam energy is termed *photon tagging*. This method consists of bending the scattered electron, which has lost its energy in the radiator and created the photon, in a momentum spectrometer in order to determine its energy. The position of detection of the scattered electron along the focal plane of this spectrometer identifies its energy. Knowledge of the scattered electron energy and the initial beam energy imply knowledge of the bremsstrahlung photon energy via the formula

$$E_\gamma = E_0 - E_{e'} \tag{3.1}$$

The entire tagging process takes place in a vacuum. A typical magnetic field is around ∼0.32 T. Photons between $0.1E_0 < E_\gamma < 0.8E_0$ can be tagged. The tagging magnet houses 64 non–overlapping plastic scintillator (NE102A) detectors, which make up the focal plane. The instrumented section is ∼514 mm in length and is arranged in two groups. These are placed outside the vacuum chamber of the spectrometer, with a thin stainless steel window interface, making maintenance easier. The basic requirements met by the scintillators are that they have a high electron detection efficiency, a high count rate capability ($> 10^6$ Hz), good time resolution (∼1 ns) and an

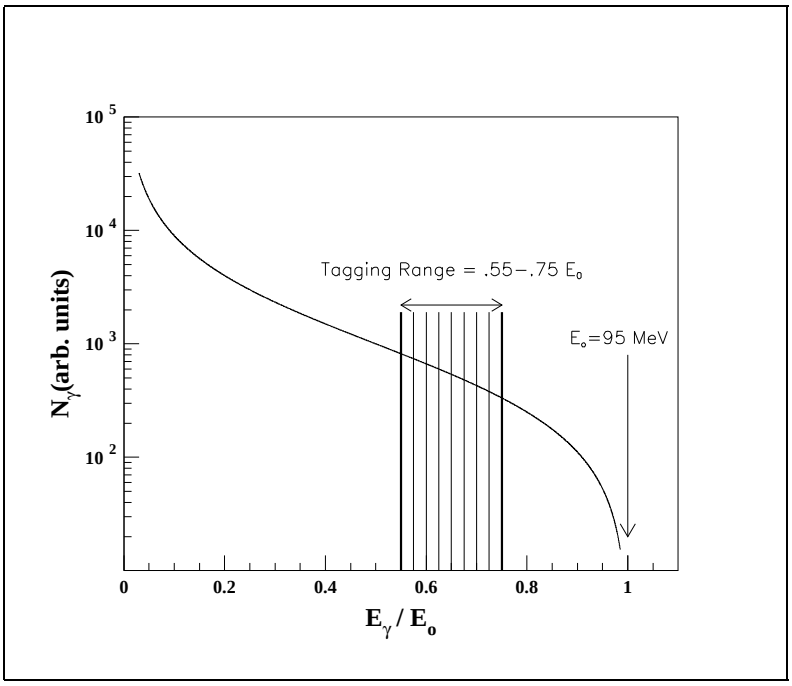

Figure 3.5: *An example of the bremsstrahlung spectrum for photon energies present in the beam as it exits the collimator. The range in which photons are tagged is marked. The electron beam energy, E_0, represents the photon end–point energy. Photons are tagged in a smaller range than is possible to improve the tagging resolution, ΔE_γ.*

energy resolution of ∼0.3 %. Cylindrical light guides (∼37.7 mm long) bring the light out of the vacuum chamber into 8 mm photomultiplier tubes, manufactured by Hamamatsu (type R1635-01). Each group of scintillators may be placed independently of the other along the focal plane for the desired photon energies. In the setting used, each of the two groups covered a ∼10 MeV range and each scintillator covered an energy of ∼260 keV. Photons were tagged in a smaller range than was possible in order to improve the tagging resolution. The total 'tagging range' was therefore ∼20 MeV with a resolution of ∼260 keV.

The photon beam has a physical diameter of ∼16 mm at the exit of the collimator and, typically, ∼32 mm at the target position, ∼1 m downstream. To measure the beam position a Polaroid film placed behind a Pb converter and a scintillating material is exposed to ∼10 s of beam. From this, the

mid–point of the geometrical beam line is determined, so that the alignment of the photon beam at the target position may be checked. The intensity of tagged γ-rays in the beam amounts to $\sim 10^6$ s^{-1}.

An indication of the performance of a photon tagging system is given by a quantity known as the 'tagging efficiency', ε_{tagg}. This is defined for each focal plane scintillator as: *The number of tagged photons passing through the collimator in the photon energy range covered by a focal plane detector, divided by the total number of electrons counted in that detector.*

The tagging efficiency is usually measured before the experimental data taking commences. The number of tagged photons is determined by a lead–glass Čerenkov detector (front face 102×79 mm, back face 102×102 mm and length 198 mm, i.e. ∼8 radiation lengths) placed in the path of the photon beam. This is connected to a photomultiplier tube (type Phillips XP2041). A signal from any one of the individual focal plane detectors is used to start a TDC which is stopped by a signal from the lead–glass detector. The electron beam intensity must be turned down from ∼20 nA to ∼0.1 nA in order that the TDC's may cope with the rate of start signals from the focal plane. The signal from the photon detector is recorded in an ADC. The tagging efficiency is then taken from the ADC spectra created in coincidence with each individual focal plane detector. Fig. 3.6 shows the summed ADC spectrum for all detectors. For each detector we calculate the number of counts in the photopeak of its spectrum and divide this by the total number of counts in the spectrum including underflows (since this equals the number of gates supplied by the

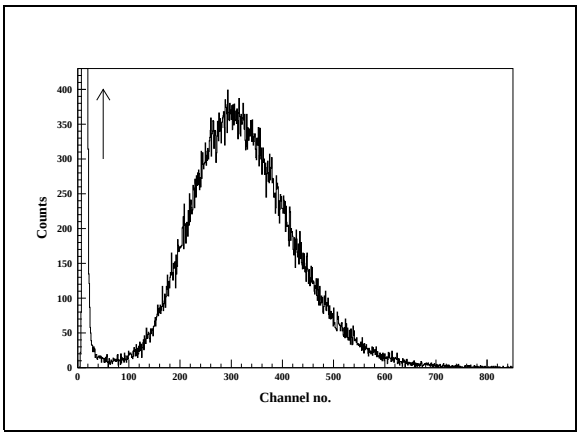

Figure 3.6: *The ADC spectrum obtained from the tagging efficiency measurement for run #1.*

focal plane detector). This fraction is the tagging efficiency.

It is not believed that ε_{tagg} varies with beam intensity or radiator thickness. When measuring relative cross sections, such as in this experiment, it is not necessary to know the absolute value of ε_{tagg}. Instead it is sufficient to know that ε_{tagg} does not vary throughout the data taking period. The tagging efficiency for runs #1 and #2 were measured to be ∼25 %, as shown in figures 3.7 and 3.8.

3.3 Targets

The next step in the process is to place a target, containing the nuclei to be studied, in the path of the photon beam. The carbon target used to study ^{12}C in run #1 was a 100×100 mm rigid graphite slate (∼99.95 % purity) of physical thickness ∼2.5 mm (∼562.5 mg/cm^2). A ∼1 mm (∼225 mg/cm^2) target was used for calibration of the proton telescope. These targets, of density ∼2.25 g/cm^3, were supplied by Goodfellows Ltd.

A powder, cyanoguanidine ($C_2H_4N_4$), was used to study ^{14}N in run #2. This was held between two thin (∼20 μm) hostaphan ($C_{10}H_8O_4$) sheets clamped in an Al frame, with an ellipsoidal window of ∼60×120 mm. The target's physical thickness was ∼1.27 mm, corresponding to ∼179 mg/cm^2. Data on a carbon target were taken for background subtraction during this experiment, using 2×∼0.5 mm thick (∼158 mg/cm^2 total) graphite slates, similar to those used in run #1.

3.4 Detecting Reaction Products

The reaction products produced in the target are detected in order to measure either their energy (momentum), direction and/or time of arrival (relative to some reference time). In these experiments, the two types of reaction product being detected were charged particles (protons or deuterons) and γ-rays. These had to be detected in coincidence. Detection of the charged

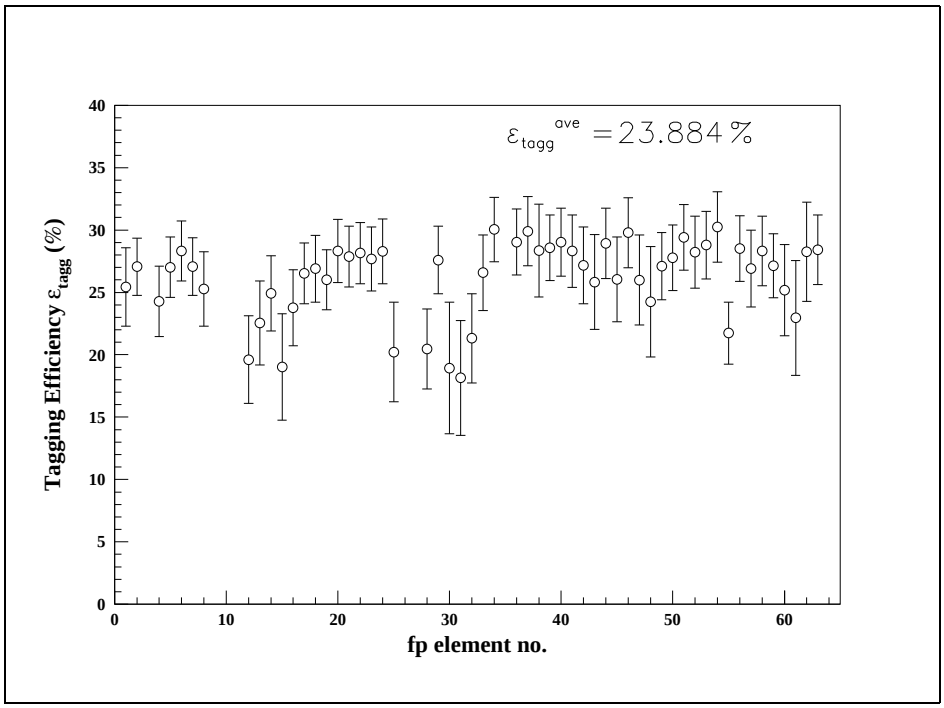

Figure 3.7: *The tagging efficiency per focal plane detector, as measured for run #1.*

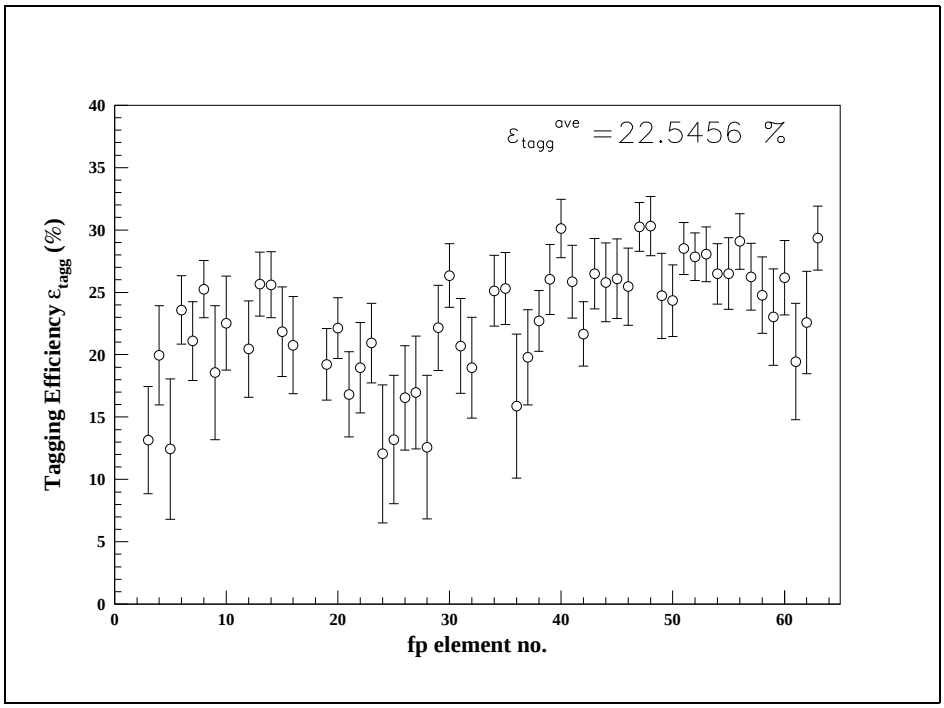

Figure 3.8: *The tagging efficiency per focal plane detector, as measured for run #2.*

particles was carried out using Si/Ge telescopes for both run #1 and run #2.

3.4.1 Charged Particles

The overall charged particle detection systems were (what have become) the 'standard' Edinburgh charged particle telescopes for photonuclear experiments, [Dav90]. They basically comprise a ΔE–E system of detectors. Charged particles are made to pass through a thin detector in which they will deposit only some of their energy, ΔE, before being stopped in a thicker detector to deposit their remaining energy, E. Fig. 3.9 shows a typical setup with two ΔE detectors in front of an E detector. Silicon detectors are used

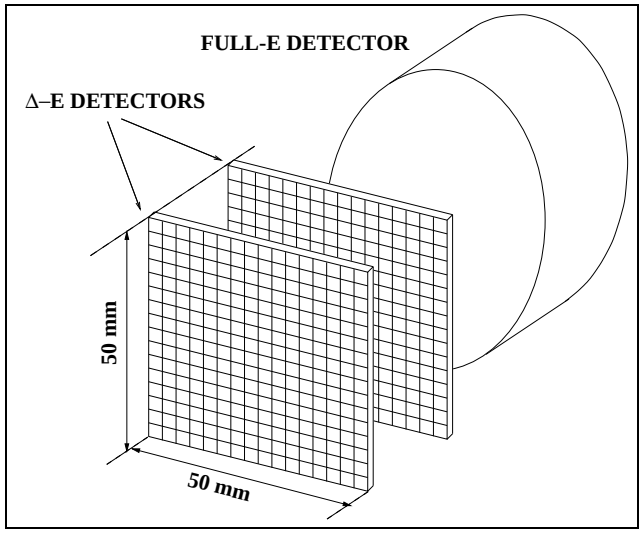

Figure 3.9: *Schematic of a charged particle telescope. (This figure shows the DSSSD's as being pixilated, whereas they actually consist of orthogonal strips on each side.)*

for the ΔE signals and a HPGe crystal is placed behind these to stop the charged particles, measuring E. This allows particle identification as well as particle tracking to be carried out. The telescopes are capable of stopping protons up to ∼80 MeV.

The photograph in fig. 3.10 shows a telescope as setup for an experiment. Only one silicon ΔE detector is visible at the front, the other is hidden from view. The telescope is under atmospheric pressure as these experiments

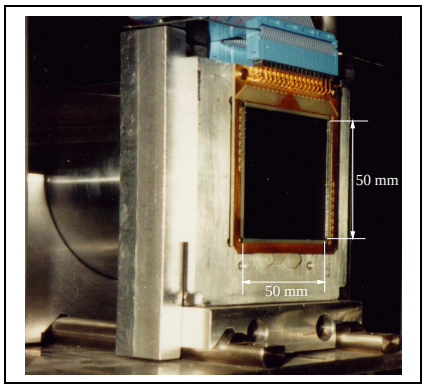

Figure 3.10: *Photograph of a telescope in an experimental setup. The cylinder at the back is the cannister of the HPGe detector. In front is the first Si ΔE detector. The second is not visible but is behind the Al mounting. The active area of the Si detectors was ∼50×50 mm^2.*

were performed in air. The high energy of the charged particles means that energy and angular straggling in the air is negligible as compared to that undergone in the target.

In both HPGe detectors (#1 and #2) the crystals are housed inside a metal cylinder, with a thin front entrance window to minimise the energy loss and straggling of the charged particles before they enter the germanium crystal. A cold finger extending from the LN_2 dewar makes thermal contact with the crystal and keeps it at its operating temperature, ∼77 K, while in use.

HPGe #1 (manufactured by A.C. Nuclear Ltd.) which was used in both experimental runs was a planar HPGe (active diameter ∼49.5 mm and active thickness ∼9 mm), with a ∼500 μm thick Be entrance window, as shown in fig. 3.11. This detector was operated at -2000 V. Its timing resolution was ∼2–3 ns [Ire91]. Typically it was operated with a dynamic range from ∼5 MeV up to ∼80 MeV.

HPGe #2 (manufactured by Canberra Industries, Inc.) was used only in run #2. The crystal itself, a LEGe (Low Energy Ge detector), had a total diameter of ∼70 mm and a thickness ∼25 mm, as shown in fig. 3.12. The timing resolution of this detector was not as good as that of HPGe #1, mainly due to the non–planar nature of its electric field. It had an active

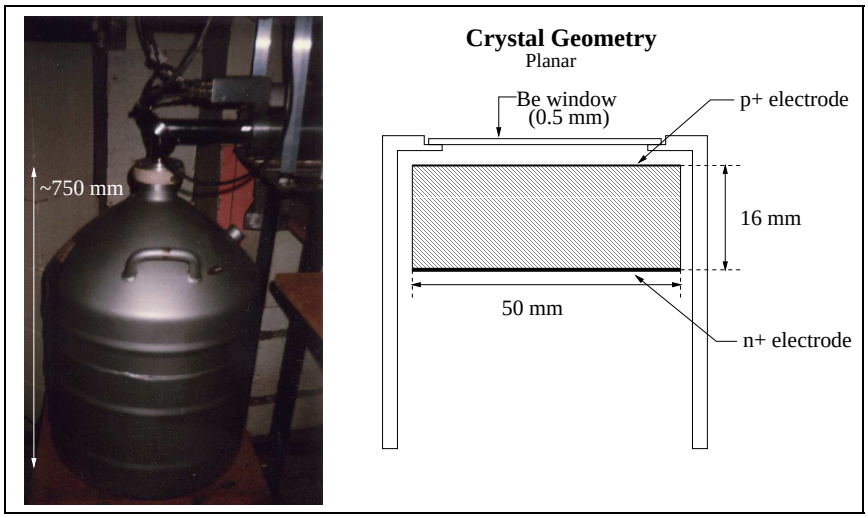

Figure 3.11: *HPGe #1 detector showing the crystal geometry (planar) and dimensions.*

area of ~3800 mm^2, with a ~500 μm thick entrance window of carbon–epoxy. Typically it was operated with a dynamic range of ~5 MeV to ~80 MeV and under a voltage of -3000 V.

The term 'planar' used in the description of HPGe #1 refers to the geometry of the electrodes which create the electric field across the germanium crystal. In this case the electrodes are flat on either side of the crystal, producing a uniform field, (parallel field lines) which gives good timing resolution. Planar detectors have better timing properties than other geometries. Good timing resolution is required here as the proton signal is used to trigger the readout of the data acquisition system.

These detectors are primarily built as Low Energy Photon Spectrometers, but were adapted for the purpose of charged particle detection. The original pre–amplifiers (with a usable range of 0–10 MeV) were modified to have a range 0–100 MeV. Measurements were made [Spr88] of the energy resolution for 18 MeV protons in such a detector, using the ^{13}C(^{3}He,p) reaction, and this was shown to be ~400 keV FWHM.

The ΔE signals were measured by Double Sided Silicon Strip Detectors (DSSSD's). The DSSSD's were manufactured by Micron Semiconductor Ltd. The active area of each detector was ~50×50 mm^2, and this was divided

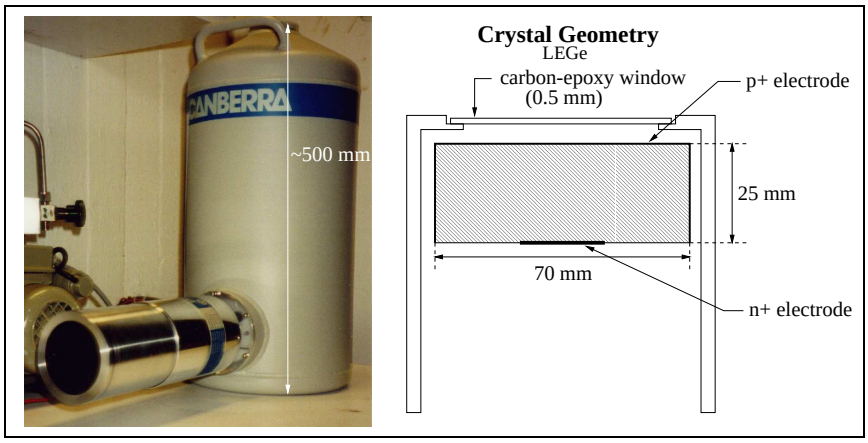

Figure 3.12: *HPGe #2 detector showing the crystal geometry (LEGe) and dimensions.*

into 16 parallel strips on each side, (oriented orthogonally to each other). Each strip was ∼50 mm long and ∼1.9 mm wide, the inter–strip region being ∼100 μm wide. The thickness of the wafers was around ∼450 μm. They were operated at a bias voltage of ∼90 V, with leakage currents being typically ∼1–2 μA.

The instrumentation of these detectors has been reported previously, [Tho90]. The DSSSD's were enclosed in a light–tight box during data taking as they are sensitive to pickup from artificial lighting, which could have affected the accuracy of the energy signals.

3.4.2 De–excitation γ-rays

The γ-ray detectors were read out after the detection of a trigger signal from the charged particle telescopes. The type of detector used here was different for the two experimental runs. For run #1 a solid–state, HPGe, device was used. For run #2 two large NaI(Tl) crystals were used.

In run #1 a 70 % relative efficiency[1] HPGe crystal was used, as shown in fig. 3.13. The detector was manufactured by Canberra Industries, Inc.

[1]This term refers to the efficiency of the detector relative to the adopted standard, which is a that of a NaI(Tl) crystal (7.62 cm×7.62 cm) at 25 cm from the source.

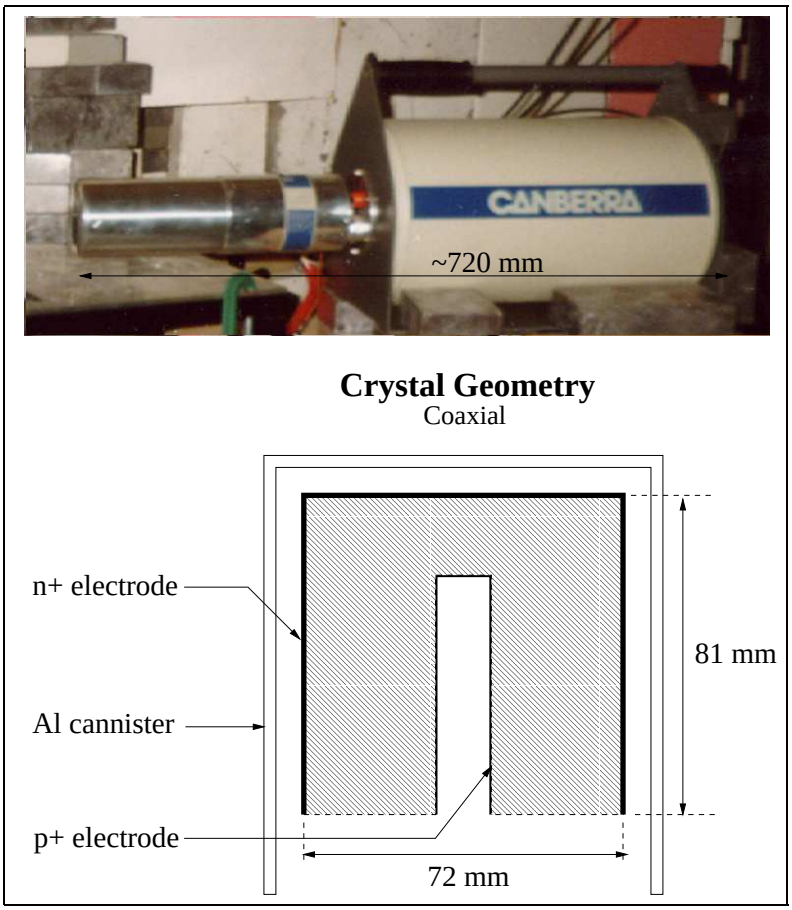

Figure 3.13: *HPGe 70 % detector showing the crystal geometry (Coaxial) and dimensions.*

[Canb]. It was a coaxial Ge detector. The crystal was a cylinder of germanium with an n–type contact (diffused lithium, ∼0.5 mm thick) on the outer surface and a p–type contact (implanted boron, ∼0.3 μm thick) on the surface of an axial well. A reverse bias of +4500 V was used to deplete the active volume between the electrodes. The crystal had a diameter of ∼72 mm and a thickness of ∼81 mm, with an active area of ∼2000 mm^2, according to the manufacturer. It was situated ∼5 mm in from the edge of the cannister. The detector was designed to be useful in the energy range from ∼50 keV to ∼10 MeV, and was operated within this range during the experiment. Again, the detector was kept at operating temperature by LN_2, stored in an all–orientation dewar, which allowed the detector to be

placed facing any direction desired. The detector had an intrinsic resolution of 2.15 keV FWHM at $E_{\gamma'}$=1.33 MeV and a peak to Compton ratio of ∼67.8:1, as quoted by the manufacturer.

To cope with the envisaged count rate of $\sim 10^5$ Hz on this detector a shaping time of 1 μs was used to amplify the signal before the ADC conversion. The manufacturer's recommended shaping time for this detector was 4 μs in order to achieve optimum energy resolution. The setting used was settled on as a compromise between count rate capability and energy resolution. Fig. 3.14 shows the resolution of the detector at $E_{\gamma'}$=1.33 MeV as a function of shaping time, measured using a ^{60}Co source, highlighting how this setting affects the achievable intrinsic resolution. The resolution

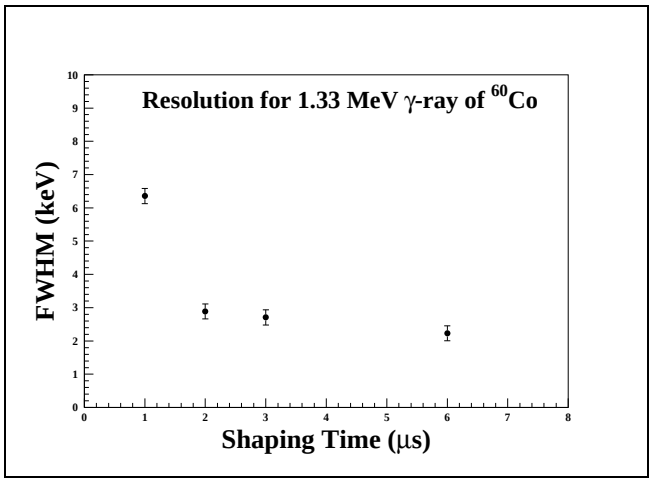

Figure 3.14: *Resolution of the HPGe 70 % detector at $E_{\gamma'}$=1.33 MeV as a function of the shaping time used to amplify the electronic signal. Measured using a ^{60}Co source.*

measured as a function of $E_{\gamma'}$, for shaping times of 1 and 6 μs, is shown in fig. 3.15. This was again measured using standard γ-ray sources and the points at ∼5.6 and ∼6.1 MeV were found using an Am–Be source.

For run #2, two γ-ray detectors were used. These were NaI(Tl) crystals (25×25 cm each) which typically have an intrinsic resolution of ∼80 keV at $E_{\gamma'}$=1.33 MeV. These detectors were operated with a dynamic range of ∼0–20 MeV.

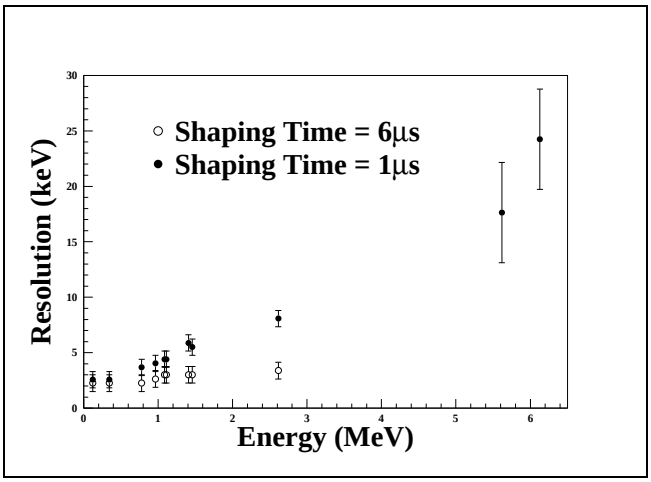

Figure 3.15: *Resolution of the HPGe 70 % detector as a function of $E_{\gamma'}$, measured using γ-ray sources.*

3.5 Detector Configuration

3.5.1 Run #1 (^{12}C(γ,pγ'))

The setup of the detectors is shown in fig. 3.16. The tagging range used in this experimental run was 49.47<E_γ<70.24 MeV. Only one charged particle telescope was used. It consisted of two DSSSD's and HPGe #1. This allowed particle tracking as well as particle identification. The telescope was placed with the front face of HPGE #1 at a distance of ∼80 mm from the target, and at an angle of ∼70° to the beam axis. This angle was chosen as it corresponded to a maximum in the cross section for the ^{12}C(γ,p$_o$) reaction, [Ire93]. The target was placed at a distance of ∼1 m from the collimator and aligned with the path of the photon beam using a laser directed along the beam axis. It was placed at ∼20° to the beam axis, so that it would be normal to the axis of the telescope. This allowed the telescope to 'see' the least possible thickness of the target, minimising energy losses for charged particles travelling straight to the telescope. The range of proton emission angles covered was $82° \lesssim \theta_p \lesssim 129°$, with an angular resolution varying from ∼8° for central angles to ∼11° at the extremes of the telescope acceptance.

The HPGe 70 % γ-ray detector was placed at ∼70 mm from the target

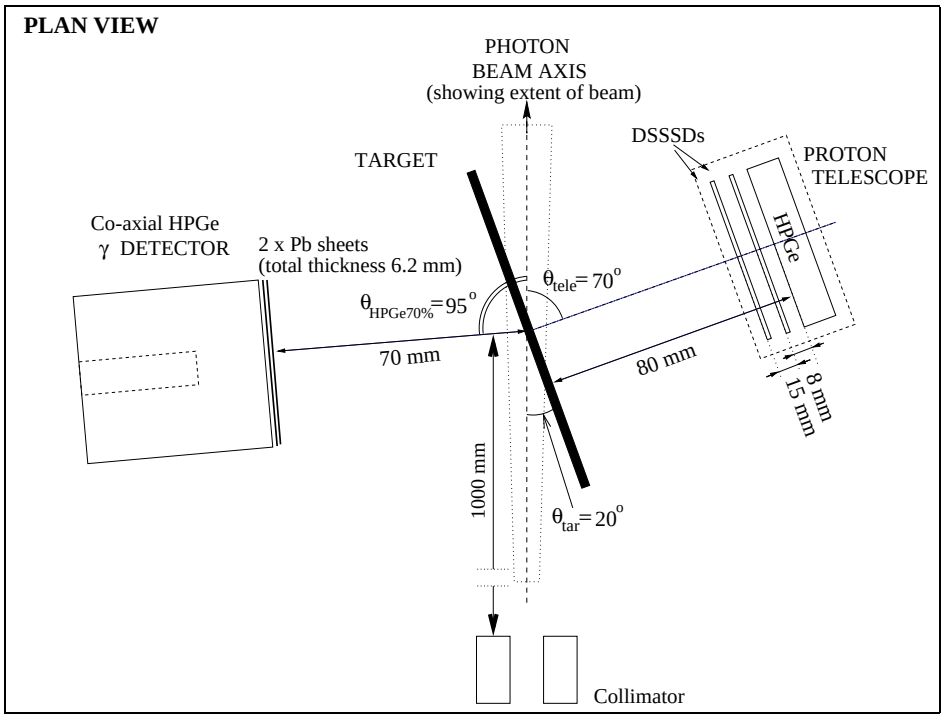

Figure 3.16: *The detector setup of run #1, the* $^{12}C(\gamma,p\gamma')$ *experiment.*

(the solid angle subtended was ∼695 msr), at ∼95° to the beam axis, on the opposite side of the target to the telescope. Two Pb sheets of total thickness ∼6.2 mm and diameter ∼87 mm (mass 391±1 g) were placed in front of the detector to attenuate low energy γ-rays. Such γ-rays were of no interest in the experiment and caused an increase in the, already high, count rate. The γ-rays of interest had an energy of ∼7 MeV, and so were not appreciably affected by this. Their attenuation in the Pb was calculated to be $\lesssim$20 %.

The position of the HPGe 70 % detector was chosen so as to minimise the effect of Doppler broadening. A major contribution to the Doppler broadening is caused by the finite size of the γ-ray detector. (Different regions of the detector see a different Doppler shift. The net result is a spectrum where all accepted energies superimpose to broaden the peak.) The distance from detector to target was chosen in order to reach a compromise between the solid angle coverage and the effect of Doppler broadening. The larger the detector to the target distance, the less the effect of the Doppler

broadening.

Energy resolution was a key factor in this experiment, and the Doppler broadening had to be reduced enough to keep the resolution below 50 keV at $E_{\gamma'}$=6.8 MeV, (the separation of the closest lying states in ^{11}B). For this purpose the detector was placed at ∼165° w.r.t. the axis of the charged particle telescope. Although this maximised Doppler shifting, approximate calculations showed that this position would correspond to a broadening of $\frac{1}{10}$ the value if the detector were placed at ∼90° w.r.t. the axis of the telescope.

3.5.2 Run #2 (^{14}N(γ,Xγ'))

The tagging range used in this experimental run was 50.2<E_γ<71.4 MeV. Two telescopes were used this time to maximise solid angle coverage for the detection of deuterons, as shown in fig. 3.17. Each was placed at ∼90° to

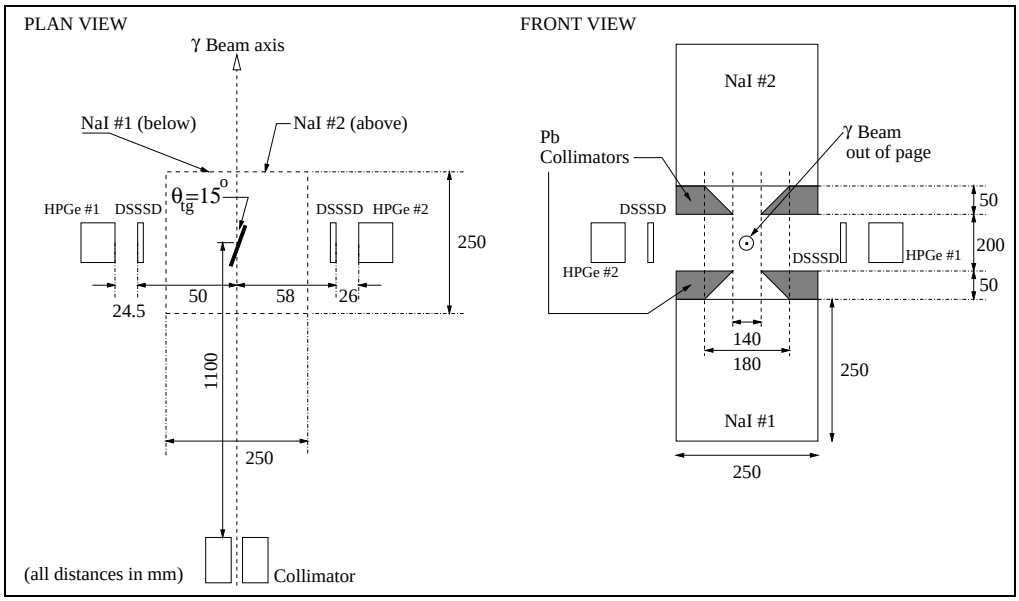

Figure 3.17: *The detector setup of run #2, the ^{14}N(γ,Xγ') experiment.*

the beam axis. HPGe #1 was at a distance of ∼74.5 mm and HPGe #2 at ∼84 mm from the target. Only one DSSSD was present in each telescope, therefore no particle tracking was made. Particle identification was still

possible. One less DSSSD on each telescope, allowed the HPGe detectors to be moved ∼15 mm closer to the target, improving the solid angle by ∼25 %, and lowering the deuteron detection threshold. The beam had a diameter of ∼25 mm at the target position. The target was at an angle of ∼15° to the beam axis.

The positioning of these detectors around the target was made to maximise solid angle. Doppler broadening was not an issue this time due to the relatively poor resolution of the NaI detectors. The solid angle coverage of the NaI γ-ray detectors, Ω_{NaI}, was determined by a Pb collimator placed around the target, and not by the size of the scintillators themselves. The total solid angle covered by both collimated detectors was ∼2.27 sr.

3.6 Electronics

The aim of the data acquisition is to produce an event by event data stream which can be written to magnetic tape for later analysis. The electronics, which process the detector signals, allow us to do this by selecting the events of interest and converting all relevant information into digital form.

This information is then written to tape for later use. The electronics associated with a photon tagging experiment must allow the focal plane element for each event to be identified. This requires measuring the time difference in the arrival of the X–trigger[2] and the signals (if any) in each focal plane element. An overview of the electronics used for signal processing in runs #1 and #2 is shown in figures 3.18 and 3.19, respectively.

3.7 Count Rates

An important task in the preparation of an experiment is to calculate the number of counts which are expected from the beam time available. This

[2]The term X–trigger (short for eXperimental trigger) represents the signal, used to define an event received by the detection system, that is of interest, and which is to be recorded.

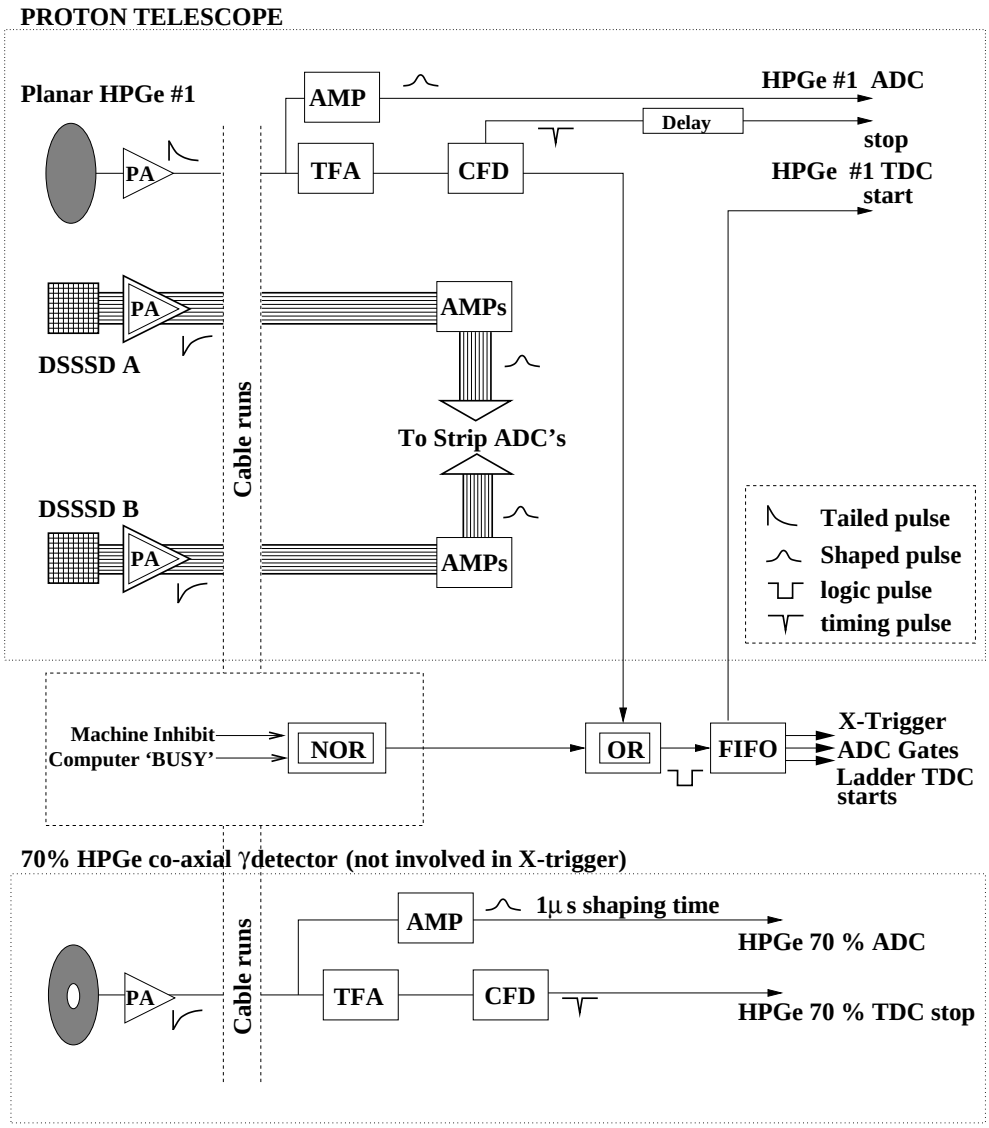

Figure 3.18: *Signal processing electronics for run #1 with the HPGe 70 % γ-ray detector. The abbreviations used are PA – Pre-amplifier, AMP – Shaping Amplifier, TFA – Timing Filter Amplifier, CFD – Constant Fraction Discriminator, FIFO – Fan In/Fan Out, ADC – Analogue-to-Digital Converter, TDC – Time-to-Digital Converter.*

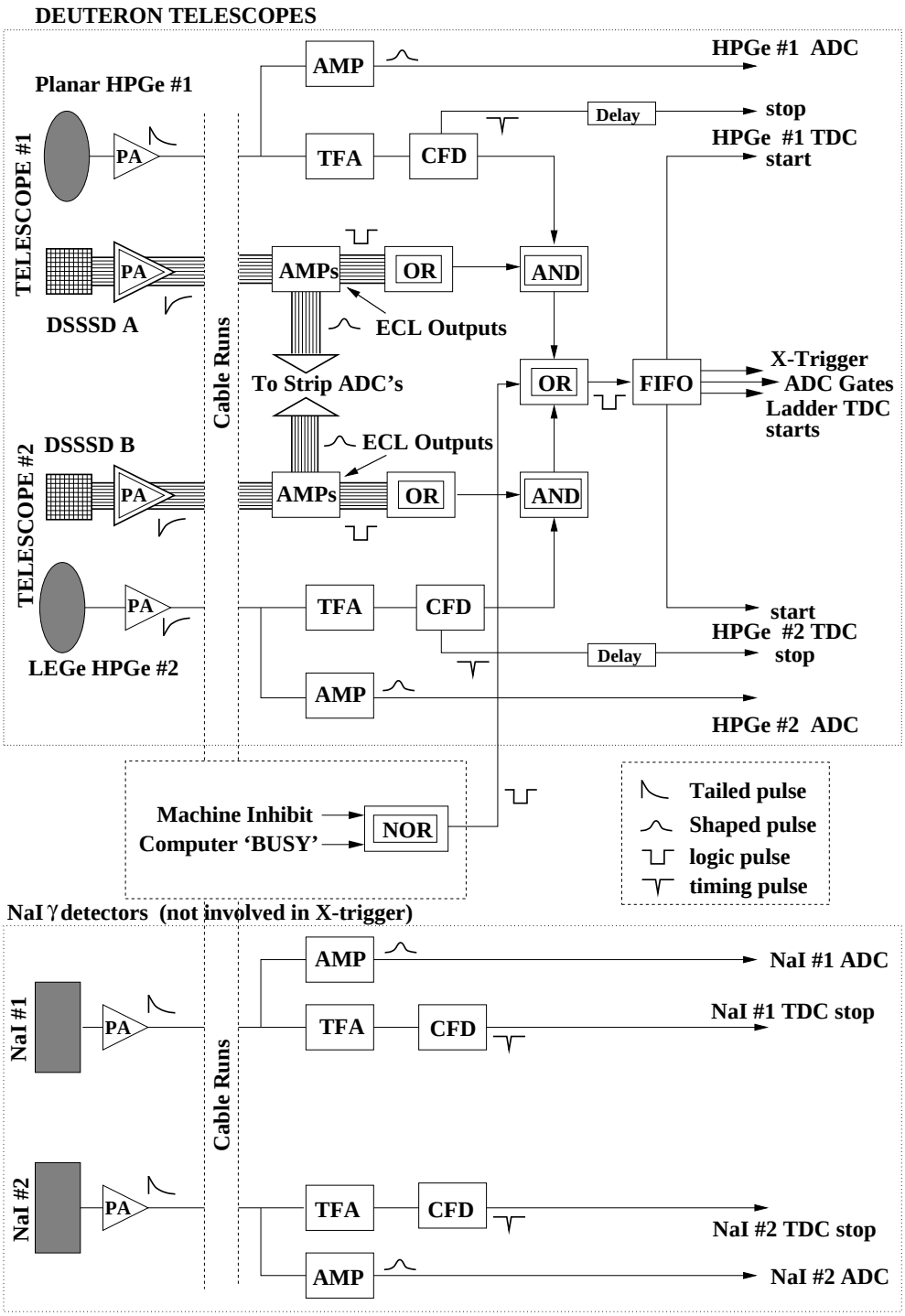

Figure 3.19: *Signal processing electronics for run #2 with the NaI γ-ray detectors, see caption on fig. 3.18 for an explanation of the abbreviations used.*

was especially important for the experiment carried out in run #1, where low statistics were anticipated. For this run the number of de–excitation γ-rays which were expected to be detected from the triplet of states at $\sim$7 MeV in ^{11}B was worked out as follows. First, the rate of tagged photons is

$$\mathrm{R}_{\gamma} = \mathrm{N}_{e'}\varepsilon_{tagg} = \mathrm{N}_{\mathrm{FP}}\mathrm{R}_{e'}\varepsilon_{tagg} \tag{3.2}$$

where

- $\mathrm{N}_{e'}$ is the count rate of electrons on the focal plane.
- N_{FP} is the number of focal plane elements.
- $\mathrm{R}_{e'}$ is the count rate per focal plane element.
- ε_{tagg} is the average tagging efficiency for all focal plane elements.

A rate of $\mathrm{R}_{\gamma} \simeq 4 \times 10^6$ s^{-1} is assumed for this estimate.

The rate of photoprotons is

$$\mathrm{R}_{\mathrm{p}} = \mathrm{R}_{\gamma}\mathrm{N}_{\mathrm{T}}\frac{\mathrm{d}\sigma}{\mathrm{d}\Omega}\Delta\Omega_{\mathrm{p}}\varepsilon_{p}\varepsilon_{live} \tag{3.3}$$

where

- $\frac{d\sigma}{d\Omega}$ is the (γ,p) cross section. The average cross section, summed over the three states of the triplet, at $\sim$70° is $\sim$6 μb/sr over the photon energy range from 50 to 70 MeV, [Hoo92a],
- $\Delta\Omega_{\mathrm{p}}$ is the total solid angle subtended by the charged particle telescope (=280.7 msr),
- ε_{p} is the efficiency for detection of the charged particles (=1),
- ε_{live} is the live time of the acquisition system (=85 %),
- and $\mathrm{N}_{\mathrm{T}} = \frac{\mathrm{t}\cdot\rho\cdot\mathrm{N}_{\mathrm{A}}}{\mathrm{A}} \simeq 1.29 \times 10^{23}$ cm^{-2} is the number of target nuclei per cm^2 in the path of the beam, where

- t is the physical target thickness, measured along the beam axis,
- ρ is the density of the target,
- N_A is Avogadro's number (6.02×10^{23}),
- A is the mass of one mole of the target in grams.

This gives a rate of $R_p \simeq 0.868$ photoprotons s^{-1}.

Assuming isotropic decay of the excited states in ^{11}B, the rate of de–excitation γ-rays from the triplet is given by

$$R_{\gamma'} = R_p \frac{\Delta\Omega_{\gamma'}}{4\pi} \varepsilon_{\gamma'} B_\gamma \tag{3.4}$$

where

- $\Delta\Omega_{\gamma'}$ is the total solid angle of the HPGe 70 % γ-ray detector,
- $\varepsilon_{\gamma'}$ is the γ-ray photopeak detection efficiency at the energy in question, $E_{\gamma'} \simeq 7$ MeV,
- and B_γ is the branching ratio for γ decay.

Taking a value of 2 % for $\varepsilon_{\gamma'}$, and a solid angle of 695 msr for the HPGe 70 %, gives a rate of $\simeq 1.2 \times 10^{-4}$ s^{-1}. This corresponds to a total of $\sim$110 counts in the photopeaks of all three levels over a (typical) 250 hour data taking period. In fact, close to 100 counts were measured for the three states in total in the final spectrum (see later), giving us confidence in the detection system.

3.8 Summary Table

Table 3.1: *Table of parameters for experimental runs #1 and #2.*

	Run #1	Run #2	
Reaction	^{12}C(γ,pγ')	^{14}N(γ,Xγ')	
Electron Beam Energy (MeV)	∼92.3	∼92.8	
Tagging Range (MeV)	∼49.47–70.24	∼50.20–71.40	
Average ε_{tagg}	∼23.9 %	∼22.5 %	
Detector Configuration;		Telescope #1	Telescope #2
HPGe	1×planar	1×planar	1×LEGe
DSSSD	2×(16×16 strip)	1×(16×16 strip)	1×(16×16 strip)
γ-ray det.	1×co–axial HPGe	2×NaI (25×25 cm^2)	
Range of $\theta_{p,X}$	∼82°–129°	∼55°– 135°	∼-50°– -120°
$\Delta\Omega_{p,X}$ (msr)	∼280.70	∼320.43	∼483.32
$\Delta\Omega_{\gamma'}$ (msr)	∼695	∼2,270	

Chapter 4

Real Photon Induced Proton Knockout from ^{12}C

This chapter describes how the ^{12}C(γ,pγ') data have been analysed, to extract the relative population of states in ^{11}B following the ^{12}C(γ,p) reaction. Essentially, the analysis is very similar to that for a (γ,p) reaction, described most recently in [Rau96]. Here the additional analysis required due to the detection of de–excitation γ-rays is explained more thoroughly. Recent work, reported by Kuzin *et al.* [Kuz99] was analysed in a similar way.

In a photon tagging experiment, each individual focal plane detector defines a photonuclear physics *experiment* entirely of its own. Each *experiment*, which is totally uncorrelated with the others, has a beam energy defined by the energy range of its focal plane element. Fig. 3.5 on page 40 showed how the bremsstrahlung spectrum is divided up within the tagging range. The analysis of (γ,p) data proceeds roughly as follows

- Obtain the kinetic energy and emission angle of the reaction product,
- Identify the energy of the photon which has induced the reaction,
- Construct the excitation spectrum of the residual nucleus.

These steps will be explained in section 4.1. In a (γ,Xγ') experiment, a fourth

stage is required to obtain the energy of the subsequent γ decay from the residual nucleus. The γ-ray analysis steps will be explained in section 4.2. The results are presented in section 4.3.

4.1 Analysis of Charged Particle Telescope Information

4.1.1 Particle Identification

A reduced data set was made, which contained only the particles of interest (e.g. protons) detected in the charged particle telescope. In order to determine the type of particle detected, use was made of the relationship between the energies (ΔE and E) measured in the DSSSD and HPGe detectors, respectively. Scatter plots of these energies show a correlation for each species of charged particle that has passed through the telescope, as depicted in fig. 4.1. In this way the large amount of background electrons detected in the telescope were removed. These electrons mainly come from pair production and Compton scattering processes in the air around the target. Other charged particles arise from photon–induced knockout processes, (γ,X), on the target, where X is neutron, deuteron, triton, etc.

A multiplicity 1 cut was demanded on each DSSSD face. For each event, each DSSSD face was checked for events within the 2–D proton window. Only events for which one, *and only one*, strip had a particle within this window on each face were accepted. Approximately 1/3 of these events also had another hit, outwith the 2–D window, present in another strip. For those events, the other particle was ignored and only the hit identified as a proton was kept.

Once the events of interest were chosen in this way they were written to a new data set which was used for all subsequent analysis. The resulting data set was a factor of $\sim$10 smaller than the original.

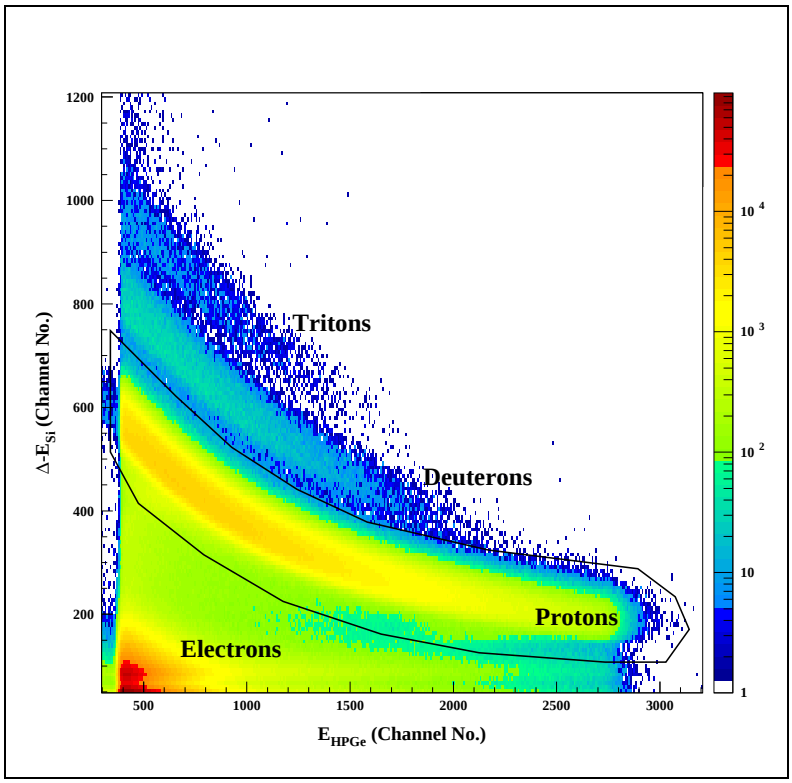

Figure 4.1: *2–D particle identification plot, showing the separation of protons, deuterons and tritons.*

4.1.2 Tagger Calibration

The photon energy associated with each channel of the focal plane tagger is derived from the electron beam energy, E_0, the magnetic field in the tagging spectrometer and the position of the detectors (in cm) along the focal plane. The calculation was carried out by the program POS, available at MAX–LAB, [Rui95b]. Fig. 4.2 shows the photon energy calibration for the two experiments described in this thesis.

4.1.3 Calibration of Proton Telescope

The thick targets (several 100 mg/cm^2) used in these measurements meant that the energy resolution for charged particle detection was poor. This, however, was not a factor in the final result as the relative population of

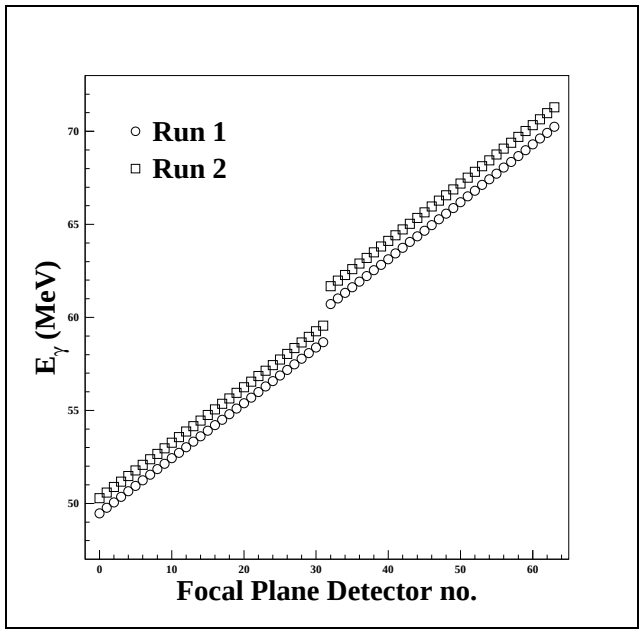

Figure 4.2: *Photon energy, E_γ, v's focal plane tagger element number for runs #1 and #2..*

states were taken from the γ-ray yields. For this reason the DSSSD's were not calibrated, i.e. they were only used for particle tracking. Only the HPGe (E) detector was calibrated. Fig. 4.3 shows some calibration spectra obtained using thin targets.

4.1.3.1 Energy Calibration of the HPGe Detector

Data from runs on the 1 mm ^{12}C target of fig. 4.3 were used to make the calibration of E_{HPGe}. This calibration depended on

- The calibration of the tagger (E_γ),
- A prediction of the energy expected to be deposited in the HPGe for each tagger element ($E_{HPGe}^{\mathrm{calc}(i)}$),
- The ADC channel number of the ground state peak in the proton energy spectra for each tagger element.

The tagger calibration gave a beam energy, E_γ, for each focal plane element. The prediction for the energy deposited in the HPGe was calcu-

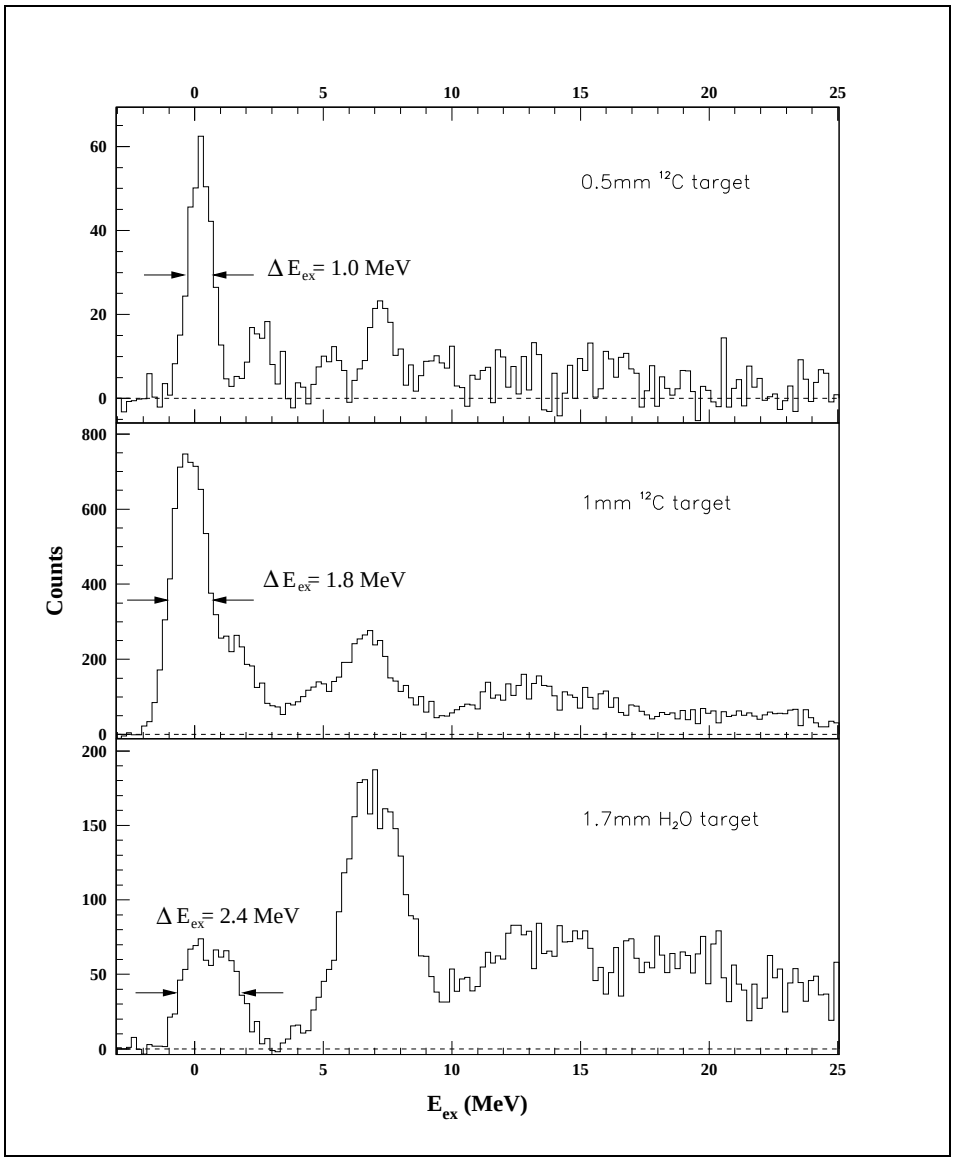

Figure 4.3: *E_{ex} spectra from thin target runs, used for calibration of E_{HPGe}.*

lated from ^{12}C(γ,p) kinematics (using the known E_γ), for the ground state transition. For a given E_γ and θ_p, a unique value for the proton's kinetic energy, $T_p(E_\gamma,\theta_p)$, was calculated (see [Rui95a] for details of (γ,p) kinematics). T_p was calculated at θ_p=70° (the central angle of the telescope), for each E_γ in the tagging range. From this T_p value the energy deposited in the HPGe was predicted after accounting for all energy losses suffered by the proton, i.e.

$$E_{HPGe}^{\mathrm{calc}(i)} = T_p{}^i - \Delta E_{tar} - \Delta E_{Front} - \Delta E_{Back} - \Delta E_{Be} \qquad (4.1)$$

where i=1,64 is the focal plane element number, and

- ΔE_{tar} is the energy lost by the proton in the target.
- ΔE_{Front} is the energy lost by the proton in the front DSSSD.
- ΔE_{Back} is the energy lost by the proton in the back DSSSD.
- ΔE_{Be} is the energy lost by the proton in the beryllium window at the entrance to the HPGe detector.

To correlate these predicted energies to channel numbers in the ADC spectrum of the HPGe, an ADC spectrum was accumulated in coincidence with each individual focal plane element. These spectra (see fig. 4.4) showed a proton ground state peak for each tagged E_γ in the beam. Finally, the channel number of the centroid of this peak was plotted against the energy predicted to be deposited in the HPGe. A direct channel number to energy correlation was then derived, as shown in fig. 4.5.

4.1.3.2 Charged Particle Trajectory

To track the trajectory of the charged particles through the telescope the DSSSD's were used. Selection of events with a multiplicity of 1 on each of the four DSSSD faces was necessary for unambiguous particle tracking. For simplicity, it was assumed that all trajectories took the protons through the centre of each strip. The first task was to convert the number of the strip which fired into a coordinate in an x–y plane (defined by the plane of the

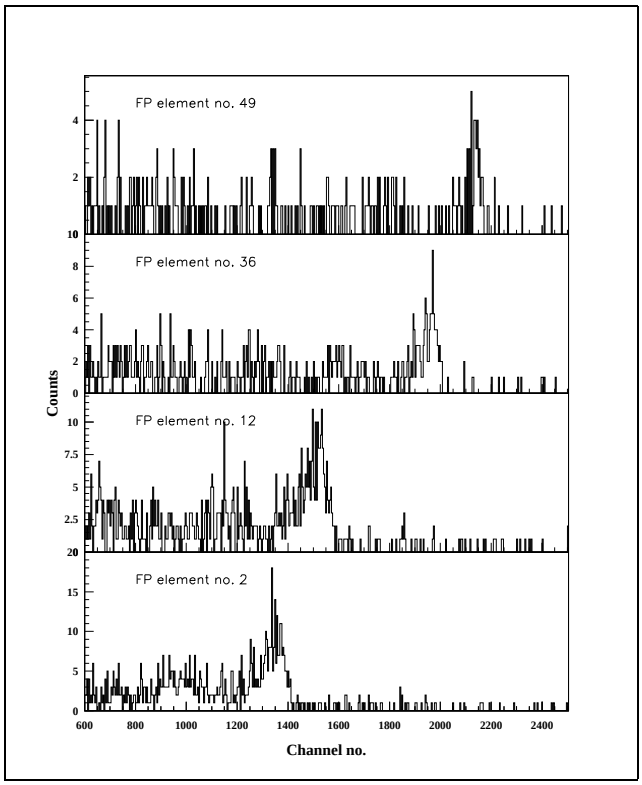

Figure 4.4: *Proton energy spectra from a 1mm thick ^{12}C target corresponding to, sample, individual focal plane detectors. The unresolved ground and 2.12 MeV states of ^{11}B are identified as the right most peak in each spectrum.*

DSSSD). This resulted in a coordinate for both the front and back DSSSD's, as shown in fig. 4.6. These coordinate pairs were labelled (x_f,y_f) and (x_b,y_b), for front and back respectively. From this information the angles θ_p and ϕ_p, which describe the trajectory of the proton, were calculated. Using (x_f,y_f), (x_b,y_b) and z_f the angles were calculated from

$$\theta_p = \sin^{-1}\left(\frac{z_f}{\sqrt{dx^2 + z_f^2}}\right) - \theta_{tar} \tag{4.2}$$

and

$$\phi_p = \sin^{-1}\left(\frac{dy}{\sqrt{dx^2 + dy^2 + z_f^2}}\right) \tag{4.3}$$

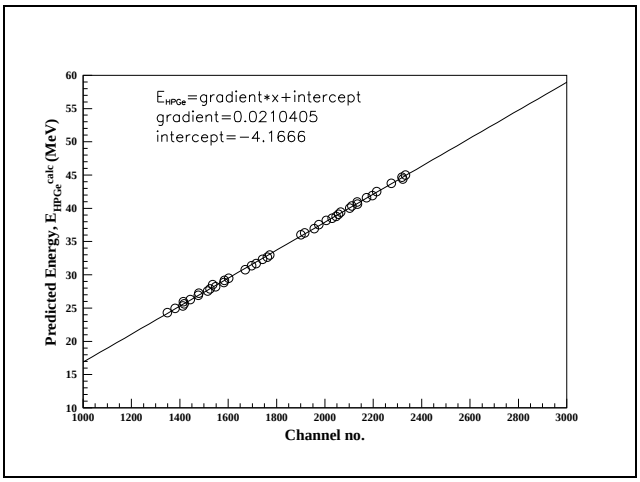

Figure 4.5: *Channel number to energy calibration for the HPGe proton detector.*

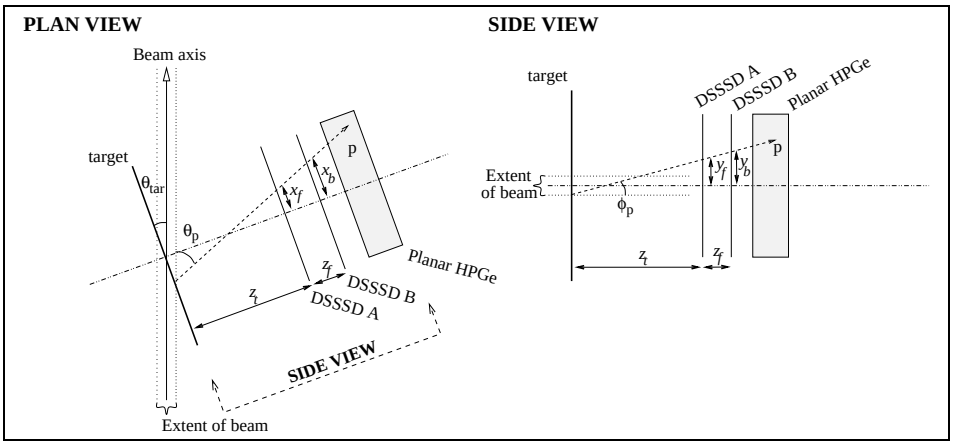

Figure 4.6: *Definition of angles θ_p and ϕ_p.*

where

$$dx = x_b - x_f$$
$$dy = y_b - y_f$$

Of course, the θ_p and ϕ_p corresponding to any coordinate pair represent the average values for all events allowed by that combination of strips. For each individual event these angles can differ from the average values over the ranges dictated by the strip pitches.

4.1.3.3 Reconstructing T_p

Following the calibration of E_{HPGe} and the particle tracking it was still necessary to reconstruct the initial proton kinetic energy, $T_p{}^{meas}$, for each event. To do this, the energy loss suffered by the proton as it passed through the materials between the target and HPGe were re–calculated. This was done on an event by event basis in the sorting code using the 'Range Method' [Kno89], which describes the range of a given particle in a given medium by two parameters, a and b, such that $\mathrm{R} = a\mathrm{E}^b$ where a and b are derived from a fit to range data.

For each event, energy losses were subtracted from the calibrated E_{HPGe} for energy lost in the Be window, air, DSSSD's (since these were not calibrated) and finally the target. Since the interaction point within the target cannot be known, all events were assumed to originate from the central plane of the target.

In calculating the energy losses for each material, the true distance, t_{true}, through which the proton has travelled was used. This is related to the normal thickness, t_{norm}, by

$$\mathrm{t}_{true} = \mathrm{t}_{norm} \frac{1}{\sin\left(\theta_p + \theta_{tar}\right)\cos\phi_p} \tag{4.4}$$

where θ_p and ϕ_p are the planar and azimuthal angles of the proton and θ_{tar} is the angle of the target with respect to the beam direction.

Finally, the initial proton kinetic energy was calculated as the sum of all the energy losses in each respective medium and the energy deposited in the HPGe detector

$$T_p = E_{HPGe} + \Delta E_{Be} + \Delta E_{Back} + \Delta E_{Front} + \Delta E_{tar} \tag{4.5}$$

where the symbols are as explained previously. Here the energy losses in each region of air, present between all materials, and the Al foil in front of the DSSSD's have been left out of the equation for clarity, but were included in the analysis.

4.1.4 Identification of Tagged Photons

TDC's measure, and digitise, the time between the arrival of an X–trigger and the bremsstrahlung electron in each focal plane element (if one arrives). The resulting spectrum is used to identify the p–e$'$ events due to true correlations between a tagged photon and its scattered electron. A large amount of background events were seen in the timing spectrum. These were caused by the large electron count rate in the focal plane ($\sim 10^6$ Hz), as compared to the much lower rate of X–triggers ($\sim$10 Hz). Three kinds of event may fill this spectrum

- True p–e$'$ coincidences – events for which the TDC of the correct focal plane element is stopped by the correct electron. This kind of event enters the prompt peak of the spectrum.

- The TDC of the focal plane element associated with the E_γ of the event is stopped by a random electron before the correlated electron reaches it. This causes the event to enter the spectrum before (to the left of) the prompt peak.

- An electron completely uncorrelated with the X–trigger stops a TDC for a focal plane element other than the one associated with the E_γ which initiated the event. This kind of event can enter the spectrum anywhere.

These three kinds of event result in a prompt peak sitting on a background of uncorrelated events. Fig. 4.7 shows the spectrum derived from these data, a timing resolution of $\sim$1-2 ns was achieved. The shape of this background has been explained in detail by [Hoo92b, Owe90]. In most practical cases however, it can be taken to be flat. The spectrum is divided into three regions. The prompt time interval, τ_P, is used to identify the correlated p–e$'$ events and the intervals τ_E and τ_L are used together to subtract the background.

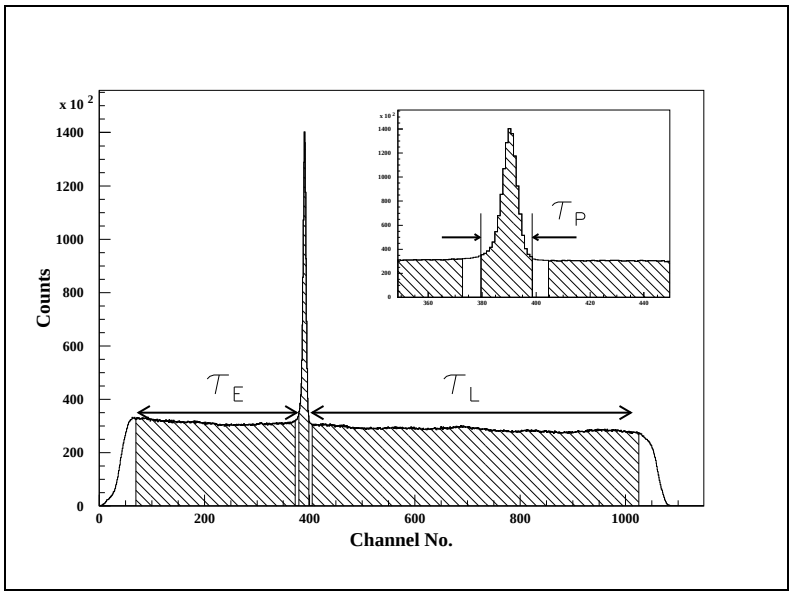

Figure 4.7: *Focal plane TDC spectrum for the $^{12}C(\gamma,p)$ data. The timing resolution is ~1-2 ns.*

4.1.5 Reconstruction of E_{ex}

With knowledge of the beam energy, E_γ, the knocked out proton's kinetic energy, T_p, and its angle, θ_p, it is now possible to calculate the missing energy, E_m. The missing energy variable is used to view the data since it is independent of E_γ, T_p and θ_p, therefore allowing statistics for all focal plane detectors and all angular combinations of silicon strips to be added together. In general, E_m is defined as

$$E_m = E_\gamma - T_p - T_{r*} \tag{4.6}$$

where

- E_γ is known from the tagger calibration,
- T_p is known from the E_{HPGe} calibration and
- T_{r*}, the kinetic energy of the residual nucleus, may be calculated uniquely from the kinematics without detection of the residual. (See

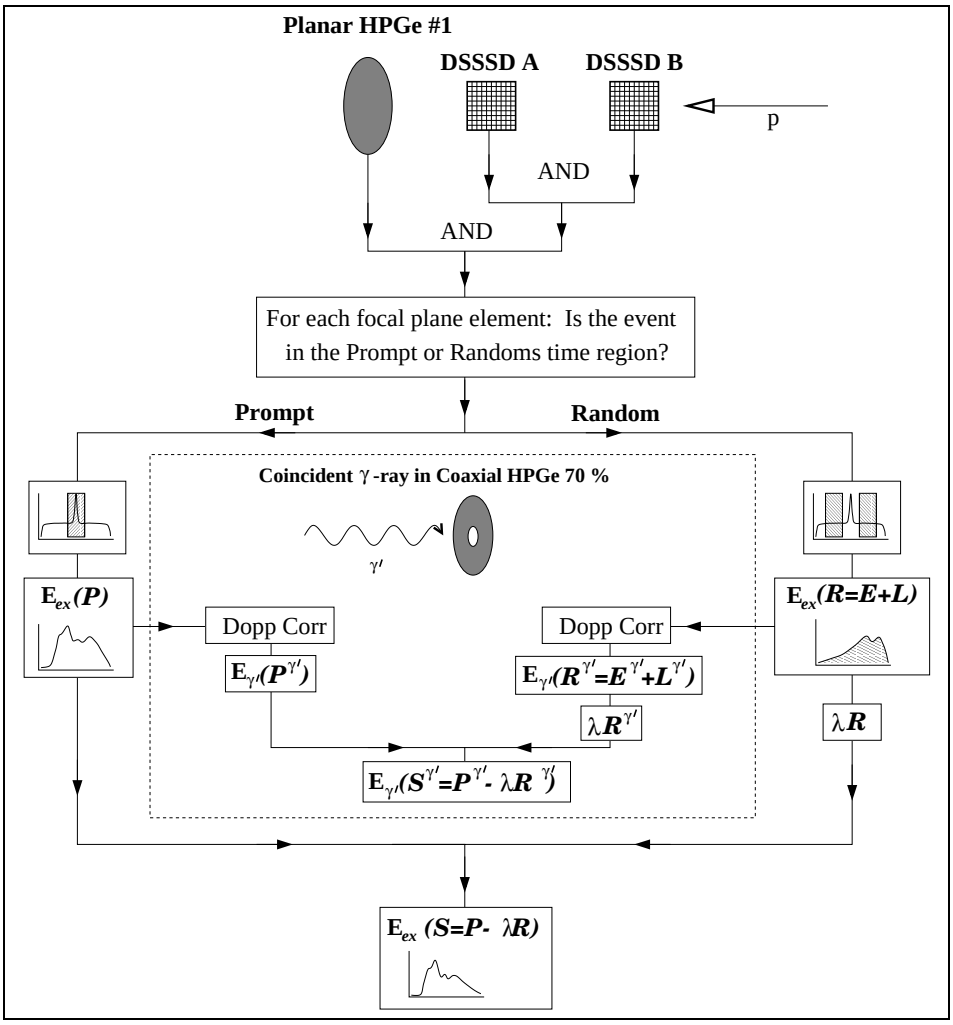

Figure 4.8: *Flowchart of the analysis steps made to arrive at the $\mathcal{S}$ and $\mathcal{S}^{\gamma'}$ spectra.*

[Rui95a] for a description of how E_m is calculated event by event from E_γ,T_p and θ_p).

Finally, the excitation energy of the residual nucleus is given by $E_{ex} = E_m + \mathrm{Q}_{gs}$, as stated in chapter 2.

An excitation energy spectrum, due only to events inside the prompt peak of the focal plane TDC spectrum of fig. 4.7 must be produced. The procedure for subtracting E_{ex} events due to the background present underneath the peak is outlined in the flowchart of fig. 4.8. Events in coincidence

with the time interval τ_P give the 'Prompt' spectrum, $\mathcal{P}$, (see the top panel of fig. 4.9). The correct number of events to subtract is found by making the 'Randoms' spectrum, $\mathcal{R}$. The spectrum $\mathcal{R}$ is found by combining the early and late spectra in coincidence with the time intervals τ_E and τ_L (i.e. $\mathcal{R}$=$\mathcal{E}$+$\mathcal{L}$). This spectrum shows a smooth distribution with E_{ex}. The spectrum of 'Real' correlations, $\mathcal{S}$, is then created by

$$\mathcal{S} = \mathcal{P} - \lambda\mathcal{R} \tag{4.7}$$

as is shown in the lower panel of fig. 4.9. The factor λ, used to normalise the Randoms spectrum, is based on the number of counts in the random time regions relative to that underneath the prompt peak, i.e.

$$\lambda = \frac{N_P}{N_E + N_L} \tag{4.8}$$

where N_P is the number of counts underneath the prompt peak and N_E and N_L are the number of counts in the $\mathcal{E}$ and $\mathcal{L}$ spectra. The number, N_P, of counts under the prompt peak was approximated by the area underneath a straight line, drawn between the edges of the τ_P time region. The dip at $E_{ex}\sim$18 MeV in the shape of the randoms spectrum is due to a physical gap between the two groups of focal plane detectors which measure E_γ. Their physical spacing corresponds to an energy gap in the tagging range of ~2-3 MeV. Following the randoms subtraction the remaining E_{ex} events are, in principle, due solely to real p–e′ correlations between the X–trigger and the focal plane.

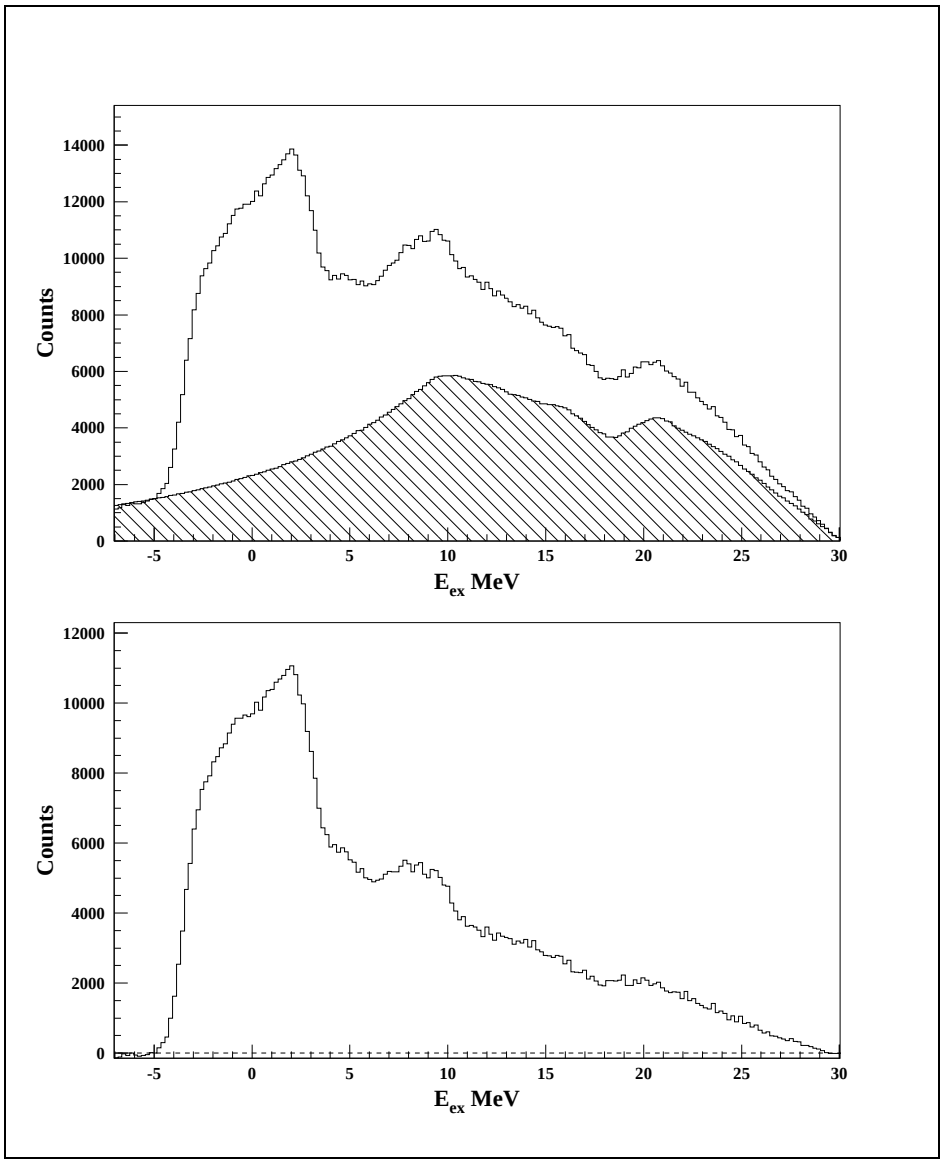

Figure 4.9: *E_{ex} spectrum from the 2.5 mm ^{12}C target showing a resolution of $\Delta E_{ex} \simeq 6$ MeV FWHM. In the upper panel the prompt, $\mathcal{P}$, spectrum is shown along with the randoms, $\mathcal{R}$ (hatched). The lower panel shows the subtracted spectrum, $\mathcal{S}$.*

4.2 Analysis of De–excitation γ-rays

The 'standard' part of the analysis has now been completed. The next step is to consider the γ-rays detected in coincidence with the protons. An important part of the γ-ray analysis is to use E_p, θ_p and ϕ_p to correct the γ-ray spectra for the Doppler shift that occurs, due to the motion of the residual nucleus as it decays. The final spectra must then be fitted with γ-ray line shapes to extract the yield from each decaying state. Then the relative population of states, created as a result of the (γ,p) reaction, is calculated taking into account the branching ratios for the γ-ray decays involved. A discussion is made here of the possible effects due to correlations of the γ-ray emission angle with the direction of the recoiling nucleus and the effect of this on the relative populations derived from the γ-ray yields.

4.2.1 Derivation of the γ' Spectra

The main background in the γ-ray spectra in this experiment came from the same source as the E_{ex} background, i.e. from random electrons striking the focal plane, where a coincident γ' was also present. These were dealt with in the same way as for E_{ex}, by filling a γ' spectrum in coincidence with the prompt time region (τ_P) of the focal plane TDC spectrum. Refer to fig. 4.8 for the basic steps used to fill the $E_{\gamma'}$ spectra.

The γ-ray randoms spectrum ($\mathcal{R}^{\gamma'}$) has structure, whereas the spectrum of E_{ex} randoms ($\mathcal{R}$) did not. When E_{ex} is calculated in coincidence with the randoms region it is reconstructed with an incorrect value for E_γ (the beam photon). Therefore the $\mathcal{R}$ spectrum is smoothly varying, due to this kinematical dependence. The energy of the de–excitation γ-ray, however, is independent of the beam energy, E_γ. Also, the de–excitation γ-ray spectrum is gated by protons, from (γ,p) events, moving away from the γ-ray detector, hence limiting the Doppler broadening. Therefore the $\mathcal{R}^{\gamma'}$ spectrum is as likely to show structure as the $\mathcal{P}^{\gamma'}$ spectrum.

Another source of background came from events in the γ-ray spectrum

caused by uncorrelated signals in the HPGe 70 % detector. To test for these events the time between the arrival of an accepted X–trigger and the subsequent γ' was measured. This spectrum (see fig. 4.10) shows a timing peak of resolution ∼30 ns (determined mainly by the timing resolution of the HPGe 70 % detector). The background here was low and therefore no

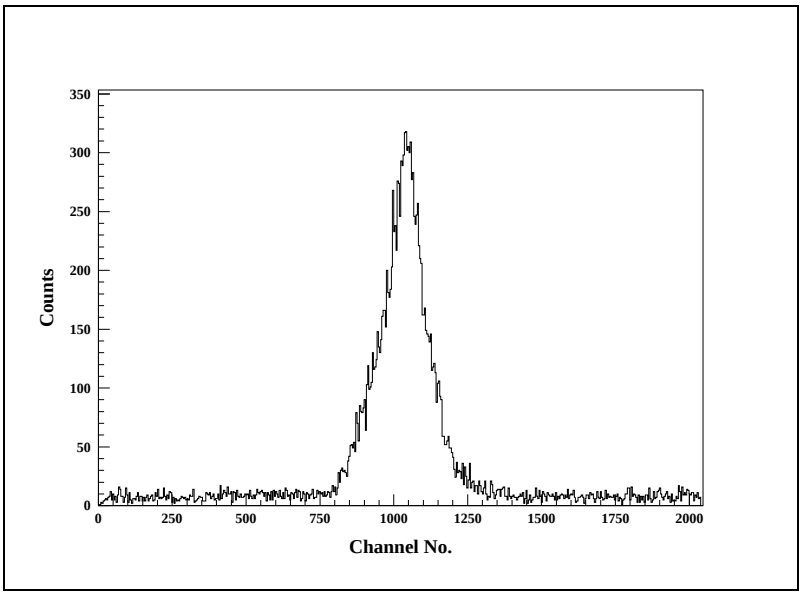

Figure 4.10: *TDC spectrum of the time correlation between X–triggers and signals from the HPGe 70 % detector. The timing resolution is ∼30 ns.*

subtraction was made for these uncorrelated γ-ray events.

It should be noted that the E_{ex} spectrum has such poor resolution that it has been impossible to make cuts to view the γ' spectra for different regions of excitation in ^{11}B. Therefore all the γ' spectra shown, unless otherwise stated, are in coincidence with the whole E_{ex} spectrum.

4.2.2 Calibration of HPGe 70 % Detector

Sources emitting γ-rays of known energy, ^{60}Co and Am–Be, were used to provide a correlation between ADC conversion and energy in the HPGe 70 % detector. The Am–Be source provided γ-ray lines up to 6.128 MeV, see [Kin84, Kno89] for details. Fig. 4.11 shows a spectrum gathered from

this source over ∼15 min, at a source to detector distance of ∼1.5 m. A

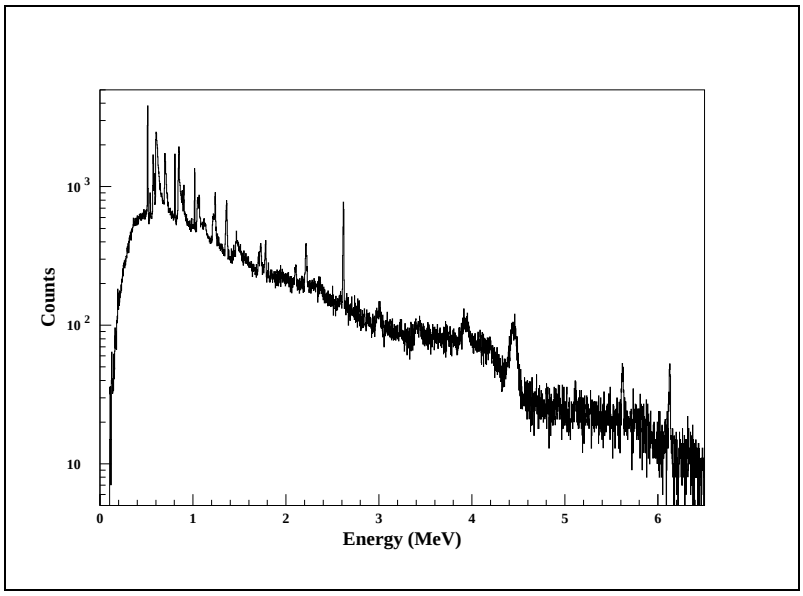

Figure 4.11: *Calibration spectrum taken with HPGe 70 % detector using an Am–Be source in a Teflon holder, see text for details.*

cubic fit was made to the calibration points and is shown in fig. 4.12. The non–linearity shown in the lower panel of this figure was calculated as the difference between the cubic fit and a linear fit to the data points. The non–linearity amounts to $\lesssim$1.5 % over the energy range of interest.

4.2.3 Doppler Correction

In order to ease interpretation of the final γ' spectra it was necessary to account for the shift in detected γ-ray energy, caused by the motion in the laboratory frame, of the residual nucleus during γ-ray emission. The kinetic energy imparted to the recoiling nuclei was of the order ∼2-3 MeV, implying a velocity, v_r, of $\sim 2.4\times10^{-2}$ c.

The Doppler correction was made to account for the Doppler shift, as well as to improve the energy resolution by accounting for the broadening effect which is caused by the finite size of the HPGe 70 % detector. The detector subtended a cone of half angle ∼18° about a point on the centre of

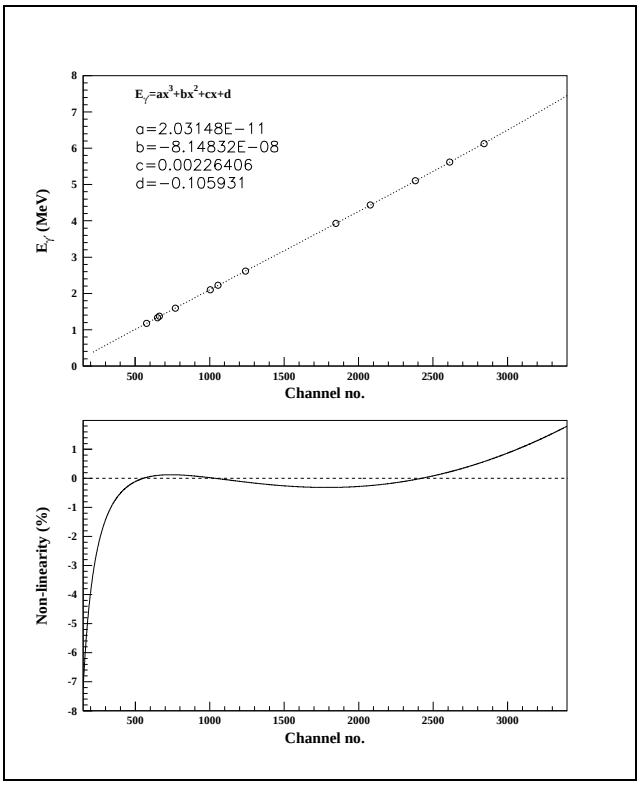

Figure 4.12: *HPGe 70 % detector calibration. The top panel shows the calibration plot. The bottom panel is the non–linearity in %.*

the beam spot.

From knowledge of the (γ,p) kinematics, (and the fact that the final state is two body), a measurement of (θ_p,ϕ_p) and T_p for an event in the telescope allowed reconstruction of the kinematics of the residual nucleus. This gave (θ_r,ϕ_r), T_r and therefore (knowing the recoil's mass) the velocity vector, $\mathbf{v}_r$. The mass of the recoiling nucleus (in its excited state) was calculated from E_m by $m_r^* = E_m + m_t - m_p$.

The actual Doppler correction is given by

$$E_{\gamma'}^{Dopp} = E_{\gamma'}^{det} \frac{1}{\sqrt{1 + \frac{v_r}{c}\cos\theta_{\gamma'}}} \tag{4.9}$$

where $E_{\gamma'}^{det}$ is the detected γ-ray energy, c is the speed of light in vacuo and $\theta_{\gamma'}$ is the angle between the velocity vector, $\mathbf{v}_r$, and the directional vector of

the emitted γ-ray, $\mathbf{r}_{\gamma'}$. Fig. 4.13 shows a schematic of the vectors involved.

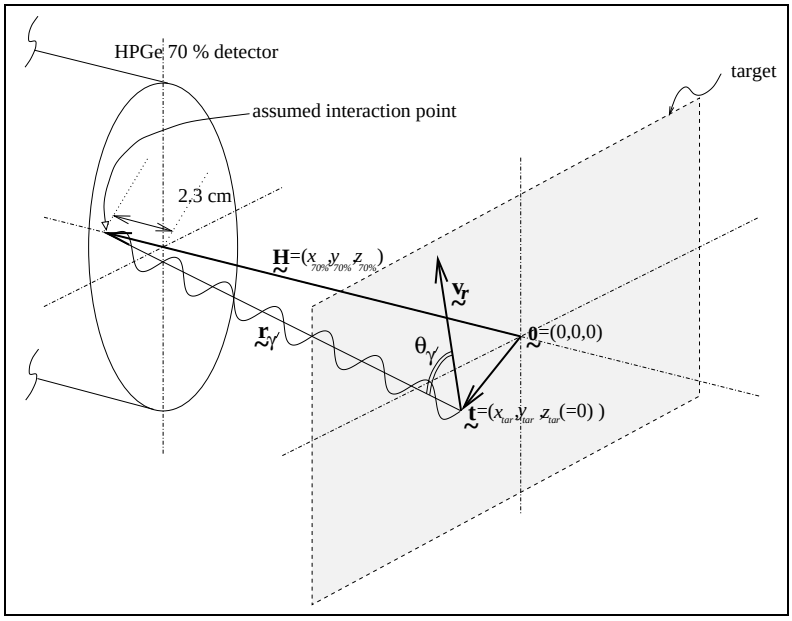

Figure 4.13: *Vector reconstruction used for Doppler correction of the γ' energy.*

Calculation of the angle $\theta_{\gamma'}$ for each event requires knowledge of the directional vector $\mathbf{r}_{\gamma'}$. However, the HPGe 70 % detector provides no positional information on the detection of a γ-ray. Only the fact that a hit has occurred, and the energy deposited, are registered. To establish a direction for each γ', an interaction point within the HPGe 70 % was chosen, and assumed for all γ-rays. This point was taken to be one radiation length for Ge (L_{rad}^{Ge}=2.3 cm [Tsa74]) into the volume of the crystal, along its central axis, measured from the front face. A straight line in 3–D space between this point and the origin of the γ-ray was used to define the directional vector $\mathbf{r}_{\gamma'}$. Although this assumption is incorrect for individual γ-rays it is expected to reproduce reasonably well the average direction.

The point of emission was taken as the point where the (γ,p) reaction occurred. This point was measured by back–tracking the proton's trajectory (from the telescope) to where it crossed the 2–D x–y plane defined by the central plane of the target. These target coordinates are described by the positional vector $\mathbf{t}$ relative to an origin, at the centre of the target face, as

depicted in fig. 4.13. Fig. 4.14 shows the measured distribution of positions, **t**, on the target face, as seen from the telescope side. The streaking in

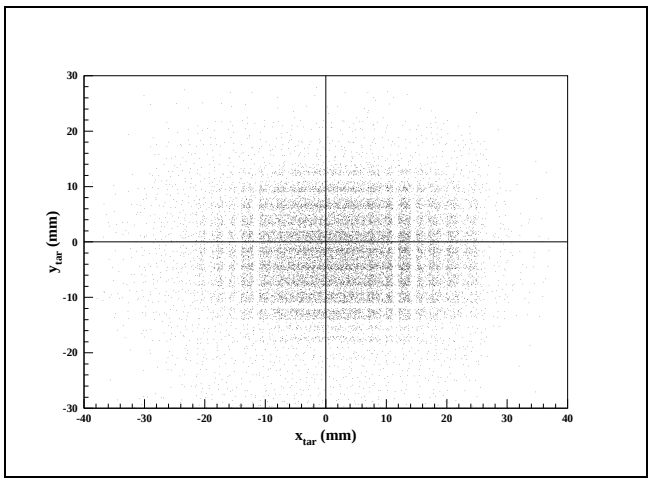

Figure 4.14: *Interaction points reconstructed on the target face, showing the physical shape of the beam spot.*

this plot is due to the angular resolution of θ_p and ϕ_p, which worsens for trajectories with increasing angle relative to the axis of the telescope.

The angle $\theta_{\gamma'}$ was reconstructed according to the scalar–product of the vectors $\mathbf{v}_r$ and $\mathbf{r}_{\gamma'}$, i.e.

$$\mathbf{v}_r \cdot \mathbf{r}_{\gamma'} = |\mathbf{v}_r||\mathbf{r}_{\gamma'}| \cos\theta_{\gamma'} = {v_r}^x {r_{\gamma'}}^x + {v_r}^y {r_{\gamma'}}^y + {v_r}^z {r_{\gamma'}}^z \tag{4.10}$$

rearranging for $\theta_{\gamma'}$ gives

$$\theta_{\gamma'} = \cos^{-1}\left(\frac{{v_r}^x {r_{\gamma'}}^x + {v_r}^y {r_{\gamma'}}^y + {v_r}^z {r_{\gamma'}}^z}{|\mathbf{v}_r||\mathbf{r}_{\gamma'}|}\right) \tag{4.11}$$

The measured distribution of $\theta_{\gamma'}$ is shown in fig. 4.15.

The Doppler correction was then performed, according to equation 4.9, for each event. Fig. 4.16 shows how the correction affected the 2.12 and 5.02 MeV γ-rays from ^{11}B. It can be seen that the Doppler shift is accounted for but the Doppler broadening is not. This is due to the lack of positional information in the γ' detection and to the resolution in the measurement of θ_p and ϕ_p. It should be noted that the correction only makes a meaningful

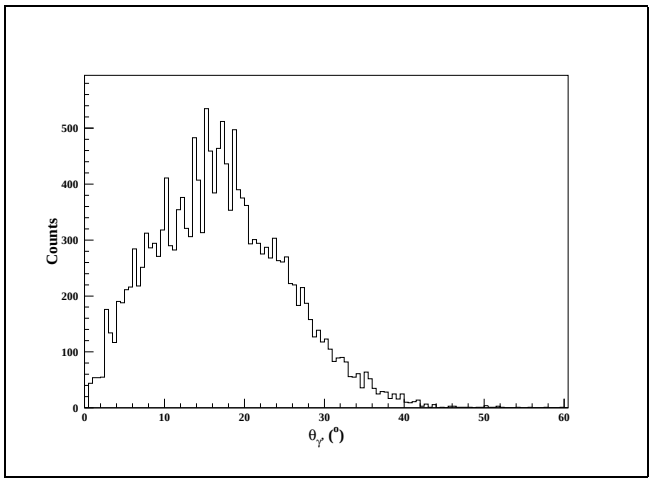

Figure 4.15: *Distribution of the angle ($\theta_{\gamma'}$) between the vectors $\mathbf{v}_r$ and $\mathbf{r}_{\gamma'}$ of fig. 4.13.*

shift to the events within the photopeak of the γ-ray spectrum. All other measured energies, i.e. those in the escape peaks and the Compton tails, were corrected by a factor inappropriate for the energy which registered in the detector. This effect is $\lesssim$3 %.

4.2.4 Efficiency of HPGe 70 %

Measurements made of the absolute efficiency of the HPGe 70 % detector, with a source to detector distance of $\sim$10 cm, for 0.2<$E_{\gamma'}$<1.4 MeV are shown in fig. 4.17. An efficiency curve (measured up to $E_{\gamma'}\simeq$11 MeV) for a 32 % relative efficiency Ge(Li) detector was taken from that used in [Ver89] to obtain the efficiency out to $E_{\gamma'}$=7 MeV in the HPGe 70 % detector. This function was normalised to the data measured for the 70 % detector at $E_{\gamma'}$<1.4 MeV. An error of 2.63 % has been estimated for the normalisation.

The present experiment is an attempt at measuring the relative population of the states around 7 MeV only. The efficiency, $\varepsilon_{\gamma'}$, does not vary much over the energy range containing the γ-rays of interest, i.e. 6.7–7.3 MeV. For this reason the error introduced by extrapolating the efficiency function does not affect the measured relative populations greatly.

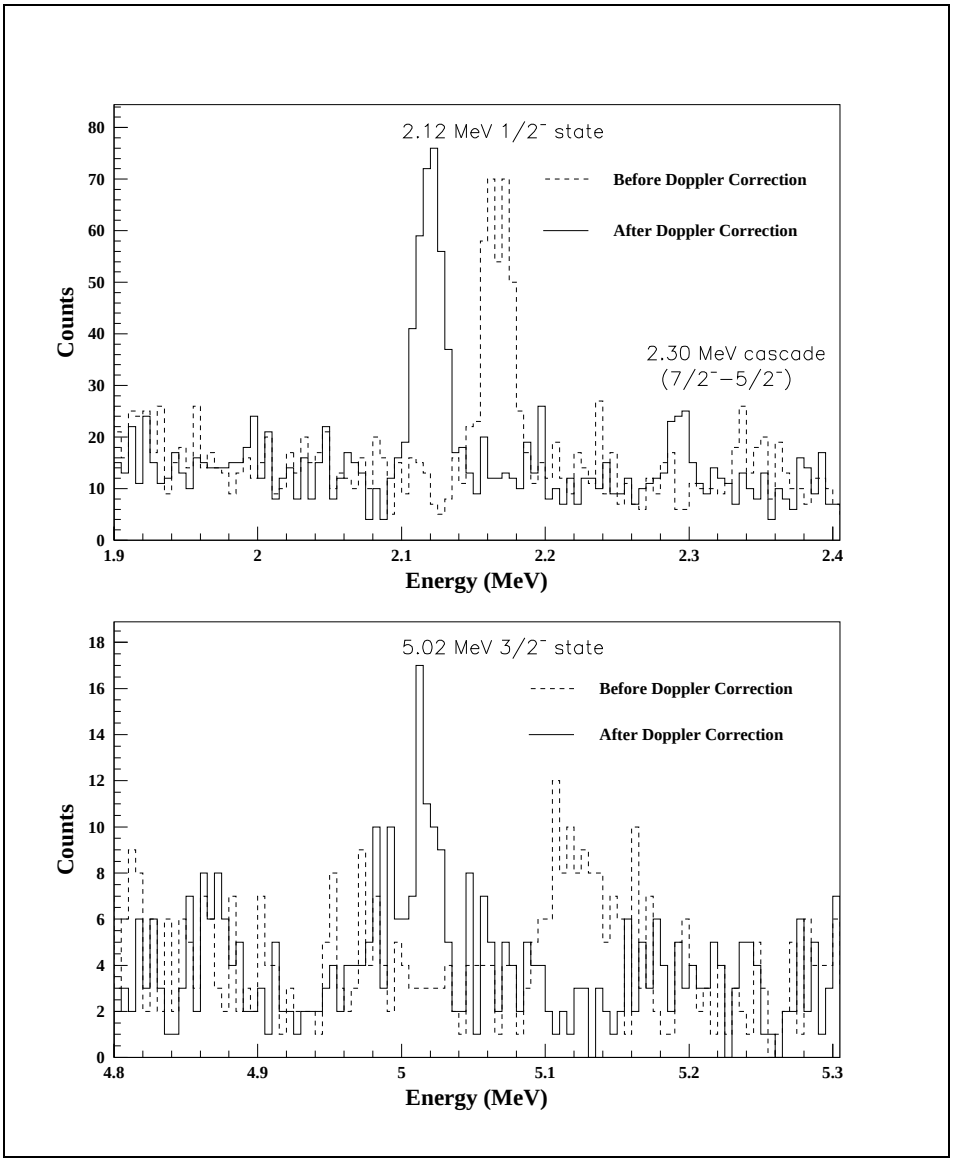

Figure 4.16: *Effect of the Doppler correction on the 2.12 and 5.02 MeV γ-rays from the de–excitation of ^{11}B. The data are presented in 5 keV bins. The spectrum shown is the $\mathcal{P}^{\gamma'}$ spectrum.*

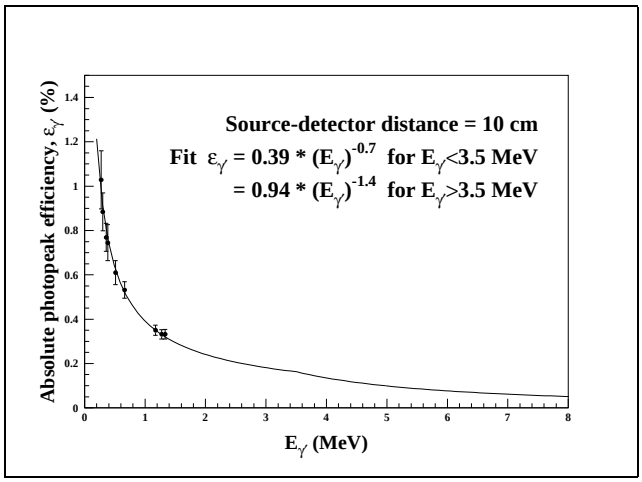

Figure 4.17: *The absolute efficiency of the HPGe 70 % detector, for a source to detector distance of ∼10 cm. See text for details of the function used to extrapolate to $E_{\gamma'}$=7 MeV.*

4.2.5 Response Function of HPGe 70 %

In order to correctly interpret the de–excitation γ-ray spectrum, account must be taken of the γ-ray line shape produced by the HPGe 70 % detector. A complex line shape is created in the energy spectrum for each energy of γ-ray incident. An example line shape, recreated by a mathematical function is shown in fig. 4.18. The shape consists of a Gaussian photopeak (PP) at the energy of the incident γ-ray, $E_{\gamma'}$, with two further peaks at energies of $E_{\gamma'}$ – 0.511 MeV and $E_{\gamma'}$ – (2×0.511) MeV. These are the single escape (SE) and double escape (DE) peaks, respectively. The three peaks sit on a Compton continuum. The Compton scattering continuum is described by the Klein–Nishina formula [Kno89, Sha67]. For a γ-ray of energy $E_{\gamma 0}$ scattering from an electron at rest, imparting to it the energy $E_{e'}$ and ending with the energy $E_{\gamma 1}$, the cross section may be written in differential form, in terms of the recoiling electron's energy, as

$$\frac{d\sigma}{dE_{e'}}(=\frac{d\sigma}{d(E_{\gamma 0}-E_{\gamma 1})}) = \frac{\sigma_0}{E_{\gamma 0}^2}\{2 + E_{e'}\frac{E_{e'}(E_{\gamma 0}+1)^2 - E_{\gamma 0}({E_{e'}}^2 + 2E_{\gamma 0})}{E_{\gamma 0}^2(E_{\gamma 0}-E_{e'})^2}\} \tag{4.12}$$

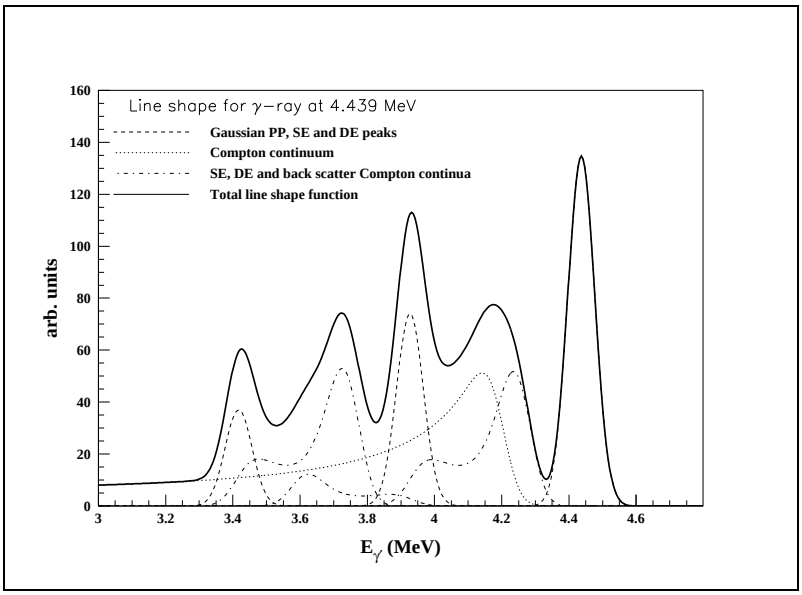

Figure 4.18: *Example of the γ-ray line shape function used to fit the de–excitation γ-ray spectra.*

where σ_0 can be treated as a normalisation parameter which gives the Compton edge the correct height with respect to the photopeak. Since the energy of the recoiling electron, $E_{e'}$, is the energy imparted to the detector in a Compton event, this is essentially the cross section for the detection of a Compton scattered γ-ray. This function was made more realistic by folding in the effect of an experimental resolution. It should be noted that this description of the Compton scattering continuum does not account for multiple scattering in the HPGe detector and so is not a perfect representation of the true continuum.

Although the general line shape is determined by the interaction of γ-rays with matter, the relative importance of the peaks and the continuum to one another, are a property of the individual detector used. They are related to its size and shape (crystal geometry). In other words, the volume of the crystal affects the probability for a Compton scattered γ-ray, or one, or both, of the 511 keV escape γ-rays to exit the crystal undetected.

The relative heights of each component in the line shape function have been found by fitting the function to a spectrum obtained from the Am–Be

calibration source described in section 4.2.2. An example of how this fit looks is shown in fig. 4.19. Fits were made to the 4.439 and 6.128 MeV

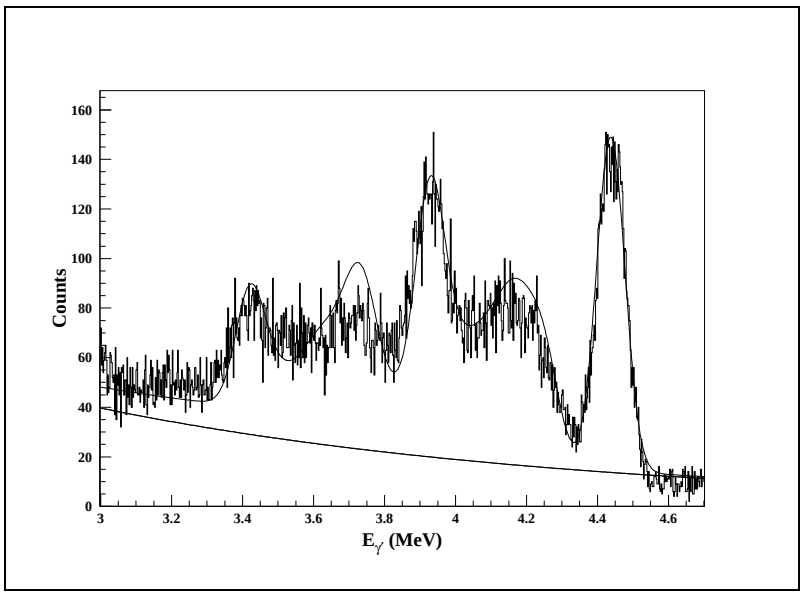

Figure 4.19: *Fit to the γ-ray at 4.439 MeV, from the Am–Be source, in order to obtain the correct escape peak normalisations for the γ-ray line shape function. The reason for the poor resolution is the fact that this γ-ray is Doppler shifted before being emitted by the Am–Be source.*

γ-ray line shapes. (An exponential background has been assumed, which was fitted to the spectrum above 6.2 MeV, and then extrapolated to lower energies.) These fits fixed the relative heights, of the escape peaks and of the Compton edge, to the photopeak at γ-ray energies of $\sim$4.4 and $\sim$6.1 MeV. By extrapolating to 6.8 MeV the γ-ray line shapes were therefore fixed when fitting the de–excitation γ' spectra at the $\sim$5 and 7 MeV regions, as will be explained in section 4.2.7.

The line shape function represents the spectrum well for the PP, the main Compton edge and the SE peak. After this the function fails. This is mainly due to multiple Compton scattering causing the continuum to differ from that described by the Klein–Nishina cross section.

4.2.6 'Untagged' γ' Spectrum

An alternative way of creating γ' spectra, to that shown in fig. 4.8, is to actually ignore the presence of the photon tagger. The tagger is necessary in a 'normal', (γ,X), experiment to provide the beam energy, which is needed to reconstruct E_m=$E_m(E_\gamma,\theta_r,T_r)$ and then E_{ex}. In the case of (γ,Xγ') the detection of the γ decay of the residual nucleus automatically provides the excitation energy, independently of the knowledge of the beam energy. Therefore it is not necessary to use the tagger information to see structure in the γ' spectrum.

Once the particles creating the X–trigger have been identified as protons, they will necessarily have originated from a ^{12}C nucleus which has absorbed a photon. So the (γ,p) reaction is selected. Fig. 4.20 shows a γ' spectrum filled by ignoring the tagger time information and accepting all events in the focal plane regardless of arrival time. This spectrum has an approximate Doppler correction, made by assuming a mean E_γ (59.9 MeV) for all events and a constant excitation energy, E_{ex}=6.8 MeV.

The population of levels *relative to one another* may, in principle, be extracted from this γ' spectrum. The E_{ex} variable, however, is not known and cannot be used to exclude the feeding of levels due to γ decay from higher excited states. This is not expected to preclude the interpretation of the spectrum as representing the relative populations of the 7 MeV triplet, since it is known, from high resolution ^{12}C(γ,p) measurements, that the higher lying states are weakly populated, (see fig. 2.11). Also, these higher lying states decay predominantly by particle emission. The events in this untagged γ' spectrum are due not only to beam photons from within the tagging range (see again fig. 3.5), but from a larger region of the bremsstrahlung spectrum. This region extends from the electron beam energy, E_0, down to a low cut–off defined by the threshold for proton detection.

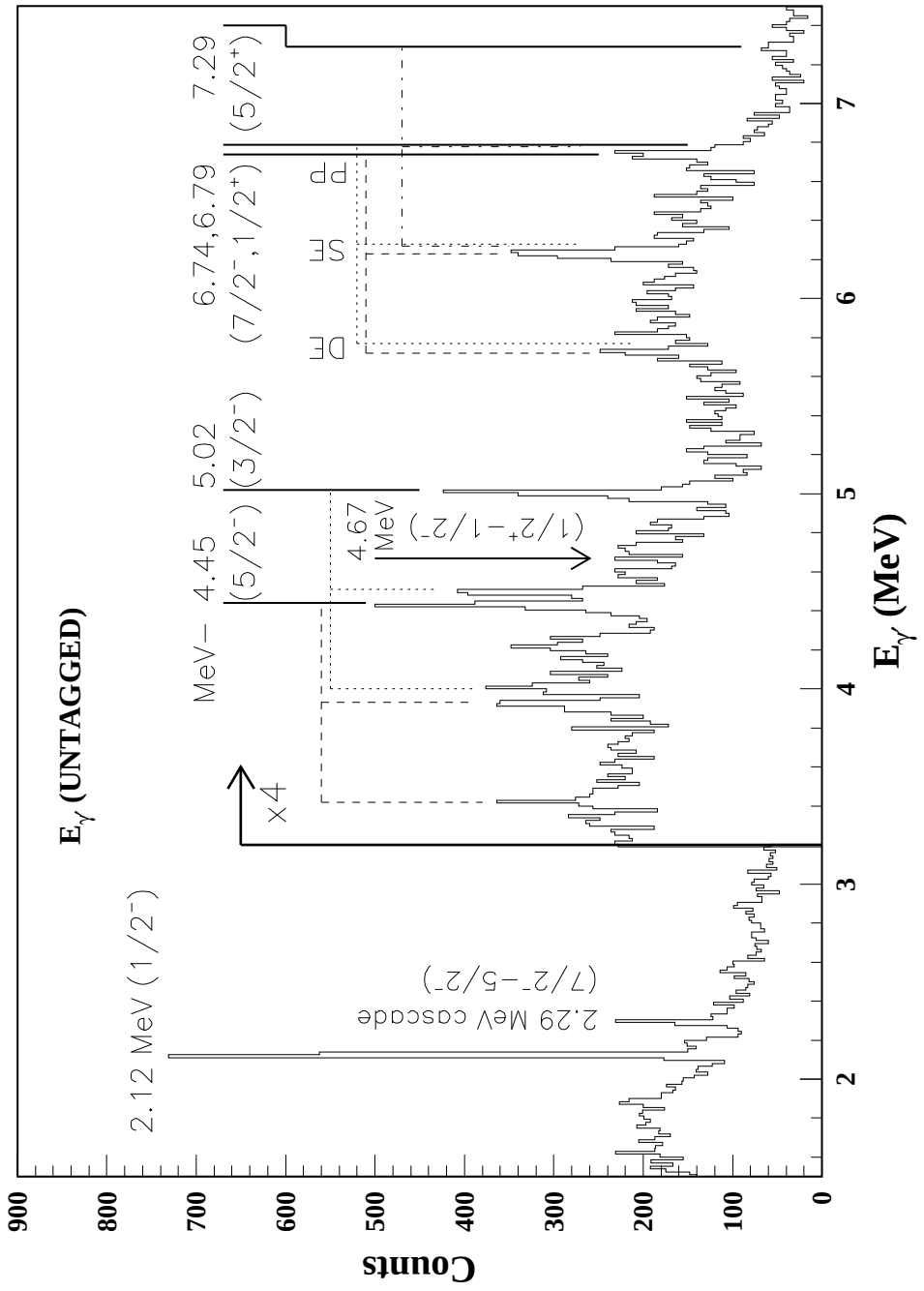

Figure 4.20: *Untagged de–excitation γ' spectrum from the HPGe 70 % detector. Filled in coincidence with protons. No restriction is made on the tagger TDC spectrum, see text for details. The data are displayed in 15 keV bins.*

4.2.7 Fitting Detector Response Functions to the De–excitation γ' Spectra

Extracting PP yields from the γ' spectra derived here is not trivial and a fitting procedure was necessary. This is due to the complicated line shape function, already discussed, and the fact that these functions may overlap as happens here at e.g. ∼4.5 and ∼6.7 MeV. Referring again to fig. 4.20, peaks were identified according to the known level scheme of ^{11}B and its γ-ray cascades, the most important of which are schematically displayed in fig. 4.21. After the Doppler correction, the spectrum shows clear peaks at

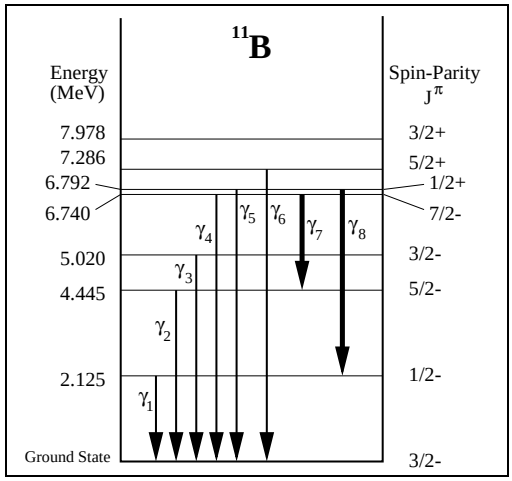

Figure 4.21: *Energy level diagram of ^{11}B, showing the main γ-ray decays.*

2.12, 4.45, 5.02 and ∼6.8 MeV (γ-ray numbers 1-5 in fig. 4.21). This is clear evidence that energy levels in ^{11}B are being observed. The main cascade γ-ray observed is at 2.29 MeV, with possible structure a 4.67 MeV (γ-ray numbers 7 and 8 in fig. 4.21).

The γ' spectrum in coincidence with the prompt focal plane TDC peak, $\mathcal{P}^{\gamma'}$, is shown in fig. 4.22. The ^{11}B levels and some of the escape peaks identified are labelled. The origin of the possible peak at ∼4.2 MeV in fig. 4.22 is not known. This energy does not fit in with any of the known nuclear levels or γ-ray cascades in ^{11}B and no line shape could be used to match it with other structure in the spectrum.

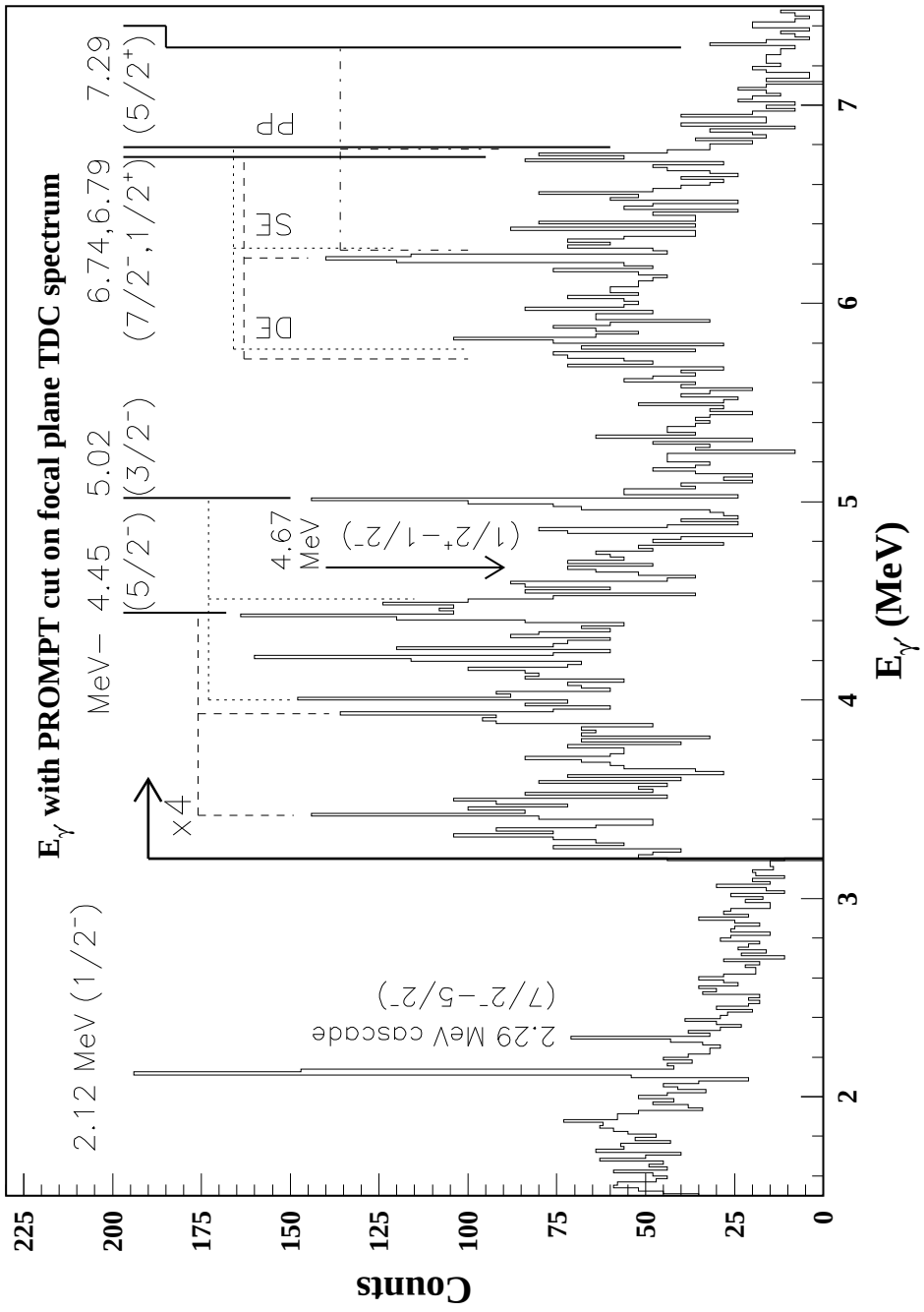

Figure 4.22: *De–excitation γ' spectrum from the HPGe 70 % detector. Filled for the prompt region of the focal plane tagger in coincidence with the protons of fig. 4.9. No randoms subtraction has been made (i.e. $\mathcal{P}^{\gamma'}$). The data are displayed in 15 keV bins.*

To extract the relative populations of the states of interest in ^{11}B the γ-ray line shapes were fitted to the derived γ' spectra. After creating the γ-ray line shapes the actual fitting procedure was quite simple. Fits to data with such poor statistics are not expected to give accurate results and so these fits may be regarded as much as a guide to interpreting the spectra as an accurate description of the data. Also, since the statistics are poor in the $\mathcal{S}^{\gamma'}$ spectrum the fits have instead been made on the $\mathcal{P}^{\gamma'}$ spectrum. This is justified since, with low statistics a randoms subtraction is not expected to be particularly useful. Fits were made to two regions of the γ' spectrum, fitting three γ-rays in each case. The first region is around $E_{\gamma'} \simeq 5$ MeV and comprises γ-rays at 4.45 MeV ($J^{\pi}_{initial}$–J^{π}_{final};$5/2^-$–$3/2^-$), 4.67 MeV ($1/2^+$–$1/2^-$) and 5.02 MeV ($3/2^-$–$3/2^-$). The second region, around $E_{\gamma'} \simeq 7$ MeV, comprises γ-rays at 6.74 MeV ($7/2^-$–$3/2^-$), 6.79 MeV ($1/2^+$–$3/2^-$) and 7.29 MeV ($5/2^+$–$3/2^-$).

The line shape was restricted by the fits made to the calibration spectrum as described in section 4.2.5. The only parameters allowed to vary in the fitting procedure were the γ-ray energy ($E_{\gamma'}$) because of the uncertainty in the accuracy of the Doppler correction, the resolution (σ) and the area (A) of the PP. The area of the escape peaks and continua were fixed relative to the PP area.

Even when using the $\mathcal{P}^{\gamma'}$ spectrum the statistics are too low for an accurate fit allowing $E_{\gamma'}$, σ, and A to vary freely. For this reason, the untagged γ' spectrum has been fitted to fix the peak positions and resolution. For these fits all 3 of the above parameters were allowed to vary (within reasonable limits) to achieve a fit. The results are shown in figures 4.23 and 4.24. A resolution of 47.14 keV was found for the peaks at $\sim$5 MeV and 48.68 keV for those at $\sim$7 MeV. The resolution of the detector was measured (see fig. 3.15) to be $\sim$15 keV at 7 MeV (with the shaping time set to 1 μs as employed in the experiment). The effects of the Doppler broadening, however, are present in the γ' spectra in addition to this intrinsic energy resolution. The peak positions found for the 6 fitted γ-rays were 4.418, 4.671, 4.999, 6.710, 6.710+0.050 and 7.280 MeV. (Note that the energy of

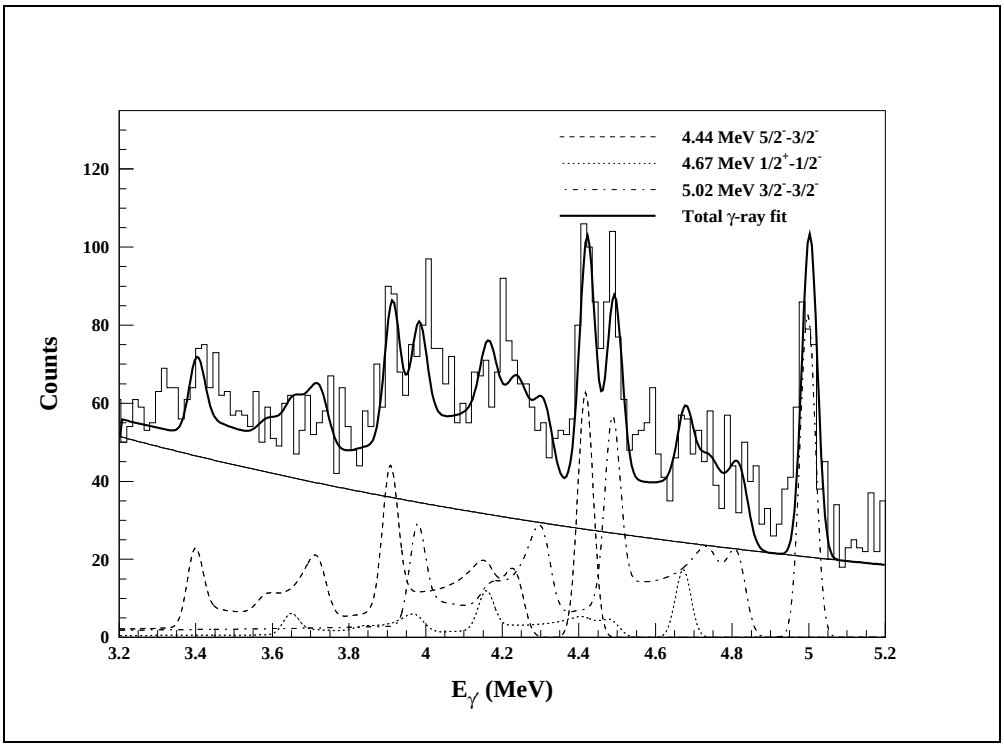

Figure 4.23: *Fits to the untagged γ' spectrum at $E_{\gamma'}$∼5 MeV.*

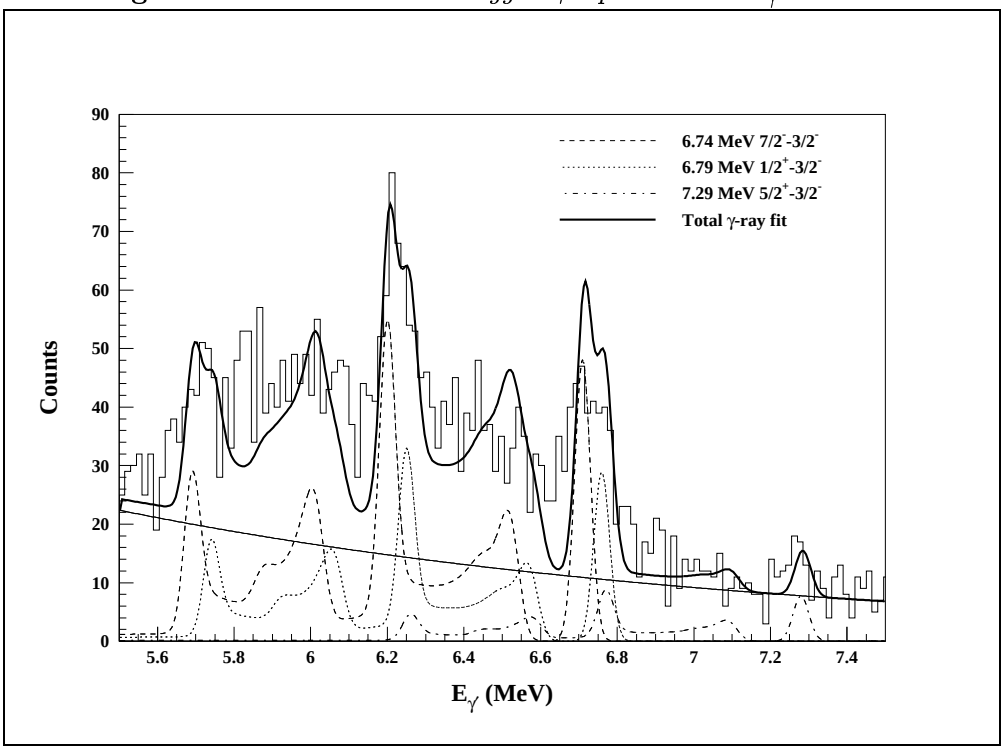

Figure 4.24: *Fits to the untagged γ' spectrum at $E_{\gamma'}$∼7 MeV.*

the $1/2^+$ to ground γ-ray transition was fixed at 50 keV above the $7/2^-$ to ground transition in the fitting procedure.) An exponential background has been assumed in all of these fits, which was fixed at regions free of peaks, above and below the fitted regions, and interpolated to the fitted regions.

In figures 4.23 and 4.24 the PP's of the 5.02 and 6.79 MeV γ-rays slightly overshoot the data. The fact that these fits cannot match the data exactly may be due to a lack of accuracy in our knowledge of the response function of the HPGe 70 % detector. Also Doppler broadened peaks are not well described by a Gaussian function. The γ-ray line shapes fail badly for the region between the DE peak and the DE Compton edge. This is believed to be due to the non–inclusion of multiple scattering in the function describing the Compton continuum. This is not highly important, however, as the only value of interest to be derived from these fits is the area of the PP's.

With fixed values for σ (from fits to the untagged spectrum) and $E_{\gamma'}$ (from the literature values), the line shapes were next fitted to the $\mathcal{P}^{\gamma'}$ spectrum, allowing only the heights of each line shape to vary. The resulting fits are shown in figures 4.25 and 4.26.

4.3 Results

4.3.1 Population of levels in ^{11}B

The fits to the $\mathcal{P}^{\gamma'}$ spectrum, shown in figures 4.25 and 4.26 have been used to extract the PP yields. Even without calculating quantitative populations the main result may be seen straight away. The fit at $\sim$7 MeV in fig. 4.26 indicates that the yield from the 6.74 MeV transition is much higher than that from the 6.79 MeV transition. It is also quite obvious that the 7.29 MeV level contributes little. Although the resolution is not completely adequate to distinguish transitions which are 50 keV apart, the centroid of the observed peak at $\sim$6.7 MeV is too low in energy to be due predominantly to the 6.79 MeV ($1/2^+$) level of ^{11}B. The evidence for this

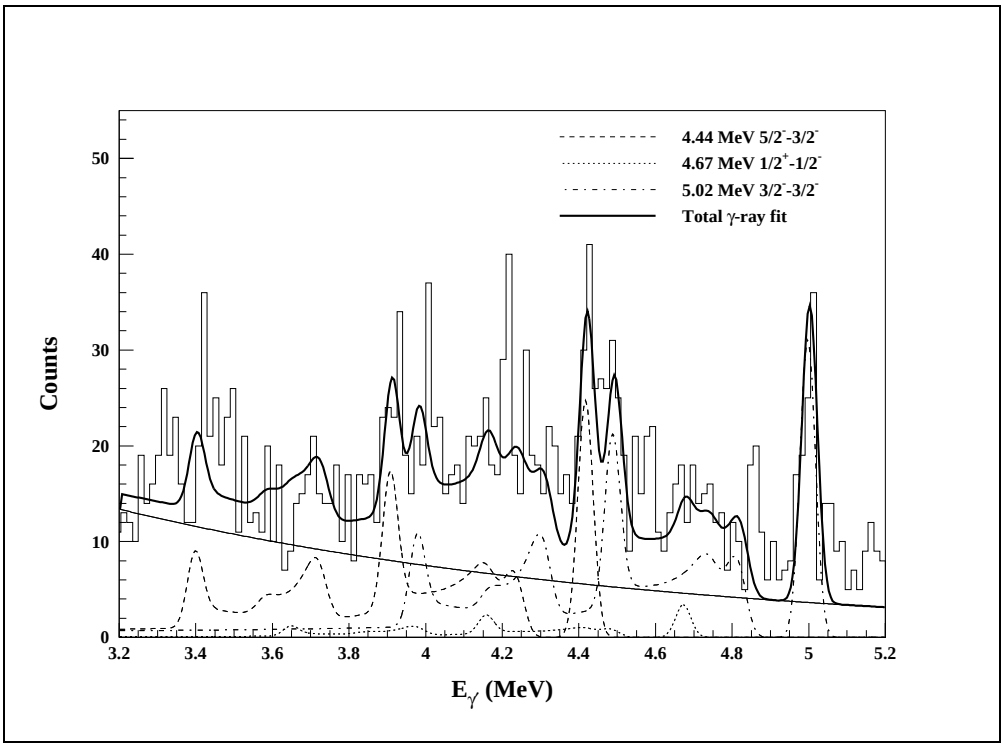

Figure 4.25: *Fits to the $\mathcal{P}^{\gamma'}$ spectrum at $E_{\gamma'}\sim 5$ MeV.*

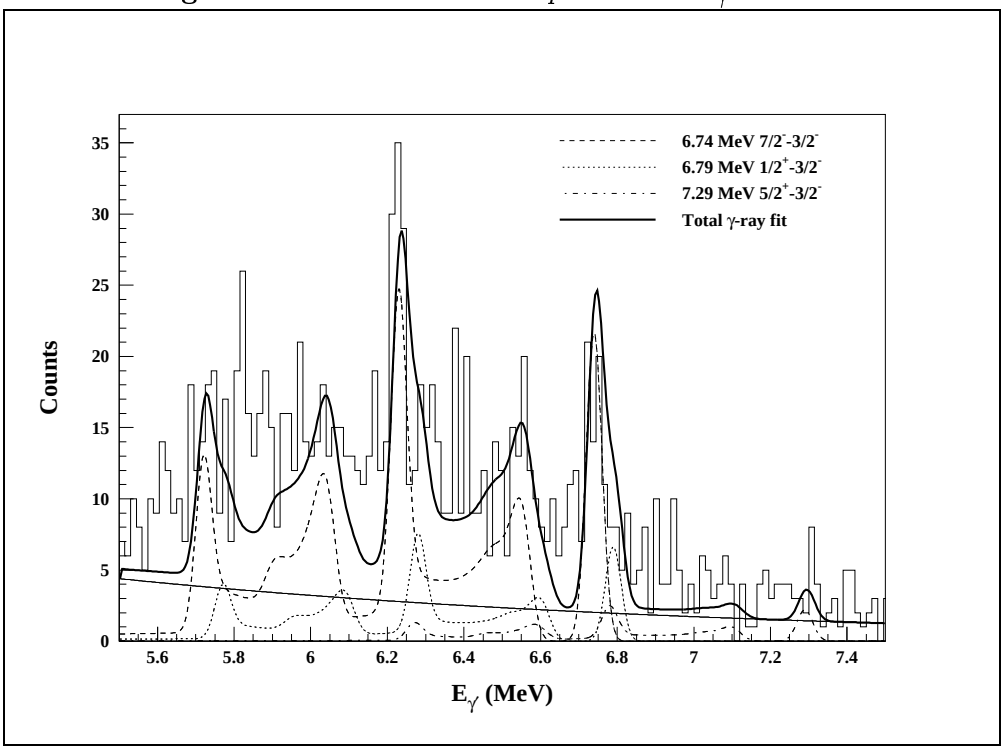

Figure 4.26: *Fits to the $\mathcal{P}^{\gamma'}$ spectrum at $E_{\gamma'}\sim 7$ MeV.*

conclusion is further backed up by looking at the $\mathcal{P}^{\gamma'}$ spectrum around ~2.3 and ~4.6 MeV, as shown in fig. 4.22. This shows that the 4.67 MeV γ-ray (number 8 in fig. 4.21) is not strong. This transition (with a branching ratio B_γ=28.5±1.1 %) would be expected if the 6.79 MeV level were populated strongly following the ^{12}C(γ,p) reaction. In fig. 4.22 on the other hand the 2.29 MeV cascade (number 7 in fig. 4.21, B_γ=30±2 %) is clearly seen. These two facts lend support to the conclusion that it is the level at 6.74 MeV (and not at 6.79 MeV) in ^{11}B which contributes most strongly to the γ-ray yields.

The PP yields, extracted from the line shape fits, were next used to assign tentative relative populations to some of the levels in ^{11}B. Account has been taken of the branching ratios, B_γ, for each γ-ray transition (see table 4.1), the γ-ray detection efficiency, $\varepsilon_{\gamma'}$, and the attenuation effect of the 6.2 mm of Pb shielding in front of the detector, $a_{\gamma'}$. The population due to the (γ,p) reaction, $P_i^{\gamma p}$, of each level, i, in ^{11}B is given by

$$P_i^{\gamma p} = \frac{Y^{PP}}{B_\gamma \varepsilon_{\gamma'} a_{\gamma'}} - \Sigma_j N_\gamma(j \to i) \tag{4.13}$$

where Y^{PP} is the PP yield and $N_\gamma(j \to i)$ are the number of γ-rays feeding this level, summed over all higher levels, j. The feeding from higher γ-rays, $N_\gamma(j \to i)$, may be calculated from either

$$N_\gamma(j \to i) = P_j \times B_\gamma(j \to i) \tag{4.14}$$

where P_j is the population of the level j and $B_\gamma(j \to i)$ is the branching ratio for level j to feed level i. Or from

$$N_\gamma(j \to i) = \frac{Y^{PP}_{(j \to i)}}{\varepsilon_{\gamma'} a_{\gamma'}} \tag{4.15}$$

where $Y^{PP}_{(j \to i)}$ is the yield of the PP of the γ-ray emitted by the cascade; and $\varepsilon_{\gamma'}$ and $a_{\gamma'}$ must be calculated at the appropriate γ-ray energy.

The extracted relative populations, with estimated systematic and statistical errors, for some of the levels in ^{11}B are displayed in table 4.2,

Table 4.1: *Electromagnetic transitions in ^{11}B, showing branching ratios to the final state, from [Ajz90].*

Initial state (MeV)	J^π	Γ_γ (total) (eV)	Branching ratios (%) to the final state						
			g.s.	2.12	4.45	5.02	6.74	6.79	7.29
2.12	$1/2^-$	0.120±0.009	100						
4.45	$5/2^-$	0.56±0.02	100						
5.02	$3/2^-$	1.963±0.067	85.6±0.6	14.4±0.6					
6.74	$7/2^-$	0.030±0.007	70±2	<3	30±2	<1			
6.79	$1/2^+$	0.385±0.044	67.5±1.1	28.5±1.1	<0.04	4.0±0.3			
7.29	$5/2^+$	1.149±0.080	87.0±2.0	<1	5.5±1	7.5±1			
7.98	$3/2^+$	1.15±0.15	46.2±1.1	53.2±1.2	<0.06	<0.09		<0.1	<1
8.56	$(3/2^-)$	0.946±0.090	56±2	30±2	5±1	9±1			
8.92	$5/2^-$	4.368±0.021	95±1	<1	4.5±0.5	<1	<1	<1	
9.19	$7/2^+$	$0.17^{+0.06}_{-0.03}$	0.9±0.3		86.6±2.3		12.5±1.1	<1.3	
9.27	$5/2^+$	1.15±0.16	18.4±0.9		69.7±1.4		11.9±0.6	<0.6	

relative to the population of the 6.74 MeV level. For the 6.79 MeV level it

Table 4.2: *The population of levels in ^{11}B following $^{12}C(\gamma,p)$ relative to the population of the 6.74 MeV state.*

Level (MeV)	J^π	$Y^{PP}\pm\sqrt{Y^{PP}}$	Sys. error (%)	$P_i^{\gamma p}$ ($\times 10^3$) (arb. units)	$P_i^{\gamma p}/P_{6.74}^{\gamma p}$
5.02	$3/2^-$	103.93±10.19	10.13	391±55	0.76±0.16
6.74	$7/2^-$	74.99±8.60	10.31	512±79	1.00
6.79	$1/2^+$	22.96±4.79	10.17	165±38	0.32±0.09
	($1/2^+$-$1/2^-$)	(11.38±3.37)	(10.17)	(117±37)	(0.23±0.08)
7.29	$5/2^+$	7.60±2.76	10.31	47±18	0.09±0.04

has been possible to calculate the population twice, by making use of the cascade γ-ray in the γ' spectrum at 4.67 MeV. The result of both methods should agree within errors. The result derived from the cascade PP is shown in brackets in table 4.2.

Due to the fact that $\varepsilon_{\gamma'}$ was extrapolated to such high energies the γ-rays at ∼2 MeV have not been used to measure the population of levels relative to those at ∼7 MeV. The error in the knowledge of the relative $\varepsilon_{\gamma'}$ between the energies $E_{\gamma'}\simeq$2 and 7 MeV following this extrapolation is too high.

4.3.1.1 4.45 MeV level

This level is populated strongly from the higher lying excited states at 6.74, 9.19 and 9.27 MeV (see table 4.1). The resulting cascade γ-rays appear at $E_{\gamma'}$=2.29, 4.75 and 4.83 MeV. A peak at 2.29 MeV is clearly visible in fig. 4.22. There is possibly some structure at 4.83 MeV in this spectrum, but it is not visible in the untagged spectrum.

Due to the poor resolution of the E_{ex} spectrum it has not been possible to separate the ∼4, ∼7 and ∼9 MeV regions, in order to identify the cascading γ-rays, and measure the amount of feeding from higher levels. A

population for the 4.45 MeV level has therefore not been extracted from these data.

4.3.1.2 5.02 MeV level

This state is not populated strongly by higher excited states in ^{11}B. The strongest feeding of this level comes from the 6.79, 7.29 and 8.56 MeV levels. The resulting γ-rays have energies of $E_{\gamma'}$=1.77, 2.27 and 3.54 MeV. These γ-rays are not visible in either the untagged or $\mathcal{P}^{\gamma'}$ spectra. Therefore the population of this level has been extracted by assuming no feeding from higher levels, i.e. the N_γ=0 for all j in equation 4.13. The Y^{PP} yield was taken from the fit to the $\mathcal{P}^{\gamma'}$ spectrum of fig. 4.25.

4.3.1.3 7 MeV triplet states

The only state in the $\sim$7 MeV triplet fed from higher excited states is at 6.74 MeV. It is fed from the 9.19 and 9.27 MeV levels, giving cascade γ-rays at $E_{\gamma'}$=2.45 and 2.53 MeV. Cascades at $E_{\gamma'}$=4.75 and 4.83 MeV, which feed the 4.45 MeV level, are also produced with higher branching ratios. As discussed previously the spectra do not show strong evidence for these γ-rays. Measuring the amount of feeding from these levels with the E_{ex} spectrum is, again, not possible due to the poor resolution. However, previous high resolution ^{12}C(γ,p) data [Bob95, Asc97] show that these levels are populated very weakly. The relative populations measured here have simply been taken from the $\mathcal{P}^{\gamma'}$ spectrum, as for the 5.02 MeV state, thereby not accounting for any feeding from higher levels.

In an attempt to estimate the importance of such feeding, a γ-ray spectrum has been obtained in coincidence with 60.71<E_γ<70.24 MeV only. The E_{ex} spectrum for this data is shown in fig. 4.27. The shaded region of E_{ex} (3.3<E_{ex}<10.6 MeV) has been used to fill the γ-ray spectrum of fig. 4.28. This spectrum indicates the position of the 6.74, 6.79 and 7.29 MeV γ-rays. This spectrum again shows that the 6.74 MeV state produces the strongest γ-ray yield, despite the poor statistics, even after selection of 3.3<E_{ex}<10.6 MeV.

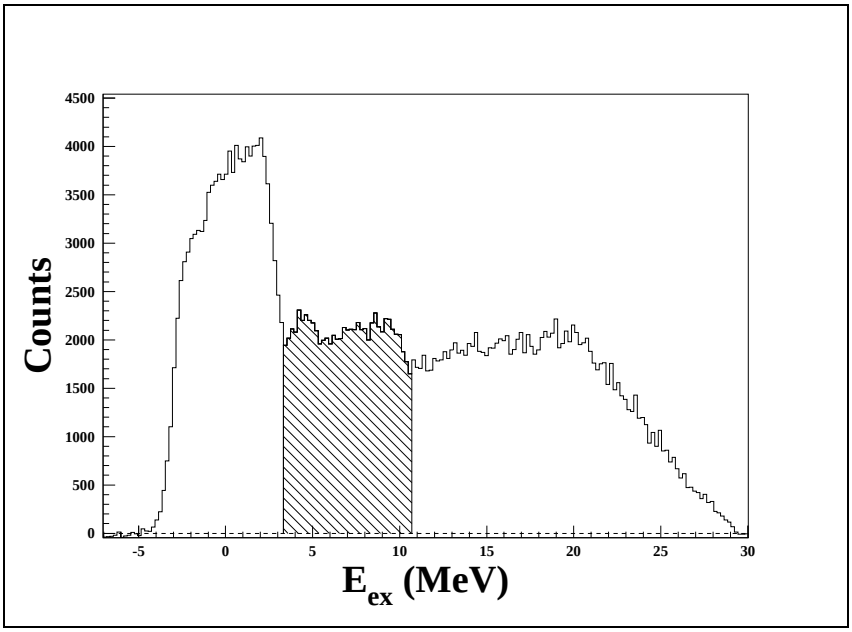

Figure 4.27: *E_{ex} $\mathcal{S}$ spectrum for 60.71<E_γ<70.24 MeV.*

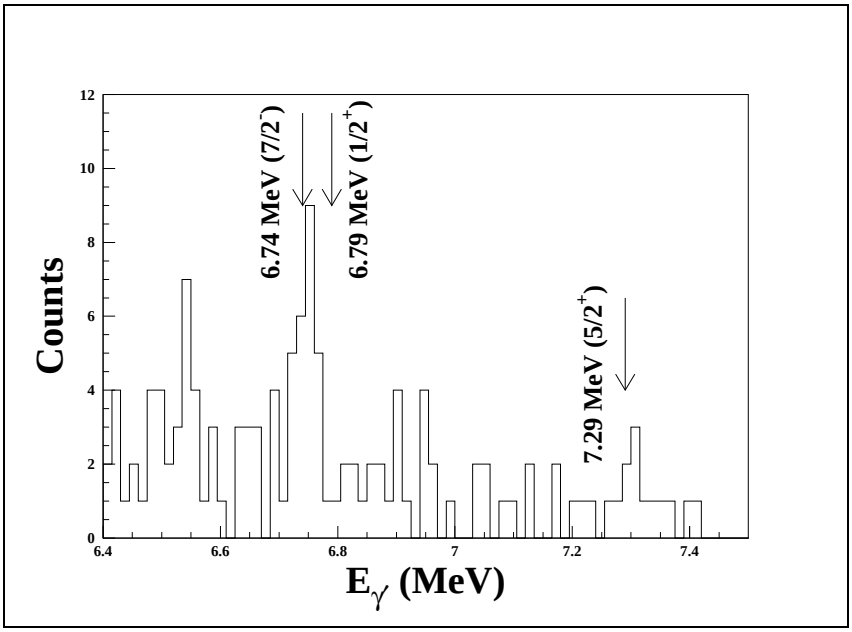

Figure 4.28: *$\mathcal{P}^{\gamma'}$ spectrum for 60.71<E_γ<70.24 MeV and 3.3<E_{ex}<10.6 MeV.*

4.3.2 Angular Correlations

An important effect to be considered, in the analysis of a (γ,Xγ') experiment such as this, is that of angular correlations between the direction of the emitted γ-ray and the recoiling nucleus. This anisotropy in the γ-ray's emission probability implies that the measured γ-ray yields may not represent the true population of states following the reaction ^{12}C(γ,p)^{11}B.

In this experiment, protons have been detected in a relatively small solid angle ($\sim$4 % of 4π) causing all detected de–excitation γ-rays to result from ^{11}B nuclei recoiling in a kinematically restricted cone. The recoiling nucleus and ejected proton define a plane, which is limited in orientation by the proton detection solid angle. Any preferential alignment of the recoil's spin relative to this plane may bias the direction of γ-ray emission, depending on the multipolarity of the electromagnetic transition involved.

Using the known J$^\pi$ of the relevant states in ^{11}B, the angular distribution for γ-ray emission may be calculated for each transition relative to the nuclear axis of quantization. According to [Ros67], the angular distribution, $W(\theta_{\gamma'})$, is given by

$$W(\theta_{\gamma'}) = \Sigma_k a_k Q_k P_k(\cos\theta_{\gamma'}) \tag{4.16}$$

where $P_k(\cos\theta_{\gamma'})$ are the Legendre Polynomials; the a_k are coefficients depending on the experimentally measured multipole mixing ratio, δ, and some tabulated parameters for each magnetic sub–state, m$_l$, taken from [Ros67]; and the factor

$$Q_k = \Sigma_k \frac{\int_0^{\theta^{max}} P_k(\cos\theta_{\gamma'}) \sin\theta_{\gamma'}\, d\theta_{\gamma'}}{\int_0^{\theta^{max}} P_0(\cos\theta_{\gamma'}) \sin\theta_{\gamma'}\, d\theta_{\gamma'}} \tag{4.17}$$

takes into account the finite size of the detector (see [Win68], and App. 9 of [Sie65]), where θ^{max} is the maximum angle subtended by the detector. The values used for the Q_k were Q_2=0.80, Q_4=0.40 and Q_6=0.05.

Such a calculation of $W(\theta_{\gamma'})$ is *only* possible if the magnetic sub–states of the residual nucleus, populated by the (γ,p) reaction, are known. Since these are not known an attempt has been made to estimate the maximum effect of these angular correlations. If no alignment of the residual nuclei to

the axis of quantization is present then all γ-ray emission from these nuclei will be isotropic. Where there is preferential alignment then the isotropy is removed. A worst case scenario has been calculated, in which all γ-rays are in $m_l = \pm\frac{1}{2}$ levels relative to the momentum vector of the recoil. This case has been compared to that of isotropic γ-ray emission in order to estimate the maximum effect which may occur due to the correlations.

The case of $m_l = \pm\frac{1}{2}$ has been chosen from a simple argument concerning the angular momentum imparted to the target nucleus by the incoming photon. The angular momentum is defined classically as

$$\mathbf{L} = \mathbf{r} \times \mathbf{p}_\gamma \tag{4.18}$$

where $\mathbf{r}$ is defined from the centre of the target nucleus, and $\mathbf{p}_\gamma$ is the linear momentum brought in by the beam photon. In this simple picture, the vector $\mathbf{L}$ is perpendicular to the plane of the reaction. Neglecting any spin brought in by the photon, this would imply that only m_l=0 alignments are possible for the residual, [Cle61]. Since the proton carries away J=$\frac{1}{2}$ from the reaction, and the residual nucleus, ^{11}B, is odd (i.e. its J is half–integer), then the closest possible alignments to zero are $m_l = \pm\frac{1}{2}$. From this, and assuming no polarisation (i.e. no preference for a positive or a negative m_l), we can say that our best estimate for the magnetic substate populations, P, of the m_l are P(m_l=+$\frac{1}{2}$)=P(m_l=−$\frac{1}{2}$)=50 %.

Using experimentally measured multiple mixing ratios (δ) [Ajz90] for each transition it is then possible to calculate the angular distributions. The acceptance of the current experimental setup to the angle $\theta_{\gamma'}$, as measured directly from the data was shown in fig. 4.15. The half height angle at the tail of this distribution is ∼25°. This has been combined, in quadrature, with the angle subtended by the detector about the centre of the beam spot, to give an effective angle, $\theta_{\gamma'}^{eff}$, over which to integrate the γ-ray angular distributions. (The angle subtended by the detector was found from the angle subtended at a distance L_{rad}^{Ge} into the crystal, where L_{rad}^{Ge} is the radiation length for germanium.) This calculation found the effective angle to be $\theta_{\gamma'}^{eff}$=32.1°.

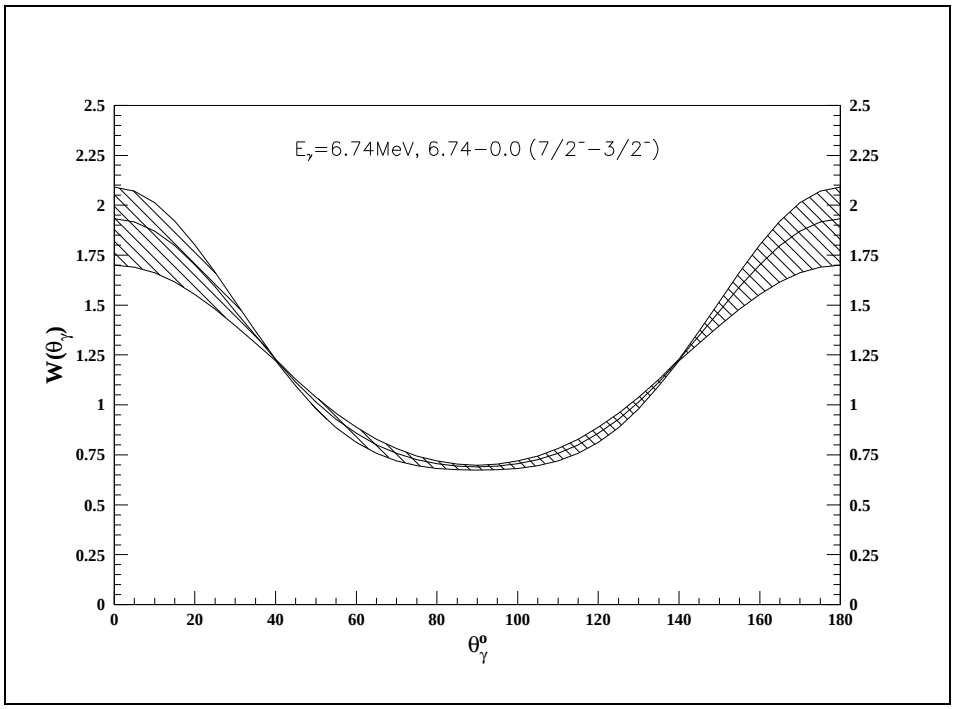

Figure 4.29: *Angular distribution for the 6.74 MeV (7/2$^-$–3/2$^-$) γ-ray decay of ^{11}B, assuming $m_l = \pm\frac{1}{2}$ alignment, relative to the momentum vector of the recoiling nucleus. The shaded band represents the error due to the experimental error in the multipole mixing ratio, δ. The effective acceptance of the current experimental setup was $0.0^\circ<\theta_{\gamma'}<32.1^\circ$, and that of [Kuz98] was $70^\circ<\theta_{\gamma'}<110^\circ$.*

The $E_{\gamma'}$=2.12, 4.67 and 6.79 MeV γ-ray transitions from ^{11}B are isotropic. This is due to the fact that they all result from J=$\frac{1}{2}$ states. For J=$\frac{1}{2}$ the $m_l = \pm\frac{1}{2}$ are the only possible alignments, which is equivalent to no preferential alignment, and therefore isotropic γ-ray emission. The only γ-rays for which a calculation was required were then the $E_{\gamma'}$=2.29, 4.44, 5.02, 6.74 and 7.29 MeV transitions. The result of the calculation for the worst affected transition ($E_{\gamma'}$=6.74 MeV) is shown in fig. 4.29. A maximum estimated enhancement factor to the PP yields has been found for each of these five γ-rays from the $W(\theta_{\gamma'})$ distribution. It was calculated as the ratio, R_γ, of the area under $W(\theta_{\gamma'})$ from 0–$\theta^{eff}_{\gamma'}$, to the same area derived from an isotropic distribution. Therefore the corrected yield is given by Y^{PP}/R_γ. The resulting factors are displayed in table 4.3 for each of the transitions.

Table 4.3: *Estimated worst case effect on the measured γ-ray yields, for all the recoil nuclei to be aligned in $m_l = \pm\frac{1}{2}$ magnetic substates. The factor R_γ is explained in the text. It has been calculated for the present data based on an acceptance of $0.0^\circ < \theta_{\gamma'} < 32.1^\circ$, and for that of [Kuz98] with $70^\circ < \theta_{\gamma'} < 110^\circ$.*

$E_{\gamma'}$ (MeV)	Transition (J_i^π–J_f^π)	Multipole Mixing Ratio, δ	Maximum estimated effect on γ-ray yield, R_γ	R_γ for [Kuz98]
2.12	$1/2^-$–$3/2^-$	Isotropic	1.000	1.000
4.45	$5/2^-$–$3/2^-$	-0.19±0.03	1.032±0.045	1.004±0.021
4.67	$1/2^+$–$1/2^-$	Isotropic	1.000	1.000
5.02	$3/2^-$–$3/2^-$	0.03±0.05	1.279±0.078	0.880±0.039
6.74	$7/2^-$–$3/2^-$	-0.45±0.018	1.797±0.206	0.717±0.053
6.79	$1/2^+$–$3/2^-$	Isotropic	1.000	1.000
7.29	$5/2^+$–$3/2^-$	0.0	0.750±0.097	1.136±0.048

The errors are due to the experimental error on the multipole mixing ratio and also allow for a 10 % error in Q_2. The effect of errors on Q_4 and Q_6 were seen to be negligible. The correction factor for angular correlations has been worked out for the data of Kuzin *et al.* also. For these data R_γ has been calculated in exactly the same way, based on an acceptance of $70^\circ < \theta_{\gamma'} < 110^\circ$, [Kuz98].

The relative populations for the states in ^{11}B from the present data, corrected by R_γ for the effect of angular correlations, are shown in table 4.4. These have been re–normalised relative to the yield of the 6.74 MeV γ-ray. In table 4.5 the relative populations, both before and after application of the correction factor R_γ, are normalised to the data of [Spr90, Rui96] to give absolute cross sections for the 3 states at θ_p=70°. This normalisation has been performed in exactly the same way as described by [Kuz98] so that the results of both measurements may be compared. In figures 4.30 and 4.31 both data sets are shown, both before and after inclusion of the factor R_γ, respectively. The strength of the $7/2^-$ state is in agreement within error bars between both data sets, however, the agreement is less good after correction by R_γ. As can be understood from fig. 4.29 the angular correlation factor

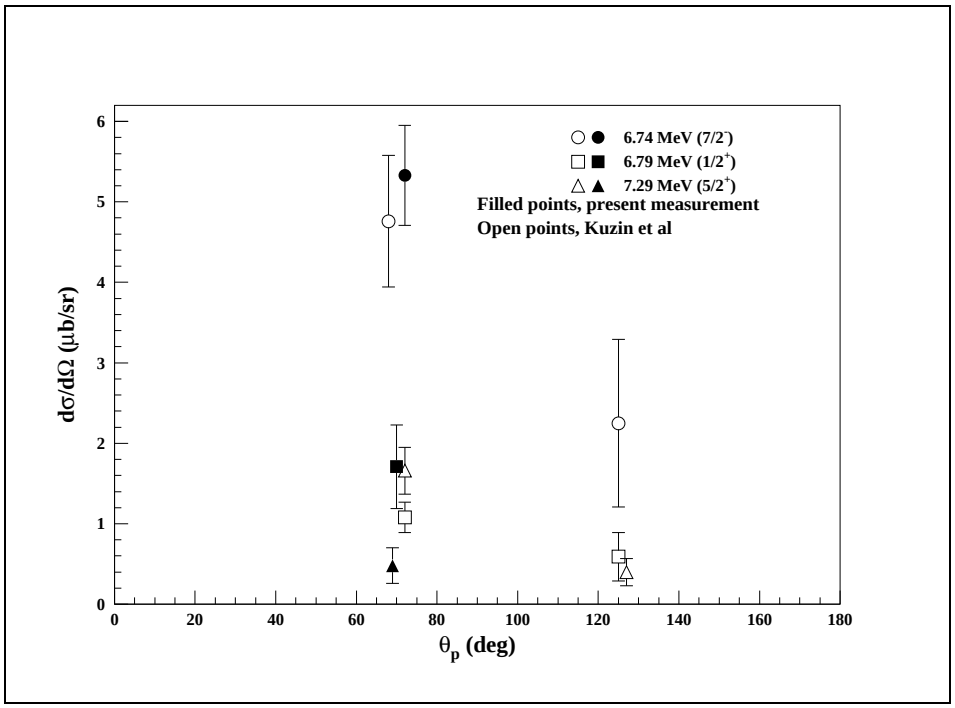

Figure 4.30: *Normalised cross sections for the triplet of states in ^{11}B following $^{12}C(\gamma,p)$, without inclusion of the factor R_γ. The present data are compared with the measurement of [Kuz98].*

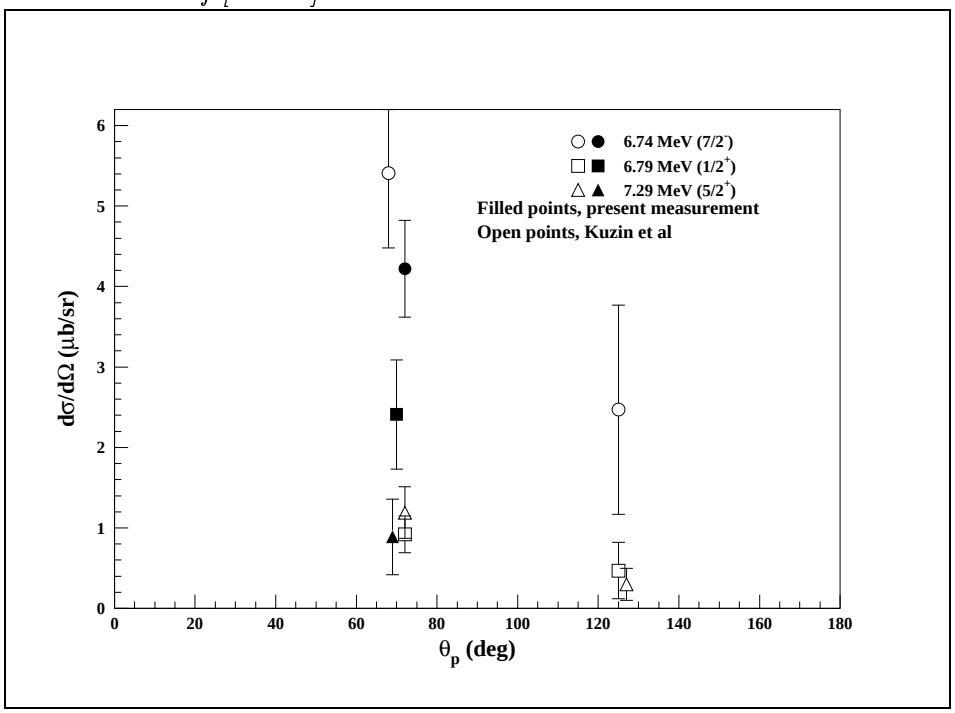

Figure 4.31: *Normalised cross sections for the triplet of states in ^{11}B following $^{12}C(\gamma,p)$, after inclusion of the factor R_γ. The present data are compared with the measurement of [Kuz98].*

Table 4.4: *The relative population of levels in ^{11}B following $^{12}C(\gamma,p)$, including the effect of angular correlations. The populations after inclusion of the factor R_γ are re–normalised relative to the population of the 6.74 MeV state.*

Level (MeV)	J^π	$P_i^{\gamma p}/P_{6.74}^{\gamma p} = R_i^{*\gamma p}$	$R_i^{*\gamma p}/R_\gamma = R_i^{\gamma p}$	$R_i^{\gamma p}/R_{6.74}^{\gamma p}$
5.02	$3/2^-$	0.76±0.16	0.59±0.13	1.05±0.23
6.74	$7/2^-$	1.00	0.56	1.00
6.79	$1/2^+$	0.32±0.09	0.32±0.09	0.57±0.16
	($1/2^+$-$1/2^-$)	(0.23±0.08)	(0.23±0.08)	(0.41±0.14)
7.29	$5/2^+$	0.09±0.04	0.12±0.06	0.21±0.11

Table 4.5: *Normalised cross sections at θ_p=70° for the ∼7 MeV triplet ^{11}B, following $^{12}C(\gamma,p)$, compared to the results of [Kuz98]. The cross sections have been normalised relative to the absolute cross section measurements of [Spr90, Rui96]. The cross sections without account taken of angular correlations are represented as $\frac{d\sigma}{d\Omega}^*$ and those with as $\frac{d\sigma}{d\Omega}$.*

Level (MeV)	J^π	Present data		[Kuz98]	
		$\frac{d\sigma}{d\Omega}^*$ $(\frac{\mu b}{sr})$	$\frac{d\sigma}{d\Omega}$ $(\frac{\mu b}{sr})$	$\frac{d\sigma}{d\Omega}^*$ $(\frac{\mu b}{sr})$	$\frac{d\sigma}{d\Omega}$ $(\frac{\mu b}{sr})$
6.74	$7/2^-$	5.33±0.62	4.22±0.60	4.76±0.82	5.41±0.93
6.79	$1/2^+$	1.71±0.52	2.41±0.68	1.08±0.19	0.92±0.23
7.29	$5/2^+$	0.48±0.22	0.89±0.47	1.66±0.29	1.19±0.32

has the opposite effect on each of the two data sets for this transition. The relative strength of the $1/2^+$ and $5/2^+$ states is in disagreement between the two data sets. The main difference between the two measurements is the strength attributed to the 6.79 MeV ($1/2^+$) transition, which is seen to be higher here than measured by Kuzin *et al.* This is true even before application of the angular correlation factor, which further enhances the relative strength of the $1/2^+$ state for the present measurement.

Chapter 5

Electron Induced Proton Knockout from ^{12}C

This chapter deals with the analysis of and shows the results from a study of the reaction ^{12}C(e,e′p). The missing momentum probed in this study was deliberately chosen to be the same as that of typical (γ,p) data. The data are presented as reduced cross sections and the structure functions W_L and W_T; both as functions of $\mathbf{p}_m$.

Section 5.1 describes the general formalism, used in this thesis, to describe an (e,e′p) reaction. Section 5.2 explains the NIKHEF experimental setup. Only the main details are given as an introduction, more information can be found in [Vri84, Her87, Her88, Qui88]. Section 5.3 outlines the analysis of a typical (e,e′p) experiment to the stage of extracting momentum distributions. Next, section 5.4 explains the procedure of an L–T separation. Finally in section 5.5, the results are presented as spectral functions, momentum distributions and the structure functions W_L and W_T.

5.1 Formalism of an (e,e′p) Reaction

The kinematics of an (e,e′p) reaction are shown schematically in fig. 5.1. An incoming electron of momentum $\mathbf{e}$ is scattered from a target nucleus at rest

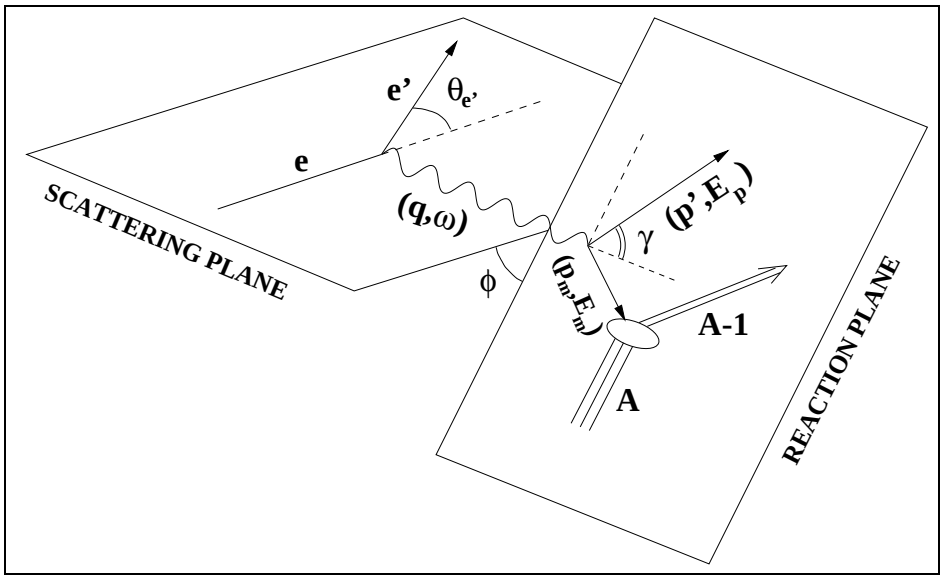

Figure 5.1: *Scattering and Reaction planes of an (e,e'p) reaction.*

in the laboratory and is detected with a momentum $\mathbf{e}'$ at an angle $\theta_{e'}$ to the initial beam direction. In the exclusive process, (e,e'p), a proton is knocked out of the target nucleus and is detected with a momentum $\mathbf{p}'$ at an angle θ_p. The electron exchanges with the (ejected) proton a virtual photon[1], of momentum $\mathbf{q}(= \mathbf{e}-\mathbf{e}')$ and energy $\omega(= E_0-E_{e'})$, where E_0 and $E_{e'}$ represent the total energy of the incoming and scattered electrons, respectively. It is assumed that the photon couples to a single proton, the same proton that is knocked out of the nucleus in this process and that the coupling is the same as for a free proton[2].

From the measurement of $\mathbf{e}$, $\mathbf{e}'$ and $\mathbf{p}'$ we can calculate the quantities missing momentum and missing energy. These have been defined already in equations 2.1 and 2.2, as

$$\mathbf{p}_m = \mathbf{p}' - \mathbf{q} = \mathbf{p}' - (\mathbf{e} - \mathbf{e}') \tag{5.1}$$

[1]One photon exchange between the electron and proton is assumed, i.e. The Born Approximation.

[2]This is the Impulse Approximation (IA).

and

$$E_m = \omega - T_p - T_r = (E_0 - E_{e'}) - T_p - T_r \tag{5.2}$$

The missing energy is related to the excitation energy of the residual by

$$E_{ex} = E_m + Q_{gs} \tag{5.3}$$

where Q_{gs} is the Q–value for the reaction to populate the ground state of the residual A-1 nucleus.

As can be seen from fig. 5.1 the proton may be emitted in a plane different to that of the scattering plane, defined by the vectors **e** and **e**$'$. The situation in which both of these planes coincide is called coplanar kinematics. Measuring in this regime restricts the degrees of freedom available in the system by causing the angle ϕ to be either 0 or π.

In the coplanar case two further kinds of kinematics may be defined, as depicted in fig. 5.2. In $(\mathbf{q}, \omega)$ kinematics, γ (the angle between $\mathbf{p}'$ and $\mathbf{q}$)

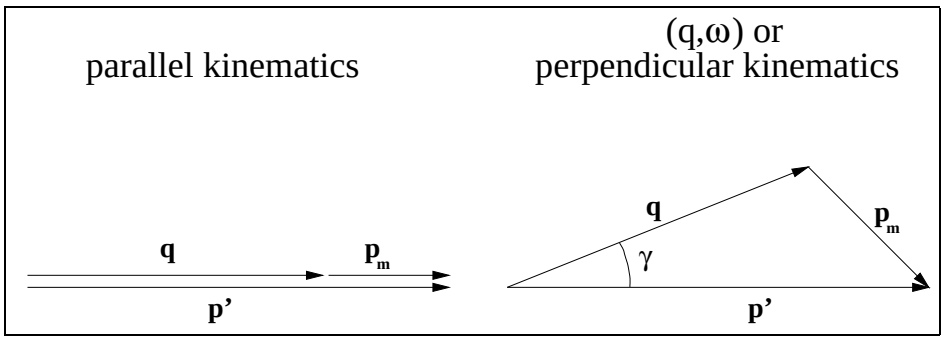

Figure 5.2: *Parallel and perpendicular kinematics in an (e,e'p) reaction.*

is allowed to vary; $(\mathbf{q}, \omega)$ kinematics is also called perpendicular kinematics (despite the name, none of the vectors actually need to be perpendicular, although they will have components which are). Parallel kinematics, on the other hand, makes the restriction γ=0, such that $\mathbf{p}'$ and $\mathbf{q}$ are parallel. This has a significance for the present experiment, which was performed in coplanar, parallel, kinematics.

In chapter 2, equation 2.4 gave the factorised (e,e'p) cross section in the PWIA for a specific transition. Considering the general case for all E_m

and $\mathbf{p}_m$ covered in a measurement the cross section may also be written as

$$\frac{d^6\sigma}{dE_{e'}\ d\Omega_e\ dE_p\ d\Omega_p} = \mathrm{K}\sigma_{ep}\mathrm{S}(E_m,\mathbf{p}_m) \tag{5.4}$$

where $K = E_p\mathbf{p}'$, E_p is the total proton energy, σ_{ep} represents the (off–shell) electron–proton cross section and $\mathrm{S}(E_m,\mathbf{p}_m)$, is the spectral function. The spectral function is the joint probability of finding a proton with a momentum $\mathbf{p}_m$ and a binding energy E_m inside the nucleus, and therefore holds all the nuclear structure information.

The spectral function, $\mathrm{S}(E_m,\mathbf{p}_m)$, is a 2–D function in ($E_m$, $\mathbf{p}_m$) space. By integrating over a discrete peak in the spectrum of E_m it is possible to define the *reduced cross section*

$$\rho(\mathbf{p}_m) = \int_{\Delta E_m} \mathrm{S}(E_m,\mathbf{p}_m)dE_m \tag{5.5}$$

where ΔE_m represents the integration over an individual peak.

5.2 Electron Scattering at NIKHEF

5.2.1 The MEA Accelerator and AmPS

The NIKHEF laboratory where this experiment was carried out has since been decommissioned. Experiments at NIKHEF were carried out with the Medium Energy Accelerator (MEA) [Vri84, Her88] and the Amsterdam Pulsed Stretcher Ring (AmPS), [Wit93]. Electron beams of energy 700 MeV with duty factors of >80 % were possible. Although using a higher beam energy, the basic procedure for creation of the high duty factor electron beam was similar to that described in section 3.1 for MAX–LAB. A pulsed beam was circulated in a stretcher ring to increase its duty factor. This beam was delivered by MEA, a 200 m long LINAC, which produced an intensity of 10 μA, corresponding to $\sim 10^{13}$ electrons/s. The pulsed beam was injected into AmPS with a repetition rate of 50–150 Hz. Pulse lengths varied from

0.7 to 2.1 μs, corresponding to 1 or 3–turn injection into the ring. The AmPS ring was 21.2 m in circumference and the injected electrons traversed this in 0.71 μs. Pulses from MEA were stretched to a continuous beam, which, in stretcher mode, would then be slowly extracted. For this experiment electron beams of energy ∼380 and 580 MeV were delivered by MEA and AmPS.

5.2.2 Product Detectors and Target

In this experiment, the reaction products were detected by two magnetic spectrometers. One high resolution ($\Delta p/p \leqslant 1 \times 10^{-4}$; $\Delta\Omega$ =5.6 msr) Quadrupole–Dipole–Dipole (QDD) for the electrons and one large solid angle ($\Delta p/p \leqslant 3 \times 10^{-4}$; $\Delta\Omega$ =17.2 msr) Quadrupole–Dipole–Quadrupole (QDQ) for the protons. Fig. 5.3 shows a schematic of these two spectrometers. Both

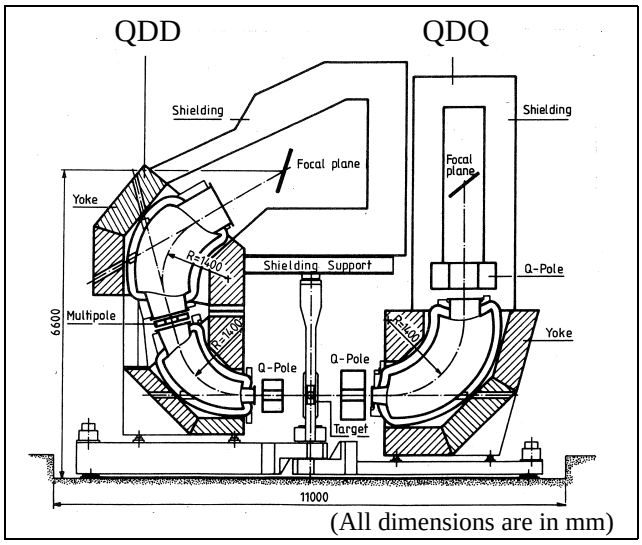

Figure 5.3: *The QDD and QDQ magnetic spectrometers at* NIKHEF. *The figure has been taken from [Her87]. The beam direction is perpendicular to and entering the page.*

were restricted to rotate within the horizontal plane, therefore confining the measurements to coplanar kinematics. The coincident timing resolution between the spectrometers was ≃1 ns.

Each of the spectrometers was free to rotate in the angular range 25°–155° around the scattering chamber. The accuracy of the angular setting and readout was 0.01°. The position and direction of the particles in two planes were determined from four multi–wire drift chambers (MWDC). The optical parameters of both spectrometers were described with matrix elements so that the trajectory of each particle from the target could be reconstructed.

During the run two different carbon targets were used. One was a single foil (102.9 mg/cm^2) and the other a triple foil (3×34.3 mg/cm^2). The use of triple foil targets in the NIKHEF setup is described in [Bob95]. The targets were held in a cylindrical scattering chamber (height 500 mm, diameter 420 mm). The target angle and height could be set to within 0.01° and 0.01 mm respectively.

5.2.3 Kinematical Conditions

As stated in chapter 2 the purpose of this experiment was to carry out an L–T separation to determine the structure functions for the ^{12}C(e,e′p) cross section. For this to be done, special attention had to be made to the kinematics in which the reaction was studied. The main restriction to the kinematics chosen was that the experiment was carried out in so-called parallel kinematics. The criteria for carrying out an L–T separation are

- Measurements at more than one scattering angle, $\theta_{e'}$,
- Constant momentum and energy transfer to the target nucleus for each scattering angle.

To do this, it is necessary to make measurements at a different beam energy for each scattering angle. In this measurement cross sections were measured at two beam energies. A schematic vector diagram of the kinematical settings in each of the two measurements is shown in fig. 5.4. The energy and momentum transferred, q and ω, were equal in each of the two cases. The photon polarisation parameter (defined later in equation 5.14),

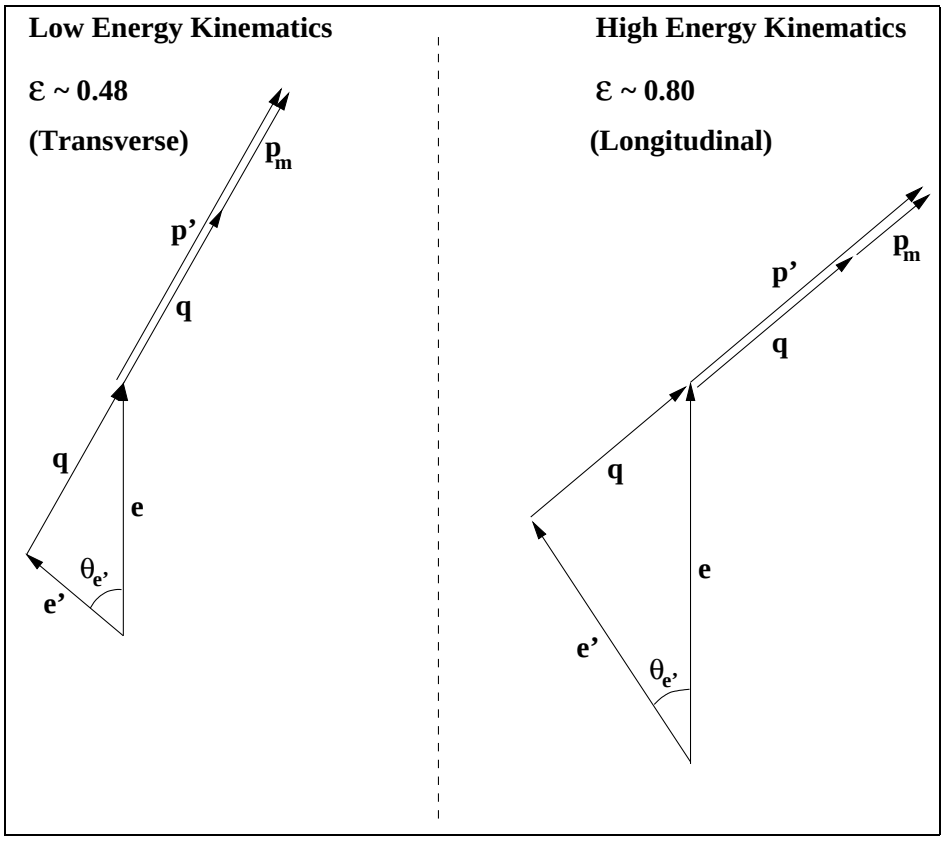

Figure 5.4: *Particle vectors for the high and low beam energy measurements. The momentum and energy transfers are equal in each of the two cases. The parameter ϵ is the photon polarisation parameter which is defined later.*

which is dependent on the electron scattering angle, was different in each case.

To cover the required $\mathbf{p}_m$ range, more than one measurement at each beam energy was needed. Table 5.1 gives the central kinematical settings for each measurement. The missing energy–missing momentum, (E_m–$\mathbf{p}_m$), phase spaces which these covered are represented in the 2–D scatter plot of fig. 5.5.

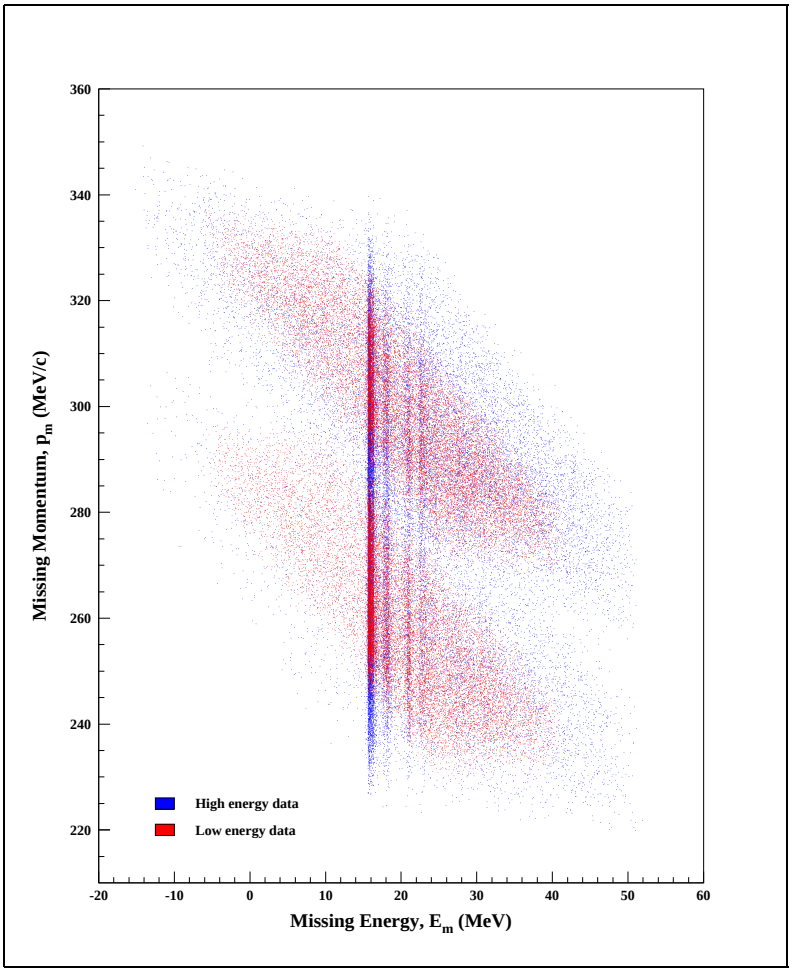

Figure 5.5: *The (E_m,$\mathbf{p}_m$) phase spaces covered by the high and low beam energy measurements. The intense vertical bands correspond to resolved states in the residual nucleus, ^{11}B. Events in other regions are due to random electron–proton coincidences which were subtracted later.*

Table 5.1: *Central kinematics for each of the experimental measurements. (*These runs were made with a triple foil target.)*

$\mathbf{p}_m$ ($\frac{\text{MeV}}{\text{c}}$)	$\mathbf{q}$ ($\frac{\text{MeV}}{\text{c}}$)	$\theta_{e'}$ (deg)	θ_p (deg)	T_p (MeV)	ϕ_{tg} (deg)	t_{tg} ($\frac{\text{mg}}{\text{cm}^2}$)	Q (mC)	E_0 (MeV)
259.9	338.2	63.2	-28.5	173.9	-159.5	102.9	209.219	378.55
299.8	298.3	50.5	-27.7	173.9	-160.0	102.9	231.785	378.55
257.9	338.4	33.5	-39.2	173.0	-110.0	3×34.3*	90.389	585.10
298.5	298.6	27.1	-36.1	173.3	-110.0	3×34.3*	137.122	585.10

5.3 Analysis

The first, standard part of (e,e′p) analysis is to extract from the data the spectral functions and reduced cross sections. The procedure for this is discussed in section 5.3.1. The next part, pertinent to this experiment, is to carry out an L–T separation on the cross sections, in order to determine the structure functions. Section 5.3.2 discusses finite acceptance effects in the L–T separation procedure. Section 5.3.3 explains the handling of errors.

5.3.1 GLANCE Analysis of (e,e′p) Experiments

The basic procedure used in analysing (e,e′p) data at NIKHEF is standard and has been used many times in the past. It is therefore well described already in other references, e.g. [Her87]. All codes used were supplied at NIKHEF. The overall procedure is outlined in fig. 5.6.

The main program is GLANCE (GLobal ANalysis of Coincidence Experiments). To begin with, an event is analysed when an $\mathbf{e}'$-$\mathbf{p}'$ coincidence is found between the two spectrometers. At this point ADC, TDC and MWDC information from the spectrometers are turned into particle vectors at the interaction point in the target. The difference in arrival times between particles in each of the two spectrometers is measured and then corrected for time–of–flight effects caused by unequal flight paths in each of the two spectrometers (see fig. 5.7). A time window is applied to the corrected QDD–QDQ time and fig. 5.8 shows an E_{ex} histogram created in coincidence with this cut before randoms subtraction.

The spectrometers have a specific acceptance with respect to energy and scattering angles. This leads to a block shaped detection volume (see again fig. 5.5), corresponding to the probability of detecting specific $\mathbf{e}'$-$\mathbf{p}'$ combinations. The detection probability is unequal throughout this volume. This is accounted for by defining a 'detection volume function', V(E_m,$\mathbf{p}_m$) in (MeV.sr)^2, which is folded in to the measured data. The function, V, is calculated for each bin in the (E_m,$\mathbf{p}_m$) phase space with a Monte–Carlo sim-

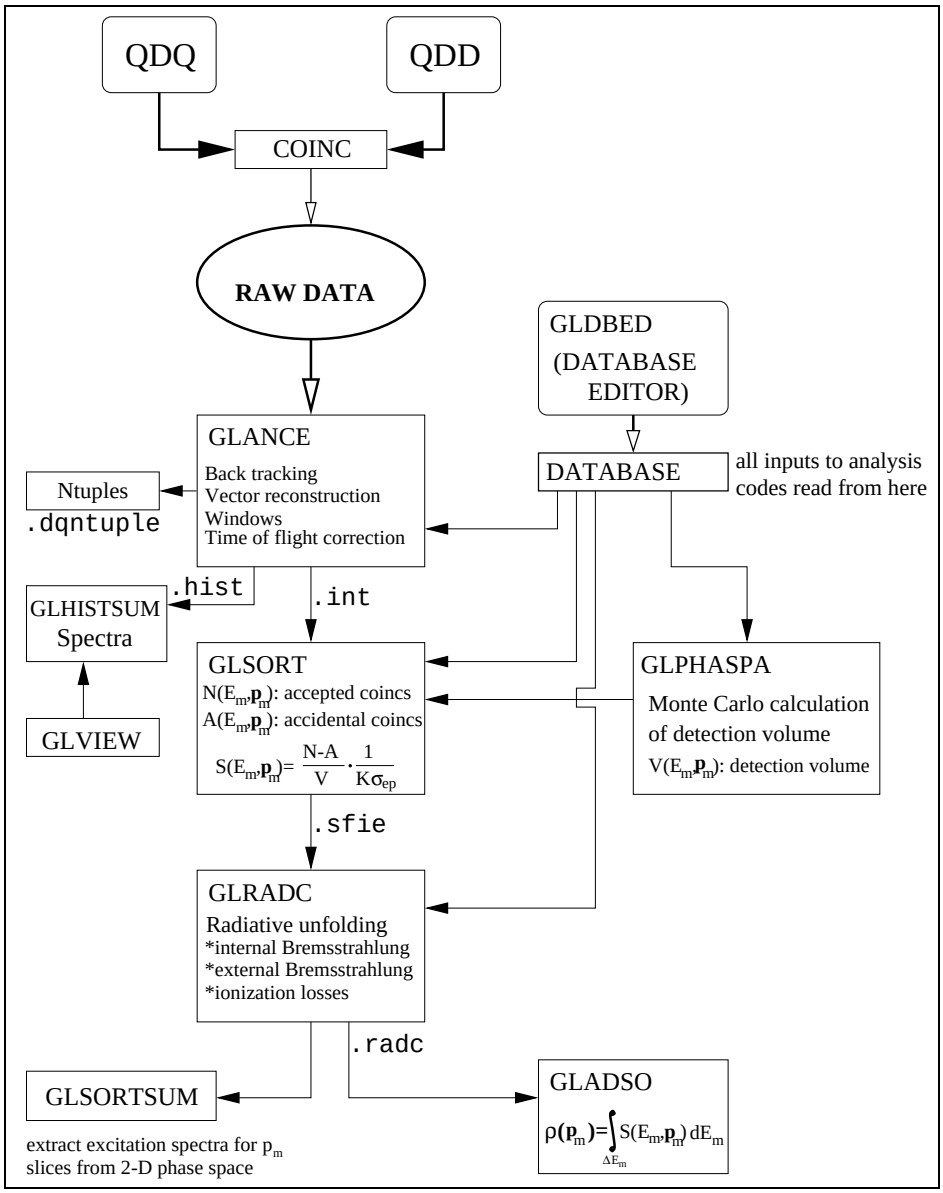

Figure 5.6: *Flowchart of the analysis procedures used in* GLANCE *to produce reduced cross sections, $\rho(\mathbf{p}_m)$, from coincident $(e,e'p)$ data taken at* NIKHEF *with the QDQ–QDD spectrometer setup.*

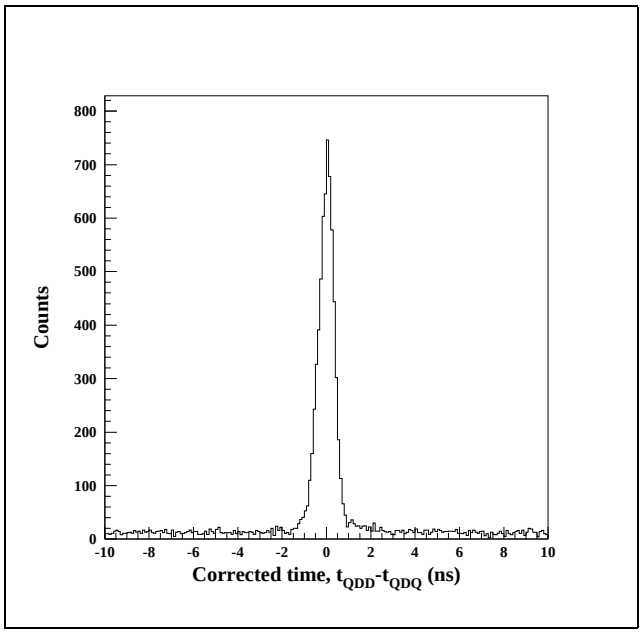

Figure 5.7: *Spectrum of corrected time between spectrometers, showing a FWHM resolution of ∼1 ns.*

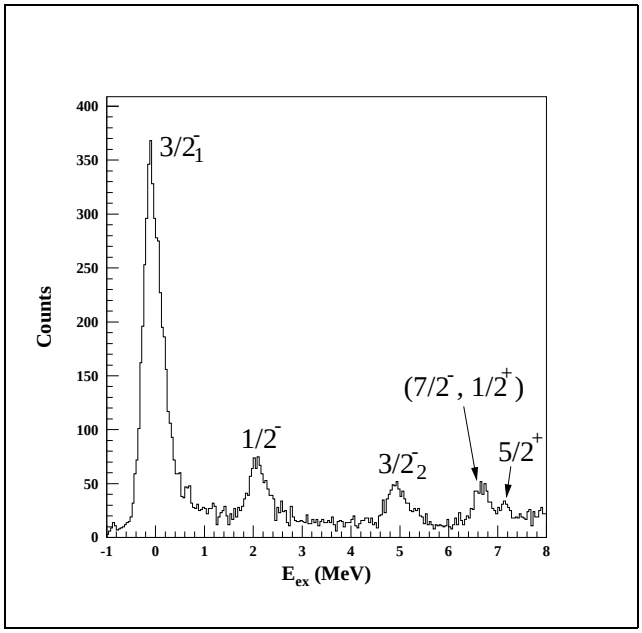

Figure 5.8: *An E_{ex} spectrum derived from* GLANCE*, after calibration and vector reconstruction. This spectrum shows data for ∼1/2 of the statistics available in the high beam energy measurement. Approximately 800 counts are present in the region of the ($7/2^-$,$1/2^+$,$5/2^+$) triplet at 7 MeV. (No radiative corrections have been made for this spectrum.)*

ulation, which generates events within the spectrometer acceptances [Qui88].

Assuming the factorization of the six–fold cross section, described in equation 5.4, the factor $K\sigma_{ep}$ holds information due only to the electron–proton scattering. Here the definition of deForest [DeF83] for σ_{ep}^{cc1} has been used. The factor $K\sigma_{ep}$ is divided out event–by–event at this stage, therefore leaving only nuclear structure information in the form of the spectral function, $S(E_m,\mathbf{p}_m)$.

The penultimate step, before extraction of the reduced cross sections, is to correct the spectral function for radiative effects. These effects are caused by contributions from other processes undergone by the electron while it is in the region of the target. They can be processes in which the electron radiates virtual or real photons during the interaction with the target nucleus (internal bremsstrahlung), or real photons due to interaction with other target nuclei, before and after the scattering process (external bremsstrahlung). Ionisation losses due to collisions of electrons and protons with the atomic electrons also contribute. The overall effect is that the excitation spectra show radiative tails extending to the high energy side of each peak, see again fig. 5.8. See [Her87, Qui88] and references therein for an explanation of how these effects are accounted for in the analysis.

When extracting cross sections from the data, the total charge collected in the Faraday cup (beam dump) is used. The charge collected in this dump has been seen to be duty factor dependent as well as having an offset current of ∼20–50 nA present. This dependence has been parameterised and is explained in [Sta99].

After this step, excitation spectra are binned into $\mathbf{p}_m$ slices from the $(E_m,\mathbf{p}_m)$ phase space. The reduced cross sections are then extracted for each resolved transition according to equation 5.5. The sequence of integrations thus obtained map out the $\mathbf{p}_m$ dependence of the cross section for each individual peak. To do this each resolved transition was fitted with a Gaussian peak, making five in all. Fig. 5.9 shows an example of the fits made. Since the energy levels of ^{11}B are well known, the fitting procedure used the expected peak positions. Only the width and height of each Gaussian was

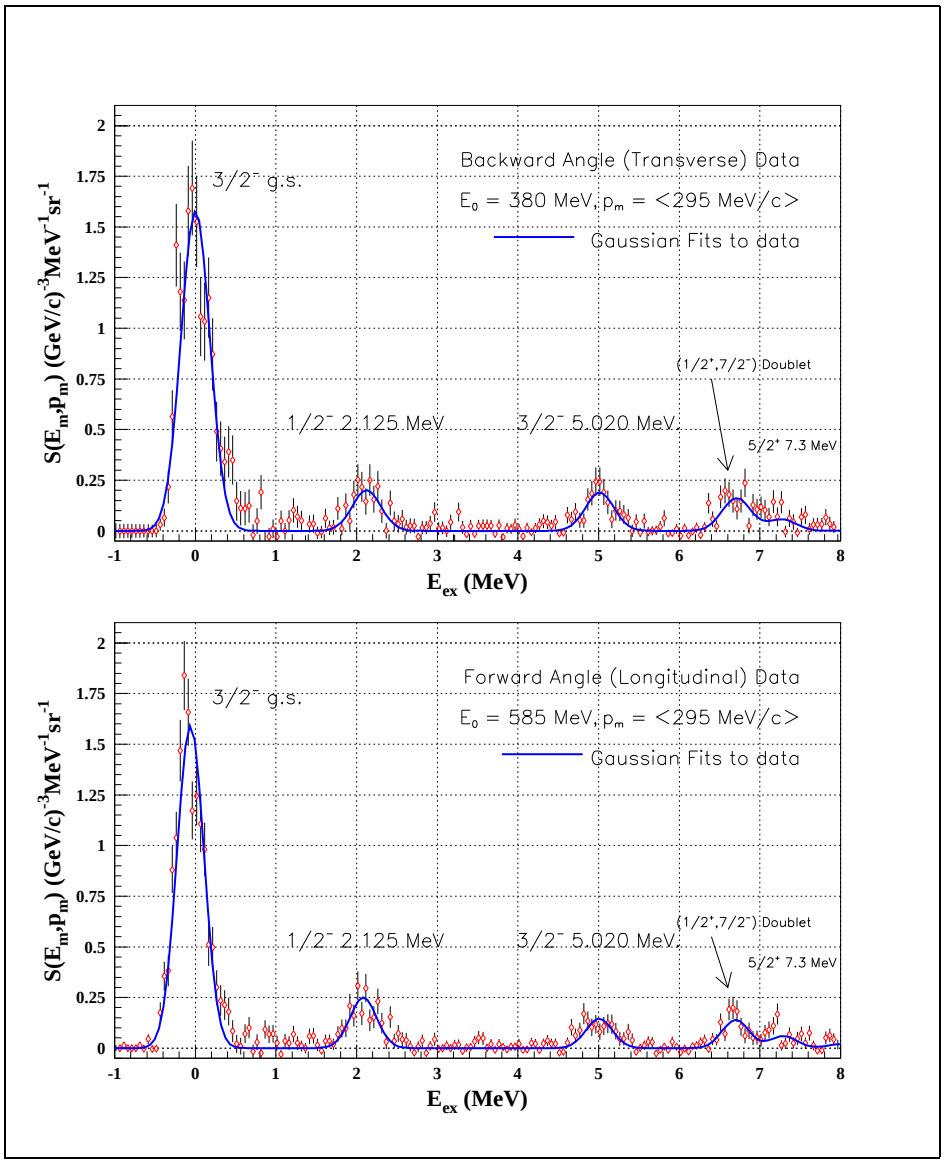

Figure 5.9: *$^{12}C(e,e'p)$ excitation spectra for both the high and low energy measurements, in terms of the spectral function, $S(E_m,\mathbf{p}_m)$. The data are centred at a $\mathbf{p}_m$ of 295 MeV/c in a slice 10 MeV/c wide. The E_{ex} resolution is ∼400 keV FWHM.*

allowed to vary.

5.3.2 Finite Acceptance Effects

Ultimately structure functions must be extracted from momentum distributions measured at two different incident beam energies. This is done in $\mathbf{p}_m$ space on a bin–by–bin basis for each discrete state. Ideally, in each measurement, the energy (ω) and momentum ($\mathbf{q}$) transferred to the target would be exactly equal in each bin. In practice however, finite acceptances of solid angle and momentum in both spectrometers allow for a range of kinematics in each bin, which all contribute to the cross section at that $\mathbf{p}_m$. These can be seen in fig. 5.10 as the scatter of data around the black points in each panel. Each point represents the so called *working point*, the point at which the separation is carried out for that $\mathbf{p}_m$. The scatter of data around this point is seen to be up to ± 8 %. The mean value for each of the variables q, ω, $E_{e'}$, $\theta_{e'}$, θ_p and p′ are calculated for each 10 MeV/c wide $\mathbf{p}_m$ bin in which a cross section has been measured. This defines the working point value for each of these variables.

Three contributions have been identified by [Sch91] for finite acceptances affecting the separated structure functions

- Contributions from events where the kinematics are not perfectly parallel.
- The range of $\mathbf{p}_m$ values within one bin, (which here is 10 MeV/c).
- A variation of σ_{ep} (and also σ_{Mott}) within a bin.

Non–parallel contributions are neglected here as a typical value found for the angle γ is in the range 1-2°. This has a negligible ($\sim$0.07 %) effect on the magnitude of the $\mathbf{p}_m$ vector. One also expects the ± 5 MeV/c on either side of centre in a $\mathbf{p}_m$ bin to cancel out in its effect on the cross section. The remaining effect is that of variations in σ_{ep} and σ_{Mott} within a bin. This effect worsens with increasing bin width, (the bin width is chosen as a compromise between the finite acceptance effect and the statistics per bin).

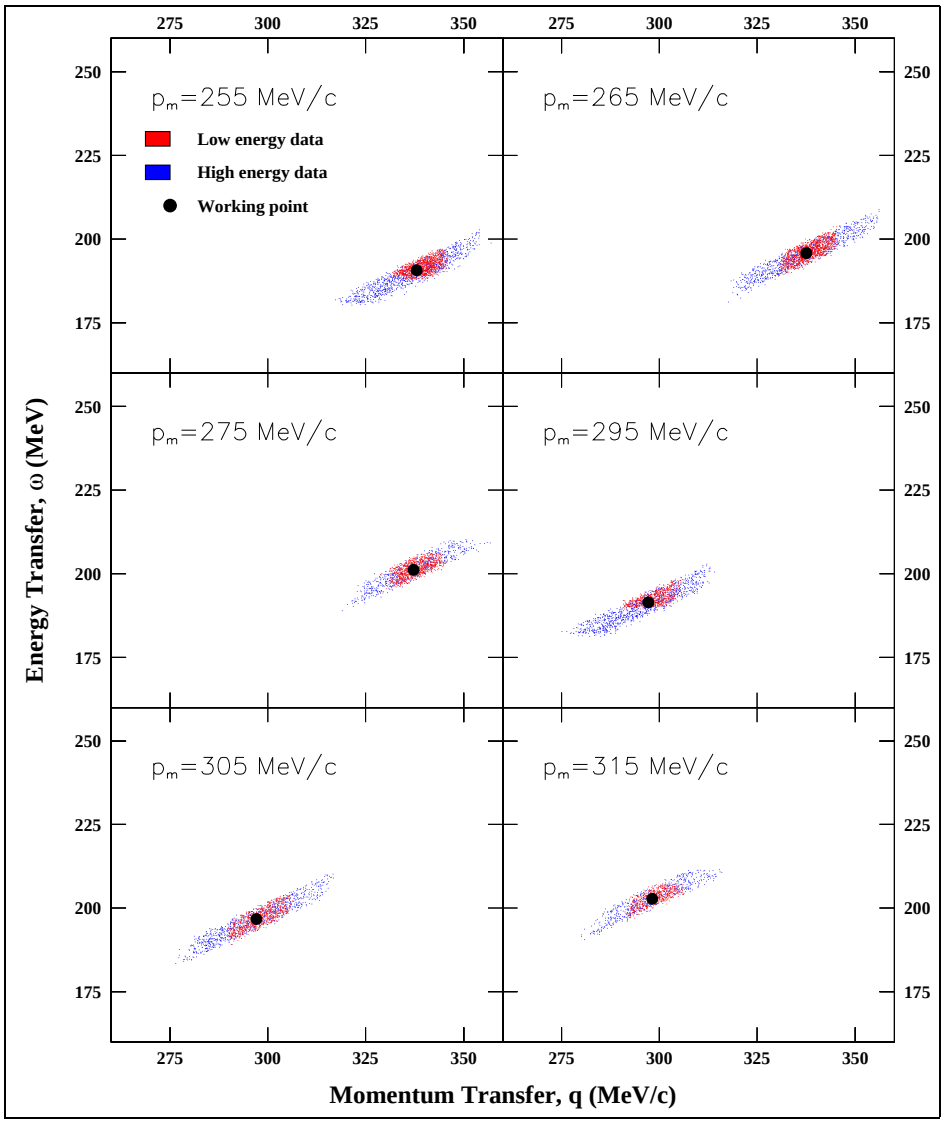

Figure 5.10: *Kinematical domains in* $\mathbf{q}$ *and* ω *for the* $\mathbf{p}_m$ *bins from 255 MeV/c to 315 MeV/c. Each panel corresponds to a bin 10 MeV/c wide centred at the value shown, (the data shown is for the ground state transition).*

The quantities $< \mathrm{K}\sigma_{ep} >^{ave}$ and $< \mathrm{K}\sigma_{Mott}\frac{\mathrm{Q}^2}{\mathrm{q}^2} >^{ave}$, which enter the L–T separation formula directly, were averaged over all events in each $\mathbf{p}_m$ bin, i.e.

$$< \mathrm{K}\sigma_{ep} >^{ave} = \frac{\sum_{n=1}^{N}(\mathrm{K}\sigma_{ep})^n}{N} \tag{5.6}$$

$$< \mathrm{K}\sigma_{Mott}\frac{\mathrm{Q}^2}{\mathrm{q}^2} >^{ave} = \frac{\sum_{n=1}^{N}(\mathrm{K}\sigma_{Mott}(\frac{\mathrm{Q}^2}{\mathrm{q}^2}))^n}{N} \tag{5.7}$$

where the sum is over all N events in each bin. These formulae gave the quantities to be used in the L–T separation, (see equations 5.16 and 5.17 later).

5.3.3 Error Propagation

The total systematic error in the calculation of the reduced cross sections has a large number of contributing factors. Calculation of these has been discussed in detail by [Her87]. No discussion is made here, except to show the estimates for each contribution in table 5.2. The total systematic error has

Table 5.2: *Contributions to the systematic errors on the $^{12}C(e,e'p)$ experiment, (see [Her87, Ste88a]).*

source	accuracy	effect on $\rho(\mathbf{p}_m)$
beam energy, E_0	200 keV	0.5 %
electron angle, $\theta_{e'}$	3 mr	1.5 %
proton angle, θ_p	5 mr	0.3 %
electron solid angle, $\Omega_{e'}$	1.0 %	1.0 %
proton solid angle, Ω_p	2.0 %	2.0 %
target thickness	2.5 %	2.5 %
target angle	0.3°	0.6 %
electron efficiency, ϵ_e	0.2 %	0.2 %
coincidence efficiency	1.3 %	1.3 %
dead time corrections	0.3 %	0.3 %
current integrator	0.2 %	0.2 %
Total systematic error		4.0 %

been evaluated by quadratically adding the individual contributions. This has led to an estimate of 4 % for the total systematic error contributing to the $\rho(\mathbf{p}_m)$ at each beam energy. This error was propagated through the L–T separation procedure to calculate the error on the structure functions.

The structure functions are essentially a function of the measured cross sections at the high and low beam energy, $\rho^{h,l}(\mathbf{p}_m)$, where the superscripts h and l represent the high and low beam energies, respectively. They are also dependent on the kinematical variables ${E_0}^{h,l}$, ${\theta_{e'}}^{h,l}$, ${\theta_p}^{h,l}$ and ${\mathrm{p}'}^{h,l}$, but this contribution to the systematic error on $\rho(\mathbf{p}_m)$ is included in the 4% mentioned previously. Since the systematic error in the W_i (where i=L,T) have a contribution from the measurement at each of the two beam energies, then

$$W_i = W_i(\rho^h, \rho^l) \tag{5.8}$$

i.e. the error may be worked out in two parts. The first contribution to the error, from the high beam energy measurement, was worked out as

$$\Delta W_i^{(1)} = |W_i(\rho^h, \rho^l) - W_i(\rho^h(1 + \frac{4}{100}), \rho^l)| \tag{5.9}$$

where the factor $\frac{4}{100}$ accounts for the 4 % error on ρ. The second contribution, from the low beam energy measurement, was worked out as

$$\Delta W_i^{(2)} = |W_i(\rho^h, \rho^l) - W_i(\rho^h, \rho^l(1 + \frac{4}{100}))| \tag{5.10}$$

such that the total systematic error, the quadratic addition of the individual parts, was calculated as

$$\Delta W_i = \sqrt{(\Delta W_i^{(1)})^2 + (\Delta W_i^{(2)})^2} \tag{5.11}$$

The statistical error on the structure functions has been calculated by propagating the statistical error on the $\rho(\mathbf{p}_m)$ through the L–T separation procedure. The total error was then the quadratic sum of the statistical and systematic errors.

5.4 The L–T Separation

This section will explain the calculation of the structure functions W_L and W_T from the reduced cross section, $\rho(\mathbf{p}_m)$, measured at the two beam energies. Equation 5.4 related the six–fold cross section to the spectral function

$$\frac{d^6\sigma}{dE_{e'}\ d\Omega_e\ dE_p\ d\Omega_p} = \mathrm{K}\sigma_{ep}\mathrm{S}(E_m,\mathbf{p}_m) \tag{5.12}$$

This allows us to convert the measurement of $\rho(\mathbf{p}_m)$ back into a six–fold cross section. Here we again use $\sigma_{ep}^{\mathrm{cc1}}$ of [DeF83] for the electron–proton cross section. If neither the beam nor the target are polarised then the six–fold cross section itself may be expressed in terms of four structure functions, [DeF67]

$$\begin{aligned}\frac{d^6\sigma}{dE_{e'}\ d\Omega_e\ dE_p\ d\Omega_p} &= \mathrm{K}\sigma_{Mott}\frac{Q^2}{\mathrm{q}^2\epsilon}\{\mathrm{W_T} + \epsilon\mathrm{W_L} \\ &+\epsilon\mathrm{W_{TT}}\cos 2\phi - (\epsilon(\epsilon+1))^{1/2}\mathrm{W_{LT}}\cos\phi\}\end{aligned} \tag{5.13}$$

where $\sigma_{Mott} = \{\frac{\alpha\cos(\theta_{e'}/2)}{2E_{e'}\sin^2(\theta_{e'}/2)}\}^2$ is the Mott cross section; Q is the 4-momentum transfer, defined as $Q^2 = \mathrm{q}^2 - \omega^2$; q is the 3-momentum transfer; ω is the energy transfer and ϕ is the azimuthal angle between the scattering plane and the reaction plane. The photon polarisation parameter ϵ is given by

$$\epsilon = \{1 + 2(\frac{q^2}{Q^2})\tan^2(\theta_{e'}/2)\}^{-1} \tag{5.14}$$

and determines the longitudinal–transverse character of the transferred virtual photon. It may vary from 0–1.

The structure functions $W_i = W_i(\omega, \mathrm{q}, \mathrm{p}', \gamma)$ depend on the electron–proton coupling, the nuclear structure and the final–state interaction between the outgoing proton and the residual nucleus. They therefore contain the information which we want to extract from an (e,e'p) experiment.

When a measurement is made in parallel kinematics, the angle γ=0 and only two structure functions remain [Bof82]. The cross section may then

be written (multiplying out the bracket by ϵ^{-1}) as

$$\frac{d^6\sigma}{dE_{e'}\ d\Omega_e\ dE_p\ d\Omega_p} = \mathrm{K}\sigma_{Mott}\frac{Q^2}{\mathrm{q}^2}\{\epsilon^{-1}\mathrm{W_T} + \mathrm{W_L}\} \tag{5.15}$$

The separation procedure is therefore equivalent to solving a pair of simultaneous equations of type

$$(\sigma_{ee'p})^h = \mathrm{K}(\sigma_{Mott})^h\frac{Q^2}{\mathrm{q}^2}\{\epsilon^{-1}\mathrm{W_T} + \mathrm{W_L}\} \tag{5.16}$$

$$(\sigma_{ee'p})^l = \mathrm{K}(\sigma_{Mott})^l\frac{Q^2}{\mathrm{q}^2}\{\epsilon^{-1}\mathrm{W_T} + \mathrm{W_L}\} \tag{5.17}$$

where $\sigma_{ee'p}$ represents the 6–fold cross section, and again the h and l represent the high and low beam energy measurements, respectively. The K, Q and q are made constants by the choice of kinematics. These equations describe a linear relationship between $\frac{\sigma_{ee'p}}{\mathrm{K}\sigma_{Mott}}\frac{\mathrm{q}^2}{Q^2}$ and ϵ^{-1} which are plotted in a 'Rosenbluth plot'. Fig. 5.11 shows the Rosenbluth plots for each of the $\mathbf{p}_m$ bins in the ground state transition.

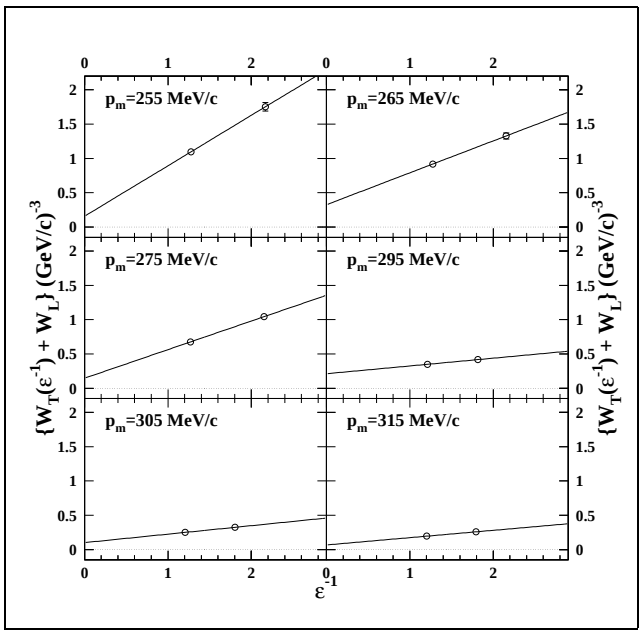

Figure 5.11: *Rosenbluth plots for each $\mathbf{p}_m$ bin in the L–T separation for the transition to the ground state of ^{11}B.*

5.5 Results

An overview of the current NIKHEF data set on ^{12}C(e,e′p) in parallel kinematics is shown in figures 5.12 and 5.13. The momentum distributions, $\rho(\mathbf{p}_m)$, as measured in the present experiment (for beam energies of 378.5 and 585.1 MeV), are plotted alongside previous data of van der Steenhoven *et al.* [Ste88a, Ste88b] and Kester *et al.* [Kes96]. The data of van der Steenhoven *et al.* for anti–parallel kinematics ($\mathbf{p}_m$<0) have not been shown here as they add no further information to the comparison.

The difference in normalisation of the data for each separate experiment is explained as being due to the difference in kinetic energy of the emitted proton. The data of [Ste88a, Ste88b] were taken at T_p=70 MeV. This corresponded to a greater absorption of the outgoing proton wave as compared to the present data and that of Kester *et al.*, which had T_p=175 MeV and 190 MeV, respectively. For this reason, the match in normalisation (for the ground state and ∼7 MeV triplet transitions) between the present data and that of Kester *et al.* is much better than between the present data and that of van der Steenhoven *et al.*

The present data are also displayed as momentum distributions in figures 5.14 and 5.15, and as structure functions in figures 5.16 and 5.17. (In addition all momentum distributions and structure functions are tabulated in Appendix A.) It can be seen that the error bars are amplified due to the L–T separation procedure. The data are displayed with CDWIA calculations and calculations in the RPA framework, both with and without (MEC) and Δ–Isobar (IC) contributions. These calculations are explained in the following sections.

5.5.1 CDWIA Calculations

The experimental data have been compared with calculations based on the Complete Distorted Wave Impulse Approximation (CDWIA). The results of the calculations are displayed as the dotted lines in figures 5.14 and 5.15,

respectively. These calculations were made using a non–relativistic, unfactorised DWIA [Bof80a, Bof80b] code which includes an approximate treatment of the distortion of the electron waves due to the Coulomb field of the nucleus [Giu80, Giu87, Giu88].

As has already been stated in Chapter 2, in the PWIA both the incoming and scattered electron, and the outgoing proton, are represented by plane waves. The cross section for the (e,e′p) reaction in this approximation can be factorised into a term describing the electron–proton coupling and a term describing the nuclear structure effects, (the spectral function, $S(E_m,\mathbf{p}_m)$). In the DWIA the FSI effect of the residual (A-1) nucleus on the outgoing proton is taken into account. This is done by distorting the proton wave with a (non–relativistic) optical–model potential. This potential is taken from analysis of elastic proton scattering data on the residual nucleus, and parameterised as a function of T_p. See Appendix B for the potential parameters used in the present calculations.

In the CDWIA calculations a bound state wave function for the knocked out nucleon is calculated by solving the Schrödinger equation for a Woods–Saxon potential well. The bound state wave function is then related to the momentum distribution via a Fourier transformation.

The range of $\mathbf{p}_m$ covered in the present experiment was not sufficient to allow a complete analysis with the CDWIA. Therefore spectroscopic factors, S_α, and the root-mean-square radii, r_{rms}, of the bound–state wave functions for each state were taken from the data of [Ste88a, Ste88b]. Although more recent analyses have published values for S_α and r_{rms} (e.g. [Lap00, Ire94]), the references used are the only ones to quote values for all states in ^{11}B up to the 7.29 MeV state, including values for both the 1s and 2s contributions to the $1/2^+$ state at 6.79 MeV. To fit the calculations to the r_{rms} of [Ste88a, Ste88b] the potential well depth (V_0) and diffuseness parameter (a_0) of the Woods–Saxon potential were kept constant and the radius (r_0) was varied until a consistent r_{rms} was found. The value of V_0 was fixed at -55 MeV and a_0 at 0.65 fm for all states. Table 5.3 lists the values of r_0 used for the current analysis and the r_{rms} from [Ste88a, Ste88b] to which these calculations were

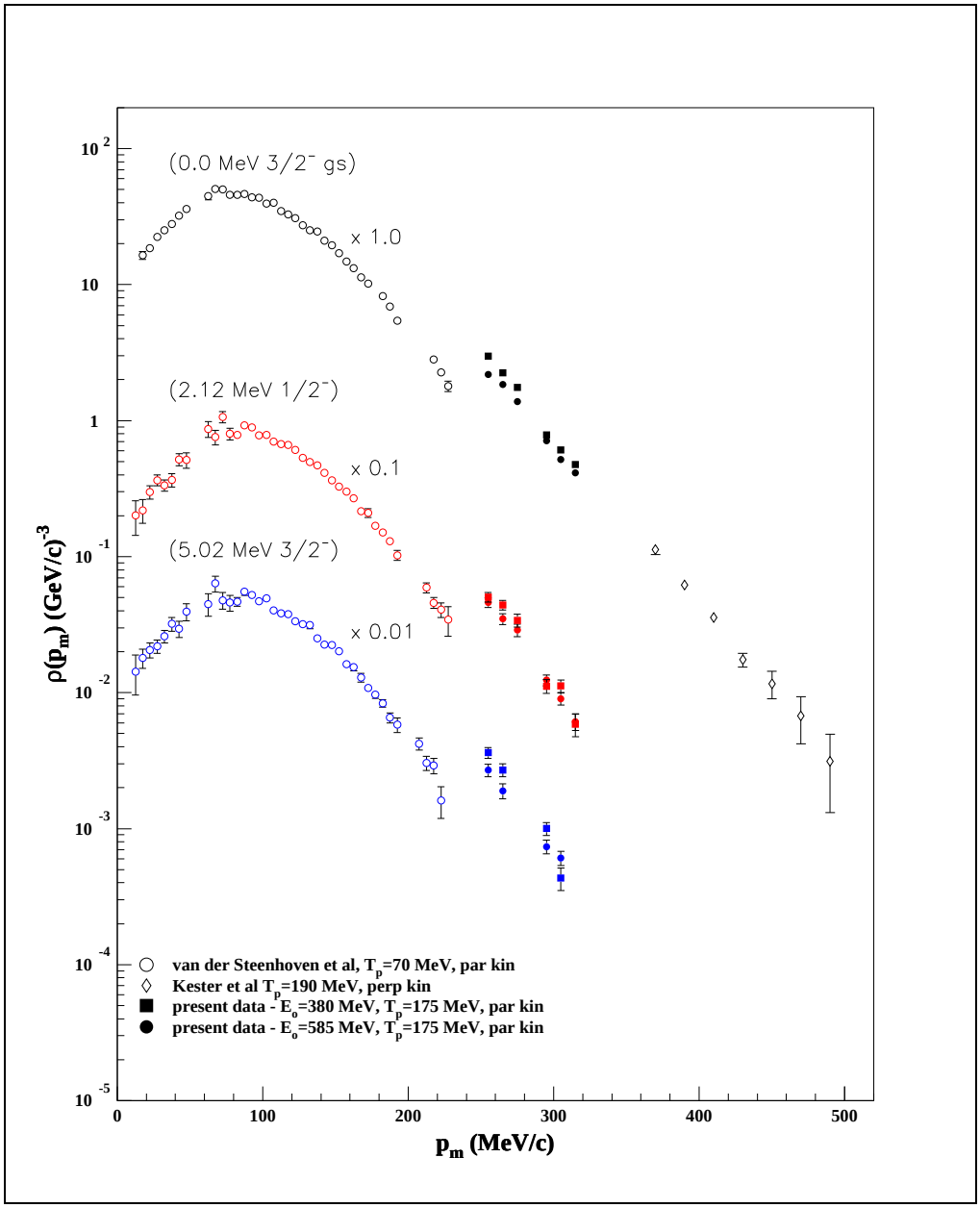

Figure 5.12: *Momentum distributions for the ground state, 2.12 and 5.02 MeV transitions, corresponding to 1p knockout from ^{12}C. Open circles represent the data of van der Steenhoven et al. [Ste88a, Ste88b] and the open diamonds the data of Kester et al. [Kes96]. The solid data points are from the present experiment, solid squares representing the data with a beam energy of 378.5 MeV, and solid circles representing the data with a beam energy of 585.1 MeV. The present data are shown with statistical errors only. The mismatch in normalisation between the $T_p \geq 175$ MeV and $T_p = 70$ MeV data sets is explained in the text.*

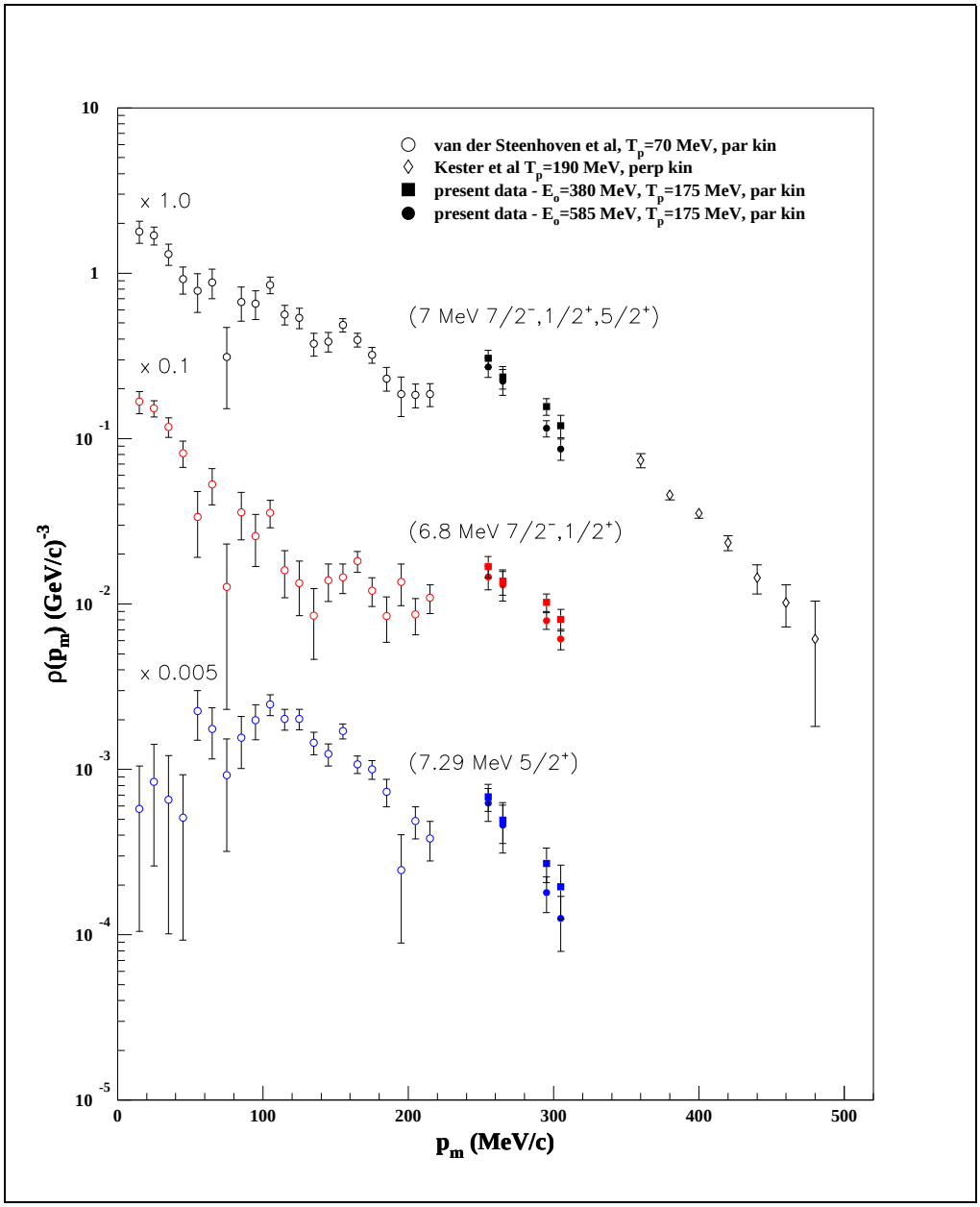

Figure 5.13: *Momentum distributions for transitions to the states in the 7 MeV triplet. See fig. 5.12 for a description of the data displayed. The present data are shown with statistical errors only. The mismatch in normalisation between the $T_p \geq 175$ MeV and $T_p = 70$ MeV data sets is explained in the text.*

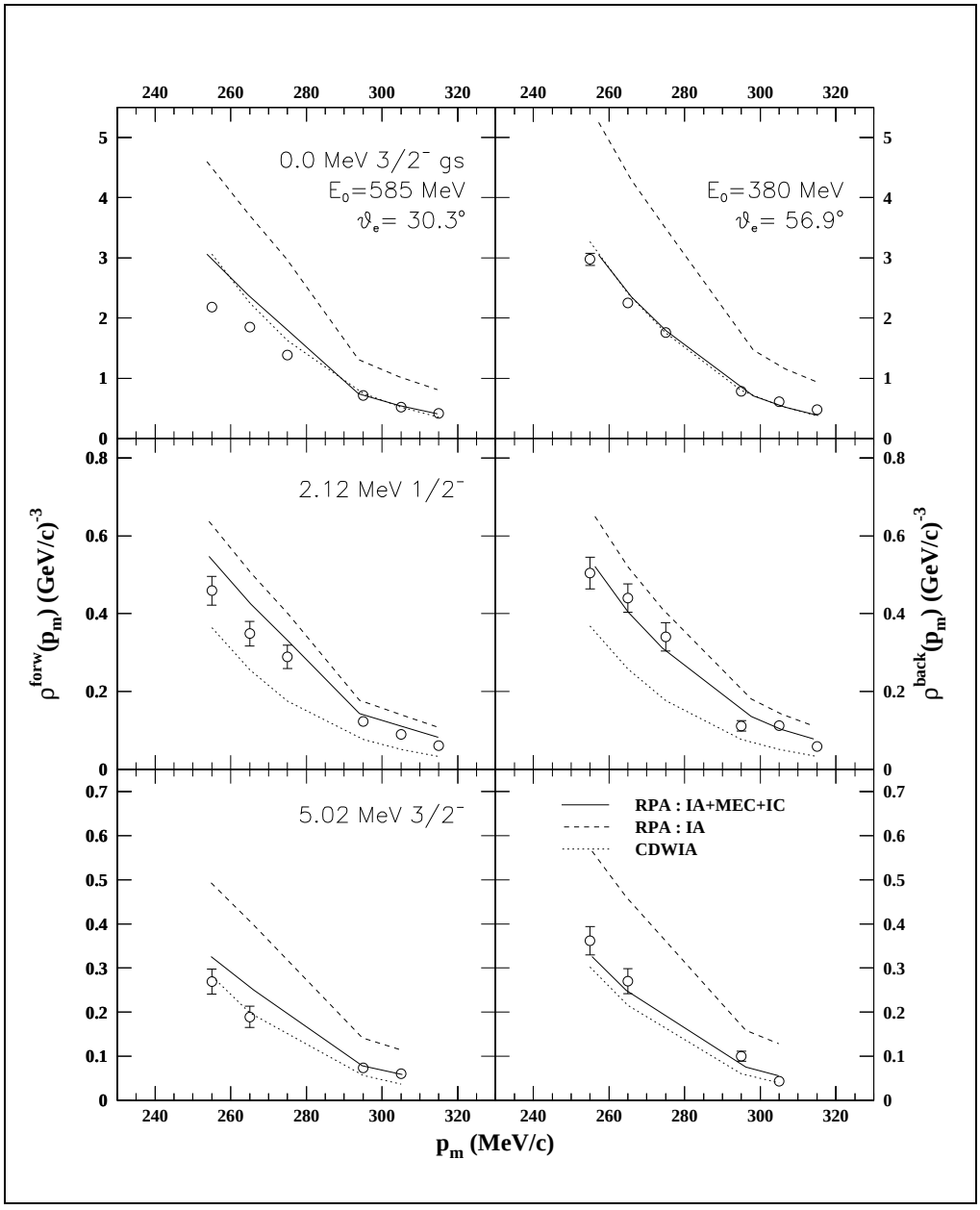

Figure 5.14: *Momentum distributions for the strongly excited 1p transitions to states in ^{11}B. RPA calculations, by Ryckebusch [Ryc99], are shown with (solid lines) and without (dashed lines) MEC and IC. The dotted lines represent CDWIA calculations, see the text for details. The data are shown with statistical errors only.*

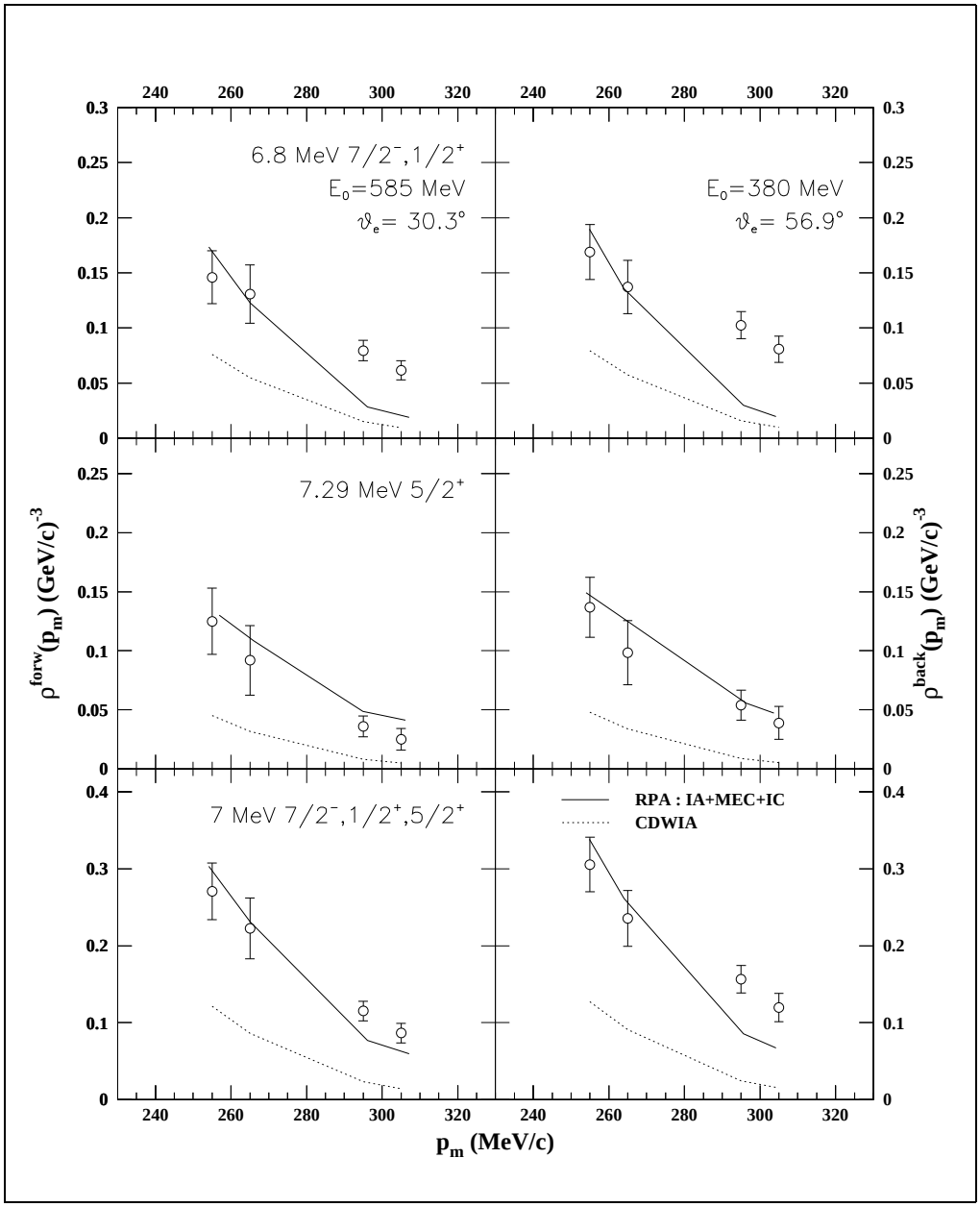

Figure 5.15: *Momentum distributions for the weakly excited transitions to states around 7 MeV in ^{11}B. See fig. 5.14 for an explanation of the different lines in the plot. The data are shown with statistical errors only.*

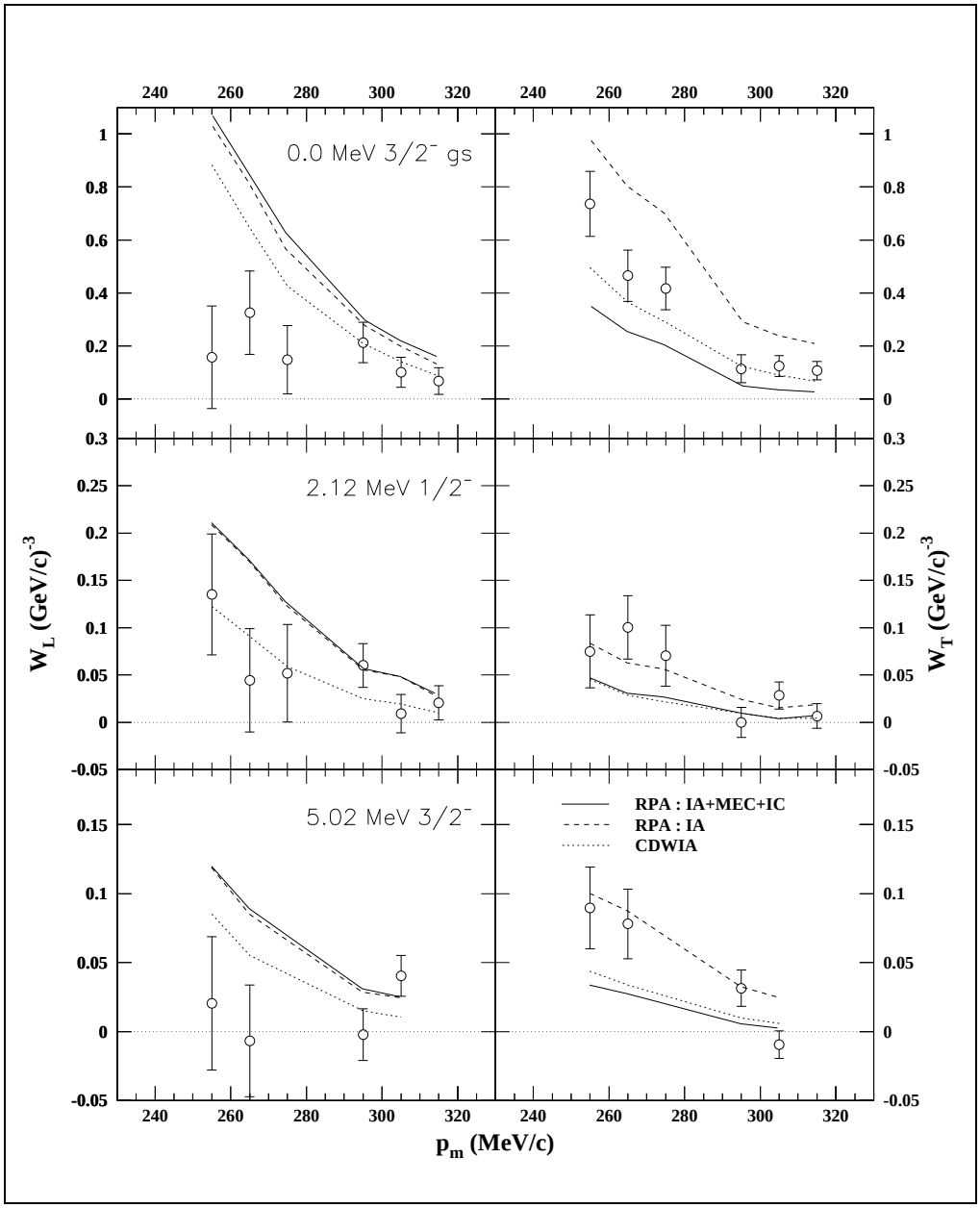

Figure 5.16: *Structure Functions W_L and W_T for the strongly excited 1p transitions to states in ^{11}B, v's $\mathbf{p}_m$. See fig. 5.14 for an explanation of the different lines in the plot. The data are shown with both statistical and systematic errors.*

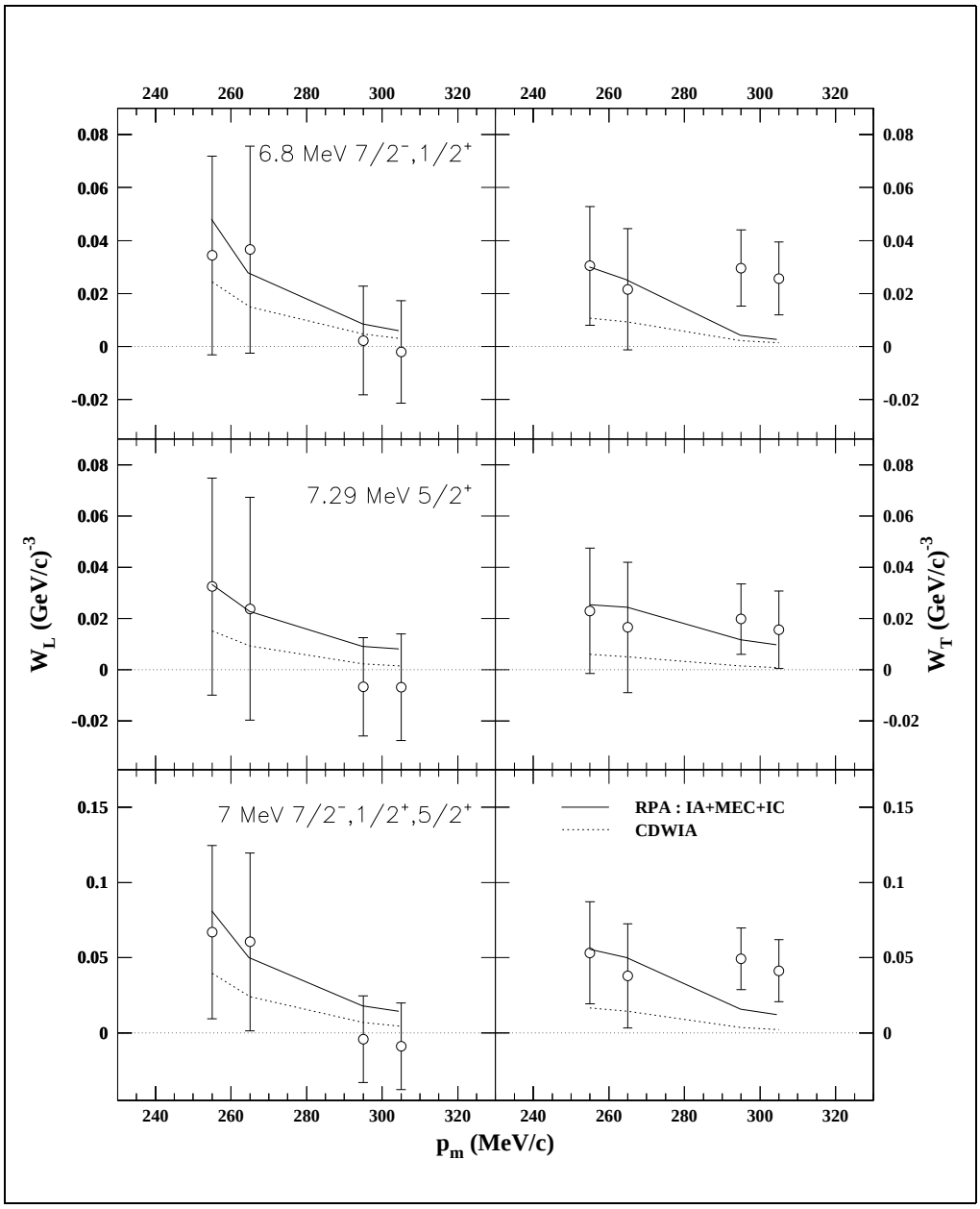

Figure 5.17: *Structure Functions W_L and W_T for the weakly excited transitions to states around 7 MeV in ^{11}B, v's $\mathbf{p}_m$. See fig. 5.14 for an explanation of the different lines in the plot. The data are shown with both statistical and systematic errors.*

fitted. The experimentally unresolved states were combined in order to make

Table 5.3: *The values of r_0, and the r_{rms} and S_α taken from [Ste88a, Ste88b], used in the CDWIA calculations.*

J^π	E_{ex} (MeV)	r_0 (fm)	r_{rms} (fm)	S_α
$3/2^-$	0.00	3.1448	2.724	1.900
$1/2^-$	2.12	3.9378	2.945	0.235
$3/2^-$	5.02	3.5730	2.804	0.200
$7/2^-$	6.74	5.5090	4.295	0.0038
$1/2^+(1s)$	6.79	1.0431	1.894	0.0031
$1/2^+(2s)$	6.79	4.8330	3.527	0.018
$5/2^+$	7.29	4.5457	3.525	0.017

comparison with the data.

From fig. 5.15 it can be seen that the CDWIA calculations are consistently below the data for the ∼7 MeV triplet states. This is to be expected if there are non–DKO effects such as MEC or 2–step processes contributing to these states in this $\mathbf{p}_m$ range.

The CDWIA cross sections for the high and low beam energy measurements were used to carry out an L–T separation. This was done with the bin–by–bin kinematics from the experimental data and using exactly the same procedure as for the experimental data. The results are shown in figures 5.16 and 5.17 for the 1p knockout and ∼7 MeV triplet states respectively. The separated structure functions are more in agreement with the CDWIA calculations than the momentum distributions. This is mainly due to the larger error bars on the structure functions.

5.5.2 MEC and Δ–Isobar Calculations

Calculations were also made by Ryckebusch [Ryc99] of the (e,e′p) cross section in the RPA model with and without the inclusion of virtual photon coupling to 2–body currents. The 2–body current operators included both MEC and IC contributions. The results, again, are shown in figures 5.14 and

5.15, respectively. The dashed lines represent the result of the calculations accounting for 1–body currents only (the impulse approximation). The solid lines represent the result of including the 2–body currents. The 2–body current calculations for the ∼7 MeV triplet states were made according to a procedure (outlined in [Kuz98]) whereby the initial state wave function is constructed as

$$\alpha|(1h) > +\beta|(2h-1p) > \tag{5.18}$$

where α is determined by the spectroscopic factor, S_α, again taken from [Ste88a, Ste88b]. The parameter β comes from shell model calculations. The calculations which only include 1–body currents have not been made for the triplet states.

As with the CDWIA calculations an L–T separation was performed on these cross sections using exactly the same procedure as for the experimental data. This is again represented in figures 5.16 and 5.17. When neglecting the MEC and IC, the (2h–1p) contribution vanishes, leaving only the (1h) contribution. The (1h) contribution represents the population of states above the Fermi surface for the states at ∼7 MeV. The (1h) contribution explains the non-vanishing longitudinal structure function calculated for the triplet states, [Rycpc].

5.5.3 Comparison to ^{12}C(γ,p) Data

As the initial motivation for this measurement was an unexplained experimental result in ^{12}C(γ,p) data, a comparison has been made between the two reactions. In fig. 5.18 the ^{12}C(e,e′p) data are presented as a 'transverse reduced cross section' [Lappc], which has been defined as W_T/F_T, where

$$F_T(Q^2) = (Q^2/4{m_p}^2)(G_M^p(Q^2))^2 \tag{5.19}$$

where G_M^p is the proton magnetic form factor. This has been plotted alongside the ^{12}C(γ,p) data of Ruijter *et al.* [Rui96]. Ruijter's data have been converted from angular distributions to reduced cross sections according to

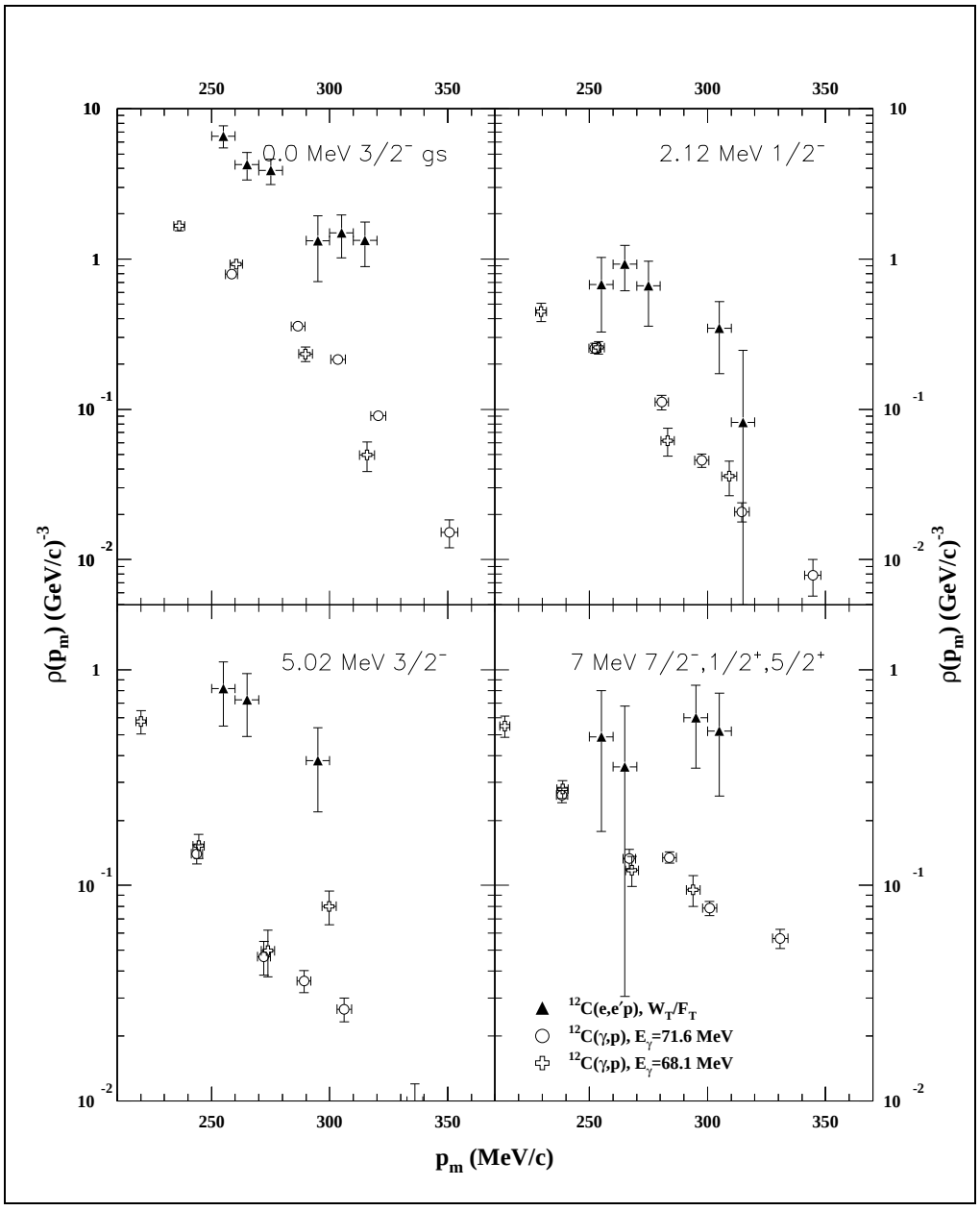

Figure 5.18: *Comparison of the present transverse (e,e′p) data with the four resolved transitions in the $^{12}C(\gamma,p)$ data of Ruijter et al. [Rui96].*

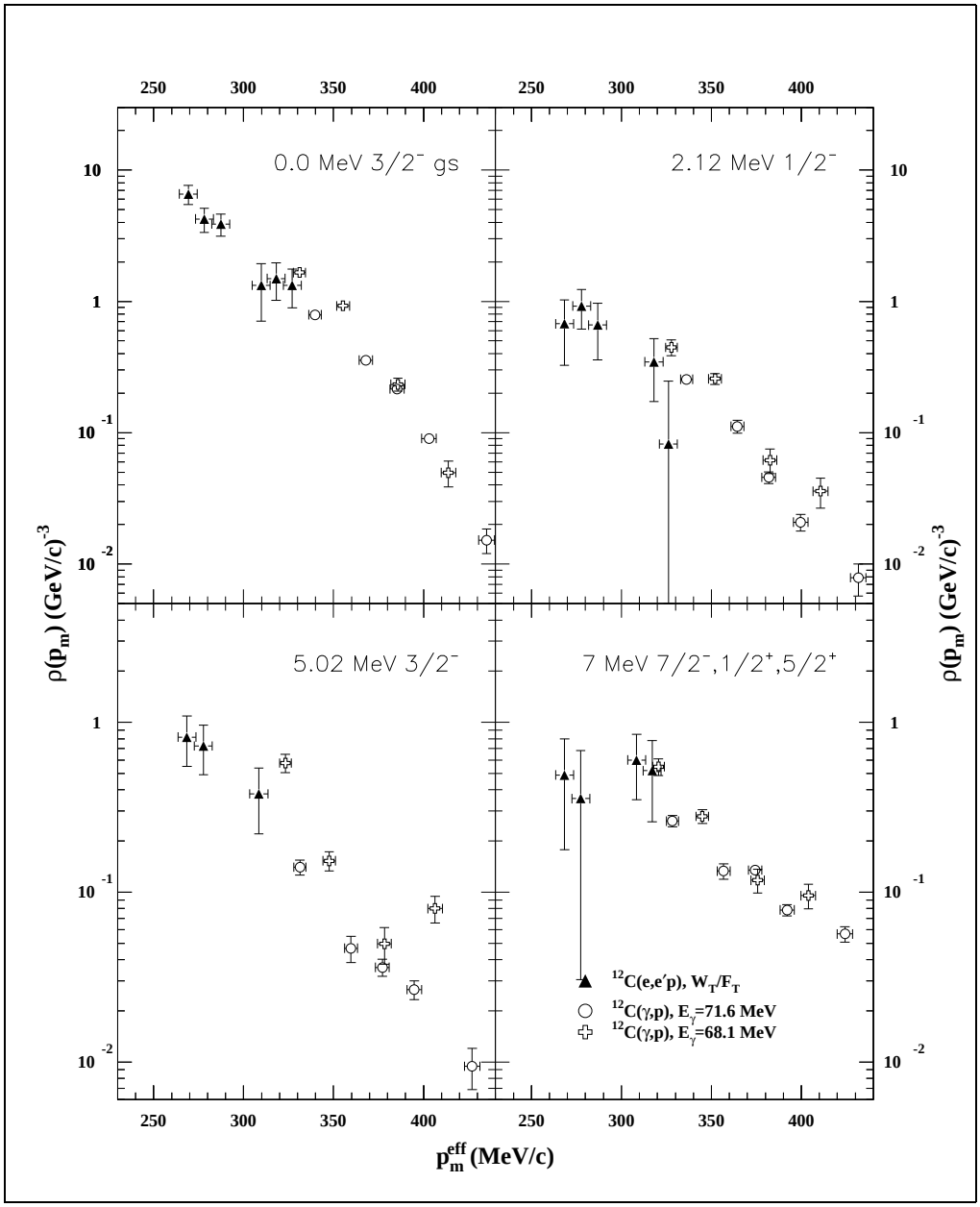

Figure 5.19: *Comparison of the present transverse (e,e′p) data with the four resolved transitions in the $^{12}C(\gamma,p)$ data of Ruijter et al. [Rui96], plotted as a function of $\mathbf{p}_m^{eff}$.*

the procedure suggested by [Ire94]. The transformation (which holds only in the PWIA) is given by equation 2.6 on page 8. In the PWIA the momentum distributions for both (e,e′p) and (γ,p) correspond to the square of the Fourier transform of the radial overlap wave function.

The comparison is shown for four resolved transitions. The top left panel of fig. 5.18 shows the 0.0 MeV g.s., the top right panel the 2.12 MeV 1st excited state. The 4.45 and 5.02 MeV states, which are unresolved in the (γ,p) data are shown in the bottom left panel (the 4.45 MeV state is not observed in (e,e′p) in parallel kinematics, see fig. 5.9). Finally, the three unresolved states of the ∼7 MeV triplet are shown in the bottom right panel.

In order to compare the two data sets on an equal footing, the only remaining difference between them was the T_p value at which each measurement had been made. A difference in these values leads to a different susceptibility of each data set to FSI effects. The T_p of the (γ,p) data is ∼50 MeV, whereas the T_p for the (e,e′p) data is ∼175 MeV. To account for this, the data have also been plotted as a function of $\mathbf{p}_m^{eff}$ as shown in fig. 5.19. The $\mathbf{p}_m^{eff}$ was defined using the following effective proton momentum,

$$p'^{eff} = p' \sqrt{1 + \frac{V_0}{T_p}} \tag{5.20}$$

where V_0 represents the potential well from which the exiting proton must escape to leave the target nucleus. The potential used for V_0 was the real part of the optical potential used in the CDWIA calculations to describe the FSI effect. This potential was T_p dependent.

Comparisons of these reactions have been made in the past, e.g. [Ire94], for (e,e′p) data with $\mathbf{p}_m$<220 MeV/c, but never for $\mathbf{p}_m^{ee'p}$=$\mathbf{p}_m^{\gamma p}$, and never using the purely transverse component of the (e,e′p) cross section. Fig. 5.19 appears to show that the reactions converge when compared on an equal footing.

Chapter 6

Analysis and Results of the ^{14}N(γ,Xγ') Experiment

This chapter describes the analysis and presents the results of an experiment designed to study two nucleon knockout from ^{14}N by measuring the de–excitation γ-ray decay of the residual nucleus, ^{12}C. The experimental setup for this measurement has already been explained in chapter 3. The analysis was largely similar to that of the ^{12}C(γ,pγ') experiment described in chapter 4. Only differences with that experiment will be explained here.

6.1 Charged Particle Analysis

Analysis of the charged particle arm of this experiment was almost identical to that for the ^{12}C experiment described previously. Particle identification was made in the same way, however, both deuteron and proton knockout channels were selected, as shown in fig. 6.1. Two charged particle telescopes were used, refer to section 3.5 and fig. 3.17 for a description of the detector setup. Calibration of the photon tagger and of the HPGe detectors were carried out as described in sections 4.1.2 and 4.1.3. The HPGe's were also calibrated with the ^{12}C(γ,p) reaction, as before. Fig. 6.2 shows the focal plane TDC spectra used to identify tagged photon events. The upper panel

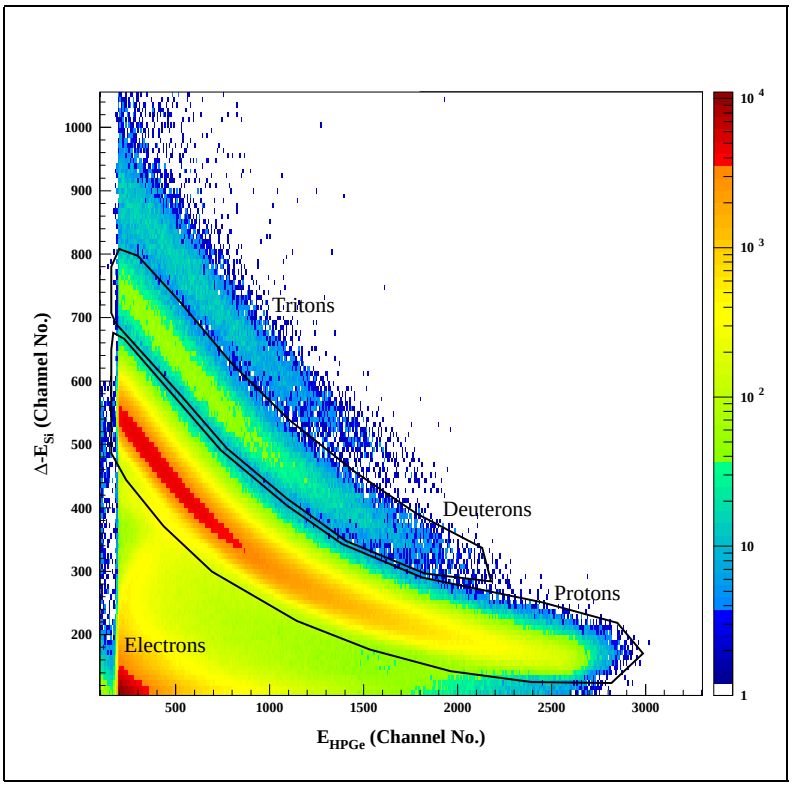

Figure 6.1: *Particle ID for the $^{14}N(\gamma,X\gamma')$ measurement.*

is in coincidence with protons, while the lower panel is coincident with deuterons. Both spectra are for telescope #1 only and show timing resolutions of ∼2.4 and ∼5.9 ns, for protons and deuterons respectively. Telescope #2 had a timing resolution of ∼6.8 and ∼7.8 ns, for protons and deuterons, respectively.

6.2 E_m & ^{12}C Background Subtraction

The main experimental target was not pure nitrogen. It was a compound, $C_2H_4N_4$ (see section 3.3), and so subtraction was made of events due to reactions on the carbon contaminant by taking separate data with a pure carbon target. The spectrum $\mathcal{S}^N$, due to reactions on nitrogen only, was obtained

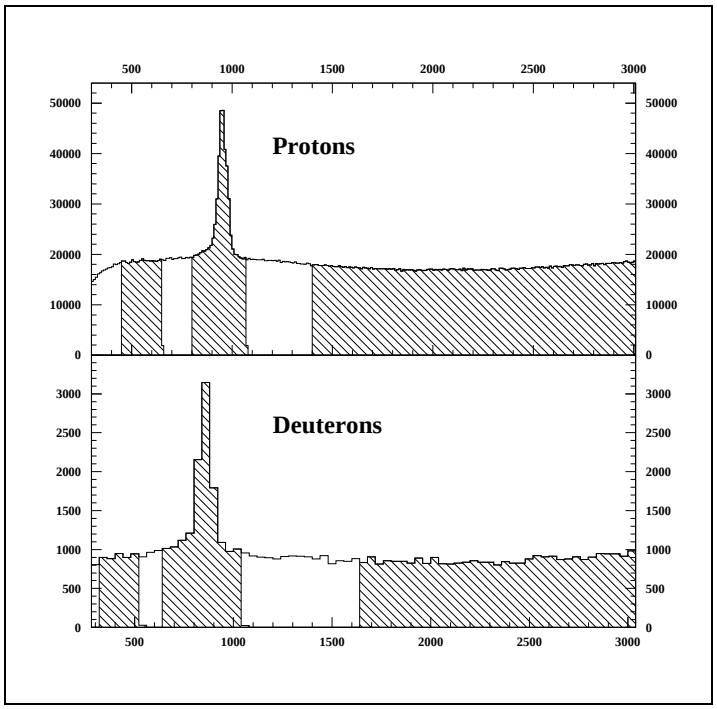

Figure 6.2: *Focal plane TDC Spectrum for the $^{14}N(\gamma,X\gamma')$ experiment. The timing resolution is approx. ~2.4 ns for protons and ~5.9 ns for deuterons.*

by subtracting the yield from the background carbon target according to

$$\mathcal{S}^N = \mathcal{S}^{CHN} - R \times \mathcal{S}^C \tag{6.1}$$

where $R = R_\gamma R_C$. The factor $R_\gamma = I_\gamma^{CHN}/I_\gamma^C$ represents the ratio of tagged photon fluxes incident on each of the two targets and was derived from scalers during the experimental run. The factor $R_C = N^{CHN}/N^C$ which represents the ratio of carbon nuclei in each of the two targets, was calculated as follows.

The number of molecules, of molecular weight ω, in a target, of mass M, is given by $N = \frac{MN_A}{\omega}$, where N_A is Avogrado's number. Therefore the number of carbon atoms in the pure carbon target was, $N^C = \frac{M^C N_A}{\omega^C}$. Also, the number of carbon atoms in the $C_2H_4N_4$ target was, $N^{CHN} = 2\frac{M^{CHN} N_A}{\omega^{CHN}}$, since there are two carbon atoms per $C_2H_4N_4$ molecule.

The intercepted volume of each target is given by At, where A is the surface area illuminated and t is the physical thickness of the target. The

mass of the intercepted volume may then be expressed as $M = \rho At = dA$, where ρ is the density of the target material and $d = \rho t$. The number of carbon nuclei in each of the two targets, N^{CHN} and N^{C}, may now be written

$$N^{CHN} = 2\frac{d^{CHN} A N_A}{\omega^{CHN}} \tag{6.2}$$

and

$$N^{C} = \frac{d^{C} A N_A}{\omega^{C}}. \tag{6.3}$$

Assuming equal areas, A, are illuminated on each target, this implies the ratio, R_C, is given by

$$R_C = 2\frac{d^{CHN}}{d^{C}}\frac{\omega^{C}}{\omega^{CHN}}. \tag{6.4}$$

Finally, the subtraction of the carbon contaminant was given by

$$\mathcal{S}^{N} = \mathcal{S}^{CHN} - 2\frac{I_\gamma^{CHN}}{I_\gamma^{C}}\frac{d^{CHN}}{d^{C}}\frac{\omega^{C}}{\omega^{CHN}}\mathcal{S}^{C} \tag{6.5}$$

The factor R amounted to a multiplication of the $\mathcal{S}^C$ spectrum by 1.3354. In addition, because the $C_2H_4N_4$ target was held between two hostaphan sheets (see section 3.3) data were taken using an empty target cell, and the resulting spectrum was also subtracted.

Reconstruction of the missing energy, E_m, was made as described in section 4.1.5. In this measurement, the angles $\theta_{p/d}$ were not measured, but were instead estimated by the mean angle of each telescope ($\pm 90^\circ$), resulting in a kinematical broadening of the reconstructed E_m. Fig. 6.3 shows the E_{ex} spectra acquired from both the $C_2H_4N_4$ and pure carbon targets. The spectrum taken from the background target is represented as the hatched histogram. The ground state of the ^{12}C(γ,p) E_{ex} spectrum was expected at 8.41 MeV in the ^{14}N(γ,p) spectrum. The background subtracted histogram is shown in fig. 6.4. This spectrum compares with those measured by [Ire91, Rau96] for ^{14}N(γ,p). The difference observed in this spectrum at $E_{ex}\sim$10 MeV is most likely due to an inaccuracy in the position of the ground state peak in the subtracted carbon spectrum. The calibration of

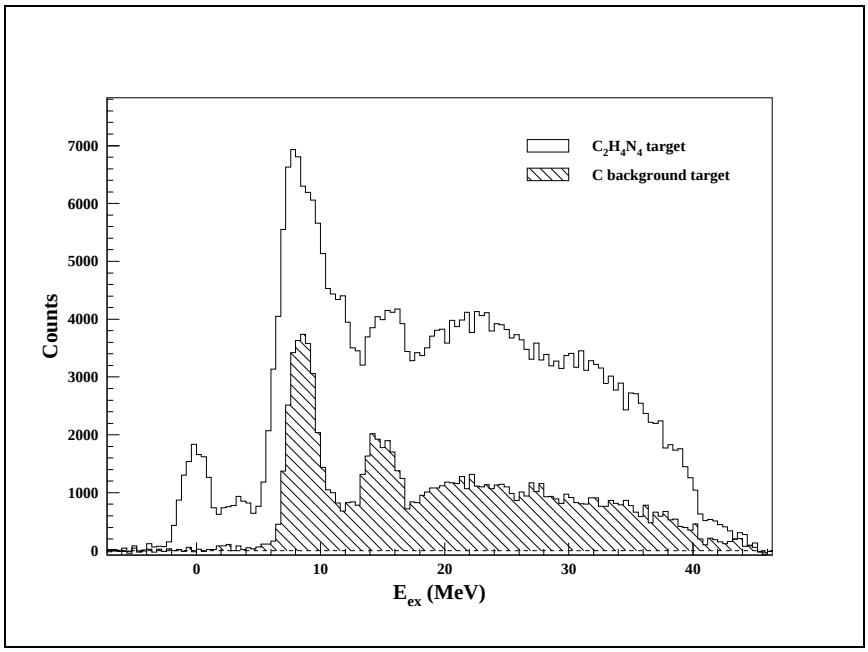

Figure 6.3: *E_{ex} spectrum for $^{14}N(\gamma,p)$, showing ^{12}C background. The data shown are the total for both telescopes and are presented in 400 keV bins.*

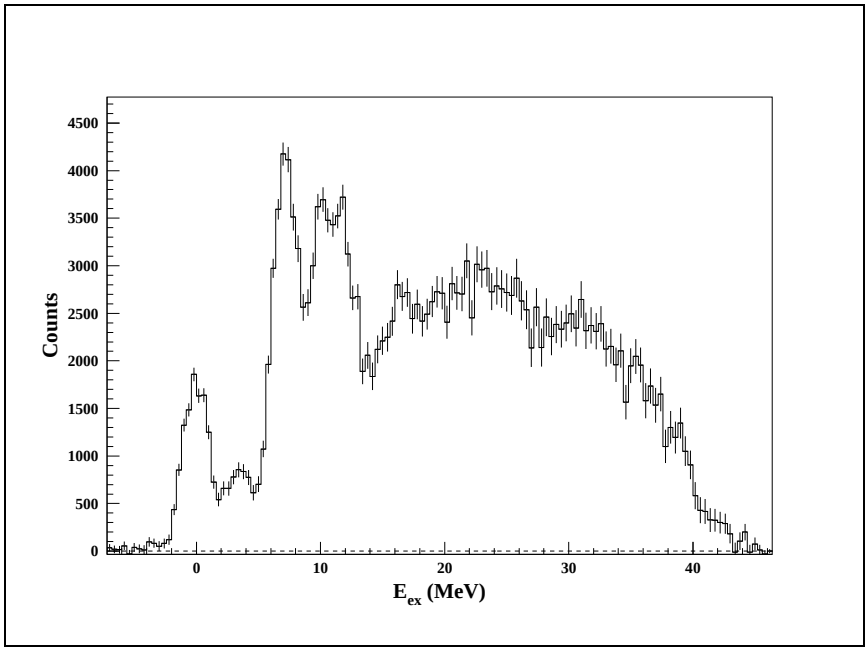

Figure 6.4: *E_{ex} spectrum for $^{14}N(\gamma,p)$, ^{12}C background subtracted. An E_{ex} resolution of $\sim$2.5 MeV was achieved for the ground state transition. The data shown are the total for both telescopes and are presented in 400 keV bins.*

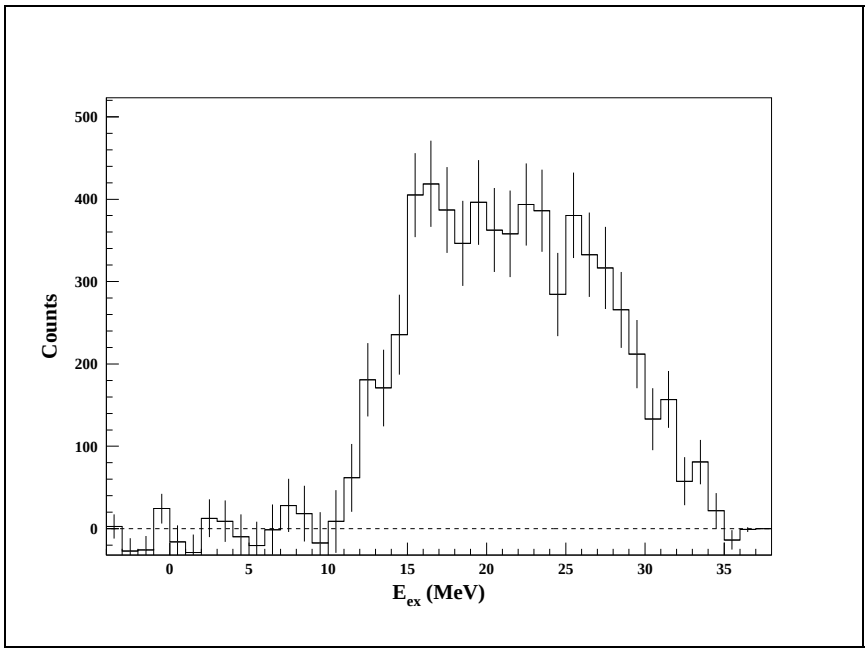

Figure 6.5: *E_{ex} spectrum for $^{14}N(\gamma,d)$, ^{12}C background subtracted. The data shown are the total for both telescopes and are presented in 1 MeV bins.*

E_{ex} used the ^{12}C(γ,p) kinematics, however, the lack of θ_p information and the relatively thick target combine to make this method less accurate than the calibrations made in [Ire91, Rau96]. This discrepancy is not important, however, as the main spectra of interest in this measurement come from the de–excitation γ-rays. The E_{ex} spectrum of fig. 6.4 is not used to derive the final result. In fig. 6.5 the E_{ex} spectrum derived from ^{14}N(γ,d) is shown, after the subtraction of events from the carbon target. This spectrum compares with that of [Ire91], shown in fig. 2.19. However, there is no evidence of the population of the 4.44 MeV state of ^{12}C, as was reported by [Ire91].

The energy loss of deuterons leaving the target is more than for the protons. Therefore the deuteron detection threshold was much higher in this measurement. The detection threshold for both deuterons and protons is shown in fig. 6.6. In this plot, 'final energy' is the energy deposited in the HPGe detectors and 'initial energy' is the particle energy before leaving the target, reconstructed from energy losses. As can be seen deuterons with an initial energy of $\gtrsim$21 MeV were detected. This allowed all deuterons,

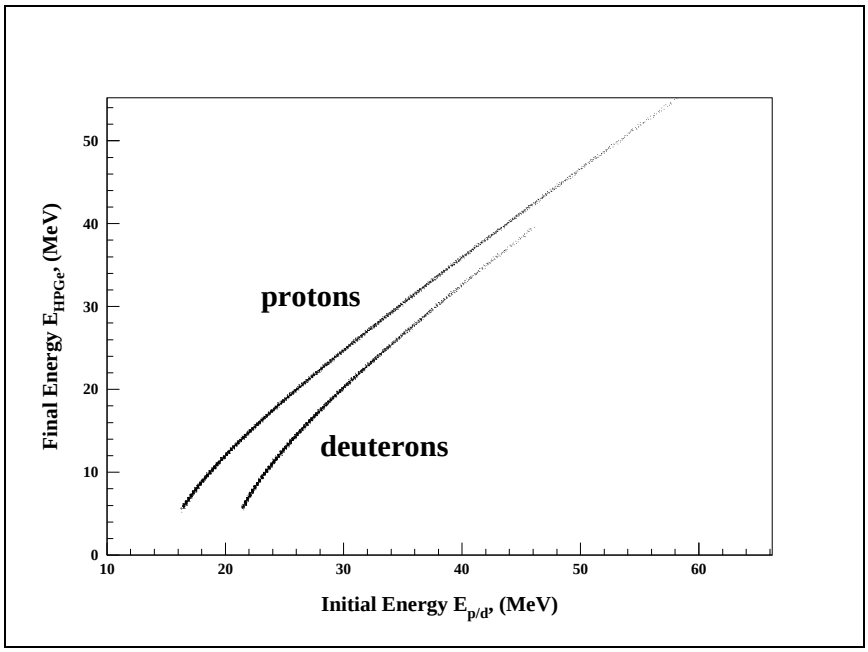

Figure 6.6: *The threshold for detection of protons and deuterons in the charged particle telescopes. The threshold energy for protons is seen to be ∼16 MeV and for deuterons ∼21 MeV.*

from reactions initiated by photons within the tagging range, to be detected (depositing an energy $\gtrsim$5 MeV in the HPGe's).

6.3 Derivation of De–excitation γ' Spectra

Calibration of the NaI detectors was made using γ-ray sources as well as with the γ' spectra from ^{12}C(γ,pγ') data, taken using the background target. A calibration with points up to ∼7 MeV was made for each NaI and then a linear extrapolation was made to ∼15 MeV. This is shown for both NaI detectors in fig. 6.7. A calibration point was found from the spectrum of an Am–Be source (described in section 4.2.2) at 6.83 MeV due to ^{127}I(n,γ) reactions occurring within the NaI detectors (6.83 MeV is the Q–value for the reaction to occur, and since all γ-rays caused by the reaction are emitted within the NaI crystals their total energy is detected as one signal). The resolution of NaI #1, as measured from the calibration sources is shown for

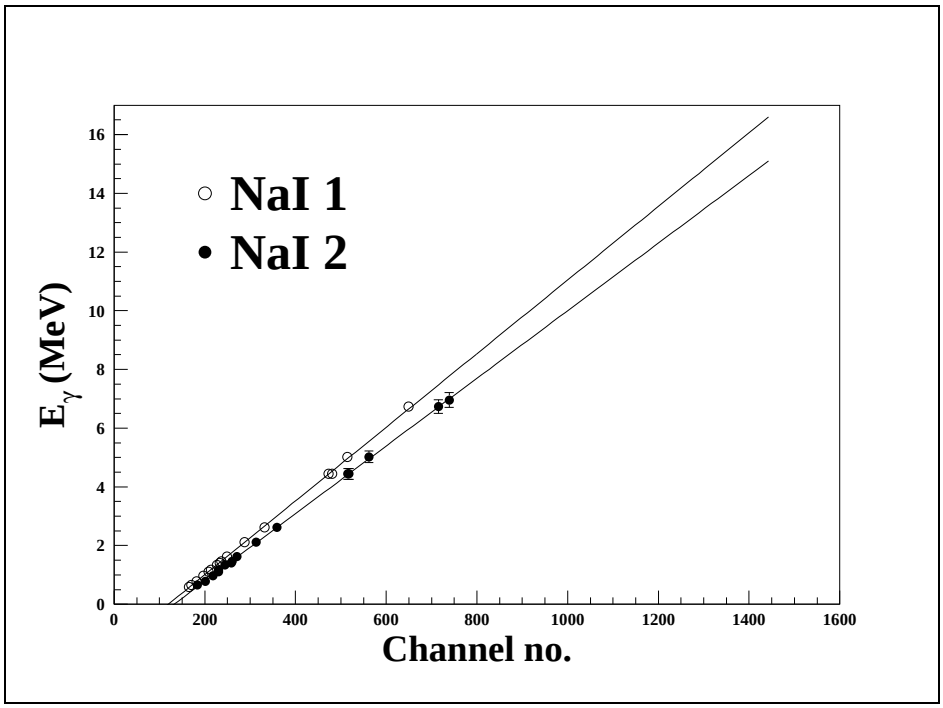

Figure 6.7: *NaI detector calibrations made using γ-ray sources and $^{12}C(\gamma,p\gamma')$ data.*

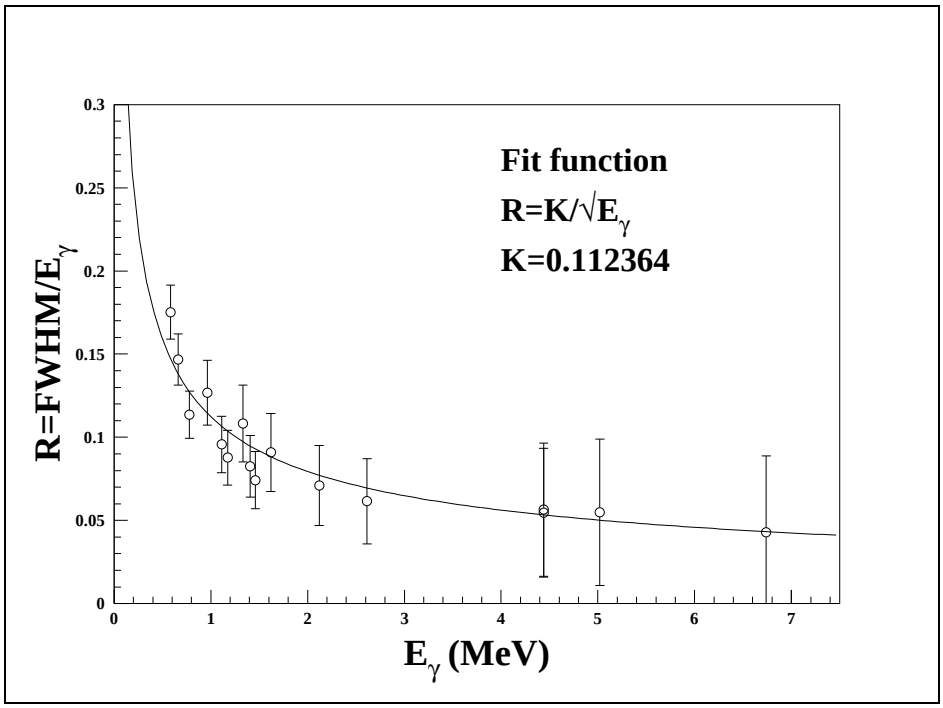

Figure 6.8: *NaI #1 resolution measured using γ-ray sources.*

completeness in fig. 6.8. The basic form of these data is described by a fit of the form $K/\sqrt{E_\gamma}$, where K is a constant, [Kno89].

Analysis of the de–excitation γ-rays, once again, proceeded in much the same way as for the ^{12}C(γ,pγ') measurement. Resolution requirements, however, did not deem a Doppler correction necessary, and the lack of charged particle tracking made it infeasible. The γ' spectra were derived as depicted in the flowchart of fig. 4.8. An extra step was required this time, when incrementing the $\mathcal{S}^{\gamma'}$ spectra, to correctly identify γ-rays in the NaI detectors.

The p–γ' spectrum of fig. 6.9 shows that a high neutron flux was observed in the NaI detectors in coincidence with protons. Due to the small detector to target distance ($\sim$15 cm), these neutrons were not separable from the γ-rays by their time–of–flight. The γ-rays were instead identified, as well as possible, by the 2–D cut, shown in fig. 6.10, of time of arrival vs. energy in the NaI detectors. The spectrum of energy, detected from the events identified as neutrons, measured from the region labelled 'neutrons' of fig. 6.10, is shown in fig. 6.11.

6.4 Selection of the (γ,pn) Channel from the (γ,pγ') Data

With this experimental setup it was possible to select the (γ,pn) reaction channel from the (γ,pγ') data, by removing the contribution to the γ' spectrum from (γ,p) events populating states in ^{13}C. This was done by selecting events from the ^{12}C+n continuum by cutting on E_{ex}>4.95 MeV in the excitation function of ^{13}C (fig. 6.4), as depicted in fig. 6.12. The contribution from (γ,pγ') events due only to states with E_{ex}<4.95 MeV in ^{13}C, can be seen in fig. 6.13. This corresponds only to a set of states at $\sim$3.68 MeV excitation energy. Above the (γ,pn) threshold the remaining γ' spectrum, displayed in fig. 6.14, shows structure believed to be mainly from ^{12}C.

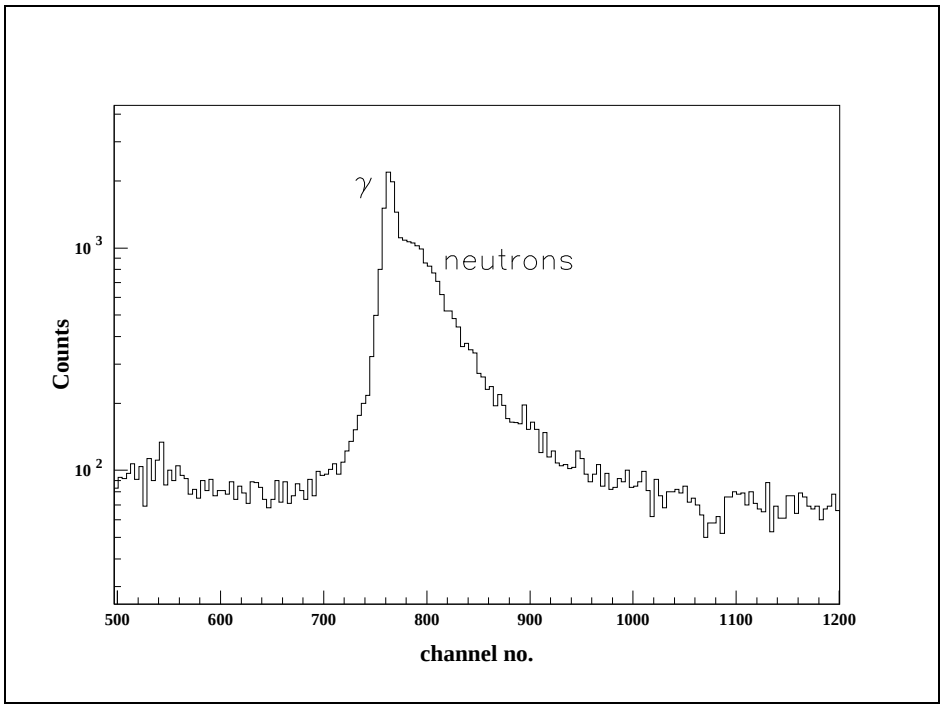

Figure 6.9: *NaI p–γ' TDC spectrum showing the presence of neutrons as well as γ-rays.*

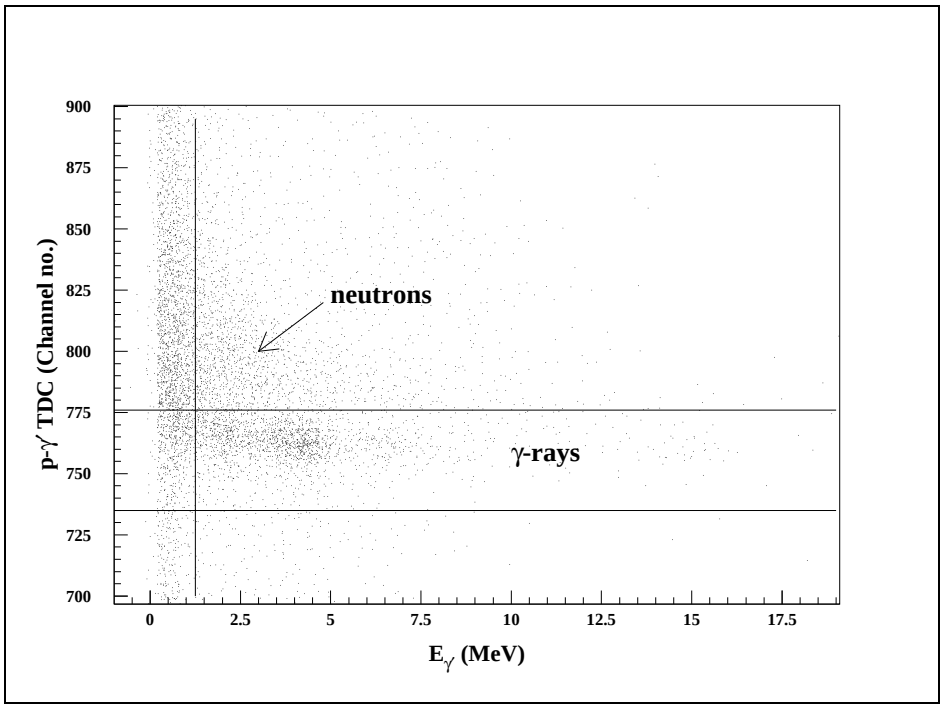

Figure 6.10: *$E_{\gamma'}$ vs. p–γ' TDC showing neutron discrimination in the NaI detectors.*

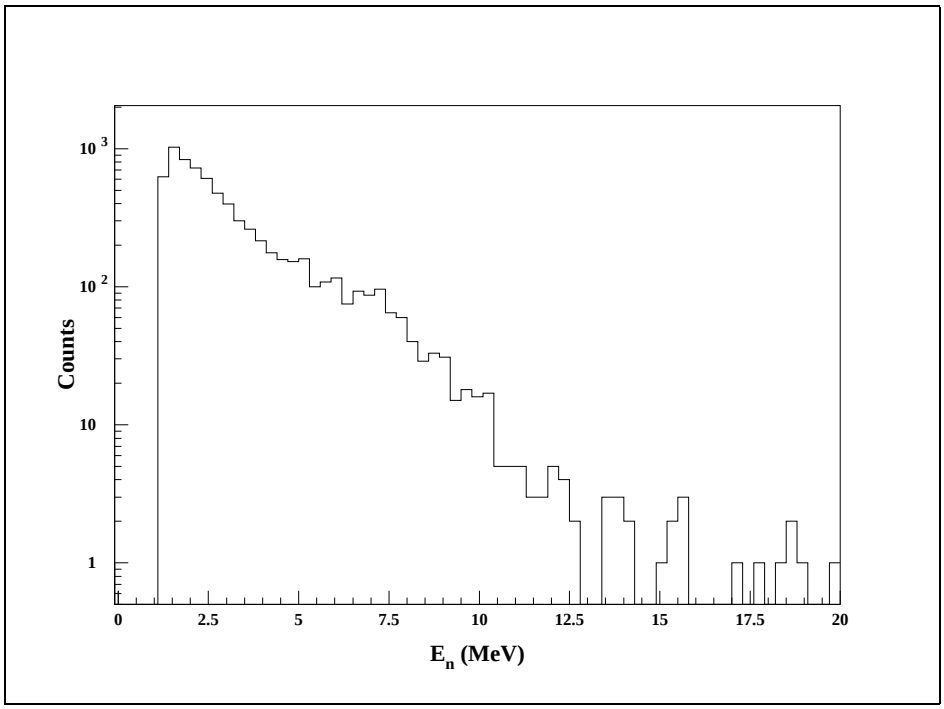

Figure 6.11: *Energy deposited in the events from the region labelled 'neutrons' in fig. 6.10.*

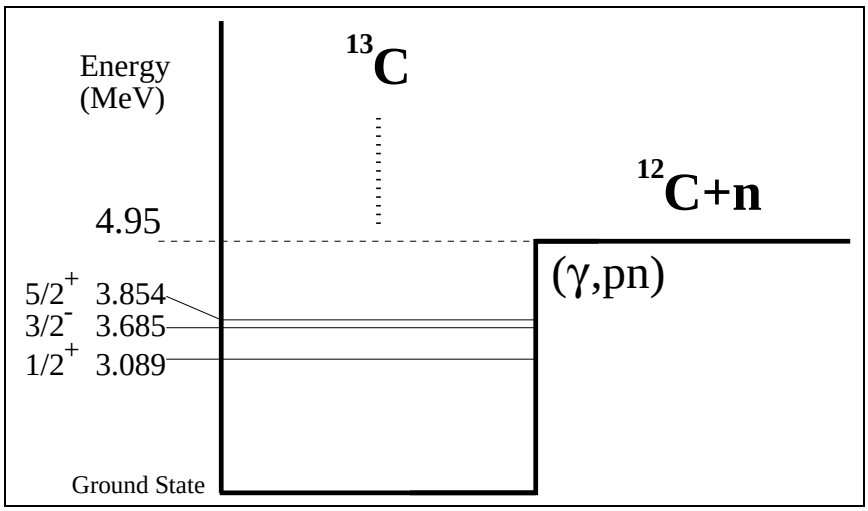

Figure 6.12: *Level scheme of ^{13}C showing the relative position of $^{12}C + n$ system.*

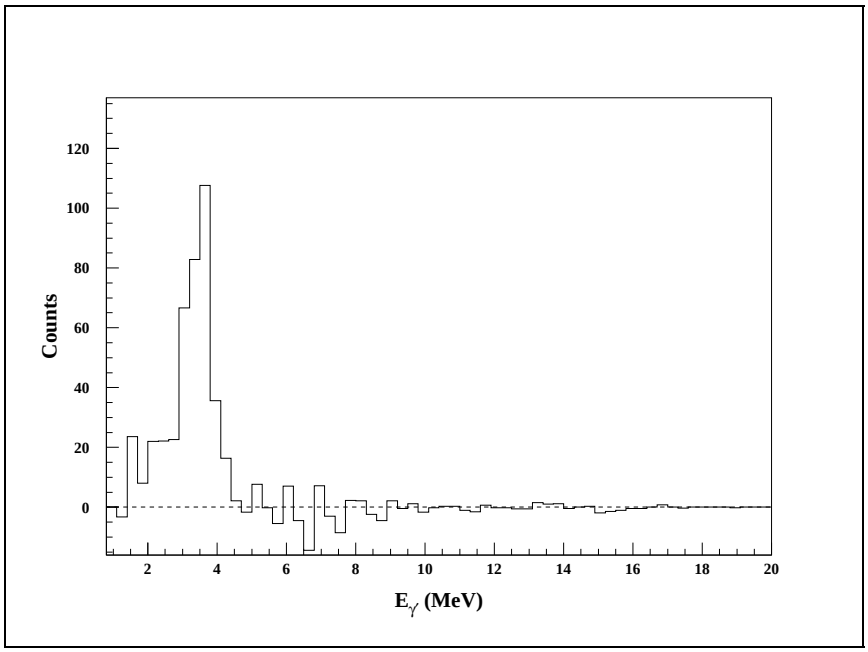

Figure 6.13: *De–excitation γ-ray spectrum from $^{14}N(\gamma,p\gamma')$ for $E_{ex}<4.95$ MeV in ^{13}C. The data are for the sum of both NaI detectors and are presented in 300 keV bins.*

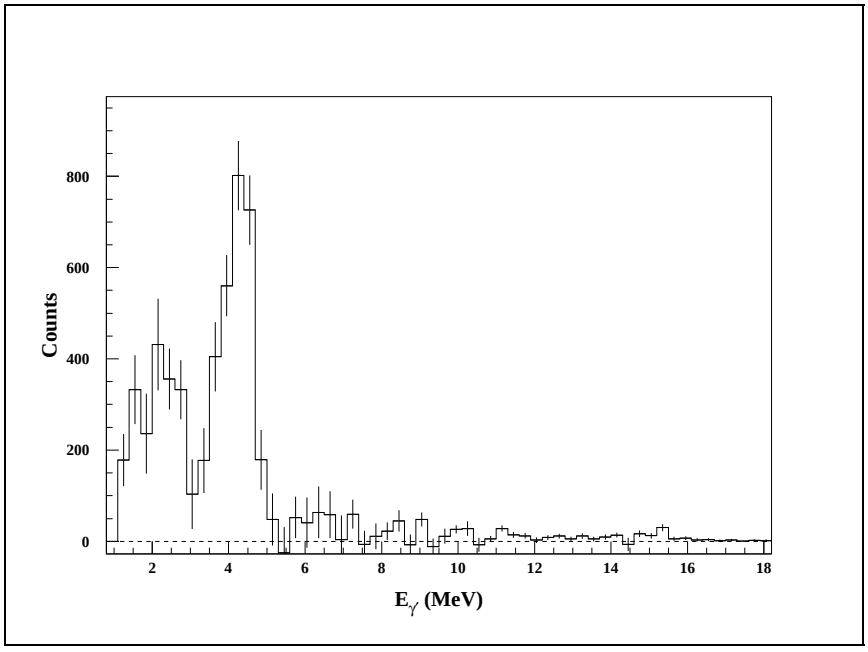

Figure 6.14: *De–excitation γ-ray spectrum from $^{14}N(\gamma,p\gamma')$, for $E_{ex}>4.95$ MeV, with tagged photons from $50.29<E_\gamma<71.29$ MeV. The data are for the sum of both NaI detectors and are presented in 300 keV bins.*

6.5 Results

The relative populations of the 4.44 and 15.11 MeV states in ^{12}C, following the ^{14}N(γ,pn) reaction has been extracted from the γ' spectrum of fig. 6.14, taken on ^{14}N(γ,pγ') (with E_{ex}>4.95 MeV). In this spectrum the main feature is a peak at ∼4.4 MeV, which corresponds to the 1st excited state of ^{12}C, at 4.44 MeV (T=0). There are also a small number of counts at ∼15 MeV. These correspond to the (T=1) 15.11 MeV state of ^{12}C, a state which is unexpected following photon absorption on T=0 p–n pairs. This spectrum is interpreted as showing evidence of a strong preference for photons to be absorbed on T=0 p–n pairs.

Only the 4.44 and 15.11 MeV states of ^{12}C are likely to be observed in this γ-ray spectrum. Even if others are populated by the reaction these are the only states which decay predominantly by γ-ray emission. Other states at 7.65, 9.64 and 12.71 MeV (with $\Gamma_\alpha/\Gamma_{total}$=99, 99 and 97.8 %, respectively) are mainly α emitting.

The structure seen at ∼2.5 MeV could be due to non–complete discrimination of the neutrons displayed in fig. 6.10 or, more probably, γ-rays from other nuclei populated by (γ,pX) reactions, where the X goes undetected.

The relative populations of the 4.44 and 15.11 MeV states were extracted from the spectrum after accounting for the γ-ray branching ratios, taken from [Ajz90], and the efficiency of the NaI detectors at the two energies. The branching ratio to the ground state for the 4.44 MeV γ-ray transition is 100 % and this state decays purely by γ-ray emission. Therefore the measured yield for this state did not require correction for other decay channels. The 15.11 MeV state, on the other hand, may decay by α emission as well as γ emission ($\Gamma_\gamma/\Gamma_{total}$=95.9 ± 4.0 %). In addition, the γ-ray branching ratio for the transition to occur between the 15.11 MeV state and the ground state of ^{12}C is $\Gamma_{15.11\rightarrow 0.0}/\Gamma_\gamma$=92±2 %. This implies a total probability of 88.3±3.2 % that a 15.11 MeV γ-ray will be emitted from ^{12}C following population of its 15.11 MeV level.

Total detection efficiencies of 100 % were assumed for the 4.44 and 15.11 MeV γ-rays in the NaI detectors, however, the measured yields were corrected with peak-to-total ratios of 56±3 and 40±3 %, respectively. These values were taken from measurements made on a similar NaI detector by [Wat72]. When measuring yields, the peaks were integrated from -27.9–+12.6 % of the peak centroid values.

Due to the fact that the Compton continuum of the 15.11 MeV γ-ray extents to zero energy, a correction was made for the yield measured from the 4.44 MeV γ-ray. The amount of contribution from this Compton continuum, beneath the 4.44 MeV peak, was estimated by calculating the average channel content from 5–14 MeV, in the spectrum of fig. 6.14. The average channel content from 5–14 MeV was 17.25 counts, which, in the 6 channels over which the 4.44 MeV γ-ray yield was integrated amounted to 103.5 counts. These counts were subtracted from the yield of the 4.44 MeV peak shown in table 6.1. Finally, the relative population between the 4.44 and 15.11 MeV states in ^{12}C, following the ^{14}N(γ,pn) reaction, was calculated and is displayed in table 6.1.

Table 6.1: *The relative population of the 4.44 and 15.11 MeV levels in ^{12}C following $^{14}N(\gamma,pn)$ relative to the population of the 4.44 MeV state.*

Level (MeV)	J^π;T	peak–to–total ratio (%)	Total Branching Ratio (%)	(γ,pnγ') Yield	Relative Population (4.44=1)
4.44	2^+;0	56±3	100	2745.5±52.4	1.00
15.11	1^+;1	40±3	88.3±3.2	196.0±14.0	0.11±0.01

The effect of angular correlations on the γ-rays detected following ^{14}N(γ,pn) events has not been accounted for in this analysis. It was deemed unnecessary for two reasons. Firstly, the spin of the target nucleus in this case is non–zero ($J^\pi=1^+$). This implies that the initial orientation of the target nucleus, with respect to the beam direction (which is totally random) may affect the m_l of the recoiling nucleus. Secondly, only the proton has

been detected and states in ^{12}C have been identified by their de–excitation γ-ray decays. Therefore, due to the neutron being undetected and the final state being 3 body, the recoiling (A-2) nucleus may have an arbitrary direction in space with respect to the direction of the detected proton. Therefore this situation is distinct from that of the ^{12}C(γ,pγ') experiment described in chapter 4. In that case the target had zero spin and the recoiling nuclei (defined by the proton detection, in a two body final state) were confined to travel in a cone directed towards the γ-ray detector. For this measurement, the effect of the target spin and the large acceptance of the angle $\theta_{\gamma'}$ have been used to assume the γ-ray distribution averages to isotropy.

It has also been assumed that, following the E_{ex}>4.95 MeV cut, the γ-ray decays from the 4.44 and 15.11 MeV states of ^{12}C all follow ^{14}N(γ,pn) events. It is true that these γ-rays may also be due to reactions of the type

$$^{14}\mathrm{N}(\gamma,\mathrm{p})^{13}\mathrm{C}^* \longrightarrow {}^{12}\mathrm{C}^*_{4.44/15.11} + n \longrightarrow {}^{12}\mathrm{C}_{gs} + \gamma' + n.$$

However, to populate the 4.44 or 15.11 MeV states of ^{12}C in this way would require the (γ,p) reaction to populate states in ^{13}C with E_{ex}>9.39 or 20.06 MeV, respectively. States with E_{ex}>20 MeV are not generally populated by the (γ,p) reaction. Some states around $E_{ex}\sim$9 MeV in ^{13}C are populated by ^{14}N(γ,p) [Ire91], but neutron decay of these states directly to the ground state of ^{12}C would be energetically favourable. It is reasonable therefore, to say that the γ-ray decays observed from states in ^{12}C follow direct population by the ^{14}N(γ,pn) reaction.

A spectrum of γ-rays from ^{14}N(γ,dγ') events was also accumulated. Unfortunately, the statistics were too poor to make any conclusions from this spectrum. The E_{ex} spectrum of ^{14}N(γ,d) (shown in fig. 6.5), however, shows strong evidence of the population of the 15.11 MeV (T=1) state of ^{12}C, with no evidence of the 4.44 MeV (T=0) 1st excited state. As stated in [Adl97b], the (γ,d) spectrum was expected to give an adequate indication of the population of this state, without use of the de–excitation γ-rays. The current finding is in disagreement with that of [Ire91], where evidence for the population of the 4.44 MeV state of ^{12}C was observed.

Chapter 7

Discussion & Summary

This thesis has presented a measurement of the reaction ^{12}C(γ,pγ'), made for the sole purpose of resolving the triplet of states at $E_{ex}\simeq$7 MeV in ^{11}B, observed previously in studies of ^{12}C(γ,p). This measurement constitutes the best energy resolution ever achieved in a measurement of the reaction (γ,p) on any nucleus, by separating the transitions to excited states in ^{11}B with a resolution of $\Delta E_{\gamma'}\sim$48 keV FWHM, for the triplet states. Therefore a factor $\sim$10 improvement in resolution, compared to that from previous (γ,p) measurements, has been achieved. The resolution is also $\sim$5 times better than that achieved by Kuzin *et al.* [Kuz98], who measured the ^{12}C(γ,pγ') reaction with NaI detectors to detect the de–excitation γ-rays. This, as far as we know, is the first time that a measurement of this kind has been made using a HPGe crystal to detect the de–excitation γ-rays.

Although the statistics available from the measurement were poor the result has proven that this experimental technique, with the detection system used, is capable of providing an accurate result. The poor statistics have disallowed the mapping out of angular distributions. However, a measurement over an integrated angular range, from direct observation of the individual states, is still new. A lack of adequate E_{ex} resolution, due to the thick (562.5 mg/cm^2) C target, did not allow separation of the various proton groups in the excitation spectrum of ^{11}B. (This thickness of target was required to increase the available statistics.) The E_{ex} resolution

(∼6 MeV FWHM) limited the possibility for identification of cascade γ-rays from states with E_{ex}>7.3 MeV in ^{11}B, which could contribute to the measured γ-ray yields at $E_{\gamma'}\simeq$6.74–7.29 MeV. It has been estimated, however, from high resolution ^{12}C(γ,p) data and the cascades which were observed in the γ' spectrum, that the contribution from this effect is low.

The $E_{\gamma'}$ resolution achieved was limited due to the shaping time (of 1 μs) used to amplify the HPGe 70 % detector signals. (This setting was required to cope with the high count rate of background signals seen by the detector.) In future measurements the $E_{\gamma'}$ resolution could possibly be improved through a better Doppler correction, if θ_p and ϕ_p were measured with improved resolution, or (through the use of segmented γ-ray detectors) if positional information on the de–excitation γ-rays were provided.

The experimental method was complicated by the γ-ray line shapes produced by the HPGe detector. The fitting procedure, necessary to extract the photopeak yields, requires accurate knowledge of the detector response function. In this measurement the response function was not well known for the main region of interest, $E_{\gamma'}\simeq$7 MeV. This is due to difficulty in finding an efficiency calibrated source with strong γ-rays at this energy. The PP efficiency, $\varepsilon_{\gamma'}$, and resolution, as well as the ratios $\frac{\varepsilon^{PP}_{\gamma'}}{\varepsilon^{SE}_{\gamma'}}$ and $\frac{\varepsilon^{PP}_{\gamma'}}{\varepsilon^{DE}_{\gamma'}}$, must be known accurately in the energy region required, for such a fitting procedure to work well.

The closeness of some energy levels, and the fact that in two cases the SE and DE peaks (*inconveniently*) coincided with, or were very close to, the PP's of lower energy γ-rays, made the de-excitation γ-ray spectrum even more difficult to interpret. It would of course be advantageous to eliminate the need for such precise knowledge of the γ-ray detector response function. The use of Compton suppression shields and pair spectrometers would make the γ' spectrum much simpler to interpret. An experiment adopting such techniques would not suffer from the problematic fitting procedure required by either the present measurement or that of Kuzin *et al.*

The main qualitative conclusion drawn from the data, however, is still clear. In the tagged photon range covered, the 6.74 MeV ($7/2^-$) state

of ^{11}B, has been observed to be the most strongly populated state of the triplet, with a strength of at least ∼1.2 times the other two, positive parity, states combined (after inclusion of the maximum angular correlation effect). This is therefore in basic agreement with the findings of Kuzin *et al.* This measurement has, however, found a stronger contribution from the $1/2^+$ state. This can be seen from the direct resolving of the two states, especially in the untagged spectrum of fig. 4.24 where the two transitions are almost equal over a larger range of incident photon energies. This measurement disagrees with [Kuz98] over the relative strength of the two positive parity states within the tagged photon range. Here the $5/2^+$ state was not seen with any considerable strength within the tagged photon range for the statistics available.

Angular correlations have also been included in the analysis. Their maximum effect on the measured cross sections has been estimated by making simplifying assumptions as to the magnetic substates (m_l) populated in the residual nucleus following the (γ,p) reaction. This effect was not studied by [Kuz98]. After applying the derived angular correlation correction factor to both data sets their agreement is less convincing. Despite this the $7/2^-$ state is still measured as the most strongly populated state of the triplet in both experiments.

The derived correction factor is a best estimate for the maximum effect which the angular correlations may have on this measurement and is not an accurate calculation of such. Precise calculation of the effect is not possible, due to the lack of knowledge of the population of the m_l magnetic substates of the residual nucleus. A direct measurement of the effect is therefore required through detection of de–excitation γ-rays both in and out of the plane of proton detection. Only such a measurement will truely resolve the issue of the importance of angular correlations in a (γ,Xγ') measurement such as this.

In the second experiment presented in this thesis an electro–induced proton knockout experiment has been performed on ^{12}C in the $\mathbf{p}_m$ range comparable to existing (γ,p) data. Transitions to the $(3/2^-)_1$, $(1/2^-)$, $(3/2^-)_2$,

$(7/2^-,1/2^+)$ doublet and $(5/2^+)$ states of ^{11}B have been resolved. A separation of the longitudinal and transverse structure functions has been performed, in parallel kinematics, for each of these transitions. The momentum distributions and separated structure functions have been compared with calculations based on the RPA model with and without the inclusion of MEC and IC contributions. The data have also been compared with CDWIA calculations constrained by the data of [Ste88a, Ste88b].

The CDWIA calculations show that the DKO model underestimates the reduced cross sections for population of the $\sim$7 MeV states in ^{11}B. This shows clearly that additional processes are required to describe the data for these states. This is confirmed by the results of the RPA calculations with MEC and IC, which reproduce the cross sections for these states more closely. Fig. 5.14 shows that this applies to the $(1/2^-)$ and $(3/2^-)_2$ states, as well as to the $\sim$7 MeV triplet states. Unfortunately, in the case of the structure functions, comparison between experiment and theory is not as conclusive as for the reduced cross sections. For the 1p–knockout transitions the RPA calculations do not provide a good description of the data. The transitions to the triplet states show better agreement, however, this is mainly due to the larger error bars on the experimental points.

The fact that the MEC effects are required to account for the (e,e′p) data implies that the (e,e′p) and (γ,p) reactions are becoming more alike at higher $\mathbf{p}_m$. Calculations for the (γ,p) reaction which include MEC's have also reproduced the data of [Kuz98] well.

In fig. 5.19 the transverse part of the ^{12}C(e,e′p) cross section has been compared with the ^{12}C(γ,p) cross sections of Ruijter *et al.* in the same $\mathbf{p}_m$ range. This is the first time that such a comparison has been undertaken. All previous comparisons of these two reactions have involved ^{12}C(e,e′p) data measured at $\mathbf{p}_m \lesssim 250$ MeV/c, and have included longitudinal contributions in the (e,e′p) cross sections.

An effective missing momentum has been employed to account for the different kinetic energy of the exiting proton, T_p, in each of the data sets. After calculation of this effective momentum, the (γ,p) data are shifted to a

higher $\mathbf{p}_m$, (these data are affected more by the effective momentum because of their lower T_p). Now the two reactions appear to show broad agreement. This suggests that the reaction mechanisms converge when studied in equivalent kinematics. There is a smooth connection for the transitions to the ground and 2.12 MeV states. The data for the 5.02 MeV transition are in agreement within the spread of the (γ,p) data. Finally, there is no longer a large discrepancy between the two reactions for the transition to the $\sim$7 MeV states, as has been reported in previous comparisons, [Ire94, Rui95a]. Even without considering how well the effective momentum accounts for the difference in FSI between the two data sets, the fact that all four transitions compare similarly, implies that the reactions have become closer. The $\sim$7 MeV states are now seen to compare almost as well as the other transitions. This has never been the case in previous comparisons [Ire94], and was the driving motivation for this thesis.

Finally, a measurement has been performed of the relative population of states in the residual nucleus, ^{12}C, following the two–nucleon knockout reaction ^{14}N(γ,pn). This measurement was made, as for the ^{12}C(γ,p) case, utilising the detection of de–excitation γ-ray emission from the residual nucleus. In this reaction the transition to the 4.44 MeV (T=0) state of ^{12}C was observed strongly. Conversely, only a weak population of the (T=1) state at 15.11 MeV was observed. No measurement for population of the (T=0) ^{12}C ground state was possible since the de–excitation γ-ray decays were being used to observe all transitions to states of ^{12}C.

An excitation spectrum has also been obtained from the reaction, ^{14}N(γ,d). Following this reaction, the population of the 15.11 MeV (T=1) state was clearly observed. The 4.44 MeV (T=0) state was not seen, in disagreement with the measurement reported by [Ire91].

The observation of suppression of the 15.11 MeV (T=1) state in ^{12}C following ^{14}N(γ,pn) is in agreement with the findings of [Isa99]. In this reference the T=1 state, at 2.31 MeV in ^{14}N, following ^{16}O(γ,pn), was not observed despite clear observation of the ground, 3.95 and 7.03 MeV (T=0) states. This result was interpreted as a preference for the absorption of

photons on p–n pairs with the quantum numbers of the free deuteron ($^3S_1$ and T=0).

In summary, this thesis has presented two new measurements which have utilised the γ decay of a residual nucleus, following population by a photonuclear reaction, to achieve high resolution data on its excitation function. These data can be used to constrain theoretical calculations of photonuclear reactions, which will in turn help to better understand the underlying structure of the nuclei involved.

In addition to this, a comparison between photo– and electro–induced proton knockout from ^{12}C has been made. This adds vital information to the comparison of real and virtual photon induced reactions. The type of comparison made here is unique as it has not been attempted in previous comparisons of the two reactions. These data can be used to interpret both reactions in an equivalent framework, which will in turn help in understanding the behaviour of nucleons in nuclei over an extended range of the nuclear wavefunction.

Appendix A

Numerical Results from the ^{12}C(e,e′p) Experiment

Tables of reduced cross sections, kinematics per $\mathbf{p}_m$ bin and the structure functions, W_L and W_T, for each resolved transition in ^{11}B following the ^{12}C(e,e′p) reaction.

Table A.1: *Reduced cross sections for the 5 resolved transitions to states in ^{11}B following the $^{12}C(e,e'p)$ reaction. Superscripts h & l represent the high and low beam energy measurements, respectively.*

$\mathbf{p}_m$ (MeV/c)	$\rho(\mathbf{p}_m)^h$ $(\mathrm{GeV/c})^{-3}$	$\Delta\rho$ (stat.) $(\mathrm{GeV/c})^{-3}$	$\rho(\mathbf{p}_m)^l$ $(\mathrm{GeV/c})^{-3}$	$\Delta\rho$ (stat.) $(\mathrm{GeV/c})^{-3}$
Ground state				
255	$2.1848\times10^{+00}$	7.5404×10^{-02}	$2.9760\times10^{+00}$	1.0168×10^{-01}
265	$1.8484\times10^{+00}$	6.7155×10^{-02}	$2.2525\times10^{+00}$	7.5381×10^{-02}
275	$1.3851\times10^{+00}$	6.0933×10^{-02}	$1.7557\times10^{+00}$	6.8256×10^{-02}
295	7.1333×10^{-01}	2.4886×10^{-02}	7.8325×10^{-01}	3.6824×10^{-02}
305	5.1893×10^{-01}	2.0310×10^{-02}	6.0735×10^{-01}	2.5075×10^{-02}
315	4.1364×10^{-01}	1.9478×10^{-02}	4.7723×10^{-01}	2.4020×10^{-02}
2.12 MeV state				
255	4.5892×10^{-01}	3.7237×10^{-02}	5.0449×10^{-01}	4.0837×10^{-02}
265	3.4883×10^{-01}	3.1528×10^{-02}	4.4021×10^{-01}	3.6280×10^{-02}
275	2.8885×10^{-01}	3.0163×10^{-02}	3.4033×10^{-01}	3.6309×10^{-02}
295	1.2360×10^{-01}	1.1055×10^{-02}	1.1171×10^{-01}	1.3121×10^{-02}
305	9.0257×10^{-02}	9.2597×10^{-03}	1.1198×10^{-01}	1.2016×10^{-02}
315	6.1162×10^{-02}	8.4276×10^{-03}	5.8698×10^{-02}	1.1415×10^{-02}
5.02 MeV state				
255	2.6935×10^{-01}	2.8275×10^{-02}	3.6157×10^{-01}	3.2281×10^{-02}
265	1.8937×10^{-01}	2.3860×10^{-02}	2.7022×10^{-01}	2.8754×10^{-02}
295	7.3818×10^{-02}	8.5754×10^{-03}	1.0005×10^{-01}	1.1060×10^{-02}
305	6.0782×10^{-02}	7.3952×10^{-03}	4.3344×10^{-02}	8.1706×10^{-03}
6.74 & 6.79 MeV doublet				
255	1.4592×10^{-01}	2.4018×10^{-02}	1.6885×10^{-01}	2.4897×10^{-02}
265	1.3077×10^{-01}	2.6553×10^{-02}	1.3718×10^{-01}	2.4086×10^{-02}
295	7.9341×10^{-02}	9.2515×10^{-03}	1.0249×10^{-01}	1.2377×10^{-02}
305	6.1597×10^{-02}	8.8079×10^{-03}	8.0693×10^{-02}	1.2038×10^{-02}
7.29 MeV state				
255	1.2494×10^{-01}	2.7966×10^{-02}	1.3680×10^{-01}	2.5319×10^{-02}
265	9.1959×10^{-02}	2.9497×10^{-02}	9.8415×10^{-02}	2.7156×10^{-02}
295	3.5938×10^{-02}	8.7662×10^{-03}	5.4024×10^{-02}	1.2780×10^{-02}
305	2.5025×10^{-02}	9.1221×10^{-03}	3.8872×10^{-02}	1.3900×10^{-02}

Table A.2: *Kinematics for the 1p transitions to states in ^{11}B following the $^{12}C(e,e'p)$ reaction. The variables q, ω and T_p were chosen to be constant between the high and low beam energy measurements. The values quoted for these variables are the mean of the values measured in each of the two measurements.*

$\mathbf{p}_m$ (MeV/c)	q (MeV/c)	ω (MeV)	T_p (MeV)	E_0 (MeV)	$E_{e'}$ (MeV)	θ_e (deg)	θ_e (deg)
Ground state						HIGH energy kinematics	
255	338.03	190.63	171.45	585.10	395.50	33.614	38.918
265	337.54	195.84	176.43	585.10	389.61	33.423	38.971
275	337.18	201.19	181.52	585.10	384.10	33.148	38.967
295	297.12	191.44	171.18	585.10	394.91	27.215	36.003
305	297.03	196.73	176.22	585.10	388.90	26.893	35.887
315	298.17	202.84	182.03	585.10	382.40	26.691	35.982
						LOW energy kinematics	
255	338.03	190.63	171.45	378.50	186.89	63.576	28.564
265	337.54	195.84	176.43	378.50	182.34	63.203	28.462
275	337.18	201.19	181.52	378.50	177.19	63.037	28.422
295	297.12	191.44	171.18	378.70	185.96	50.972	27.769
305	297.03	196.73	176.22	378.70	181.34	50.449	27.590
315	298.17	202.84	182.03	378.70	175.63	50.204	27.734
2.12 MeV state						HIGH energy kinematics	
255	337.58	192.38	171.11	585.10	393.29	33.502	39.117
265	338.17	198.27	176.74	585.10	386.84	33.512	39.044
275	336.96	203.06	181.26	585.10	381.78	33.101	39.220
295	296.63	193.14	170.77	585.10	392.93	27.033	35.782
305	298.54	199.71	177.10	585.10	385.28	27.079	36.001
315	297.31	204.12	181.25	585.10	380.72	26.443	35.761
						LOW energy kinematics	
255	337.58	192.38	171.11	378.50	185.57	63.361	28.557
265	338.17	198.27	176.74	378.50	180.29	63.175	28.468
275	336.96	203.06	181.26	378.50	175.76	62.768	28.453
295	296.63	193.14	170.77	378.70	184.54	50.677	27.830
305	298.54	199.71	177.10	378.70	178.99	50.371	27.579
315	297.31	204.12	181.25	378.70	174.74	49.779	27.991
5.02 MeV state						HIGH energy kinematics	
255	337.76	195.28	171.17	585.10	390.02	33.536	39.110
265	338.12	201.14	176.82	585.10	383.55	33.394	39.097
295	296.76	195.93	170.72	585.10	389.52	26.929	36.018
305	299.00	202.62	177.11	585.10	382.27	26.975	36.260
						LOW energy kinematics	
255	337.76	195.28	171.17	378.50	183.02	63.131	28.452
265	338.12	201.14	176.82	378.50	177.78	63.092	28.525
295	296.76	195.93	170.72	378.70	182.33	50.338	27.942
305	299.00	202.62	177.11	378.70	176.21	50.209	27.796

Table A.3: *Kinematics for the transitions to the triplet of states in ^{11}B at $E_{ex} \simeq 7$ MeV following the $^{12}C(e,e'p)$ reaction. The variables q, ω and T_p were chosen to be constant between the high and low beam energy measurements. The values quoted for these variables are the mean of the values measured in each of the two measurements.*

$\mathbf{p}_m$ (MeV/c)	q (MeV/c)	ω (MeV)	T_p (MeV)	E_0 (MeV)	$E_{e'}$ (MeV)	θ_e (deg)	θ_e (deg)
6.74 & 6.79 MeV doublet					HIGH energy kinematics		
255	337.51	196.98	171.10	585.10	388.30	33.404	39.113
265	337.34	202.24	176.06	585.10	382.65	33.142	39.432
295	298.13	198.46	171.49	585.10	386.40	27.076	36.044
305	299.20	204.41	177.14	585.10	379.83	26.905	35.717
					LOW energy kinematics		
255	337.51	196.98	171.10	378.50	181.36	63.098	28.324
265	337.34	202.24	176.06	378.50	176.59	63.018	28.781
295	298.13	198.46	171.49	378.70	180.34	50.395	27.860
305	299.20	204.41	177.14	378.70	175.11	50.003	27.737
7.29 MeV state					HIGH energy kinematics		
255	338.26	198.02	171.52	585.10	386.32	33.660	39.330
265	337.50	203.10	176.38	585.10	381.64	33.250	39.083
295	297.82	198.81	171.30	585.10	386.64	26.926	35.777
305	298.40	204.46	176.66	585.10	379.90	26.729	36.343
					LOW energy kinematics		
255	338.26	198.02	171.52	378.50	181.30	62.935	28.790
265	337.50	203.10	176.38	378.50	175.83	62.812	28.597
295	297.82	198.81	171.30	378.70	179.42	50.453	27.554
305	298.40	204.46	176.66	378.70	174.92	49.837	27.464

Table A.4: *Structure functions for the 5 resolved transitions to states in ^{11}B following the $^{12}C(e,e'p)$ reaction.*

$\mathbf{p}_m$ (MeV/c)	$\mathbf{p}_m^{eff}$ (MeV/c)	W_T $(\mathrm{GeV/c})^{-3}$	ΔW_T $(\mathrm{GeV/c})^{-3}$	W_L $(\mathrm{GeV/c})^{-3}$	ΔW_L $(\mathrm{GeV/c})^{-3}$
Ground state					
255	269.32	0.736	0.123	0.157	0.193
265	278.18	0.465	0.097	0.325	0.158
275	287.32	0.417	0.081	0.147	0.129
295	309.77	0.113	0.053	0.212	0.076
305	318.13	0.124	0.039	0.101	0.057
315	327.08	0.106	0.035	0.067	0.050
2.12 MeV state					
255	268.35	0.075	0.039	0.135	0.064
265	277.84	0.100	0.033	0.044	0.055
275	286.75	0.070	0.032	0.052	0.052
295	308.99	0.000	0.016	0.060	0.023
305	318.09	0.028	0.014	0.009	0.020
315	326.06	0.006	0.013	0.021	0.018
5.02 MeV state					
255	268.53	0.090	0.030	0.020	0.048
265	277.66	0.078	0.025	-0.007	0.040
295	308.47	0.031	0.013	-0.002	0.019
305	317.78	-0.009	0.010	0.040	0.015
6.74 & 6.79 MeV doublet					
255	268.38	0.030	0.022	0.034	0.038
265	277.38	0.022	0.023	0.037	0.039
295	308.40	0.030	0.014	0.002	0.020
305	317.06	0.026	0.014	-0.002	0.019
7.29 MeV state					
255	268.38	0.023	0.024	0.032	0.042
265	277.38	0.016	0.025	0.024	0.043
295	308.40	0.020	0.014	-0.007	0.019
305	317.06	0.016	0.015	-0.007	0.021

Appendix B

Optical Model Parameters for CDWIA Calculations

Table B.1: *Optical potential parameters used to simulate FSI for the exiting proton in the CDWIA calculations.*

V_0 (MeV)	r_0 (fm)	a_0 (fm)	W (MeV)	r (fm)	a (fm)	V_{so} (MeV)	r_{so} (fm)	a_{so} (fm)
6.571	1.2	0.686	14.478	1.156	0.603	3.054	0.899	0.447

Bibliography

[Adl90] Jan–Olof Adler *et al.*, Nucl. Instr. and Meth. **A294**, 15 (1990).

[Adl97a] Jan–Olof Adler *et al.*, Nucl. Instr. and Meth. **A388**, 17 (1997).

[Adl97b] Jan–Olof Adler *et al.*, MAX–LAB proposal (1997), unpublished.

[Ajz90] F. Ajzenberg–Selove, Nucl. Phys. **A506**, 1 (1990).

[Asc97] E.C. Aschenauer *et al.*, Nucl. Phys. **A615**, 33 (1997).

[Bob92] I. Bobeldijk *et al.*, Phys. Lett. **B281**, 25 (1992).

[Bob95] I. Bobeldijk, Ph.D. Thesis, Universiteit van Utrecht (1995), unpublished.

[Bof80a] S. Boffi, C. Giusti and F.D. Pacati, Nucl. Phys. **A336**, 416 (1980).

[Bof80b] S. Boffi, C. Giusti and F.D. Pacati, Nucl. Phys. **A336**, 437 (1980).

[Bof82] S. Boffi *et al.*, Nucl. Phys. **A386**, 599 (1982).

[Bof96] S. Boffi, C. Giusti, F.D. Pacati and M. Radici, "Electromagnetic Response of Atomic Nuclei", Clarendon Press, Oxford (1996).

[Canb] Canberra Nuclear Instruments Catalogue, 9^{th} Edition.

[Cav84] M. Cavinato *et al.*, Nucl. Phys. **A422**, 237 (1984).

[Cle61] A.B. Clegg and G.R. Satchler, Nucl. Phys. **27**, 431 (1961).

[Dav90] T. Davison *et al.*, Nucl. Instr. and Meth. **A288**, 245 (1990).

[DeF67] T. de Forest Jr., Ann. of Phys. **45**, 365 (1967).

[DeF83] T. de Forest Jr., Nucl. Phys. **A392**, 232 (1983).

[Dog95] I.V. Dogyust *et al.*, Phys. of Atomic Nuclei **58**, No. 5, 712 (1995).

[Eis76] J.M. Eisberg and W. Greiner, Nuclear Theory: Vol. 2, 2^{nd} Ed., "Excitation Mechanisms of the Nucleus", North–Holland Publishing Co., (1976).

[Eri82] M. Eriksson, Nucl. Instr. and Meth. **196**, 331 (1982).

[Fin77] D.J.S. Findlay and R.O. Owens, Nucl. Phys. **A292**, 53 (1977).

[Fin78] D.J.S. Findlay and R.O. Owens, Phys. Lett. **B74**, 305 (1978).

[Fru84] S. Frullani and J. Mougey, Adv. Nucl. Phys. **14**, 1 (1984).

[Gar81] M. Gari and H. Hebach, Phys. Rep. **72**, 1 (1981).

[Gel53] M. Gell–Mann and V.L. Telegdi, Phys. Rev. **91**, 169 (1953).

[Giu80] C. Giusti and F.D. Pacati, Nucl. Phys. **A336**, 427 (1980).

[Giu87] C. Giusti and F.D. Pacati, Nucl. Phys. **A473**, 717 (1987).

[Giu88] C. Giusti and F.D. Pacati, Nucl. Phys. **A485**, 461 (1988).

[Her87] J.W. den Herder, Ph.D. thesis, Universiteit van Amsterdam, (1987), unpublished.

[Her88] J.W. den Herder, Nucl. Phys. **A490**, 507 (1988).

[Hoo90] L. Van Hoorebeke *et al.*, Phys. Rev. **C42**, R1179 (1990).

[Hoo92a] L. Van Hoorebeke *et al.*, Phys. Rev. **C45**, 482 (1992).

[Hoo92b] L. Van Hoorebeke *et al.*, Nucl. Instr. and Meth. **A321**, 230 (1992).

[Ire91] D.G. Ireland, Ph.D. thesis, University of Edinburgh (1991), unpublished.

[Ire93] D.G. Ireland *et al.*, Nucl. Phys. **A554**, 173 (1993).

[Ire94] D.G. Ireland and G. van der Steenhoven, Phys. Rev. **C49**, 2182 (1994).

[Isa96] L. Isaksson, Ph.D. thesis, Lund University, (1996), unpublished.

[Isa99] L. Isaksson *et al.*, Phys. Rev. Lett. **83**, 3146 (1999).

[Joh96] J.I. Johansson *et al.*, Nucl. Phys. **A605**, 517 (1996).

[Joh97] J.I. Johansson and H.S. Sherif, Phys. Rev. **C56**, 328 (1997).

[Kes96] L.J.H.M. Kester *et al.*, Phys. Lett. **B366**, 44 (1996).

[Kin84] K.J. King and T.L. Johnson, Nucl. Instr. and Meth. **227**, 257 (1984)

[Kno89] G.F. Knoll, "Radiation Detection and Measurement", 2nd Ed., J. Wiley and Sons, (1989).

[Kuz98] A. Kuzin *et al.*, Phys. Rev. **C58**, 2167 (1998).

[Kuz99] A. Kuzin, Ph.D. thesis, University of Melbourne (1999), unpublished.

[Lap00] L. Lapikás *et al.*, Phys. Rev. **C61**, 064325 (2000).

[Lappc] L. Lapikás, private communication.

[Lev51] J.S. Levinger, Phys. Rev. **84**, 43 (1951).

[Lev79] J.S. Levinger, Phys. Lett. **B82**, 181 (1979).

[Lin83] L.J.Lindgren and M. Eriksson, Nucl. Instr. and Meth. **214**, 179 (1983).

[Lin90] L.J.Lindgren and M. Eriksson, Nucl. Instr. and Meth. **A294**, 10 (1990).

[Lot92] G.M. Lotz and H.S. Sherif, Nucl. Phys. **A537**, 285 (1992).

[Mat76] J.L. Matthews *et al.*, Nucl. Phys. **A267**, 51 (1976).

[McD88] J.P. M^{c}Dermott *et al.*, Phys. Rev. Lett. **61**, 814 (1988).

[McG86] J.C. M^{c}George *et al.*, Phys. Lett. **B179**, 212 (1986).

[Owe90] R.O. Owens, Nucl. Instr. and Meth. **A288**, 574 (1990).

[Owe91] R.O. Owens *et al.*, J. Phys. G: Nucl. Part. Phys **17**, 261 (1991).

[Qui88] E.N.M. Quint, Ph.D. thesis, Universiteit van Amsterdam, (1988), unpublished.

[Rau96] A.W. Rauf, Ph.D. thesis, University of Edinburgh, (1996), unpublished.

[Ros50] M.N. Rosenbluth, Phys. Rev. **79**, 615 (1950).

[Ros67] H.J. Rose and D.M. Brink, Rev. Mod. Phys. **39** No. 2, 306 (1967).

[Rui95a] H. Ruijter *et al.*, Ph.D. thesis, Lund University, (1995), unpublished.

[Rui95b] H. Ruijter, User Manual – Lund Data Acquisition System, (1995), unpublished.

[Rui96] H. Ruijter *et al.*, Phys. Rev. **C54**, 3076 (1996).

[Ryc88] J. Ryckebusch *et al.*, Nucl. Phys. **A476**, 237 (1988).

[Ryc92] J. Ryckebusch *et al.*, Phys. Rev. **C46**, R829 (1992).

[Ryc99] J. Ryckebusch *et al.*, Phys. Rev. **C60**, 034604 (1999).

[Rycpc] J. Ryckebusch, private communication.

[Sau95] P. Sauer, Ph.D. thesis, Institute für Kernphysik, Johannes Gutenberg–Universität, Mainz (1995), unpublished.

[Sch78] B. Schoch, Phys. Rev. Lett. **41**, 80 (1978).

[Sch91] M. van der Schaar, Ph.D. thesis, Rijksuniversiteit van Utrecht (1991), unpublished.

[Sha67] S.M. Shafroth, "Scintillation Spectroscopy of Gamma Radiation", Vol. 1, Gordon and Breach Science Publishers (1967).

[Sho88] A.C. Shotter *et al.*, Phys. Rev. **C37**, 1354 (1988).

[Sie65] Siegbahn, "α-, β- and γ-ray spectroscopy", Vol. 2, North–Holland Publishing Company, Amsterdam (1965).

[Sim92] D.A. Sims, Phys. Rev. **C45**, 479 (1992).

[Spr88] S.V. Springham, Ph.D thesis, University of Edinburgh (1988), unpublished.

[Spr90] S.V. Springham *et al.*, Nucl. Phys. **A517**, 93 (1990).

[Ste88a] G. van der Steenhoven *et al.*, Nucl. Phys. **A480**, 547 (1988).

[Ste88b] G. van der Steenhoven *et al.*, Nucl. Phys. **A484**, 445 (1988).

[Ste90] G. van der Steenhoven and H. Blok, Phys. Rev. **C42**, 2597 (1990).

[Sta99] R. Starink, Ph.D. thesis, Vrije Universiteit van Amstersam (1999), unpublished.

[Tho90] S.L. Thomas *et al.*, Nucl. Instr. and Meth. **A288**, 212 (1990).

[Tsa74] Yung–Su Tsai, Rev. Mod. Phys. **46**, 815 (1974).

[Übe71] H. Überall, "Electron Scattering from Complex Nuclei", Vols. 1 and 2, Academic Press, (1971).

[Ver89] W.J. Vermeer *et al.*, Phys. Lett. **B217**, 28 (1989).

[Vri84] C. de Vries *et al.*, Nucl. Instr. and Meth. **223**, 1 (1984).

[Wat72] R.B. Watson, Ph.D. Thesis, Australian National University (1972), unpublished.

[Win68] W.G. Winn and D.G. Sarantities, Nucl. Instr. and Meth. **66**, 61 (1968).

[Wit90] P.K.A. de Witt Huberts, J. Phys. G: Nucl. Part. Phys. **16**, 507 (1990).

[Wit93] P.K.A. de Witt Huberts, Nucl. Phys. **A553**, 845c (1993).

[Wit96] P.K.A. de Witt Huberts *et al.*, Nucl. Phys. News **6**, No. 2, 15 (1996).